STRUCTURE AND BONDING

Volume 20

Editors: J. D. Dunitz, Zürich
P. Hemmerich, Konstanz · R. H. Holm, Cambridge
J. A. Ibers, Evanston · C. K. Jørgensen, Genève
J. B. Neilands, Berkeley · D. Reinen, Marburg
R. J. P. Williams, Oxford

With 57 Figures

The format of the volumes in this series has been changed and slightly enlarged to allow a more rational use of paper. More text than before can now be printed on each page. We hope in this way to counter the effects of rising prices.

Das Format der Bände dieser Reihe ist geändert und geringfügig vergrößert worden. Das neue Format gestattet eine bessere Papiernutzung, da auf jeder Seite mehr Text untergebracht werden kann als zuvor. Wir wollen durch diese Rationalisierungsmaßnahme dem Preisanstieg entgegenwirken.

Contents

The Role of Divalent Cations in the Mechanism of Enzyme Catalyzed Phosphoryl and Nucleotidyl Transfer Reactions*

Albert S. Mildvan and **Charles M. Grisham**

The Institute for Cancer Research, 7701 Burholme Avenue, Fox Chase, Philadelphia, PA, USA

Table of Contents

I. Introduction

The enzyme-catalyzed transfer of simple and substituted phosphoryl groups, such as nucleotidyl groups, are among the most ubiquitous and fundamental processes in biochemistry. Thus organisms conserve and expend energy by phosphoryl transfer to ADP and from ATP. They synthesize, repair and degrade nucleic acids by nucleotidyl transfer to polynucleotides or to water. Almost all of the enzymes which catalyze these reactions require divalent cations as added cofactors or contain them as tightly bound components which purify with the enzyme. In animal cells the predominant divalent cation available for enzyme activation is Mg^{2+}. For magnetic resonance studies with pure enzymes, Mg^{2+} may generally by replaced by the paramagnetic ions Mn^{2+} or Co^{2+} which provide comparable activation and which serve as probes for investigating structural and kinetic properties of the active site (1, 2).

This article will consider recent advances in the mechanism of model phosphoryl transfer reactions, magnetic resonance studies of phosphoryl and nucleotidyl transerring enzymes in solution and Xray diffraction studies in the crystalline state which have clarified or at least have suggested the role of the essential divalent cation.

II. Chemical Mechanisms of Phosphoryl Transfer

Phosphoryl and nucleotidyl transfer reactions are nucleophilic displacements on phosphorus (3—6), and like analogous displacements on carbon (7) or on metal ions (5), have been found to take place by mechanisms varying between two extreme or limiting cases: 1. In the dissociative or $S_N 1$ mechanism the initial departure of the leaving nucleophile, yields the planar triply coordinate metaphosphate anion as a reactive chemical intermediate (3, 8), which then combines with the entering ligand on either face of the metaphosphate plane 2. In the associative

$$\text{X} - \overset{\overset{\displaystyle O}{\|}}{\underset{\underset{\displaystyle \bar{O}}{}}{\text{P}}} \overset{\bar{O}}{} \longrightarrow \text{X:} + \overset{O - O^-}{\underset{O}{\text{P}}} \xrightarrow{:Y} \overset{O\ O^-}{\underset{\bar{O}}{\text{P}}} - Y \quad (1)$$
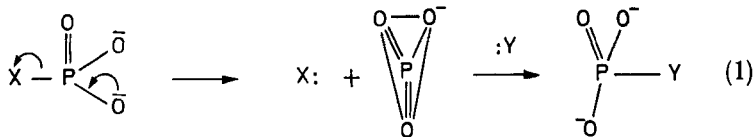
or $S_N 2$ mechanism, the entering nucleophile first binds to phosphorus along the axis of the trigonal bipyramid resulting in the formation of a pentacoordinate phosphorane either as a transition state with a lifetime $\tau = 10^{-13}$ sec or as a reactive intermediate, ($\tau > 10^{-13}$ sec). The leaving

nucleophile then dissociates along the opposite axis of the trigonal bypyramid. As described by Equation 2, the stereochemistry of the

$$X-\overset{\overset{\displaystyle O}{\|}}{\underset{\displaystyle\bar{O}}{P}}\diagdown\bar{O} \ + \ Y \ \longrightarrow \ X-\overset{\bar{O}-\bar{O}}{\underset{O}{P}}-Y \ \longrightarrow \ X \ + \ \overset{\bar{O}\ \ \bar{O}}{\underset{O}{P}}-Y \quad (2)$$
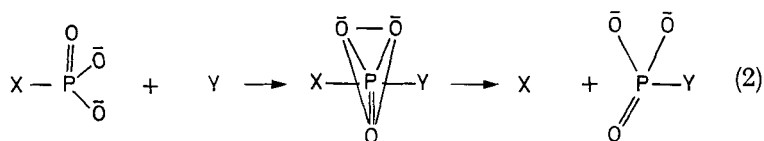
S_N2 displacement is "in line", that is, the bond angle between entering and leaving groups is 180°.

A stereochemical possibility unique to the associative mechanism is "adjacent" displacement in which the bond angle between entering and leaving groups is 90°. This possibility results from the ability of the pentacoordinate phosphorane intermediate to undergo pseudorotation (9, 10) which, with certain restrictions (11) interchanges axial and equatorial ligands. Nucleophilic displacements on stable phosphoranes appear to proceed via an associative mechanism with hexacoordinated phosphorus intermediates (12, 13). The biochemical relevance of such displacements has not been established.

As in carbon chemistry (6) and in coordination chemistry (5) mechanisms intermediate between the limiting dissociative and associative cases are found. Model studies (3, 4) indicate that both of the limiting mechanisms of phosphoryl transfer are substantially accelerated by electron withdrawal from the leaving group, lowering its pK_A. Such electron withdrawal may be accomplished by selective protonation, metal coordination or by appropriate covalent substituents.

Protonation, metal coordination, or further esterification of the transferrable phosphoryl group itself, profoundly retards the S_N1 mechanisms (3), presumably because of the decreased availability of lone pair electrons of oxygen for π bonding to phosphorus as metaphosphate is expelled, but accelerates the S_N2 mechanism by charge neutralization (6), and possibly by electron withdrawal from phosphorus. In addition, metal coordination could accelerate S_N2 displacements by five additional mechanisms (5). Chelation of the phosphoryl group could

a) induce strain in the ground state,

b) stabilize the phosphorane transition state,

c) or serve as a template for pseudorotation.
   Metal ions could also

d) coordinate and promote the nucleophilicity of the entering ligand or

e) simultaneously coordinate the entering ligand and the phosphoryl group undergoing nucleophilic attack transforming a bimolecular to a unimolecular reaction (5, 6).

Since more modes of accelerating S_N2 displacements have been defined, and since greater stereochemical control is possible with them, it might be anticipated that more enzymes would utilize associative rather than dissociative pathways.

III. Metal-Phosphorus Distances

Almost all enzyme catalyzed nucleophilic displacements on phosphorus require divalent metal ions either as added cofactors or in metalloenzymes. From the above mechanistic considerations, direct coordination by the metal ion of the phosphoryl group undergoing transfer or of the attacking nucleophile or both would strongly suggest an S_N2 mechanism and would argue against an S_N1 mechanism, while coordination of the leaving group would facilitate either an S_N1 or S_N2 mechanism. Hence, a determination of the location of the metal ion with respect to the phosphoryl group undergoing transfer in the active complex would yield insight into the mechanism. As pointed out in detail elsewhere (1, 2), nuclear relaxa-
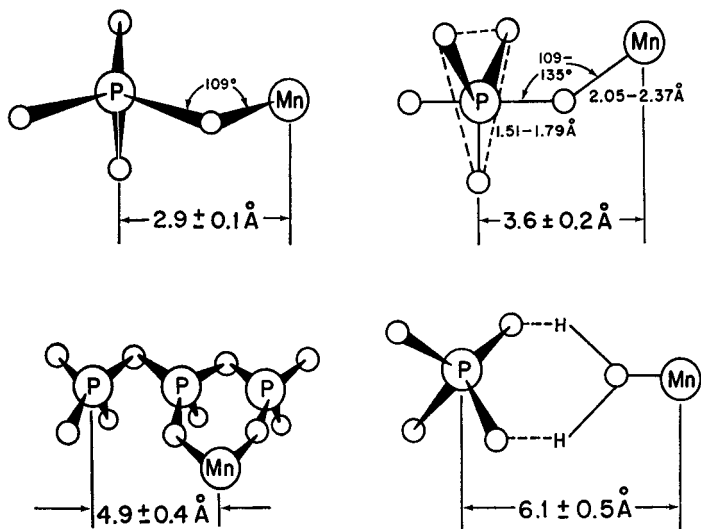
Fig. 1. Manganese to phosphorus distances in inner sphere, distorted inner sphere, adjacent pyrophosphate and second sphere complexes from crystallographic and model building studies. Original references are given in (14—16). Corresponding distances in Ca^{2+} complexes would be 0.2 Å greater and in Mg^{2+} complexes 0.1 Å smaller

tion induced by paramagnetic metal ions such as Mn^{2+} can be used to determine distances between the paramagnetic metal ion and magnetic nuclei (^{19}F, ^{1}H, ^{31}P, ^{13}C) of substrates and substrate analogs in enzyme complexes. When such studies are carried out at several magnetic fields to yield an independent evaluation of the correlation time, the precision attainable in such distance calculations, (≤ 0.1 Å) exceeds that of protein crystallography. This results from the fact that the nuclear relaxation rate obtained from the NMR data is inversely related to the sixth power of the distance while the electron density map derived from the crystallographic data is related to the first power of the distance. Small molecule crystallography is a higher resolution technique with a precision better than ± 0.01 Å. From the results of small molecule crystallography and molecular model studies summarized in Fig. 1 (14—16) the Mn^{2+} to phosphorus distance is ~ 3 Å for an inner sphere monodentate complex of tetrahedral phosphate; ~ 4 Å for an axial oxygen complex of a penta-coordinate phosphorane i.e., a "distorted" inner sphere complex; ~ 5 Å for Mn^{2+} chelated by an adjacent pyrophosphate in a triphosphate chain; and ~ 6 Å for a second sphere complex in which an inner sphere water or a ligand of comparable size intervenes between the Mn^{2+} and phosphate. Corresponding distances in Ca^{2+} complexes would be 0.2 Å greater and in Mg^{2+} complexes 0.1 Å smaller.

IV. Nucleotidyl Transfer Enzymes

A. Staphylococcal Nuclease

As a result of extensive studies of its primary, secondary and tertiary structure by chemical degradation (17), and synthesis (18), crystallographic (19, 20), and magnetic resonance techniques (21), a great deal of information is available on the active site of this Ca^{2+} activated nucleotidyl transfer enzyme. Comprehensive reviews of each aspect of this work have been published (17, 22, 23), and various mechanisms of this reaction have been considered in detail (16). A reasonable mechanism, consistent with all of the structural and kinetic data is an in-line, associative (S_N2) nucleophilic displacement on the phosphodiester phosphorus by a hydroxyl ligand coordinated to the enzyme bound Ca^{2+} (Fig. 2). An S_N1 mechanism is deemed unlikely because of the strong hydrogen bonding of the phosphate oxygens by two arginine-guanidinium cations from the enzyme ((22), Fig. 2)) which would inhibit an S_N1 mechanism, and by the lack of a catalytic role for the nearby and essential Ca^{2+} in such a mechanism. The enzyme bound Ca^{2+}, which is coordinated by

5
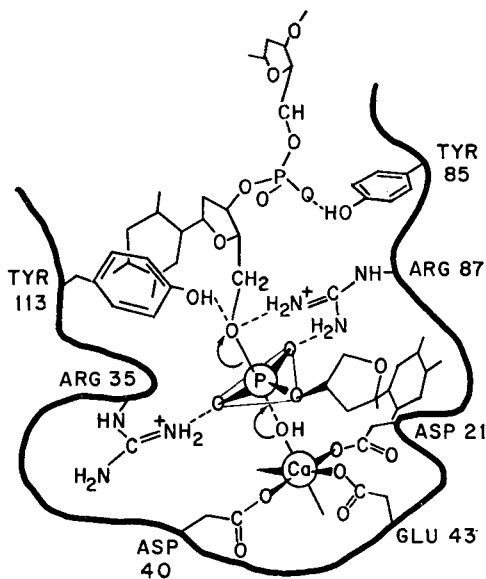
Fig. 2. Suggested mechanism for Staphyloccal nuclease based on crystallography (*19, 20, 22*), chemical degradation (*17*), synthesis (*18*), nuclear magnetic resonance (*21, 23, 24*), and kinetic studies (*25*)

3 or 4 carboxylate ligands, is at a distance from the phosphorus (4.7 $\pm$ 0.2 Å) which could permit an intervening water or hydroxyl ligand. Alternatively the value of 4.7 Å could result from a time or space average of 50% inner sphere complex (3.1 Å) and 50% second sphere complex (6.3 Å).

B. DNA Polymerases

The reaction catalyzed by this class of enzymes is (*26, 27*):

$$(3)$$
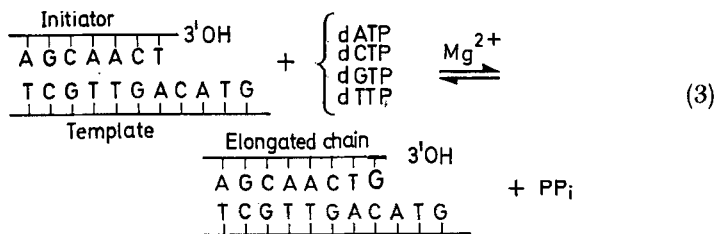
The templates which determine the base sequence of the product are either polydeoxyribonucleotides or polyribonucleotides, the initiator is either an oligodeoxyribonucleotide or an oligoribonucleotide, and the substrates are deoxyribonucleoside triphosphates. A proposed distinction between enzymes which utilized only polydeoxyribonucleotide templates from those which used only polyribonucleotide templates, and the introduction of the term "reverse transcriptase" for the latter are probably not justified on chemical grounds since DNA polymerases and "reverse transcriptases" can, with varying efficiencies, copy either template (28—30).

It is now clear that tightly bound, stoichiometric Zn^{2+} is present in homogeneous DNA polymereases purified from four diverse sources: a bacterial enzyme (E. coli. polymerase I (31, 32)), two viral enzymes (T_4 bacteriophage (32) and avian myeloblastosis virus (Poiesz, B., Battula, N. and Loeb, L. A., unpublished results), and an animal enzyme (sea urchin polymerase (31)). Kinetic analysis of the inhibition of sea urchin polymerase and E. coli DNA polymerase I by o-phenanthroline reveals that this inhibition is wholly or in part competitive with respect to DNA (27, 31) suggesting that the enzyme bound Zn^{2+} interacts with DNA. This suggestion is supported by the observation that DNA polymerase enhances the effect of Zn^{2+} on the nuclear quadrupolar relaxation rate of Br^- ions indicating that the enzyme bound Zn^{2+} can coordinate Br^- ions (32). This enhanced effect is progressively reduced on titration with an oligonucleotide, $(dT)_{6-9}$, to 1/3 of its original value with an end point suggesting that 1 molecule of oligonucleotide binds to 1 molecule of polymerase and displaces 2/3 of the Br^- from the enzyme bound Zn^{2+}. The presence of Zn^{2+} at the DNA binding site is further supported by the detection of 2 Zn^{2+} per mole of E. coli RNA polymerase (33) which also must bind a DNA template. A mechanistic role for Zn^{2+} rather than simple DNA binding is suggested by the specific inhibition by o-phenanthroline of RNA chain initiation with RNA polymerase (33), and by the negative finding by B. M. Alberts, C. Springgate, L. A. Loeb, and A. S. Mildvan that the gene 32 protein, a non-basic and non-catalytic protein which binds tightly to single stranded DNA, does not contain significant amounts of Zn^{2+} (less than 0.1 g atoms/mole).

A reasonable mechanistic role for Zn^{2+} at the DNA site consistent with the above results is to coordinate and promote the nucleophilicity of the 3'-OH group of deoxyribose at the growing point of the initiator strand ((32, 34), Fig. 3)). Model reactions of this type (35) and their microscopic reverse (36, 37) have been described. This role for Zn^{2+} would be assisted by a nearby general base to deprotonate the 3' hydroxyl

7

group. In this regard it is of interest that several, but not all DNA polymerases appear to be sulfhydryl enzymes (26, 27).
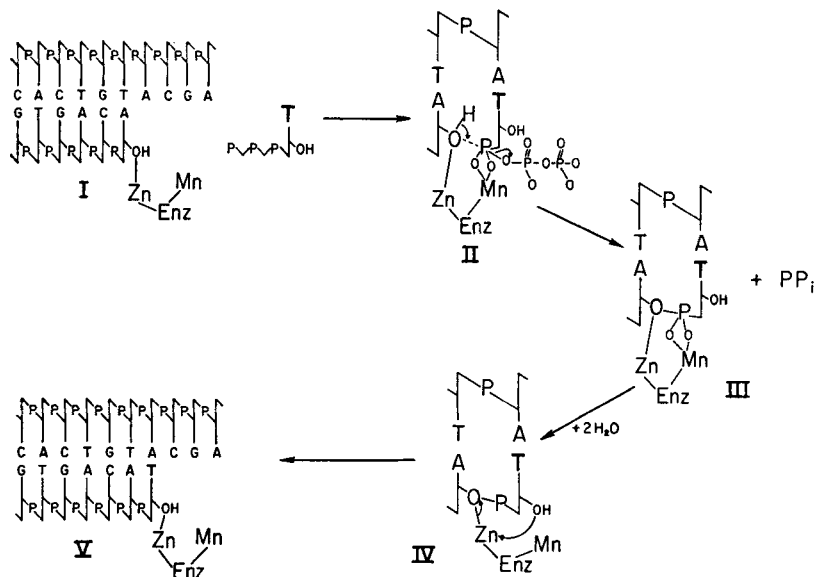
Fig. 3. Proposed mechanism of E. coli DNA polymerase I showing the role of the metal ions (34). Steps I→II→III represent primer elongation and III→IV→V represent primer translocation as discussed in Ref. (34)

Unlike DNA analogs, deoxynucleoside triphosphate substrates do not displace Br^- ions from the enzyme-bound Zn^{2+} of E. coli polymerase I (32). In an important series of papers reviewed elsewhere (26) Kornberg and his colleagues established that this enzyme binds template in absence of the added divalent cation activator, Mg^{2+} (38), but requires Mg^{2+} for the tight binding of the substrates (39). A quantitative study of the binding of the divalent activator, Mn^{2+}, and nucleotides to E. coli polymerase I using EPR and water proton relaxation (34) revealed that the enzyme binds Mn^{2+} at three types of sites: one very tight site ($K_D \leq 10^{-6}$ M), five intermediate sites ($K_D \cong 10^{-5}$ M), and ~ 12 weak sites ($K_D = 10^{-3}$ M). From kinetic studies, the tight and intermediate sites may function catalytically but the weakest sites are probably inhibitory. The tight site and intermediate sites all interact with deoxynucleoside triphosphates or monophosphates, suggesting that the enzyme pre-aligns substrate molecules prior to polymerization (34). Moreover, the relaxation rates of water in solutions of ternary com-

plexes of deoxynucleoside triphosphates and monophosphates are the same (34) and the affinities for triphosphates and monophosphates are similar (34, 38, 39) suggesting that both compounds interact with the enzyme bound Mn^{2+} in the same way, presumably through their α-phosphoryl groups. All of these findings are consistent with an associative nucleophilic displacement mechanism for DNA polymerase ((34) Fig. 3)).

The geometry of this displacement, in line or adjacent, is unknown.

V. Phosphoryl Transfer Enzymes

A. Pyruvate Kinase

From ^{31}P-NMR studies at one frequency of the ternary complex of muscle pyruvate kinase, Mn, and phosphoglycolate, a competitive analog of the substrate phosphoenolpyruvate, a Mn to P distance of 3.5 ± 0.3 Å was obtained suggesting a distorted inner sphere complex ((15), Fig. 4)).

Fig. 4. Proposed mechanism of pyruvate kinase in A, the phosphoryl transfer reaction and B, the enolization of pyruvate, based on nuclear relaxation (15, 43, 45—48) and chemical modification studies (49—51)

An alternative explanation of this distance, suggested by the EPR spectrum of Mn^{2+} (40), is that it represents a time average of two complexes: 32% inner sphere (2.9 Å) and 68% second sphere (6.1 Å). This possibility arises because of the inherently higher frequency or "shutter speed" of the EPR experiment (2×10^{10} sec^{-1}) as compared with that of the nuclear relaxation experiment (5×10^6 sec^{-1}). Hence exchange between the two complexes with a rate constant k such that 5×10^6 sec$^{-1} < k < 2 \times 10^{10}$ sec^{-1} would result in an average structure

in the NMR experiment but not in the EPR experiment. The addition of the activator K^+ which may form a metal bridge between the enzyme and the carboxyl group of phosphoenolpyruvate and its analogs (15) causes a reorientation of the inner sphere complex as indicated by proton NMR and an increase in the amount of inner sphere complex as suggested by EPR (40). A pyruvate kinase-Mn-O_3PF bridge complex has previously been found by ^{19}F NMR (41). A reevaluation of the Mn to F distance in this complex (14) using better estimates of the correlation time at one frequency (3.7×10^{-9} sec) and of the extent of formation of the ternary complex in the NMR experiment (4%) from computer analyzed titration curves (15) yields a Mn to F distance of 4.3 ± 1.5 Å in agreement with the Ca to F distance of 4.2 Å in the monodentate crystalline Ca—O_3PF complex (42). Hence the phosphoenolpyruvate analogs phosphoglycolate and FPO_3^{2-} (which is also a product of the fluorokinase reaction) form inner sphere E-Mn-phosphoryl bridge complexes consistent with an associative or S_N2 nucleophilic displacement on the phosphorus of phosphoenolpyruvate by ADP ((43), Fig. 4A)). Although phosphoenolpyruvate itself could not be studied by NMR because of slow exchange it competes with these analogs in the NMR and in kinetic studies (15, 41, 44) and it yields a very similar EPR spectrum for enzyme-bound Mn as that observed in the quaternary pyruvate kinase-Mn-K-phosphoglycolate complex (40).

The geometry of a kinetically active complex of pyruvate kinase, Mn^{2+}, K^+, phosphate, and pyruvate which catalyzes the enolization of pyruvate has been elucidated by ^{13}C and ^{31}P NMR ((45) Fig. 4B)). The distances from Mn to the carboxyl and carbonyl carbon atoms of pyruvate (7.3 ± 0.1 Å) establish the substrate to be in the second coordination sphere, while the lower limit Mn^{2+} to phosphorus distance (4.5 ± 0.4 Å) suggests either a distorted inner sphere complex or the rapid averaging of 6% inner sphere complex with 94% second sphere complex. Mechanisms for pyruvate kinase, consistent with the geometries are given in Fig. 4 (15, 43, 45).

The distance between the bound monovalent cation and bound paramagnetic divalent cation, originally determined by Tl^+ NMR to be 5 Å and 8 Å in the presence and absence of phosphoenolpyruvate (46, 47) has been confirmed by Na^+ NMR (*Gupta, R. K.*, and *Mildvan, A. S.*, unpublished), and by frequency dependent proton NMR using monomethylammonium as the activator (48). The possible widespread applicability of the use of monomethylammonium rather than Na^+ or Tl^+ would render such distance determinations much easier because of the general availability of proton NMR spectrometers (48).

With respect to the ADP binding site of pyruvate kinase, a functional lysyl ammonium group and a thiol group have been detected by a com-

bination of methods: chemical modification (*49, 50*), combined with binding studies using EPR and nuclear relaxation (*51*) and kinetic studies of the detritiation of pyruvate, a partial reaction (*51*). The modification of the thiol group consisted of converting it to a disulfide, a reaction mediated by 5,5'-dithio-bis-2-nitrobenzoate. While the modifications of both groups abolish ADP or ATP binding and preserve the binding and detritiation of pyruvate, the thiol group is closer to the Mn^{2+} and phosphoenolpyruvate binding sites as indicated by large decreases in the number and exchange rate of rapidly exchanging water ligands on Mn^{2+} and in the affinity for phosphoenolpyruvate in the disulfide enzyme (*51*).

B. Phosphoenolpyruvate Carboxylase

PEP Carboxylase catalyzes a reaction homologous with that of pyruvate kinase (*52*) in which an oxygen of bicarbonate attacks the leaving phos-

$$
\bar{O}O-\overset{\text{\raisebox{2pt}{$\pm$}}}{\underset{\text{O}^-}{C}}\overset{\text{O}}{\diagup} \quad + \quad \underset{\bar{C}H}{\overset{\bar{O}OC}{\underset{\|}{C}}\diagup O-P^+O_3^=} \quad \xrightarrow{M^{2+}} \quad \underset{\underset{COO^-}{\overset{|}{CH_2}}}{\overset{COO^-}{\underset{|}{\overset{|}{C}=O}}} \quad + \quad PO_3OH^= \tag{4}
$$

phoryl group of phosphoenolpyruvate and the CO_2 derived from bicarbonate adds to the C_3 position of the pyruvate enolate to form oxaloacetate. Mn^{2+} and substrate binding studies measuring the proton relaxation rate of water suggested the formation of an enzyme-Mn-PEP complex with carboxylase from peanut cotyledons (*52*). More recent kinetic data with the enzyme purified from spinach provides additional indirect evidence for a metal bridge complex to the phosphoryl group (*Miziorko, H., Nowak, T.*, and *Mildvan, A. S.*, unpublished). Thus, changing the divalent cation from Mg^{2+} to Mn^{2+} produces a 49-fold decrease in the dissociation constant of the competitive inhibitor L-phospholactate. From the dissociation constants of the inhibitors L-lactate and methyl phosphate the factor of 49 is ascribed to a 9-fold tightening of phosphate binding but only a 5-fold tightening of carboxyl binding of L-phospholactate.

C. Fructose Diphosphatase

From ^{31}P nuclear relaxation studies (*53*), an S_N2 mechanism seems likely for the reaction catalyzed by the alkaline form of fructose diphosphatase

since an enzyme-Mn-fructose-1-phosphate bridge complex with a Mn to P distance of 3.3 ± 0.3 Å has been detected.

D. Creatine Kinase

As implied above, a dissociative or S_N1 mechanism for phosphoryl transfer is more difficult to establish than an S_N2 mechanism. An S_N1 mechanism may be operative in the reaction catalyzed by creatine kinase as suggested by the observation that planar trigonal monoanions such as nitrate and formate (54) which are analogs of metaphosphate, (Fig. 5)
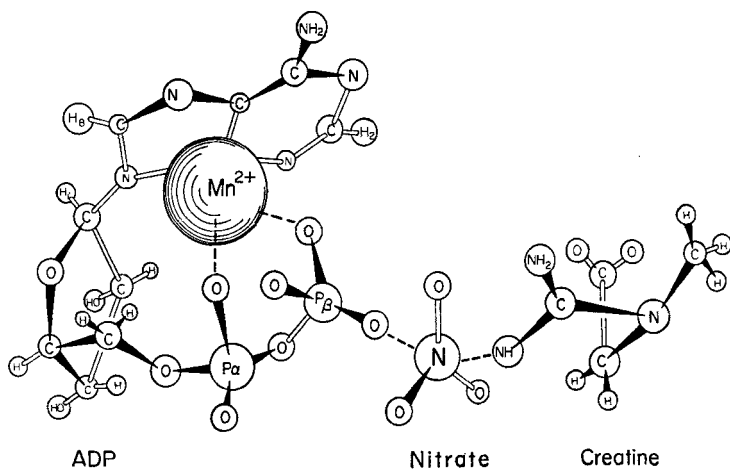

ADP   Nitrate   Creatine

Fig. 5. Proposed structure of the abortive quaternary nitrate complex of creatine kinase (55) which may mimic the transition state of the enzymatic reaction, based on kinetic (54), EPR (55) and nuclear relaxation studies (88)

protect the enzyme from modification of its essential thiol. However, the finding that M^{2+}-ADP and creatine raise the affinity of the enzyme for nitrate as detected kinetically (54) and by proton relaxation (55, 56), and, conversely, that nitrate raises the affinity of the enzyme for creatine and ADP as detected by kinetics (54) and proton relaxation (55, 57) suggest the formation of a complex in which there is significant ADP---NO_3^- bonding and creatine---NO_3^- bonding. Such a complex would mimic a transition state structure for an in line S_N2 mechanism ((55) (Fig. 5)). A crucial question in this connection is the location of the bound divalent cation.

A model of the substrates at the active site, based on the superposition of the geometry of several inactive and active "ground state"

complexes determined by proton NMR suggests that the Mn coordinates the leaving ADP group (58). Moreover, the long Mn^{2+} creatine-CH_2-distance (9.8 Å) did not differ in the enzyme-creatine-Mn-ADP complex and in the equilibrium mixture, suggesting that Mn^{2+} remains on the α and β phosphorus atoms in the quaternary ATP complex. X-ray diffraction studies of the phosphoglycerate kinase-Mn-ADP system reveals an enzyme-metal-substrate bridge complex to both phosphoryl groups of ADP (59). However, more recent data on the ground state and "transition state" complexes of creatine kinase, substrates, and formate, indicate the Mn^{2+} to creatine distance to be ≤ 8.5 Å (56). The Mn to formate proton distance (< 5.1 Å) is compatible with but does not establish direct coordination of formate (56, 60). EPR and proton relaxation data reveal a progressive decrease in the symmetry of the ligand field at Mn^{2+} as the ternary and quaternary complexes are formed (54–57, 60), consistent with the entrance of ligands on Mn^{2+} from the protein and possibly from the formate. Nucleotides or creatine analogs with a higher V_{max} appear to form larger fractions of the more asymmetric complex (56, 57, 60). Hence while the Mn^{2+} appears not to coordinate the transferable phosphoryl group in the ground state complexes. it may well do so in the transition state and in the ternary-enzyme-ATP-Mn complex. If this were the case, an S_N2 mechanism would be indicated, as with pyruvate kinase, and the metal would have to migrate during the course of the reaction. The failure of Cr^{III} ADP (61–63) and Cr^{III} ATP (63) to serve as substrates for various kinases may be due in part to the inability of this trivalent metal to migrate in these stable complexes.

E. Phosphoglucomutase

Phosphoglucomutase catalyzes the reversible transfer of a phosphoryl group from the 1 or 6 position of glucose 1,6 diphosphate to a serine hydroxyl group on the enzyme yielding a phosphoenzyme intermediate (64). Direct observation of this enzyme-bound group by ^{31}P-NMR (65) established it to be a phosphoserine from its chemical shift and that of the protons to which it is coupled and shows it to be highly immobilized or "frozen to the enzyme" from its relaxation rates suggesting direct activation of the phosphoryl group (W. J. Ray, Jr., and A. S. Mildvan, unpublished). The metal ion required for this reaction is bound at a site 6 Å from the phosphoserine P suggestive of a second sphere complex, (Fig. 6) although only 20% of the phosphorus was visualized in this relaxation experiment, leaving open the possibility of an extensively broadened additional signal due to an inner sphere component. A predominantly (96%) second sphere complex with only a 4% inner sphere contribution is supported by the detection of a 4.8 ± 0.1 Å Mn-to-P

distance in the ternary complex of the dephospho-enzyme with Mn and methyl phosphonate, an analog of phosphate *(66)*. The methyl phosphonate is very weakly bound to the enzyme at this site with a dissociation constant of 0.1 M. This site is absent on the phosphoenzyme. On both forms of the enzyme, a second binding site for methyl phosphonate is found 10.5 ± 0.5 Å from the metal with a lower dissociation constant of 1 mM which apparently serves to position the binding of either of the phosphates of the intermediate glucose 1,6 diphosphate *(66, 67)*. Hence a "one dimensional model" of the active site may be constructed (Fig. 6)
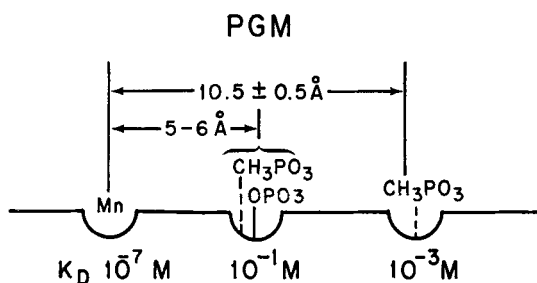
Fig. 6. One dimensional model of the active site of phosphoglucomutase from ^{31}P and proton relaxation studies *(65, 66, 68)* and Mn^{2+} and $CH_3PO_3^{2-}$ binding studies *(67, 68)*. K_D represents the dissociation constants of Mn^{2+} and $CH_3PO_3^-$ from the indicated sites. The weaker $CH_3PO_3^-$ binding site represents the phosphoryl transfer site and the stronger binding site positions the substrate

with the metal ion as the reference point, the weak phosphate binding site (corresponding to the phosphoserine phosphate hence to the phosphoryl transfer site) at ~ 5 Å from the metal and the tighter binding phosphate positioning site 10—11 Å away. The glucose 1,6 diphosphate which interchanges its phosphoryl group 100 times faster than it dissociates *(64)* must therefore alternatively shift the binding of its two phosphates between the two sites without dissociating from the enzyme. The calculated distances, together with water proton relaxation *(68)* and molecular model studies, suggest two possible roles for the metal ion (Fig. 7). By coordinating the 3-OH group of the sugar the metal-sugar bond could serve as the pivot for the phosphate shift. Alternatively, or additionally, by coordinating the serine hydroxyl, the metal could increase its nucleophilicity on phosphorus and its effectiveness as a leaving group from phosphoserine (Fig. 7). The second role is suggested by the decrease in water relaxation caused by the phosphoenzyme-Mn complex as compared with the dephosphoenzyme-Mn complex *(67)*.

Similarly the possibility of an S_N2 mechanism is suggested by the immobilization of phosphorus and by the possibility of an inner sphere contribution to the Mn-P distance.
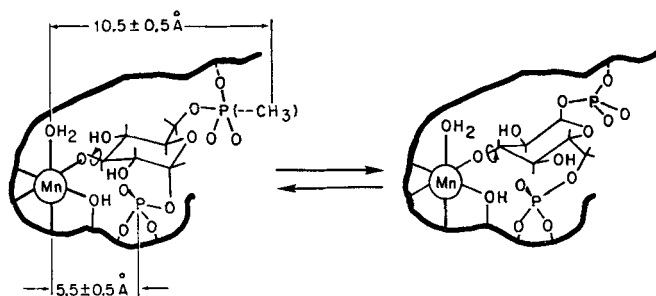

Fig. 7. Modes of binding of the intermediate glucose 1,6 diphosphate to phosphoglucomutase consistent with the geometry of Fig. 6. The enzyme bound Mn^{2+} promotes the nucleophilicity of the serine hydroxyl group and provides a pivot for the interchange of the 1 and 6 phosphoryl groups between the phosphoryl transfer and phosphoryl positioning sites

F. Alkaline Phosphatase

The presence of a metal on a phosphoryl transferring-enzyme provides no assurance that the metal is directly involved in phosphoryl transfer. Thus with alkaline phosphatase, no direct interactions of Cl^- with enzyme bound Zn^{2+} (69) or water with enzyme-bound Mn^{2+} (70) were detected by nuclear relaxation. Similarly no direct interaction of phosphate with enzyme bound Co^{2+} (71) or Mn^{2+} (71, 72) was detected by ^{31}P nuclear relaxation. A Mn^{2+} to phosphate distance of 7.3 Å was calculated from NMR data on the inactive Mn^{2+}-enzyme (73) indicative of a second sphere complex. These results are in accord with crystallographic data on the enzyme which at 7.7 Å resolution indicate that substrates cannot easily gain direct access to the metal site (74). More recent proton relaxation studies with the Cu^{2+} enzyme, which retains 5% of the activity, indicate the presence of a rapidly exchanging axial hydroxyl ligand on Cu^{2+} suggesting that the active metals may promote the nucleophilicity of the water molecule which is to attack the phosphorus (75).

G. (Na$^+$ + K$^+$)-ATPase

The membrane-bound Na$^+$ and K$^+$ activated ATPase partially purified from kidney microsomes is believed to function in the active transport

15

of Na^+ and K^+ (76). A phosphoenzyme intermediate has been detected (77), in which the phosphoryl group is covalently bound in a mixed anhydride linkage to the carboxyl group of aspartic acid (78). Interestingly, this high energy intermediate appears to form from ATP in the presence of Na^+ (77) or from P_i in the presence of K^+ (79) suggesting that the nature of the monovalent cation influences the mode of phosphorylation of the enzyme. In addition to Na^+ and K^+ the ATPase requires a divalent cation such as Mg^{2+} or Mn^{2+} for activity (76).

The interactions of Mn^{2+} with the membrane-bound $(Na^+ + K^+)$-ATPase from sheep kidney medulla have been examined by kinetic and magnetic resonance techniques (80, 81). EPR and water proton relaxation rate studies show that the enzyme binds Mn^{2+} at one tight binding site $(K_D = 0.88\ \mu M)$. Kinetic studies yield an activator constant for Mn^{2+} of 0.88 μM, identifying the one tight Mn^{2+} binding site as the active site of the ATPase.

Competition studies indicate that Mg^{2+} binds at this site with a dissociation constant of 1 mM (80) in agreement with its activator constant (82). Inorganic phosphate and methylphosphonate bind to the enzyme-Mn^{2+} complex with similar, extremely high affinities suggesting covalent bonding, and decrease the enhancement, ε^*, of $1/T_1$ of water protons. Analysis of the frequency dependence of $1/T_1$ of water indicates that this change in enhancement is due to a decrease from 4 to 3 in the number of rapidly exchanging water protons in the coordination sphere of enzyme-bound Mn^{2+}. The relative effectiveness of Na^+ and K^+ in facilitating ternary complex formation with P_i was found to be a function of pH (80). The fraction of the total de-enhancement produced by P_i in the presence of Na^+ and Mn^{2+} closely follows the titration curve for the second ionization of P_i. Analogous behavior at a higher pH was observed for methylphosphonate, which has a pK_a for its second ionization which is 0.9 pH units higher than that of P_i. These results indicate that Na^+ induces the phosphate monoanion to coordinate to the enzyme-bound Mn^{2+}, while K^+ causes the phosphate dianion to coordinate to the enzyme-bound Mn^{2+}. Thus protonation of an enzyme-bound phosphoryl group would convert a K^+ binding site to a Na^+ binding site. Dissociation constants for K^+ and Na^+ estimated from the NMR titrations (80) agreed with kinetically determined activator constants of these ions (83, 84) consistent with binding to the active site. All of these results are consistent with the mechanism of Fig. 8 for the ATPase and for monovalent cation transport (80). Because of direct coordination to Mn^{2+} (80) the phosphoryl transfer reactions (85) are depicted as S_N2 processes. In this mechanism the ionization state of phosphate at a single enzyme active site controls the binding and transport of Na^+ or K^+. This model also accounts for the order of magnitude weaker binding of
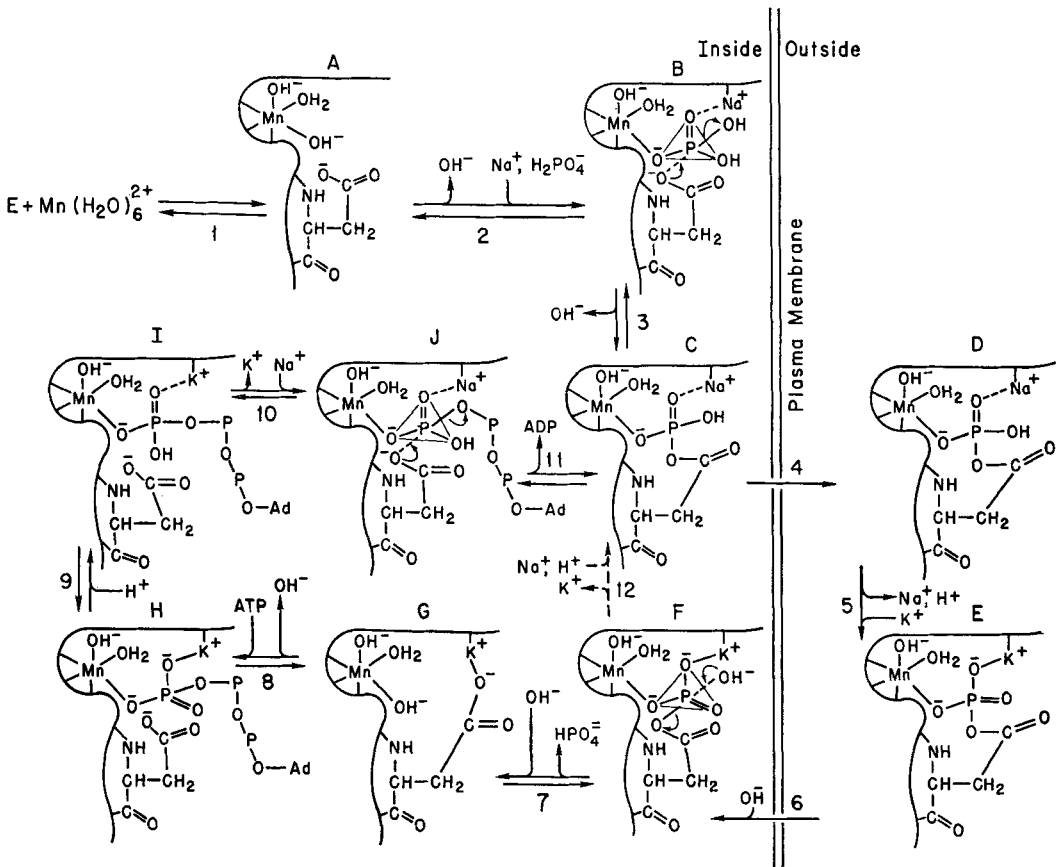
Fig. 8. Proposed mechanism for the (Na+ + K+)-ATPase and for cation transport (80), based on EPR (80), nuclear relaxation (80, 81) and kinetic studies (80, 86), the detection of phosphoryl transfer (85) to an aspartyl residue (78), yielding a covalent phosphoenzyme intermediate (77, 79). Steps (1—3) show the binding of Mn^{2+}, Na+ and the phosphate monoanion to the enzyme. Steps (4—11) represent the ATPase activity. Active cation transport occurs via steps (4—6)

Na+ compared to K+, since Na+ binds to a phosphate monoanion and K+ binds to a dianion. Recent Tl+-NMR data indicates this monovalent cation binds 4.0 Å from the enzyme bound Mn^{2+} and that this distance increases to 5,4 Å on binding of phosphate consistent with the mechanism of Fig. 8 (81). However, the possibility of Tl+ binding at an inhibitory site rather than its activating site has not been excluded.

17

VI. Summary and Conclusions

1. The detection of metal to phosphorus distances intermediate between those of inner sphere and second sphere complexes on Staphylococcal nuclease, pyruvate kinase, and phosphoglucomutase may well reflect the averaging of two or more complexes exchanging rapidly within the sampling time defined by the X-ray and NMR methods. Multiple complexes could result from the rapid exchange of inner and second sphere complexes or from the rapid migration of a metal along a polyphosphate chain. Alternatively unusual distances may reflect distortion of the metal-phosphoryl complexes on the enzyme. Such distortion may be a part of the catalytic process itself (87).

2. Since metal coordination or immobilization of the transferred phosphoryl group by multiple hydrogen bonds would inhibit the formation of a metaphosphate intermediate in an S_N1 mechanism and would facilitate nucleophilic attack in an S_N2 mechanism, the latter process seems likely for the reactions catalyzed by staphylococcal nuclease, DNA polymerase, pyruvate kinase, fructose diphosphatase, phosphoglucomutase, $(Na + K)$ ATPase and possibly PEP carboxylase. In creatine kinase where an S_N1 mechanism is possible, the enzyme would have to prevent access of nucleophiles other than ADP and creatine to the reactive metaphosphate intermediate.

3. In four of the enzymes considered here, Staphylococcal nuclease, DNA polymerase (Zn site), phosphoglucomutase, and possibly alkaline phosphatase, a reasonable role for the enzyme-bound divalent cation is to promote the deprotonation and thereby to increase the nucleophilicity of water or of the hydroxyl group of the substrate which is to attack the phosphoryl group undergoing transfer. In the microscopic reverse of this mechanism, the role of the metal would be to promote the electrophilicity of the oxyanion which is leaving phosphorus. This role may also be operative in the creatine kinase reaction in which Mn^{2+} may coordinate the leaving ADP portion of ATP in the phosphoryl transfer. In the reactions catalyzed by pyruvate kinase, DNA polymerase (Mg site), and $(Na^+ + K^+)$ ATPase, the role of the divalent cation appears to be directly at the transferred phosphoryl group itself — either to shield charge, to withdraw electrons, or to stabilize the pentacovalent intermediate or transition state. Analogous roles may well be operative with fructose diphosphatase and PEP carboxylase in which no ambiguities are introduced by a polyphosphate chain in the substrate. Metals thus appear to play either of two general roles in phosphoryl and nucleotidyl transfer reactions. They may coordinate the atom or group which attacks (or leaves) the transferred phosphoryl group, or they may coordinate an oxygen atom of the transferred phosphoryl group itself.

VII. References

1. *Mildvan, A. S., Cohn, M.:* Advan. Enzymol. *33*, 1 (1970).
2. — *Engle, J. L.:* Methods in enzymology XXVI, Part C, p. 654 (1972).
3. *Benkovic, S. J., Schray, K. J.:* In: The enzymes (ed. *P. D. Boyer*), Vol. VIII, 201 (1973).
4. *Gillespie, P., Ramirez, F., Ugi, I., Marquarding, D.:* Angew. Chem. *12*, 91 (1973).
5. *Mildvan, A. S.:* In: The enzymes (ed. *P. D. Boyer*), Vol. II, p. 445 (1970).
6. *Cooperman, B.:* In: Metal ions in biol. systems (ed. *H. Sigel*), Vol. V, in press. New York: Marcel Dekker 1973.
7. *Ingold, C. K.:* Structure and mechanism in organic chemistry, p. 310. London: Bell 1953.
8. *Bunton, C. A., Fendler, E. J., Humeres, E., Yang, K.-U.:* J. Org. Chem. *32*, 2806 (1967).
9. *Berry, R. S.:* J. Chem. Phys. *32*, 933 (1960).
10. *Westheimer, F. H.:* Accounts Chem. Res. *1*, 70 (1968).
11. *Muetterties, E. L., Schunn, R. A.:* Quart. Rev. Chem. Soc. *20*, 245 (1966).
12. *Ramirez, F., Tasaka, K., Desai, N. B., Smith, C. P.:* J. Am. Chem. Soc. *90*, 751 (1968).
13. *Archie, W. C., Westheimer, F. H.:* J. Am. Chem. Soc. *95*, 5955 (1973).
14. *Mildvan, A. S., Nowak, T., Fung, C.-H.:* Ann. N. Y. Acad. Sci., *222*, 192 (1973).
15. *Nowak, T., Mildvan, A. S.:* Biochemistry *11*, 2819 (1972).
16. *Mildvan, A. S.:* Annual review of biochemistry, Vol. 43, in press (1973).
17. *Anfinsen, C. B., Cuatrecasas, P., Taniuchi, H.:* In: The enzymes (ed. *P. D. Boyer*), 3rd edit., Vol. IV, p. 177 (1971).
18. *Chaiken, I. M., Anfinsen, C. B.:* J. Biol. Chem. *246*, 2285, (1971). — *Sanchez, G. R., Chaiken, I. M., Anfinsen, C. B.:* J. Biol. Chem. *248*, 3653 (1973).
19. *Arnone, A., Bier, C. J., Cotton, F. A., Hazen, E. E., Jr., Richardson, D. C., Richardson, J. S.:* Proc. Natl. Acad. Sci. U.S. *64*, 420 (1969).
20. — — — *Day, V. W., Hazen, E. E., Jr., Richardson, D. C., Richardson, J. S., Yonath, A.:* J. Biol. Chem. *246*, 2302 (1971).
21. *Markley, J. L., Jardetzky, O.:* J. Mol. Biol. *50*, 223 (1970).
22. *Cotton, F. A., Hazen, E. E., Jr.:* In: The enzymes (ed. *P. D. Boyer*), 3rd edit., Vol. IV, p. 153 (1971). — *Cotton, F. A., Bier, C. J., Day, V. W., Hazen, E. E., Jr., Larsen, S.:* Cold Spring Harbor Symp. *36*, 243 (1971).
23. *Roberts, G. C. K., Jardetzky, O.:* Advan. Prot. Chem., Vol. 24, p. 447 (1970).
24. *Furie, B., Eastlake, A., Schechter, A. N., Anfinsen, C. B.:* J. Biol. Chem. *248*, 5821 (1973).
25. *Dunn, B. M., DiBello, C., Anfinsen, C. B.:* J. Biol. Chem. *248*, 4769 (1973).
26. *Kornberg, A.:* Science *163*, 1410 (1969).
27. *Loeb, L. A.:* In: The enzymes (ed. *P. D. Boyer*). New York: Academic Press, *10*, 173, (1974).
28. *Cavalieri, L. F., Carroll, E.:* Biochem. Biophys. Res. Commun. *41*, 1055 (1970).
29. *Wells, R. D., Flügel, R. M., Larson, J. E., Schendel, P. F., Sweet, R. W.:* Biochemistry *11*, 621 (1972).
30. *Loeb, L. A., Tartof, K. D., Travaglini, E. C.:* Nature New Biol. *242*, 66 (1973).
31. *Slater, J. P., Mildvan, A. S., Loeb, L. A.:* Biochem. Biophys. Res. Commun. *44*, 37 (1971).
32. *Springgate, C. F., Mildvan, A. S., Abramson, R., Engle, J. L., Loeb, L. A.:* J. Biol. Chem. *248*, 5987 (1973).
33. *Scrutton, M. C., Wu, C. W., Goldthwait, D. A.:* Proc. Natl. Acad. Sci. U.S. *68*, 2497 (1971).

34. *Slater, J. P., Tamir, I., Loeb, L. A., Mildvan, A. S.:* J. Biol. Chem. 247, 6784 (1972).
35. *Sigman, D. S., Wahl, G. M., Creighton, D. L.:* Biochemistry 11, 2236 (1972).
36. *Benkovic, S. J., Dunikoski, L. K., Jr.:* J. Am. Chem. Soc. 93, 1526 (1971).
37. *Murakami, Y., Takagi, M.:* J. Am. Chem. Soc. 91, 5130 (1969).
38. *Englund, P. T., Kelley, R. B., Kornberg, A.:* J. Biol. Chem. 244, 3045 (1969).
39. *Englund, P. T., Huberman, J. A., Jovin, T. M., Kornberg, A.:* J. Biol. Chem. 244, 3038 (1969).
40. *Reed, G. H., Cohn, M.:* J. Biol. Chem., 248, 6436 (1973).
41. *Mildvan, A. S., Leigh, J. S., Cohn, M.:* Biochemistry 6, 1805 (1967).
42. *Perloff, A.:* Acta Cryst. B 28, 2183 (1972).
43. *Mildvan, A. S., Cohn, M.:* J. Biol. Chem. 241, 1178 (1966).
44. *Nowak, T., Mildvan, A. S.:* J. Biol. Chem. 245, 6057 (1970).
45. *Fung, C.-H., Mildvan, A. S., Allerhand, A., Komoroski, R., Scrutton, M. C.:* Biochemistry 12, 620 (1973).
46. *Reuben, J., Kayne, F. J.:* J. Biol. Chem. 246, 6227 (1971).
47. *Kayne, F. J., Reuben, J.:* J. Am. Chem. Soc. 92, 220 (1970).
48. *Nowak, T.:* J. Biol. Chem. 248, 7191 (1973).
49. *Hollenberg, P. F., Flashner, M., Coon, M. J.:* J. Biol. Chem. 246, 946 (1971).
50. *Flashner, M., Hollenberg, P. F., Coon, M. J.:* J. Biol. Chem. 247, 8114 (1972).
51. *— Tamir, I., Mildvan, A. S., Meloche, H. P., Coon, M. J.:* J. Biol. Chem. 248, 3419 (1973).
52. *Miller, R. S., Mildvan, A. S., Chang, H. C., Easterday, R. L., Maruyama, H., Lane, M. D.:* J. Biol. Chem. 243, 6030 (1968).
53. *Benkovic, S. J., Villafranca, J. J., Kleinschuster, J. J.:* Arch. Biochem. Biophys. 155, 458 (1973).
54. *Milner-White, E. J., Watts, D. C.:* Biochem. J. 122, 727 (1971).
55. *Reed, G., Cohn, M.:* J. Biol. Chem. 247, 3073 (1972).
56. *Reed, G. H., McLaughlin, A. C.:* Ann. N. Y. Acad. Sci., 222, 118 (1973).
57. *McLaughlin, A. C., Cohn, M., Kenyon, G. L.:* J. Biol. Chem. 247, 4382 (1972).
58. *Cohn, M., Leigh, J. S., Jr., Reed, G. H.:* Cold Spring Harbor Symp. Quant. Biol. 36, 533 (1971).
59. *Blake, C. C. F., Evans, P. R.:* Abs. 9th Int. Congress Biochem., Stockholm, p. 40, (1973).
60. *Cohn, M.:* In: Enzymes, Structure and Function, Proceedings, 8th F. E. B. S. Meeting, Amsterdam, Vol. 29, p. 59 (1972).
61. *Hirsch, K., Mildvan, A. S., Kowalsky, A.:* Abs. 158th American Chem. Soc. Mtg. New York, Biology Section, Abs. 52 (1969).
62. *Foster, D., Mildvan, A. S.:* Bioinorganic Chem. 1, 133 (1972).
63. *DePamphilis, M. L., Cleland, W. W.:* Biochemistry, 12, 3714 (1973).
64. *Ray, W. J., Peck, E. J., Jr.:* In: The enzymes (ed. *P. D. Boyer*), 3rd edit., Vol. VI, p. 408. New York: Academic Press 1972.
65. *Ray, W. J., Jr.:* Abs. 166th American Chem. Soc. Mtg., Chicago, AGFD-5 (1973). — *Mildvan, A. S.:* Abs. 166th American Chem. Soc. Mtg., INOR-95 (1973).
66. *— Mildvan, A. S.:* Biochemistry 12, 3733 (1973).
67. *— — Long, J. W.:* Biochemistry 12, 3724 (1973).
68. *— —* Biochemistry 9, 3886 (1970).
69. *Cottam, G. L., Ward, R. L.:* Arch. Biochem. Biophys. 141, 768 (1970).
70. *— Thompson, B. C.:* J. Mag. Resonance 6, 352 (1972).
71. *Csopak, H., Drakenberg, T.:* F. E. B. S. Letters 30, 296 (1973).

72. *Zukin, R., Hollis, D. P., Gray, G. A.:* Biochem. Biophys. Res. Commun. *53*, 238 (1973).
73. — — — Biochem. Biophys. Res. Commun. *53*, 686 (1973).
74. *Knox, J. R., Wyckoff, H. W.:* J. Mol. Biol. *74*, 533 (1973).
75. *Zukin, R. S., Hollis, D. P.:* J. Biol. Chem., in press (1974).
76. *Albers, R. W.:* Ann. Rev. Biochem. *36*, 275 (1967).
77. *Post, R. L., Kume, S., Tobin, T., Orcutt, B., Sen, A.:* J. Gen. Physiol. *54*, 306s (1969).
78. *Post, R. L., Kume, S.:* J. Biol. Chem. *248*, 6993 (1973).
79. *Lindenmayer, G., Laughter, A., Schwartz, A.:* Arch. Biochem. Biophys. *127*, 187 (1968).
80. *Grisham, C. M., Mildvan, A. S.:* J. Biol. Chem., in press (1974).
81. — — *Gupta, R. K.:* Federation Proc., in press (1974).
82. *Rendi, R., Uhr, M.:* Biochim. Biophys. Acta *89*, 520 (1964).
83. *Skou, J. C.:* Biochim. Biophys. Acta *42*, 6 (1960).
84. *Post, R., Merritt, C., Kinsolving, C., Albright, C.:* J. Biol. Chem. *235*, 1796 (1960).
85. *Dahms, A., Kanazawa, T., Boyer, P.:* J. Biol. Chem. *248*, 6592 (1973).
86. *Post, R. L., Hegyvary, C., Kume, S.:* J. Biol. Chem. *247*, 6530 (1972).
87. *Jencks, W. P.:* Catalysis in chemistry and enzymology, p. 282. New York: McGraw-Hill 1969.
88. *Leigh, J. S., Jr.:* Ph. D. Dissertation, University of Pennsylvania, (1971).

The Enzymatic Reduction of Ribonucleotides

Harry P. C. Hogenkamp and Gloria N. Sando

Department of Biochemistry, University of Iowa, Iowa City, Iowa, U.S.A.

Table of Contents

I. Introduction

The ribonucleotide reductase system, consisting of ribonucleotide reductase, thioredoxin and thioredoxin reductase, catalyzes the irreversible reduction of the four common ribonucleoside-5'-phosphates to the corresponding 2'-deoxyribonucleoside-5'-phosphates. This reaction provides the deoxy ribonucleotide precursors necessary for DNA synthesis.

$$\text{Ribonucleotide} + \text{Thioredoxin-(SH)}_2 \xrightarrow[\text{Reductase}]{\text{Ribonucleotide}}$$

$$\text{Deoxyribonucleotide} + \text{Thioredoxin-S}_2$$

$$\text{Thioredoxin-S}_2 + \text{NADPH} + \text{H}^+ \underset{\text{Reductase}}{\overset{\text{Thioredoxin}}{\rightleftharpoons}}$$

$$\text{Thioredoxin-(SH)}_2 + \text{NADP}^+$$
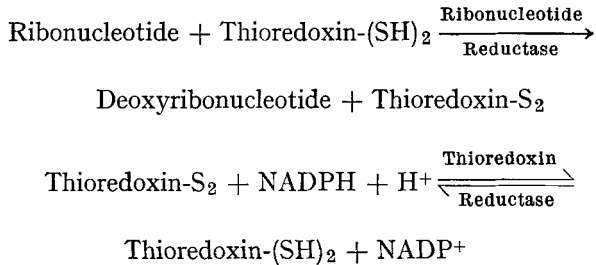
The observation that these deoxyribonucleotide precursors exist in very low concentration in cells suggests that ribonucleotide reduction is a crucial and rate-controlling step in DNA synthesis and cell division. Indeed the level of reductase activity has been correlated with DNA replication (1), cell proliferation (2) and tumor growth rate (3, 4).

Ribonucleotide reductase has been studied extensively in two bacterial systems: *Escherichia coli* (5) and *Lactobacillus leichmannii* (6). These two systems differ in their cofactor requirements and in the level of phosphorylation of the substrate.

Studies on the reductases from animal and plant origin indicate that they resemble the enzyme from *E. coli*, while the adenosylcobalamin-dependent reductase, first described in *L. leichmannii* has been so far detected only in procaryotic organisms, in the Euglenophyta, *Euglena gracilis* and *Astasia longa* (7—10) and in the fungus *Pithomyces chartarum* (11).

Ribonucleotide reductase activity in non-dividing cells is usually low; optimum enzymatic activity in microorganisms is attained during the mid-to-late-logarithmic growth phase (12—14). Striking increases in reductase activity occur following infection of bacteria or animal cells with viruses (15—19). The best characterized ribonucleotide reductases from mammalian tissues are those from Novikoff ascites hepatoma (20, 21) and regenerating rat liver (22), but reductases have also been reported in many rapidly proliferating tissues such as embryonic tissues from the chick (23) and the rat (24), leukemic mouse spleen (19),

regenerating liver (25), bone marrow (26—28), developing brain (29), leukocytes from blood of patients with acute and chronic myelocytic leukemia (27), rat hepatomas (3) and Yaba pox virus tumor (18). Ribonucleotide reductase has also been partially purified from *Saccharomyces cerevisiae* (30) and has been detected in extracts of germinating wheat embryo (31) and of root tips of the broad bean, *Vicia faba* (32), in preparations of developing adults of the silkworm, *Hyalophora cecropia* (33) and of the sea urchin, *Arbacia punctulato*, during early embryogenesis (34).

The reduction of ribonucleotides to deoxyribonucleotides is linked to NADPH by thioredoxin and thioredoxin reductase. Thioredoxin is a small protein which is oxidized from a dithiol to a disulfide form during ribonucleotide reduction. The dithiol form of thioredoxin is regenerated by NADPH and a specific flavoprotein, thioredoxin reductase. The "thioredoxin system" consisting of thioredoxin and thioredoxin reductase was first identified as the reducing system from *E. coli* by *Reichard* and co-workers (35, 36) and both proteins have since been purified to homogeneity (37, 38).

Thioredoxin systems have also been demonstrated in *L. leichmannii* (39), rat Novikoff hepatoma (40), T4 phage infected *E. coli* (41, 42), yeast (43), rat liver (44), calf liver (45) and germinating wheat embryo (32).

Very recently ribonucleotide reduction has been reviewed by *Henderson* and *Paterson* (46) and by *Follmann* (47); earlier reviews are those by *Reichard* and co-workers (48—51) and by *Blakley* (52). Ribonucleotide reduction has also been covered in several issues of Annual Review of Biochemistry (53—56).

II. Non-Heme Iron Containing Ribonucleotide Reductases

The non-heme iron containing ribonucleotide reductases catalyze the reduction of ADP, GDP, CDP and UDP to the corresponding 2'-deoxyribonucleotides. This type of reductase has been purified to homogeneity from *E. coli* B using conventional enzyme purification techniques (57—59), while a reductase has been isolated in essentially pure form from T4 phage infected *E. coli* B using affinity chromatography on dATP-Sepharose (60). Ribonucleotide reductase has also been purified to homogeneity from extracts of Novikoff rat tumor (61) and from bone marrow (28) and more than 150-fold from regenerating rat liver (22).

A. Ribonucleoside Diphosphate Reductase from *E. coli*

Ribonucleotide reductase of *E. coli* consists of two non-identical subunits, which are purified together during the initial steps of the purification procedure; however upon further purification the reductase separates into two subunits, proteins B1 and B2 (*58*). The overall yield of the two proteins is low, in particular that of protein B1, which readily decomposes into smaller subunits. This decomposition can be counteracted by the addition of dithiols. An improved procedure for the purification of protein B1 using affinity chromatography on dATP-Sepharose has been described by *Thelander* (*59*).

Separately, protein B1 (mol. weight 160,000) and protein B2 (mol. weight 78,000) are inactive and do not catalyze any known partial reaction. However, in the presence of TTP, magnesium ions and dithiothreitol proteins B1 and B2 form a 1:1 complex (mol. weight 245,000) which is catalytically active (*58, 59, 62, 63*).

Molecular weight determinations by ultracentrifugation in guanidine hydrochloride and by dodecylsulfate (SDS) polyacrylamide gel electrophoresis showed that protein B1 consists of two polypeptide chains of similar or identical size. Both chains have isoleucine as the carboxyl terminus while the amino terminal residues are different: glutamic acid and aspartic acid. In the absence of magnesium ions or upon oxidation in air protein B1 dissociates into its subunits; the latter dissociation involves the oxidation of cysteine residues and leads to inactivation. Both dissociation and inactivation can be reversed by incubation in presence of dithiothreitol. The allosteric effectors, ATP, dATP, dGTP and TTP, which regulate both the level of activity as well as the substrate specificity of the reductase bind only to protein B1. Subunit B2 does not bind any of the nucleotides. In the absence of the effectors the enzyme reduces the four ribonucleoside diphosphates at a slow rate. Addition of the positive effector ATP stimulates the reduction of the two pyrimidine nucleotides CDP and UDP, while the reduction of GDP is stimulated by TTP and that of ADP by dGTP. In contrast dATP acts as a negative effector and inhibits the reduction of all four substrates. The inhibition by dATP is counteracted by ATP and thus the ratio between these two nucleotides determines the activity of the enzyme (*51*). The results of binding studies suggest that protein B1 contains four binding sites. Two sites with high affinity for dATP and with the capacity to bind the other effectors were designated h-sites; while the other two sites with a lower affinity for dATP and with no detectable capacity to bind TTP or dGTP were designated l-sites. *Brown* and *Reichard* (*64*) have suggested that the l-sites regulate the level of activity

of the enzyme while the h-sites are involved in the regulation of the substrate specificity.

Protein B2 also consists of two identical or very similar polypeptide chains, each with a molecular weight of about 40,000 and contains two atoms of inorganic iron (65). The two polypeptide chains do not dissociate except under denaturing conditions. The metal can be removed from the protein by prolonged dialysis against 8-hydroxyquinoline or by precipitation with acid ammonium sulfate. Removal of the metal does not change the hydrodynamic properties of the protein and indeed "apoprotein B2" retains its ability to form a 1:1 complex with protein B1. However removal of iron results in loss of enzyme activity which can only be restored by treating apoprotein B2 with ferrous ion or less efficiently with ferric ion. Protein B2 has a characteristic absorption spectrum with maxima at 280 nm ($\varepsilon = 11.2 \times 10^4$), 365 nm ($6.0 \times 10^3$), 410 nm ($4.1 \times 10^3$), 480 nm ($0.5 \times 10^3$), 600 nm ($0.3 \times 10^3$) and a steep shoulder at 325 nm (7.6×10^3). The iron content of the protein is closely connected with this spectrum, the peaks at 410, 365, 480 and 600 nm disappear on removal of the metal and reappear on reactivation with Fe^{+2}. Treatment of protein B2 with hydroxyurea or hydroxylamine, which both inhibit ribonucleotide reduction, does not result in removal of the iron. However when protein B2 is treated with hydroxyurea or hydroxylamine the peak at 410 nm, but not the broad band at 365 nm, diminishes concomitant with enzyme activity. Protein B2 does not contain labile sulfide. The electron spin resonance (ESR) spectrum of protein B2 recorded from 14 to 293 °K shows a slightly asymmetric doublet centered at $g = 2.0047$ with a splitting of 16.5 gauss (66). This paramagnetic species is a stable organic free radical because Mössbauer spectra of [^{57}Fe] protein B2 as well as magnetic susceptibility measurements have shown that the iron atoms are diamagnetic. The paramagnetic species is, however, dependent on the presence of iron; apoprotein B2 does not give an ESR signal. The paramagnetic species is destroyed by treatment with hydroxylamine or hydroxyurea. On the other hand hydroxylamine treatment of [^{57}Fe] protein B2 does not affect the Mössbauer spectrum. These results clearly demonstrate that the enzymatic activity of protein B2 depends on the presence of the organic radical and that the radical in turn depends on the presence of iron (67). Aged preparations of protein B2, which show decreased enzyme activity, with simultaneous loss in radical concentration, but without changes in iron concentration, can be reactivated by removal of the metal followed by reconstitution with ferrous ions. The Mössbauer spectrum of [^{57}Fe] protein B2 as well as the electronic spectrum of protein B2 after treatment with hydroxylamine are very similar to those of methydroxohemerythrin and oxyhemerythrin, suggesting that protein B2 contains two non-identical

high spin Fe^{+3} ions in an antiferromagnetically coupled binuclear complex. Since protein B2 consists of two apparently identical polypeptide chains *Atkin* and co-workers (67) proposed that each atom of iron is bound to a separate polypeptide chain. Furthermore since the Mössbauer spectra show the presence of two equal populations of iron, they also suggested that by analogy with the proposed oxyhemerythrin structure (68) each binuclear iron complex in protein B2 is intrinsically asymmetric and contains one iron atom of each class.

When protein B1 and B2 are mixed in the presence of magnesium ions and dithiothreitol active ribonucleotide reductase with an $S_{20,w}$ of 9.7S is formed. Stimulatory effectors, such as ATP and TTP, do not effect complex formation. In contrast, in the presence of the negative effector, dATP, at concentrations which inhibit enzyme activity a larger complex is formed with an $S_{20,w}$ of 15.5S. Both complexes contain equimolar amounts of each subunit. A heavy complex is also formed in the presence of mixtures of other nucleoside triphosphates which inhibit enzyme activity. On the other hand the formation of this heavy inactive complex is prevented by ATP at concentrations which reverse the inhibition by dATP (63). More recent experiments (59) have shown that the interaction between proteins B1 and B2 in the presence of dATP is strongly influenced by the presence of sucrose, and indeed in the absence of sucrose subunits B1 and B2 with dATP form a complex with an $S_{20,w}$ of 22.1S.

B. Ribonucleoside Diphosphate Reductase Induced in *E. coli* by Infection with Bacteriophage T4

The T4 ribonucleotide reductase is similar to the enzyme from *E. coli* (60). The phage enzyme has a molecular weight of approximately 225,000 and polyacrylamide gel electrophoresis in sodium dodecylsulfate indicated the presence of equimolar amounts of 2 polypeptide chains α and β with molecular weights of 85,000 and 35,000 respectively. These observations suggest that the native phage reductase is a tetramer, $\alpha_2\beta_2$, with α_2 corresponding to protein B1 and β_2 corresponding to protein B2 of the *E. coli* reductase. In contrast to the *E. coli* reductase the phage enzyme does not dissociate into α_2 and β_2 during the purification procedure, and thus the phage enzyme does not require magnesium ions for activity. The bacterial enzyme requires Mg^{+2} for the formation of the B1—B2 complex. The electronic spectrum, ESR spectrum and iron content of the phage enzyme are similar to that of protein B2. Competition experiments with nucleotide substrates and effectors indicate that the phage enzyme contains only one catalytic site and one allosteric site (69). The allosteric properties of T4 ribonucleotide reductase

are very similar to those of the enzyme from *E. coli*. However, the action of dATP is opposite for the two reductases: dATP is a prime effector for the reduction of the pyrimidine ribonucleotides in the T4 system, while in the *E. coli* reductase reaction dATP inhibits the reduction of all ribonucleotides.

C. Ribonucleoside Diphosphate Reductase from Mammalian Sources

Ribonucleotide reductase from Novikoff ascites hepatoma resembles the enzyme from *E. coli* in its requirement for ATP, magnesium ions and a dithiol for optimal activity. The mammalian enzyme is stimulated by ferric ions and inhibited by hydroxyurea (*27*). During chromatography in the absence of magnesium ions the reductase separates into two components P1 and P2. P1 is retained by dATP-Sepharose and thus resembles the B-1 fraction of the *E. coli* system (*67*). The reductase from regenerating rat liver has been purified extensively and its requirements are also reminiscent of those of the bacterial enzyme (*22*). The purified enzyme requires the addition of ATP, Mg^{+2}, Fe^{+3} or Fe^{+2} and a dithiol reducing agent for optimal activity. Incubation of the rat liver enzyme in the presence of 8-hydroxyquinoline, hydroxylamine or 0-phenanthroline resulted in an approximately 85% inhibition of reductase activity. With some enzyme preparations only marginal stimulation with Fe^{+3} or Fe^{+2} ions was obtained, suggesting that, like the bacterial enzyme, different enzyme preparations vary with respect to iron content and probably organic radical concentration. Recently ribonucleotide reductase from rabbit bone marrow has been purified approximately 3600 fold (*28*); chromatography on dATP-Sepharose separates this reductase into two inactive protein fractions. The bound fraction (S1) was eluted with dATP and corresponds to the B1 protein of the *E. coli* reductase. The unbound fraction (S2) was further purified by chromatography on DEAE-Sephadex. During the purification ribonucleotide reductase activity became dependent on the addition of ferrous ions, suggesting that the iron cofactor is loosely bound to the bone marrow reductase.

III. Adenosylcobalamin-Dependent Ribonucleotide Reductases

Ribonucleotide reductases with an absolute requirement for adenosylcobalamin (Fig. 1) as a coenzyme have been demonstrated only in microorganisms (*7*). These reductases may be classified into two groups based on the nature of the nucleotide substrate utilized: ribonucleoside triphosphate reductases, which act upon the ribonucleoside triphosphates
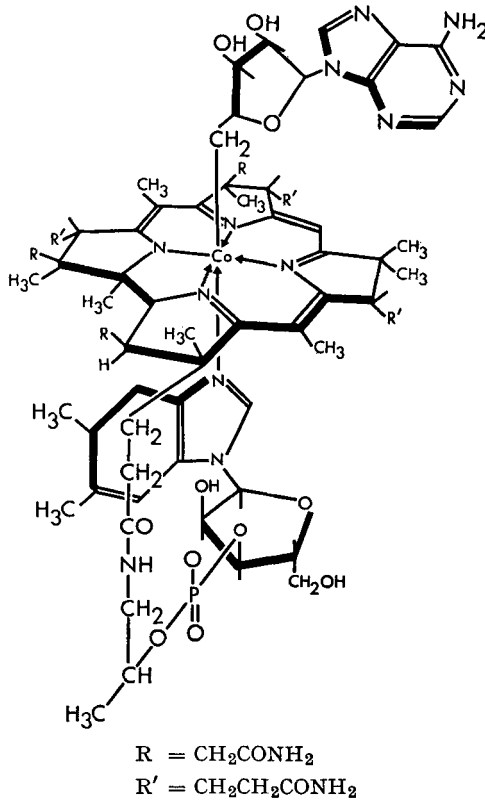
R = CH₂CONH₂
R' = CH₂CH₂CONH₂

Fig. 1. Structure of adenosylcobalamin

and ribonucleoside diphosphate reductases which prefer the ribonucleoside diphosphates as substrates.

A. Ribonucleoside Triphosphate Reductases

1. Ribonucleoside Triphosphate Reductase from L. leichmannii

The reductase from *L. leichmannii* acts only upon the nucleoside triphosphates and has an absolute requirement for adenosylcobalamin as a coenzyme. This reductase has been purified to homogeneity using conventional purification techniques (70, 71). The enzyme is also retained on an adenosylcobalamin-Sepharose column in the presence of a dithiol and dGTP, a positive effector, and can be removed from the affinity column when dGTP is omitted from the elution buffer. Unfortunately

under these conditions the enzyme is slowly inactivated (72). More recently affinity chromatography on dGTP-Sepharose has been used for the purification of the enzyme. Surprisingly this affinity column separated a homogeneous preparation of the enzyme, obtained by conventional purification techniques into four active fractions. The nature of the differences between these four forms has not yet been established. (73).

The molecular weight of the enzyme purified by conventional techniques is 76,000. Equilibrium sedimentation under various denaturing conditions as well as polyacrylamide gel electrophoresis in the presence of SDS showed no evidence of subunit structure. The reductase contains a single N-terminal amino acid, L-serine, and a single C-terminal amino acid, L-lysine, while cyanogen bromide treatment gave nine different peptide fragments expected for a protein containing eight methionine residues. The results firmly establish that the reductase from *L. leichmannii* is a monomeric enzyme with a molecular weight of 76,000. The presence of substrates or the modifier, dGTP, did not affect the hydrodynamic properties of the enzyme under the limited conditions investigated.

Like the reductase from *E. coli*, the enzyme from *L. leichmannii* is subject to allosteric control by the deoxyribonucleotide products. In the absence of effectors the enzyme reduces the nucleotide substrates at markedly different rates; however these rates are selectively modified by deoxyribonucleotide triphosphates which function as specific activators. Stimulation of ATP reduction is caused by dGTP, of CTP by dATP and of UTP by dCTP (52, 74). The reduction of GTP, the best substrate, is not affected significantly by any of the common deoxyribonucleotides. Kinetic studies have shown that activation is due to binding at an allosteric site and that such a site may accommodate not only the deoxyribonucleotide effectors but also the ribonucleotide substrates. Interaction of a deoxyribonucleotide effector with this allosteric site results in a marked decrease of the K_m for adenosylcobalamin suggesting that the enzyme undergoes a conformational change with a consequent increase in the affinity for the coenzyme (75). Indeed the observations that deoxyribonucleoside triphosphates are able to promote the hydrogen exchange reaction (76), the formation of a radical pair (77) as well as the degradation of the coenzyme (78), indicates that these allosteric effectors have a pronounced effect on enzyme-coenzyme interaction. Results from a study in which analogs of ribonucleotides were tested for their ability to act as substrates, activators or inhibitors of ribonucleotide reduction suggested that the reductase has two effector sites with different requirements for the sugar moiety of the nucleoside triphosphates (79).

In contrast, direct binding studies by equilibrium dialysis and differential fluorescence methods indicated the presence of only one binding site for all the deoxyribonucleotide effectors. Competition experiments demonstrated that ribonucleotides are weakly bound to the effector site, suggesting that at high concentration the ribonucleotide substrates can also modulate enzyme activity. On the other hand in the same study binding of ribonucleotide to a substrate site could not be demonstrated in the necessarily incomplete reaction systems. The authors suggest that their inability to detect enzyme-substrate interaction at a substrate site is a consequence of the fact that the ribonucleotide substrate is the last reactant to bind in an ordered reaction sequence (71). It should be pointed out that these binding studies, showing the presence of only one effector site, are done in incomplete reaction mixtures and thus no catalysis takes place.

In contrast with the reductase from *E. coli*, the ribonucleotide reductase system from *L. leichmannii* does not have an absolute requirement for Mg^{+2} (52, 80).

2. Ribonucleoside Triphosphate Reductase from Euglena gracilis

The adenosylcobalamin-dependent reductase from this eucaryotic organism has recently been purified to homogeneity (87). The molecular weight determined by gel filtration was approximately 440,000, while polyacrylamide gel electrophoresis in the presence of SDS showed only a single band with a molecular weight of approximately 100,000, suggesting that the native enzyme is composed of four subunits. The native enzyme readily dissociates into smaller units, this dissociation can be counteracted by dithiothreitol and dATP. Earlier the molecular weight of a partially purified preparation of the reductase was estimated to be in the range of 140,000 to 150,000 (13). Like the reductase from *L. leichmannii* the enzyme from *E. gracilis* is a nucleoside triphosphate reductase with an absolute requirement for a dithiol and adenosylcobalamin. However, unlike the bacterial enzyme the reductase from *E. gracilis* reduces GTP and ATP at approximately the same rate and CTP and UTP at approximately half this rate. Furthermore the rate of reduction is not stimulated by a specific deoxyribonucleotide but rather the reduction of a particular purine ribonucleotide is inhibited by all deoxyribonucleotides except its own product. TTP appears to be the key modulator of reductase activity in *E. gracilis*, in that this deoxyribonucleotide inhibits the reduction of all ribonucleotides. *Hamilton (87)* has found that CTP reduction is stimulated by dATP and ATP; he points out that the homogeneous reductase preparation may have lost a regulatory subunit

during the purification procedure and thus may have different kinetic properties from the partially purified reductase.

3. Ribonucleoside Triphosphate Reductase from Thermus X-1

A deoxyadenosylcobalamin-dependent ribonucleoside triphosphate reductase has been partially purified from cell free extracts of the extreme thermophile, *Thermus* X-1 (*14*). The enzyme preparation catalyzed the reduction of GTP and CTP at comparable rates, while UTP and ATP were reduced at only one-tenth the rate of GTP reduction. Only the dithiols could serve as reducing substrates. The enzyme has a temperature optimum of 70°, and the allosteric regulation of the enzyme activity is also temperature-dependent. The reduction of ATP is specifically stimulated by dGTP only at a higher temperature. Maximum stimulation of ATP reduction is observed at approximately 75°, while no stimulation can be detected at 37°. The molecular weight determined by gel filtration was approximately 80,000 but no information about the subunit structure is yet available.

4. Ribonucleoside Triphosphate Reductase from Pithomyces chartarum

The reductase detected in crude extracts of this fungus showed barely detectable activity with purine nucleoside diphosphates and was most active with ATP and GTP (*11*).

B. Ribonucleoside Diphosphate Reductases

Adenosylcobalamin-dependent reductases which utilize ribonucleoside diphosphates as substrates have been detected in three different microorganisms: *Rhizobium meliloti* (*82*), *Bacillus megaterium* (*10*) and *Corynebacterium nephridii* (*83*). These enzymes require a dithiol as the reducing substrate but do not have an absolute requirement for a divalent metal ion. The reductase from *C. nephridii* has been purified to homogeneity and preliminary experiments indicate a molecular weight of approximately 150,000 and the presence of two subunits. When *R. meliloti* is grown in a cobalt deficient medium the synthesis of ribonucleotide reductase apoenzyme is derepressed. Furthermore the cells become abnormally elongated and contain subnormal levels of DNA (*9*). The reductase from *R. meliloti* has been partially purified, while the reductase from *B. megaterium* has only been detected in crude extracts, thus firm conclusions concerning their substrate requirements and allosteric control must await further studies with more purified preparations.

IV. The Catalytic Mechanism

Although the reduction of ribonucleotides to the corresponding 2'-deoxyribonucleotides is catalyzed by enzyme systems differing in their cofactor requirements and/or in the level of phosphorylation of the substrates, the overall reduction process is very similar in all systems. For all the systems NADPH is the ultimate reductant, the hydrogen is transferred by thioredoxin reductase to thioredoxin, which in turn is oxidized by ribonucleotide reductase with the concomitant production of a 2'-deoxyribonucleotide. In these systems the thioredoxin-thioredoxin reductase reducing system can be replaced by dithiols such as dihydrolipoate or dithiothreitol.

A. The Stereochemistry of the Reduction

Initial studies with the enzyme systems from *E. coli* (*84*) and from *L. leichmannii* (*85, 86*) demonstrated that both reductases catalyze the transfer of hydrogen from water, via the hydrogens of the dithiol, to the deoxyribonucleotide. Chemical and enzymatic degradation studies of the 2'-deoxyribonucleotide product showed that tritium from tritiated water was associated exclusively with C-2' of the deoxyribosyl moiety. In further studies (*86–89*) ribonucleotide reduction was carried out in deuterium oxide and the deuterated deoxyribonucleotides analyzed by nuclear magnetic resonance (NMR) spectroscopy. The NMR spectrum of deoxyadenosine, derived from deoxyadenosine triphosphate formed by the action of the reductase from *L. leichmannii* on ATP in deuterium oxide showed the simplification of the splitting patterns of the resonances of H-1', H-2' and H-3', consistent with the stereospecific introduction of one deuterium atom (*87*). Based on an extension of the Karplus equation the downfield octet in the 2' multiplet was assigned to H-2'β (H_S) in deoxyadenosine. Since in the NMR spectrum of the enzymatically synthesized deuterated deoxyadenosine the upfield octet of the 2' multiplet was absent, the authors concluded that the deuterium atom was introduced in the H-2'α (H_R) position with retention of configuration. An independent study of the CDP → dCDP conversion by the reductase of *E. coli* in deuterium oxide (*88*) led to the same conclusions. However, *Durham* and co-workers pointed out that the Karplus equation when applied to furanoses may not be valid; thus these conclusions about the stereochemistry of the reductase reaction are not unequivocal. *Abrams* and co-workers (*89*) using the *L. leichmannii* reductase and CTP as substrate based the assignments of the chemical shifts and coupling constants of monodeuteriodeoxycytidine on the spectral properties of model compounds. Their results also suggested that the 2'-hydroxyl of CTP

had been replaced by deuterium with retention of configuration. The stereochemistry of the reductase reactions was unequivocally established by *Fraser-Reid* and *Radatus* (*90*) who prepared to two specifically labeled 2'-monodeuteriodeoxycytidines (*91*) and compared their NMR spectra with the spectrum of monodeuteriodeoxycytidine reported by *Reichard* and co-workers (*65*). This comparison proved conclusively that mono-deuteriodeoxycytidine formed enzymatically was (2'R)-[2'-^{2}H]-deoxy-cytidine. Independently *David* and *Eustache* (*92*) showed that the deuter-ated product of the reductase reaction was not the 2'S-isomer. *David* and *Rouzeau* (*93*) used [2'-^{3}H]CDP as a substrate for ribonucleotide reductase from *E. coli* and showed that the label was retained in the product without inversion. The 2'-deoxycytidine diphosphate product was trans-formed by a series of reactions into 5'-trityl-O^2, 3'-cyclouridine, which in turn in the presence of potassium tert-butoxide underwent an elimination to give radioactive 2',3'-dideoxy-2',3'-didehydrouridine. Since most of these E2 reactions involve *trans* eliminations, the presence of the label in the product indicated that the tritium label was *cis* to the leaving group thus establishing that the enzymatic reduction had occurred with reten-tion of configuration.

The results from these experiments clearly exclude reaction mecha-nisms involving first the elimination of water with the formation of 2',3' or 1',2' double bond in the ribofuranose ring followed by hydrogenation of the double bond. They also exclude a classical bimolecular nucleo-philic substitution of the hydroxyl group at C-2' by hydride ion, which would proceed with inversion of configuration at C-2'. Because the co-factor requirements for the ribonucleotide reductase system from *E. coli* (ATP and Mg^{++}) resemble those for enzymatic phosphorylation reactions, *Verheyden* and *Moffatt* (*94*) suggested that the displacement of the 2'-hydroxyl group may be facilitated through the intermediate formation of a 2'-phosphate- or pyrophosphate derivative. However cytidine 2'-phosphate 5'-diphosphate was not converted to dCDP by the reductase from *E. coli*. A different mechanism was suggested by the similarity between the adenosylcobalamin-dependent ribonucleotide reductase and dioldehydrase reactions. In the dioldehydrase reaction the partici-pation of both hydroxyl functions in the intramolecular redox reaction was demonstrated using ^{18}O-labeled propanediol (*95*). However, studies in which ^{18}O-labeled adenosine triphosphates were used as substrates for the reductase of *L. leichmannii* indicated that the 3'-hydroxyl function does not migrate during the reaction. With [2'-^{18}O]ATP as substrate the dATP product did not contain any label, while with [3'-^{18}O]ATP as substrate all the label could be recovered in the product (*96, 97*). Further-more when [2'-^{18}O]ATP was incubated with the reductase and all the other reaction components except the reducing agent, no label was lost
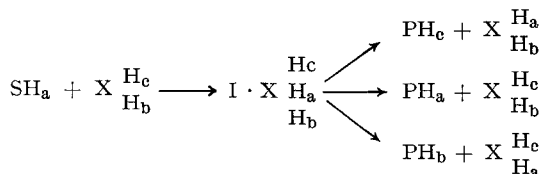
to the solvent, suggesting that in the absence of the reducing agent no reversible dissociation of the carbon-oxygen bond occurs. Indirect evidence indicates that in the *E. coli* reductase system also no oxygen migration takes place. Adenosine derived from *E. coli* grown on a medium containing [1-^{18}O]glucose or [2-^{18}O]fructose as the sole carbon source was labeled with isotopic oxygen in carbons 2′, 4′ and 5′, whereas deoxyadenosine isolated from DNA contained corresponding amounts of label only in carbons 4′ and 5′ *(98, 99)*.

B. The Nature of the Hydrogen Transfer

Both ribonucleotide reductases catalyze the transfer of hydrogen from the dithiol form of thioredoxin to the 2′-position of the deoxyribonucleotide product. In the adenosylcobalamin-dependent reductase system the mechanism of this hydrogen transfer has been studied extensively. Considerable evidence has been accumulated which indicates that in all adenosylcobalamin-dependent reactions the coenzyme functions as an intermediate hydrogen carrier. Thus when ribonucleotide reductase from *L. leichmannii* is incubated with a ribonucleoside triphosphate and a dithiol in tritiated water, tritium label is not only incorporated into the 2′-position of the deoxyribonucleotide but also into the coenzyme. Chemical degradation of the coenzyme demonstrated that during the reductase reaction *both* hydrogens of the 5′-methylene group bound to cobalt exchange with solvent hydrogens *(76, 100, 101, 102)*. Since these two C-5′hydrogens of adenosylcobalamin are not stereochemically equivalent, this observation suggests that during the reductase reaction these two hydrogens become stereochemically equivalent. In contrast to the other adenosylcobalamin-dependent reactions tritium from [5′-^{3}H$_2$]-adenosylcobalamin is not transferred to the product but only to the solvent. This is a consequence of the fact that in the reductase reaction hydrogen is transferred from a thiol, *via* adenosylcobalamin to the nucleotide. Because solvent hydrogens readily exchange with sulfur-bound hydrogens, solvent hydrogen is incorporated into the deoxyribonucleotide product and equilibration between solvent hydrogens and the C-5′ methylene hydrogens of the coenzyme occurs. This exchange reaction between labeled adenosylcobalamin and the solvent is faster than the reduction and thus no label from the tritiated coenzyme is found in the deoxyribonucleotide. Furthermore hydrogen exchange between solvent and adenosylcobalamin is not dependent on reduction of the substrate. Hydrogen transfer from coenzyme to water and from water to coenzyme is also promoted by deoxyribonucleotide triphosphates in the absence of substrates *(76)*. In spite of this the exchange reaction has been considered an integral part of the reductase reaction because both exchange and
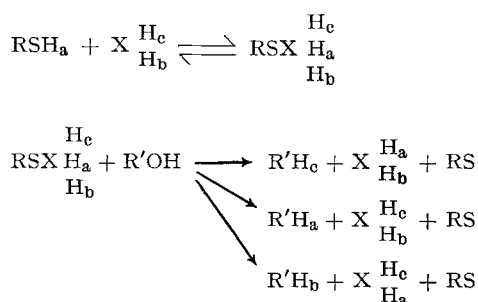
reduction have an absolute requirement for a dithiol, both reactions are catalyzed by the same homogeneous enzyme preparation and treatment of the enzyme with protein reagents, such as N-bromosuccinimide, affects the rate of reduction and exchange to the same extent.

Based on isotope exchange experiments with dioldehydrase. *Abeles* *(103)* postulated the following general mechanism for the hydrogen transfer reaction.

$$
SH_a + X{}^{H_c}_{H_b} \longrightarrow I \cdot X{}^{H_c}_{H_a}{}_{H_b}
\begin{cases}
PH_c + X{}^{H_a}_{H_b} \\
PH_a + X{}^{H_c}_{H_b} \\
PH_b + X{}^{H_c}_{H_a}
\end{cases}
$$

SH and PH represent substrate and product, XHH is enzyme bound adenosylcobalamin and I is an enzyme bound intermediate. The proposed reaction involves a two step sequence in which an intermediate is formed containing three equivalent hydrogens, two derived from the 5'-methylene carbon of the coenzyme and one from propanediol.

A similar intermediate with three equivalent hydrogens has been proposed for the ribonucleotide reductase system *(76)*. However, the ribonucleotide reductase system is unique in that it catalyzes the hydrogen transfer between two different substrates: a dithiol and a ribonucleotide.

$$
RSH_a + X{}^{H_c}_{H_b} \rightleftharpoons RSX{}^{H_c}_{H_a}{}_{H_b}
$$

$$
RSX{}^{H_c}_{H_a}{}_{H_b} + R'OH \longrightarrow
\begin{cases}
R'H_c + X{}^{H_a}_{H_b} + RS \\
R'H_a + X{}^{H_c}_{H_b} + RS \\
R'H_b + X{}^{H_c}_{H_a} + RS
\end{cases}
$$

RSH and R'OH represent the dithiol and ribonucleotide substrates, XHH is the enzyme bound adenosylcobalamin, RSXHHH is an enzyme bound intermediate and RS represents the oxidized dithiol. The isotope exchange experiments suggest that the enzyme bound intermediate can

be generated in presence of only the reducing substrate. Thus the first half reaction describes the hydrogen exchange between solvent hydrogens and the 5′-methylene hydrogens of the coenzyme, while the second half reaction depicts the reduction of the ribonucleotide by the intermediate.

C. The Nature of the Intermediate(s)

One of the subunits (protein B2) of ribonucleotide reductase from *E. coli* contains two iron atoms and a variable amount of a paramagnetic species. This paramagnetic species, which has been identified as an organic radical, is directly correlated with enzyme activity *(67)*. The iron of protein B2 does not appear to participate as an electron carrier because the part of the electronic spectrum of protein B2 due to iron is not affected by a variety of oxidizing and reducing agents. Furthermore the electronic spectrum is not affected by the addition of thioredoxin or any other component — alone or in combination — of the ribonucleotide reductase system. *Atkin* and co-workers *(67)* have suggested that the two iron atoms function in the generation as well as the stabilization of the organic free radical. Radical formation may involve an iron-catalyzed one electron aerobic oxidation of the radical precursor, or a one electron reduction of the precursor by Fe^{+2} to yield Fe^{+3} in protein B2. According to these authors the organic radical is the functional contribution of protein B2 to ribonucleotide reductase and they thus suggest that the reduction of ribonucleoside diphosphates by the *E. coli* reductase involves the participation of radical intermediates. Evidence for the presence of paramagnetic intermediates in the ribonucleotide reductase system of *L. leichmannii* has been obtained from spectrophotometric stopped flow studies *(104)* and ESR measurements *(77)* by *Blakley* and co-workers. In the presence of dGTP, an allosteric effector, and excess dihydrolipoate adenosylcobalamin reacts rapidly ($t_{1/2} = 17$ ms) with equimolar amounts of reductase. The changes in the ultraviolet and visible spectrum correspond to those predicted for the partial conversion of adenosylcobalamin to cob(II)alamin, suggesting that the carbon-cobalt bond of the coenzyme is cleaved homolytically. The other product of the homolytic cleavage, 5′-deoxyadenosyl radical, cannot be trapped in a pool of 5′-deoxyadenosine. When the temperature of the reaction mixture is lowered from 37° to 5°, the spectrum of adenosylcobalamin is regenerated, indicating that this homolytic cleavage is a reversible process. The homolytic cleavage of the carbon-cobalt bond of adenosylcobalamin can also be followed by ESR spectroscopy if the reaction mixture is freeze-quenched in isopentane at 130 °K. The ESR signal is centered on a mean effective *g* value of 2.119. Computer simulation of the spectrum is necessary for analysis of the hyperfine structure. The authors point out that

the principal features of the spectrum are due to a single paramagnetic species. On the other hand estimates of the yield of the paramagnetic species suggest the production of two unpaired electrons per molecule of intermediate. Evidently one paramagnetic species is responsible for the major features of the ESR signal while the other gives rise to a very broadened signal underlying much of the spectrum. The ESR signal of a reaction mixture containing adenosylcobalamin, selectively enriched with 90% carbon-13 in the 5'-position of the adenosyl moiety (105), does not show any additional hyperfine splitting due to the ^{13}C-nucleus. These results suggest that the major features of the ESR spectrum are due to an unpaired electron associated with Co^{+2} and that the broadened signal is due to the 5'-deoxyadenosyl radical. Thus although the electronic spectrum of the intermediate is very similar to that of cob(II)-alamin, the ESR spectrum is not at all like that of cob(II)alamin, either free in solution or enzyme-bound. These paramagnetic intermediates derived from adenosylcobalamin are formed not only in the presence of allosteric effectors such as dGTP but also in the presence of the substrates GTP and ATP. For instance in the presence of GTP the paramagnetic intermediates first accumulate, reach a maximum at 15 to 20 ms and then diminish until a low steady state concentration is reached.

The spectral studies with the E. coli and the L. leichmannii ribonucleotide reductase system indicate that in both systems one of the "active intermediates" is an organic free radical. In the E. coli system this organic free radical is generated by an unknown interaction between two iron atoms and an unknown radical precursor while in the L. leichmannii system the organic free radical is generated by a homolytic cleavage of the carbon-cobalt bond of adenosylcobalamin. In a subsequent reaction either organic radical reacts with a dithiol, such as reduced thioredoxin, to yield a reducing agent capable of the hydrogenolysis of the secondary alcohol at carbon 2' of the substrate.

Two additional paramagnetic species have been detected in the L. leichmannii ribonucleotide reductase system. When adenosylcobalamin is incubated with a molar excess of reductase, a dithiol and either a ribonucleoside triphosphate or a deoxyribonucleoside triphosphate, the coenzyme is slowly degraded ($t_{1/2} = 30$ min) to cob(II)alamin and 5'-deoxyadenosine (78, 106). The ESR spectrum of the paramagnetic cobamide shows unique hyperfine and superhyperfine splitting not observed for cob(II)alamin in solution or as a solid.

In the presence of a complete ribonucleotide reductase system: reductase, adenosylcobalamin, ribonucleoside triphosphate, appropriate allosteric effector and thiol, another type of ESR signal is produced. This signal consists of two major lines with mean g values of 2.032 and 1.965 and has been referred to as the "doublet" spectrum (107). In reac-

39

tion mixtures containing adenosylcobalamin, a molar excess of reductase, dGTP, ATP and glutathione this doublet reaches a maximum after 20 minutes at 37° and then slowly declines; during the same time the highly resolved spectrum of cob(II)alamin steadily increases. After 60 minutes incubation most of the cobalamin is degraded to cob(II)alamin and 5′-deoxyadenosine. Almost identical "doublet" ESR signals have been observed in some of the other adenosylcobalamindependent reactions such as glyceroldehydrase *(108)*, dioldehydrase *(109)*, and ethanolamine deaminase *(110)*, suggesting that in all these reactions a similar paramagnetic species is generated. It is noteworthy that the ESR spectrum of protein B2 of the *E. coli* reductase also shows a doublet structure centered at $g = 2.0047$, however in the contrast with the doublet of the cobalamindependent reaction the doublet of protein B2 is quite narrow. Of course the ESR spectrum of protein B2 does not show the broad resonance at low field, due presumably to cob(II)alamin. In the *L. leichmannii* reductase system the most pronounced doublet signal is obtained with a poor reducing substrate, glutathione, or with a ribonucleotide analog, *ara*-ATP, that is not a substrate. These results resemble those obtained by *Abeles* and co-workers with dioldehydrase *(111)*. Using a substrate analog, 2-chloroacetaldehyde, labeled with ^2H or ^{13}C they were able to demonstrate that the doublet signal represents a radical derived from the substrate analog. Although chloroacetaldehyde is not a substrate for dioldehydrase it is nevertheless able to exchange hydrogen with the 5′-methylene hydrogens of adenosylcobalamin, suggesting that the reaction of chloracetaldehyde with the dioldehydrase coenzyme complex produces an intermediate(s) similar to that (those) found in the normal catalytic process. Indeed the reaction with chloroacetaldehyde can be regarded as the first half of the hydrogen transfer reaction. In the normal catalytic process the steady state level of the intermediates is probably too low to be detected by ESR spectroscopy. This paramagnetic intermediate in the ribonucleotide reductase system has not yet been identified, however, by analogy with the dioldehydrase system, the doublet signal may represent a radical derived from the reducing substrate or from the ribonucleotide substrate. *Hamilton et al.* *(107)* have pointed out that the doublet spectrum does not resemble published spectra of sulfur radicals. On the other hand the doublet spectrum probably does not represent a 2′-deoxyribonucleotide radical, because if such a radical were formed with *ara*-ATP as the nucleotide, hydrogen exchange between the 5′-methylene hydrogens of adenosylcobalamin and the 2′-hydrogen of *ara*-ATP would be expected. Since in the ribonucleotide reductase reaction these hydrogens of the coenzyme exchange with solvent hydrogens, solvent hydrogen would be incorporated in the 2′-position of *ara*-ATP. However, no incorporation of

tritium could be demonstrated when this nucleotide was incubated in tritiated water with the reaction components required for the generation of the doublet ESR signal (*112*).

The results described above suggest the presence of at least two intermediates in the reductase reaction of *L. leichmannii* and are consistent with the following reaction scheme:

$$
\begin{array}{ccccc}
& & & \text{E}\diagup^{\text{SH}}_{\text{SH}} & \\
\overset{\text{R}}{\underset{[\text{Co}]}{\overset{|}{\text{HCH}}}} & \xrightarrow{\ 1\ } & \overset{\text{R}}{\underset{[\dot{\text{Co}}]}{\text{H-C-H}}} & \underset{\rightleftharpoons}{\overset{2}{\longrightarrow}} & \overset{\text{R}}{\underset{[\dot{\text{Co}}]}{\text{H-C-H}}}\ \ \text{H}\diagdown^{\text{S}}_{\cdot\text{S}}\diagdown\text{E}
\end{array}
$$

I   II

$$
\overset{\text{R}}{\underset{\text{H}}{\text{H-C-H}}}\ \text{H}\diagdown^{\text{S}}_{\cdot\text{S}}\diagdown\text{E}
\qquad\qquad
\overset{\text{R}}{\underset{\text{H}}{\text{H-C-H}}}\ \ \text{S}\diagup^{\diagdown}_{\diagup}\text{E}
$$

$\underset{\longleftarrow\ \ \ \ }{\overset{3}{\dashrightarrow}}$ H_2O

$\overset{\cdot}{[\text{Co}]}$ HO OH $\overset{\cdot}{[\text{Co}]}$ OH

$\text{B}\quad CH_2OP_3O_9{}^{-4}$ $\text{B}\quad CH_2OP_3O_9{}^{-4}$

III

4

$$
\overset{\text{R}}{\underset{[\dot{\text{Co}}]}{\text{H-C-H}}}
\qquad
\text{S}\diagup^{\diagdown}_{\diagup}\text{E}
\qquad\qquad
H_2O
$$

$\text{H}\ \ OH$

$\text{B}\quad CH_2OP_3O_9{}^{-4}$
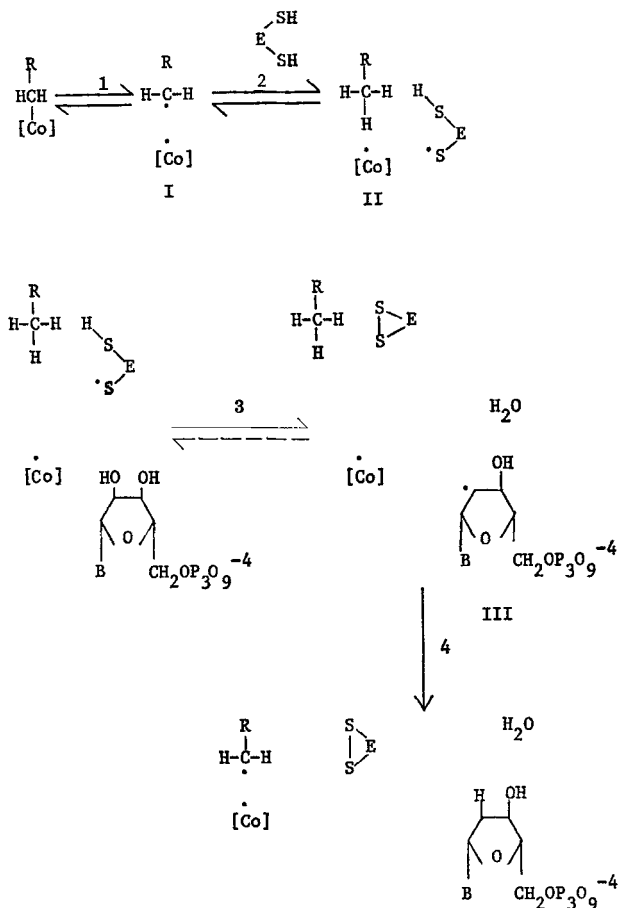
The first step in this reaction scheme involves the homolytic cleavage of the carbon-cobalt bond of the coenzyme to cob(II)alamin and a 5′-deoxyadenosyl radical. This intermediate (I) is responsible for the spectral

changes observed in the stopped-flow studies and can be detected by ESR spectroscopy if the reaction mixture is freeze-quenched. In the second step the 5'-deoxyadenosyl radical abstracts a hydrogen atom from a dithiol, provided either by the enzyme or by the reducing substrate, to yield 5'-deoxyadenosine, and a sulfur radical.

Both reactions 1 and 2 are reversible and account for the hydrogen exchange reaction. In the third reaction the dithiol radical abstracts a hydroxyl radical from carbon-2' of the nucleotide and generates a 2'-deoxyribonucleotide radical, water and a disulfide. In the last reaction the 2'-deoxyribonucleotide radical abstracts a hydrogen atom from 5'-deoxyadenosine to yield the 2'-deoxyribonucleotide and the coenzyme radical pair. The doublet spectrum is generated by either a sulfur radical (II) or a 2'-deoxyribonucleotide radical (III); the unusual line width and splitting of this signal are probably due to the interaction of the sulfur- or carbon radical with the unpaired electron of cob(II)alamin (*113*). Slow degradation of all or some of the three intermediates to 5'-deoxyadenosine and cob(II)alamin probably occurs *in vitro*.

V. The Thioredoxin System

The thioredoxin system, consisting of thioredoxin and thioredoxin reductase, was originally discovered as the hydrogen carrier system, which provides, with NADPH, the reducing potential for the reduction of ribonucleotides (*5*, *35*). Since then considerable evidence has been accumulated to indicate that this or a closely related system also participates in a variety of other enzymatic reductions. For instance thioredoxin can function as an electron carrier between NADPH and several disulfides, such as insulin, lipoate and oxidized glutathione. Furthermore *Porqué et al.* (*114*) have shown that thioredoxin and thioredoxin reductase from yeast can function as hydrogen carriers in the reduction of methionine sulfoxide and sulfate.

A. Thioredoxin

Thioredoxin from *E. coli* is a heat stable small acidic protein (pI 4.4—4.5) with a molecular weight of about 12,000 (*37*, *115—118*). It consists of a single polypeptide chain with 108 amino acid residues; the complete amino acid sequence has been determined (Fig. 2). Thioredoxin can occur in the oxidized or reduced state. Reduced thioredoxin contains two cysteine residues in positions 32 and 35 which can be oxidized enzymatically or chemically to the disulfide bridge of cystine. Only two

```
          1                 5                  10                 15
     H- Ser Asp Lys Ile Ile His Leu Thr Asp Asp Ser Phe Asp Thr Asp

                                                               Leu

                                                               Val
              30                25                 20
   ┌── Cys Trp Glu Ala Trp Phe Asp Val Leu Ile Ala Gly Asp Ala Lys
   │
   │   Gly
   │
   │   Pro
   │
   └── Cys Lys Met Ile Ala Pro Ile Leu Asp Glu Ile Ala Asp Glu Tyr
       35                40                 45

                                                            50 Gln

                                                               Gly

       Thr Gly Pro Asn Gln Asp Ile Asn Leu Lys Ala Val Thr Leu Lys
           65                60                 55
       Ala

       Pro

       Lys Thr Ile Gly Arg Gly Ile Pro Thr Leu Leu Leu Phe Lys Asn
           70                75                 80

                                                               Gly

                                                            85 Glu
       100
       Lys Leu Gln Gly Lys Ser Leu Ala Gly Val Lys Thr Ala Ala Val
                           95                 90
       Glu

       Phe
                   105
       Leu Asp Ala Asn Leu Ala -OH
```

Fig. 2. Structure of *E. coli* thioredoxin (*37*)

amino acids — glycine and proline — are spaced between the half cystines;
the proline residue holds the disulfide bridge in a fixed and exposed posi-
tion. The N-terminal half of thioredoxin contains twelve acidic amino
acids and four basic residues; on the other hand the C-terminal region
contains many hydrophobic residues. This distribution of amino acid
residues suggests that the N-terminal part of thioredoxin, including

43

the disulfide bridge of the active center is exposed to the solvent, while the C-terminal region is buried in the inside of the molecule by its hydrophobic residues. The redox potential of the couple thioredoxin S_2/thioredoxin (SH_2) is —0.26 V, pH 7.0, 20° indicating that reduced thioredoxin is a better reducing agent than glutathione and cysteine. The two tryptophan residues of thioredoxin (Trp-28 and Trp-31) are located close to the disulfide bridge and seem to play a major role in maintaining an enzymatically active conformation of the protein. Chemical modification of both tryptophans to l-formyl-tryptophanyl residues (119) or to oxindolyl residues (120) resulted in complete inactivation. Tryptophan fluorescence studies of the oxidized and reduced form of thioredoxin suggested that one or both of the residues are involved in a conformational change that occurs when the disulfide bond is reduced (121, 122). This conformational change of the protein must be localized in nature because the sedimentation behavior, the fluorescence polarization, the ORD and the CD do not change on reduction of the disulfide bridge. *Reichard* (5) suggests that this conformational change is involved in the binding of the oxidized and reduced forms to their respective proteins in the ribonucleotide reductase system. The reduced form of thioredoxin should bind preferentially to ribonucleotide reductase, while the oxidized form should bind to thioredoxin reductase. Thioredoxin has been crystallized from alcoholic solutions in the presence of cupric ions. The crystals belong to the monoclinic space group C2 with unit cell dimensions $a = 89.5$ Å, $b = 50.8$ Å, $c = 60.2$ Å and $\beta = 113.5°$ and have two molecules of thioredoxin per asymmetric unit (123).

Infection of *E. coli* with bacteriophage T4 *am* 122 induces the synthesis of a new ribonucleotide reductase and a new thioredoxin; these two proteins are able in the presence of *E. coli* thioredoxin reductase to catalyze the reduction of ribonucleotides. Phage-induced ribonucleotide reductase has a specific requirement for phage-induced thioredoxin and is unable to use reduced *E. coli* thioredoxin as a hydrogen donor; conversely, *E. coli* ribonucleotide reductase is unable to use phage thioredoxin (41, 42). Like thioredoxin from *E. coli*, phage-induced thioredoxin is a small heat stable protein containing a single disulfide bridge made up of two half cystine residues. However, the two thioredoxins differ in size, amino acid composition and redox potential. T4 thioredoxin has a molecular weight of 10,400 and consists of a single polypeptide chain with 88–89 amino acid residues. It contains three methionine residues but is completely lacking in tryptophan. Indeed the amino acid sequence of the active center of T_4-thioredoxin is quite different from that of *E. coli* thioredoxin (124). The absence of tryptophan is of interest because the two tryptophan residues in the bacterial thioredoxin are situated close to the disulfide bridge and have been

implicated in the reaction mechanism. The redox potential of T_4 thioredoxin is —0.23 V at pH 7.0 and 20°, significantly more positive than that of *E. coli* thioredoxin, indicating that oxidized T_4 thioredoxin is able to oxidize reduced *E. coli* thioredoxin *(124)*.

Both *E. coli* and T_4 thioredoxin have recently been purified by immunoabsorbent affinity chromatography. The specific immunoadsorbents were prepared by coupling the α-globular fractions of rabbit anti-thioredoxin antisera to Sepharose. This technique makes it possible to isolate both thioredoxins from phage-infected cells by two consecutive chromatography steps on the specific adsorbents *(125, 126)*.

Thioredoxin from yeast has been obtained in two forms (I and II) of which thioredoxin II has been purified to homogeneity *(43)*. Both yeast thioredoxins are able to serve as hydrogen donors for the ribonucleotide reductase from *E. coli*. The molecular weight (12,600) of thioredoxin II is similar to that of thioredoxin from *E. coli*. Although both yeast thioredoxins contain only one tryptophan residue and although their amino acid compositions differ markedly from that of *E. coli* thioredoxin, the amino acid sequences around the disulfide bridge of these three thioredoxins are identical:

$$\overline{\text{-Trp-Cys-Gly-Pro-Cys-Lys-}} \qquad (122).$$

The oxidation reduction potential of the yeast thioredoxin-II $(SH)_2$/thioredoxin-S_2 couple is —0.24 V at pH 7.

A thioredoxin has also been partially purified from *L. leichmannii* *(39)*. Although this thioredoxin is similar in size (MW approximately 12,000) to the *E. coli* thioredoxin, it is not able to function as a substrate for the *E. coli* thioredoxin reductase. More recently thioredoxins have been purified to homogeneity from rat Novikoff ascites hepatoma *(127)* and from calf liver *(45)*. The properties of these two thioredoxins are quite similar (MW 11,400 and 12,000 respectively). The amino acid compositions however, are different. For instance the Novikoff tumor thioredoxin contains six half-cysteine residues, whereas calf liver thioredoxin has only four. Both these thioredoxins have a tendency to aggregate in the oxidized form. This aggregation is probably due to mixed sulfide formation between the additional sulfhydryl groups. Like yeast thioredoxin II, calf liver thioredoxin contains only one tryptophan residue; unfortunately the tryptophan content of Novikoff tumor thioredoxin was not determined.

Of the thioredoxins studied thus far only the T_4 phage thioredoxin is unable to serve as the reducing substrate for *E. coli* ribonucleotide

reductase. T_4 thioredoxin does not contain tryptophan and the amino acid sequence around the disulphide bridge is completely different from that of the thioredoxins from *E. coli*, yeast, Novikoff hepatoma, calf liver and rat liver (*44*). Presumably these thioredoxins are able to interact with *E. coli* ribonucleotide reductase because their active sites are very similar or identical, as is the case for the thioredoxins of *E. coli* and yeast.

B. Thioredoxin Reductase

Thioredoxin reductase catalyzes the reduction of the oxidized form of thioredoxin by NADPH (*36*).

$$\text{Thioredoxin-S}_2 + \text{NADPH} + \text{H}^+ \rightleftharpoons \text{Thioredoxin-(SH)}_2 + \text{NADP}^+$$
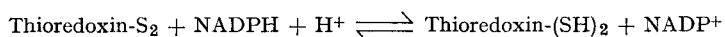
The enzyme is specific for the reduction of the disulfide bond of thioredoxin and NADPH is the preferred hydrogen donor. The hydrogen transfer reaction is stereospecific for the B-position (H_S) of the nicotinamide ring of NADPH (*128*). Although the purified enzyme shows no activity with glutathione and lipoate, thioredoxin reductase will catalyze the reduction of a variety of disulfides by NADPH in the presence of catalytic amounts of thioredoxin. Thioredoxin reductase from *E. coli* has been purified to homogeneity in two laboratories (*38, 129*) and has been studied extensively (*130—133*). The molecular weight of the enzyme determined by ultracentrifugal methods was found to be 66,000 (*128*). It contains two molecules of FAD per molecule of enzyme and its visible spectrum is very similar to the spectra of glutathione reductase and lipoyldehydrogenase. Neutron activation analysis showed that the enzyme does not contain a stoichiometric amount of a metal. The enzyme consists of two identical or very similar polypeptide chains held together by non-covalent bonds. Each of the subunits contains one molecule of FAD. The molecular weight of a subunit based on amino acid analysis and FAD content was 36,500. Each subunit contains three sulfhydryl groups and one disulfide bridge (*8*). Earlier determinations had shown the presence of only 4 half-cystines per mole of FAD (*130, 131*). The sulfhydryl groups can be reacted with alkylating agents only after complete denaturation of the enzyme with guanidine hydrochloride suggesting that they are buried in the enzyme structure.

Thelander (131) has proposed the following structure for thioredoxin reductase:
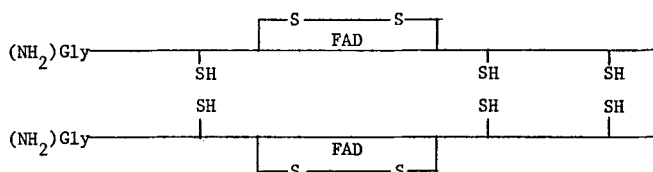
Each subunit of the enzyme functions in a series of oxidation-reduction reactions as outlined below *(130)*:
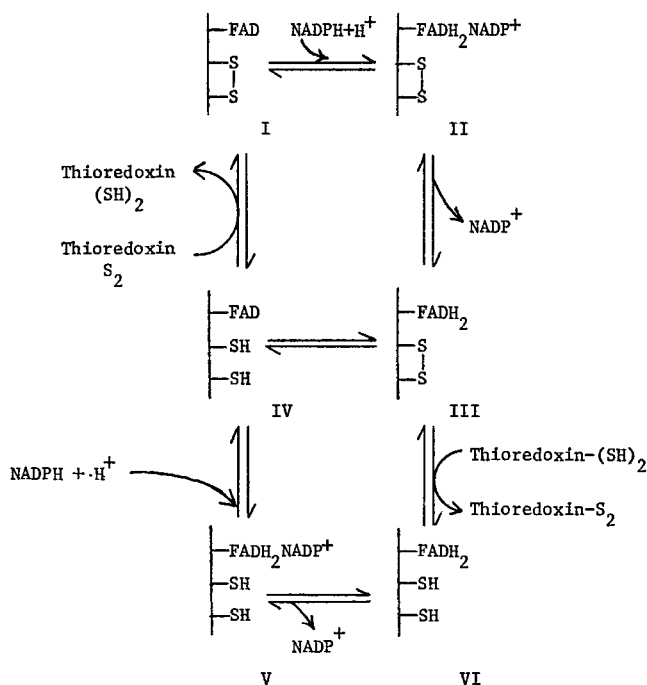
The normal catalytic process involves the sequence I→II→III→IV→I, while the steps IV→V→VI→III may also be part of the overall reaction. *Thelander (131)* has pointed out that the reaction mechanism of thioredoxin reductase differs from those of glutathione reductase and lipoyldehydrogenase because during the anaerobic titration of thioredoxin reductase no flavin semiquinone intermediate could be detected. Although thioredoxin reductase contains two subunits only one octapeptide

containing the active center of the enzyme could be isolated, indicating that the amino acid sequence around both disulfides is identical. The amino acid sequence of the cystine peptide was determined to be (132, 133):

$$
\begin{array}{ccc}
\text{S} & \rule[0.5ex]{2cm}{0.4pt} & \text{S} \\
| & & | \\
\end{array}
$$
-Ala-Cys-Ala-Thr-Cys-Asp-Gly-Phe-
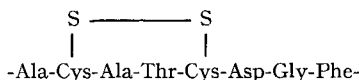
Thus thioredoxin reductase, like its substrate thioredoxin, contains only two amino acid residues between the two half cystine residues and in both proteins the disulfide defines a small loop of only 14 atoms.

Thioredoxin reductases have also been purified from yeast (43, 134) and from rat liver (135). Thioredoxin reductase from yeast is a flavoprotein with a molecular weight of approximately 75,000 and consists of two subunits, each containing one molecule of FAD. Although the amino acid composition of this thioredoxin reductase is quite different from that of E. coli, both enzymes contain 5 half-cystine residues and have almost identical absorption spectra. Like the E. coli enzyme, thioredoxin reductase from yeast is completely inhibited by p-chloromercuriphenylsulfonate (PCMS) only in the presence of NADPH suggesting that the yeast enzyme also contains a disulfide bridge at the catalytic site.

Thioredoxin reductase from calf liver was found to reduce 5,5'-dithiobis-(2-nitrobenzoic acid) (DTNB) at the expense of NADPH even in the absence of thioredoxin as an intermediate electron carrier, indicating that this mammalian reductase may have a wider substrate specificity than the corresponding enzymes from E. coli and yeast.

The thioredoxin reductases are highly specific for their thioredoxin substrate. For instance, yeast thioredoxin reductase is specific for the reduction of the homologous thioredoxins and does not interact with thioredoxins from E. coli or from T_4-infected E. coli. Furthermore E. coli thioredoxin reductase does not use the thioredoxins from Novikoff hepatoma, yeast, and L. leichmannii.

VI. The Interaction of Ribonucleotide Reductases with Nucleotide- and Coenzyme Analogs

A. Interaction with Nucleotide Analogs

The ribonucleotide reductases appear to be highly specific for the β-D-ribofuranoside moiety of their nucleotide substrates. Neither the reductase from E. coli nor the enzyme from L. leichmannii is able to

reduce the appropriate nucleotide of 3'-deoxyadenosine (136, 137). Whether the 3'-hydroxyl group is necessary for binding to the enzyme or whether it participates in the catalytic process has not yet been established. Analogs of ATP and CTP which contain 2-0-methylribose, 3-0-methylribose, arabinose, xylose (79) 2-deoxy-2-aminoribose, 2-deoxy-2-azidoribose and 2-deoxy-2-chlororibose (47) are not substrates even in the presence of a specific effector. Furthermore most of these nucleotides are unable to compete with ATP for the catalytic site.

Requirements for the interaction of the heterocyclic base of the ribonucleotide with the catalytic site are much less stringent. Kinetic studies have indicated that all ribonucleotides bind to the same substrate site, which therefore is able to accommodate a variety of bases with different functional groups; specificity is mediated through allosteric modification of the substrate site. In addition to the common ribonucleotides ATP, GTP, ITP, CTP and UTP, the reductase from *L. leichmannii* is able to reduce the triphosphates of 1-β-D-ribofuranosylbenzimidazole and of the antibiotics tubercidin, toyocamycin and sangivamycin (Fig. 3). Furthermore the rate of reduction of these four nucleotides is greatly increased by the allosteric effector dGTP (136, 137). In the ribonucleotide reductase system from *E. coli* the diphosphates of tubercidin and toyocamycin, but not sangivamycin 5'-diphosphate, are substrates. The reduction of these two substrates is also specifically stimulated by dGTP, the allosteric effector of ADP reduction. These results suggest that the pyrimidine moiety and N-7 of the imidazole ring of the adenine nucleotides are not essential for interaction with the reductases. In contrast formycinyl triphosphate is not a substrate for the *L. leichmannii* enzyme (112). The inability of formycinyl triphosphate to act as a substrate is not surprising because the modification of a purine to a pyrazolopyrimidine base brings about quite drastic changes in the conformation of the entire nucleotide. This base modification affects not only the conformation about the glycosyl bond but also the sugar phosphate backbone (138).

Reduction of CTP by *L. leichmannii* ribonucleotide reductase is specifically stimulated by its allosteric effector dATP. The structural specificity of the effector sites was studied with the same series of nucleotide analogs. Like 2'-dATP, 3'-dATP stimulated the reduction of CTP indicating that the 3'-hydroxyl group is not necessary for binding at an effector site. The pyrrolopyrimidine analogs, tubercidin- and toyocamycin triphosphate were also able to activate CTP reduction. Since these two nucleotides are also substrates for the *L. leichmannii* enzyme, they may interact with the regulatory site as the corresponding 2'-deoxyribonucleotides. Similarily in the *E. coli* ribonucleotide reductase system, 3'-dATP, as well as the two pyrrolopyrimidine triphosphates mimicked
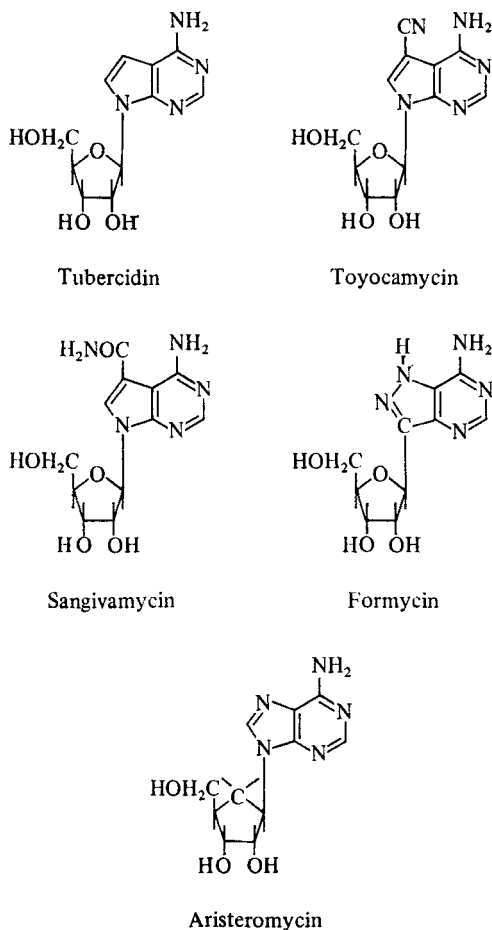
Fig. 3. Structures of nucleoside antibiotics

the effect of 2'-dATP in inhibiting the reduction of all four common nucleoside diphosphates. Both 2'- and 3'-0-methyl ATP stimulate CTP reduction, but do not promote hydrogen exchange between adenosylcobalamin and the solvent. In contrast *ara*- and *xylo*-ATP and *ara*-CTP do not act as allosteric modifiers, nor do they inhibit the action of the physiological effectors, dATP and dCTP. However, *ara*-ATP and *ara*-CTP, but not *xylo*-ATP are able to promote the hydrogen exchange reaction. The results suggested that the reductase from *L. leichmannii* has two effector sites for the interaction with these nucleotides, one site which modulates enzyme-substrate interaction and another which affects the interaction between the enzyme and coenzyme (*79*).

The effect of *ara*-ATP and *ara*-CTP on ribonucleotide reduction has also been studied in crude extracts from Novikoff (*139*) and Ehrlich (*140*) ascites tumor cells. Inhibition by these nucleotide analogs appeared to be competitive with effector nucleotides, but not with nucleoside diphosphate substrates.

Irreversible inhibition of ADP and CDP reduction in Ehrlich tumor cells was caused by ATP-, AMP- or adenosine oxidized with sodium periodate. The inhibition probably involves Schiff base formation between the 2', 3'-dialdehyde product and a lysine residue(s), because pyridoxal phosphate also inhibits ADP and CDP reduction (*141*, *142*).

B. Analogs of Adenosylcobalamin

Numerous analogs of adenosylcobalamin have been tested for their ability to replace or to inhibit the action of the coenzyme in the adenosylcobalamin-dependent ribonucleotide reductase reaction; the enzyme from *L. leichmannii* has been used in most of these studies. Kinetic studies have been used in most investigations of analog-enzyme interactions and thus the interpretation of data regarding the affinity of analogs for the reductase is subject to the limitations imposed on kinetic studies of a complex reaction.

Three classes of analogs have been studied: a) analogs in which the 5,6-dimethylbenzimidazole moiety of the nucleotide has been replaced, b) analogs with modifications on the periphery of the corrin ring and c) analogs in which the 5'-deoxyadenosyl moiety has been altered or replaced. Coenzymes in which the 5,6-dimethylbenzimidazole moiety has been replaced by benzimidazole, 5-methoxybenzimidazole, adenine and 2-methyladenine have been tested with ribonucleotide reductase. Adenosylcobamides with benzimidazole and adenine function as coenzymes in the *L. leichmannii* system (*52*, *80*), while those with 5-methoxybenzimidazole and 2-methyladenine are active with the *R. meliloti* reductase (*82*). In contrast adenosylcobinamide, which lacks the entire nucleotide moiety does probably not function as a coenzyme because it did not yield the rapidly appearing paramagnetic intermediate (*77*).

Studies with analogs modified in the corrin ring have shown that the generation of a negative charge on the periphery of the ring is detrimental to coenzymatic activity. Adenosylcobalamin b-, d- and e-carboxylic acids show coenzyme activity only at very high concentration and are poor inhibitors of ribonucleotide reduction (*72*, *143*). Blocking of the negative charge of adenosylcobalamin e-carboxylic acid by amidation, even with the bulky 2,4-dinitroaniline moiety, restores coenzyme activity.

51

Adenosylepicobalamin, in which the e-propionamide side chain is projected up rather than down relative to the plane of the corrin ring is completely inactive as a coenzyme, but does inhibit the action of adenosylcobalamin (144). X-ray analyses of cyanoepicobalamin have indicated that the e-propionamide side chain prevents the 5'-deoxyadenosyl moiety from occupying its normal position above the corrin ring (145).

The cobalt-free corrinoids discovered by Toohey (146) do not show any affinity for the reductase of *L. leichmannii* (75).

Cob(II)alamin was found to be a competitive inhibitor with respect to adenosylcobalamin of ATP reduction by the *L. leichmannii* enzyme. In the presence of 5'-deoxyadenosine the apparent K_I was decreased more than 10-fold; adenosine was able to enhance inhibition by cob(II)-alamin to a lesser extent, but 2'-deoxyadenosine, 3'-deoxyadenosine, and 4', 5'-didehydro-5'-deoxyadenosine were much less effective. These studies indicate that cobalamin and nucleoside bind at sites that are occupied by adenosylcobalamin during catalysis and that the binding of the cobalamin moiety is greatly enhanced by the presence of a specific nucleoside (106).

Cyano-, hydroxo-, methylcobalamin, or their e-amidated derivatives are ineffective as coenzymes, but all exhibit some inhibition at high concentration. Alterations of the adenosyl moiety in the upper coordination position of the coenzyme either diminishes or abolishes coenzyme activity (75, 147). Compared to adenosylcobalamin (relative activity, 100) analogs containing the following nucleosides have the indicated activities: 3-β-D-ribofuranosyladenine, 60; 9-β-D-ribofuranosylpurine, 10; 2'-deoxyadenosine, 5; tubercidin, 3; L-adenosine, 1; and *ara*-adenosine, 0.6. In contrast analogs containing 1-β-D-ribofuranosylbenzimidazole, inosine, aristeromycin (Fig. 3), 9-(5',6'-dideoxy-β-D-ribo-heptofuranosyl)adenine, thymidine, uridine, cytidine and 9-(ω-alkyl) adenines with 2 to 6 methylene groups are totally inactive (148). However all these analogs are inhibitors of *L. leichmannii* ribonucleotide reductase. The results suggest that although neither the 6-amino group nor N-7 of the purine ring are essential for activity, they nevertheless participate in the enzyme-coenzyme interaction. The results also indicate that even small changes in the ribofuranose ring have a profound effect on coenzyme function. The most potent inhibitors of adenosylcobalamin action $(K_I < K_m)$ are the analogs derived from 2'-deoxyadenosine, 9-(5',6'-dideoxy-β-D-ribo-heptofuranosyl)adenine and 9-(5'-hydroxypentyl) adenine.

Two recently synthesized analogs of adenosylcobalamin, formycinylcobalamin and N^6-ethenoadenosylcobalamin may be useful in studies of the mechanism of action of the coenzyme (149). The fluorescence of both nucleosides is completely quenched in the coenzyme form, but after

homolytic cleavage of the carbon-cobalt bond of these analogs by photolysis fluorescent nucleosides are regenerated.

C. Inhibitors of Non-Heme Iron Ribonucleotide Reductases

Several compounds capable of metal chelation inhibit the non-heme iron ribonucleotide reductases; with many of these chelators the mechanism of inhibition appears to be more complex than simple competition for the iron atom required by the enzyme. The most potent members of one such group of inhibitors are the thiosemicarbazones of 1-formyl-isoquinoline (I) and 2-formylpyridine (II).
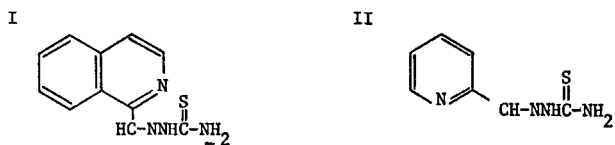
These compounds cause 50% inhibition of a partially purified reductase from Novikoff rat tumor at 10^{-8} to 10^{-7} M (150, 151). Approximately the same degree of inhibition was observed with other mammalian reductases (152, 153), but the non-heme iron containing reductase from E. coli was not affected. The inhibition of the mammalian reductases is only partially reversible (154). Since these compounds are strong metal chelators complexation of iron is probably involved in the mechanism of inhibition; however excess Fe^{2+} does not reverse the inhibition, and other evidence indicates that these compounds do not act solely by chelating free iron from solution thus depriving the enzyme of a cofactor (150, 151). Kinetic studies indicate no competition with respect to nucleoside diphosphate substrate, nucleotide effector, or magnesium ions, but partial competition for the dithiol substrate was observed.

A high degree of structural specificity for inhibitor-enzyme interaction was demonstrated in studies where several isoquinoline and pyridine derivatives were tested with the reductase (150–155). The partially competitive relationship between inhibitor and dithiol substrate and the specificity of inhibitor binding are consistent with a model in which an inhibitor-iron complex binds, or free inhibitor coordinates with holoenzyme, at or adjacent to a site normally occupied by dithiol substrate. Studies of this class of inhibitors have not only served as a probe into the structure of the mammalian reductases but also as a measure of differ-

ence with the *E. coli* reductase. The lack of inhibition on the *E. coli* enzyme suggests that the iron is bound in such a way that it is inaccessible to the inhibitor, which might indicate a substantial structural difference from the mammalian enzyme near the catalytic site.

All non-heme iron containing ribonucleotide reductases are also inhibited by hydroxyurea and related hydroxamates, while the adenosyl-cobalamin-dependent reductases are not affected (*21, 156*). The inhibition by these reagents can be partially reversed by excess Fe^{+2} or dithiols. Reaction of ribonucleotide reductase of *E. coli* with [^{14}C]hydroxyurea inactivated only the B2 subunit and this inactivation was not reversed by removal of the radioactivity (*157*). Inactivation by hydroxyurea does not affect the iron content of protein B2, but involves the destruction of the stable free radical (*66, 67*). Reactivation can be accomplished by removal of the iron and reconstitution of apoprotein B2 with Fe^{+2}. Hydroxyurea has been demonstrated to be a powerful radical scavenger in another system (*158*).

VII. References

1. *Turner, M. K., Abrams, R., Lieberman, I.:* J. Biol. Chem. *243,* 3725 (1968).
2. *Hopper, S.:* J. Biol. Chem. *247,* 3336 (1972).
3. *Elford, H. L., Freese, M., Passamani, E., Morris, H. P.:* J. Biol. Chem. *245,* 5228 (1970).
4. *Elford, H. L.:* Advan. Enzyme Regulation *10,* 19 (1972).
5. *Reichard, P.:* European J. Biochem. *3,* 259 (1968).
6. *Blakley, R. L.:* J. Biol. Chem. *240,* 2173 (1965).
7. *Gleason, F. K., Hogenkamp, H. P. C.:* Biochim. Biophys. Acta *277,* 466 (1972).
8. *Abeles, R. H., Beck, W. S.:* J. Biol. Chem. *242,* 3589 (1967).
9. *Cowles, J. R., Evans, H. J., Russell, S. A.:* J. Bacteriol *97,* 1460 (1969).
10. *Yan, S., Wachsman, J. T.:* Mol. Cell. Biochem. *1,* 101 (1973).
11. *Stutzenberger, F.:* J. Gen. Microbiol. *81,* 501 (1974).
12. *Ghambeer, R. K., Blakley, R. L.:* J. Biol. Chem. *241,* 4710 (1966).
13. *Gleason, F. K., Hogenkamp, H. P. C.:* J. Biol. Chem. *245,* 4894 (1970).
14. *Sando, G. N., Hogenkamp, H. P. C.:* Biochemistry *12,* 3316 (1973).
15. *Cohen, S. S., Barner, H. D.:* J. Biol. Chem. *237,* PC 1376 (1962).
16. *Berglund, O., Karlström, O., Reichard, P.:* Proc. Natl. Acad. Sci. U.S. *62,* 829 (1969).
17. *Kára, J., Weil, R.:* Proc. Natl. Acad. Sci. U.S. *57,* 63 (1967).
18. *Gordon, H. L., Fiel, R. J.:* Cancer Res. *29,* 1350 (1969).
19. *Fujioka, S., Silber, R.:* J. Biol. Chem. *245,* 1688 (1970).
20. *Moore, E. C., Reichard, P.:* J. Biol. Chem. *239,* 3453 (1964).

21. *Moore, E. C.:* Cancer Res. *29,* 291 (1969).
22. *Larsson, A.:* European J. Biochem. *11,* 113 (1969).
23. *Reichard, P., Canellakis, Z. N., Canellakis, E. S.:* J. Biol. Chem. *236,* 2514 (1961).
24. *Murphree, S., Moore, E. C., Beall, P. T.:* Cancer Res. *28,* 860 (1968).
25. *King, C. D., van Lancker, J. L.:* Arch. Biochem. Biophys. *129,* 603 (1969).
26. *Fujioka, S., Silber, R.:* Biochem. Biophys. Res. Commun. *35,* 759 (1969).
27. *Fujioka, S., Silber, R.:* J. Lab. Clin. Med. *77,* 59 (1971).
28. *Hopper, S.:* Proc. Fed. Am. Soc. Exp. Biol. *33,* 1747 (1974).
29. *Millard, S. A.:* J. Biol. Chem. *247,* 2395 (1972).
30. *Vitols, E., Bauer, V. A., Stanbrough, E. C.:* Biochem. Biophys. Res. Commun. *41,* 71 (1970).
31. *Müller, H., Wahl, R., Kuntz, I., Follmann, H.:* Z. Physiol. Chem. *354,* 1299 (1973).
32. *Follmann, H.:* personal communication.
33. *Swindlehurst, M., Berry, S. J., Firshein, W.:* Biochem. Biophys. Acta *228,* 313 (1971).
34. *Noronha, J. M., Sheys, G. H., Buchanan, J. M.:* Proc. Natl. Acad. Sci. U.S. *69,* 2006 (1972).
35. *Laurent, T. C., Moore, E. C., Reichard, P.:* J. Biol. Chem. *239,* 3436 (1964).
36. *Moore, E. C., Reichard, P., Thelander, L.:* J. Biol. Chem. *239,* 3445 (1964).
37. *Holmgren, A.:* European J. Biochem. *6,* 475 (1968).
38. *Thelander, L.:* J. Biol. Chem. *242,* 852 (1967).
39. *Orr, M. D., Vitols, E.:* Biochem. Biophys. Res. Commun. *25,* 109 (1966).
40. *Moore, E. C.:* Biochem. Biophys. Res. Commun. *29,* 264 (1967).
41. *Berglund, O.:* J. Biol. Chem. *244,* 6306 (1969).
42. *Berglund, O., Sjöberg, B.-M.:* J. Biol. Chem. *245,* 6030 (1970).
43. *Porqué, P. G., Baldesten, A., Reichard, P.:* J. Biol. Chem. *245,* 2363 (1970).
44. *Larson, G., Larsson, A.:* European J. Biochem. *26,* 119 (1972).
45. *Engström, N. E., Holmgren, A., Larsson, A., Söderhäll, S.:* J. Biol. Chem. *249,* 205 (1974).
46. *Henderson, J. F., Paterson, A. R. P.:* Nucleotide metabolism, an introduction, pp. 244. New York – London: Academic Press 1973.
47. *Follmann, H.:* Angew. Chem. *86,* (1974).
48. *Larsson, A., Reichard, P.:* Progr. Nucleic Acid Res. *7,* 303 (1967).
49. *Reichard, P.:* The biosynthesis of deoxyribose, Ciba lectures biochem. New York: Wiley 1968.
50. *Reichard, P.:* European J. Biochem. *3,* 259 (1968).
51. *Reichard, P.:* Advan. Enzyme Regulation *10,* 3 (1972).
52. *Blakley, R. L.:* Federation Proc. *25,* 1633 (1966).
53. *Blakley, R. L., Vitols, E.:* Ann. Rev. Biochem. *37,* 201 (1968).
54. *Hogenkamp, H. P. C.:* Ann. Rev. Biochem. *37,* 225 (1968).
55. *Koerner, J. F.:* Ann. Rev. Biochem. *39,* 291 (1970).
56. *Barker, H. A.:* Ann. Rev. Biochem. *41,* 55 (1972).
57. *Holmgren, A., Reichard, P., Thelander, L.:* Proc. Natl. Acad. Sci. U.S. *54,* 830 (1965).
58. *Brown, N. C., Canellakis, Z. N., Lundin, B., Reichard, P., Thelander, L.:* European J. Biochem. *9,* 561 (1969).
59. *Thelander, L.:* J. Biol. Chem. *248,* 4591 (1973).
60. *Berglund, O.:* J. Biol. Chem. *247,* 7270 (1972).
61. *Moore, E. C.:* personal communication.
62. *Brown, N. C., Larsson, A., Reichard, P.:* J. Biol. Chem., *242,* 4272 (1967).

63. *Brown, N. C., Reichard, P.:* J. Mol. Biol. *46*, 25 (1969).
64. *Brown, N. C., Reichard, P.:* J. Mol. Biol. *46*, 39 (1969).
65. *Brown, N. C., Eliasson, R., Reichard, P., Thelander, L.:* European J. Biochem. *9*, 512 (1969).
66. *Ehrenberg, A., Reichard, P.:* J. Biol. Chem. *247*, 3485 (1972).
67. *Atkin, C. L., Thelander, L., Reichard, P., Lang, G.:* J. Biol. Chem. *248*, 7464 (1973).
68. *Garbett, K., Johnson, C. E., Klotz, I. M., Okamura, M. Y., Williams, R. J. P.:* Arch. Biochem. Biophys. *142*, 574 (1971).
69. *Berglund, O.:* J. Biol. Chem. *247*, 7276 (1973).
70. *Panagou, D., Orr, M. D., Dunstone, J. R., Blakley, R. L.:* Biochemistry *11*, 2378 (1972).
71. *Chen, A. K., Bhan, A., Hopper, S., Abrams, R., Franzen, J. S.:* Biochemistry *13*, 654 (1974).
72. *Yamada, R.-H., Hogenkamp, H. P. C.:* J. Biol. Chem. *247*, 6266 (1972).
73. *Hoffmann, P. J., Blakley, R. L.:* Fed. Proc., Fed. Am. Soc. Exp. Biol. *33*, 1745 (1974).
74. *Beck, W. S.:* J. Biol. Chem. *242*, 3148 (1967).
75. *Vitols, E., Brownson, C., Gardiner, W., Blakley, R. L.:* J. Biol. Chem. *242*, 3035 (1967).
76. *Hogenkamp, H. P. C., Ghambeer, R. K., Brownson, C., Blakley, R. L., Vitols, E.:* J. Biol. Chem. *243*, 799 (1968).
77. *Orme-Johnson, W. H., Beinert, H., Blakley, R. L.:* J. Biol. Chem. *249* 2338 (1974).
78. *Hamilton, J. A., Yamada, R., Blakley, R. L., Hogenkamp, H. P. C., Looney, F. D., Winfield, M. E.:* Biochemistry *10*, 347 (1971).
79. *Follmann, H., Hogenkamp, H. P. C.:* Biochemistry *10*, 186 (1971).
80. *Goulian, M., Beck, W. S.:* J. Biol. Chem. *241*, 4233 (1966).
81. *Hamilton, F. D.:* J. Biol. Chem., *249*, 4428 (1974)
82. *Cowles, J. R., Evans, H. J.:* Arch. Biochem. Biophys. *127*, 770 (1968).
83. *Lee, J. P., Cain, P. T., Hogenkamp, H. P. C.:* unpublished results.
84. *Larsson, A.:* Biochemistry *4*, 1984 (1965).
85. *Gottesman, M. M. Beck W. S.:* Biochem. Biophys. Res. Commun. *24*, 353 (1966).
86. *Blakley, R. L., Ghambeer, R. K., Batterham, T. J., Brownson, C.:* Biochem. Biophys. Res. Commun. *24*, 418 (1966).
87. *Batterham, T. J., Ghambeer, R. K., Blakley, R. L., Brownson, C.:* Biochemistry *6*, 1203 (1967).
88. *Durham, L. J., Larsson, A., Reichard, P.:* European J. Biochem. *1*, 92 (1967).
89. *Griffin, C. E., Hamilton, F. D., Hopper, S. P., Abrams, R.:* Arch. Biochem. Biophys. *126*, 905 (1968).
90. *Fraser-Reid, B., Radatus, B.:* J. Am. Chem. Soc. *93*, 6342 (1971).
91. *Radatus, B., Yunker, M., Fraser-Reid, B.:* J. Am. Chem. Soc. *93*, 3086 (1971).
92. *David, S., Eustache, J.:* Carbohyd. Res. *20*, 319 (1971).
93. *David, S., Rouzeau, C.:* Biochem. Biophys. Res. Commun. *43*, 46 (1971).
94. *Verheyden, J. P. H., Moffatt, J. G.:* J. Am. Chem. Soc. *86*, 1236 (1964).
95. *Rétey, J., Umani-Ronchi, A., Seibl, J., Arigoni, D.:* Experientia *22*, 502 (1966).
96. *Follmann, H., Hogenkamp, H. P. C.:* J. Am. Chem. Soc. *92*, 671 (1970).
97. *Follmann, H., Hogenkamp, H. P. C.:* Biochemistry *8*, 3472 (1969).
98. *Caprioli, R., Rittenberg, D.:* Proc. Natl. Acad. Sci. U.S. *60*, 1379 (1968).
99. *Caprioli, R., Rittenberg, D.:* Proc. Natl. Acad. Sci. U.S. *61*, 1422 (1968).

100. *Beck, W. S., Abeles, R. H., Robinson, W. G.:* Biochem. Biophys. Res. Commun. *25*, 421 (1966).
101. *Abeles, R. H., Beck, W. S.:* J. Biol. Chem. *242*, 3589 (1967).
102. *Hogenkamp, H. P. C., Ghambeer, R. K., Brownson, C., Blakley, R. L.:* Biochem. J. *103*, 5c (1967).
103. *Abeles, R. H.:* The Enzymes, 3rd ed. *5*, 481 (1971).
104. *Tamao, Y., Blakley, R. L.:* Biochemistry *12*, 24 (1973).
105. *Walker, T. E., Hogenkamp, H. P. C., Needham, T. E., Matwiyoff, N. A.:* Biochemistry *13*, 2650 (1974).
106. *Yamada, R., Tamao, Y., Blakley, R. L.:* Biochemistry *10*, 3959 (1971).
107. *Hamilton, J. A., Tamao, Y., Blakley, R. L., Coffman, R. E.:* Biochemistry *11*, 4696 (1972).
108. *Cockle S. A., Hill, H. A. O., Williams, R. J. P., Davies, S. P., Foster, M. A.:* J. Am. Chem. Soc. *94*, 275 (1972).
109. *Finlay, T. H., Valinsky, J., Mildvan, A. S., Abeles, R. H.:* J. Biol. Chem. *248*, 1285 (1973).
110. *Babior, B. M., Moss, T. H., Gould, D. C.:* J. Biol. Chem. *247*, 4389 (1972).
111. *Valinsky, J. E., Abeles, R. H., Mildvan, A. S.:* J. Biol. Chem. *249*, 2751 (1974).
112. *Hoffmann, P. J., Blakley, R. L.:* personal communication.
113. *Babior, B. M., Moss, T. H., Orme-Johnson, W. H.:* J. Biol. Chem., *249*, 4537 (1974).
114. *Porqué, P. G., Baldesten, A., Reichard, P.:* J. Biol. Chem. *245*, 2371 (1970).
115. *Holmgren, A., Reichard, P.:* European J. Biochem. *2*, 187 (1967).
116. *Holmgren, A., Perham, R. M., Baldesten, A.:* European J. Biochem. *5*, 352 (1968).
117. *Holmgren, A.:* European J. Biochem. *5*, 359 (1968).
118. *Holmgren, A.:* European J. Biochem. *6*, 467 (1968).
119. *Holmgren, A.:* European J. Biochem. *26*, 528 (1972).
120. *Holmgren, A.:* J. Biol. Chem. *248*, 4106 (1973).
121. *Stryer, L., Holmgren, A., Reichard, P.:* Biochemistry *6*, 1016 (1967).
122. *Holmgren, A.:* J. Biol. Chem. *247*, 1992 (1972).
123. *Holmgren, A., Söderberg, B.-O.:* J. Mol. Biol. *54*, 387 (1970).
124. *Berglund, O., Holmgren, A.:* J. Biol. Chem. *245*, 6036 (1970).
125. *Holmgren, A., Sjöberg, B.-M.:* J. Biol. Chem. *247*, 4160 (1972).
126. *Sjöberg, B.-M., Holmgren, A.:* Biochim. Biophys. Acta *315*, 176 (1973).
127. *Herrmann, E. C., Moore, E. C.:* J. Biol. Chem. *248*, 1219 (1973).
128. *Larsson, A., Thelander, L.:* J. Biol. Chem. *240*, 2691 (1965).
129. *Williams, C. H., Zanetti, G., Arscott, L. D., McAllister, J. K.:* J. Biol. Chem. *242*, 5226 (1967).
130. *Zanetti, G., Williams, C. H.:* J. Biol. Chem. *242*, 5232 (1967).
131. *Thelander, L.:* European J. Biochem. *4*, 407 (1968).
132. *Thelander, L.:* J. Biol. Chem. *245*, 6026 (1970).
133. *Ronchi, S., Williams, C. H.:* J. Biol. Chem. *247*, 2083 (1972).
134. *Speranza, M. L., Ronchi, S., Minchiotti, L.:* Biochim. Biophys. Acta *327*, 274 (1973).
135. *Larsson, A.:* European J. Biochem. *35*, 346 (1973)
136 *Suhadolnik, R. J., Finkel, S. I., Chassy, B. M.:* J. Biol. Chem. *243*, 3532 (1968).
137. *Chassy, B. M., Suhadolnik, R. J.:* J. Biol. Chem. *243*, 3538 (1968).
138. *Prusiner, P., Brennan, T., Sundaralingam, M.:* Biochemistry *12*, 1196 (1973).
139. *Moore, E. C., Cohen, S. S.:* J. Biol. Chem. *242*, 2116 (1967).
140. *York, J. L., LePage, G. A.:* Can. J. Biochem. *44*, 19 (1966).

141. *Cory, J. G., George, C. B.:* Biochem. Biophys. Res. Commun. *52*, 496 (1973).
142. *Cory, J. G., Mansell, M. M.:* Fed. Proc., Fed. Am. Soc. Exp. Biol. *33*, 1746 (1974).
143. *Morley, C. G. D., Blakley, R. L., Hogenkamp, H. P. C.:* Biochemistry 7, 1231 (1968).
144. *Thachuck, R. D., Grant, M. E., Hogenkamp, H. P. C.:* Biochemistry *13*, 2645 (1974).
145. *Stoeckli-Evans, H., Edmond, E., Hodgkin, D. C.:* J. Chem. Soc., Perkin Trans. 2, 605 (1972).
146. *Toohey, J. I.:* Proc. Natl. Acad. Sci. U.S. *54*, 934 (1965).
147. *Hogenkamp, H. P. C., Sando, G. N.:* unpublished results.
148. *Hogenkamp, H. P. C.:* Biochemistry *13*, 2736 (1974).
149. *Jacobsen, D. W., Holland, R. J.:* Fed. Proc., Fed. Am. Soc. Exp. Biol. *33*, 1607 (1974).
150. *Moore, E. C., Zedeck, M. S., Agrawal, K. C., Sartorelli, A. C.:* Biochemistry *9*, 4492 (1970).
151. *Sartorelli, A. C., Agrawal, K. C., Moore, E. C.:* Biochem. Pharmacol. *20*, 3119 (1971).
152. *Brockman, R. W., Sidwell, R. W., Arnett, G., Shaddix, S.:* Proc. Soc. Exp. Biol. Med. *133*, 609 (1970).
153. *Moore, E. C., Booth, B. A., Sartorelli, A. C.:* Cancer Res. *31*, 235 (1971).
154. *Booth, B. A., Agrawal, K. C., Moore, E. C., Sartorelli, A. C.:* Cancer Res. *34*, 1308 (1974).
155. *Agrawal, K. C., Booth, B. A., Moore, E. C., Sartorelli, A. C.:* J. Med. Chem. *15*, 1154 (1972).
156. *Elford, H. L.:* Biochem. Biophys. Res. Commun. *33*, 129 (1968).
157. *Krakoff, I. H., Brown, N. C., Reichard, P.:* Cancer Res. *28*, 1559 (1968).
158. *Georgieff, K. K.:* Science *173*, 537 (1971).

The Electronic State of Iron in Some Natural Iron Compounds:
Determination by Mössbauer and ESR Spectroscopy

William T. Oosterhuis*

Physics Department, Carnegie-Mellon University, Pittsburgh, Pennsylvania, U.S.A.

Table of Contents

---

* Present Address: Division of Materials Research, National Science Foundation, Washington, D. C. 20550

I. Introduction

a) Iron in Biology

Iron is especially important in the life processes as it is directly involved in the transport and storage of oxygen (hemoglobin and myoglobin), electron transport (cytochromes and ferredoxins), the metabolism of H_2 by dehydrogenase, the utilization of peroxide (through peroxidases) and several other vital metabolic functions.

It is safe to say that with a few possible exceptions in the bacterial world, there would be no life without iron. Generally, the importance of iron in various life processes comes about because of the ability of iron to exist in two stable oxidation states (Fe^{II} and Fe^{III}) and occasionally as Fe^{I} and Fe^{IV}. The oxidation-reduction potentials of Fe which occur in various metabolic functions can vary over a wide range depending upon the ligands attached to the iron. Nature has been very clever in utilizing molecules to fulfill various needs and it is amazing how frequently iron is of central importance.

Iron is the most abundant element in the earth (29% by mass) — although most of it is in the core (about 25%). The remaining 4% is in the earth's crust, mostly in the form of FeO and Fe_2O_3.

The relevant biological questions are how the iron is converted from mineral to protein and once in the protein what is the specialized role played by the iron in the function of that protein? In this chapter we concern ourselves with the means by which iron is obtained and secured for the living organism through the iron storage and transport proteins, and in particular how Mössbauer effect and electron spin resonance spectroscopy can help to understand the electronic and molecular structure of these proteins.

Since its discovery, Mössbauer spectroscopy has grown into a highly sophisticated technology in which precise measurements (10^{-8} ev) are made and detailed information about the environment of the Mössbauer nucleus can be found. In the case of ^{57}Fe, the Mössbauer technique has seen its greatest development so that an accurate description of the chemical state of an iron ion can be determined which includes the details of the electronic states and their energies, the symmetries of the crystalline or molecular environment and the covalent sharing of the valence electrons.

In Mössbauer spectroscopy of ^{57}Fe, the radiation is specific for the ^{57}Fe which eliminates the complications caused by the presence of other atoms. Most elements do not have a suitable isotope available for Mössbauer spectroscopy. Because iron is of such paramount importance in the molecules of life it is indeed fortunate that ^{57}Fe exhibits such a good Mössbauer resonance. If a biological molecule contains iron, it is almost

certain that the biological purpose for that molecule depends on the iron and its chemical state. This is to say that the iron is at the site of the biological action.

b) Iron Transport Compounds

Iron transport compounds are found low on the evolutionary scale, in the world of microbes and bacteria where there is fierce competition for the available supply of nutrients. These organisms require iron in small, but nevertheless, vital quantities primarily for growth and respiration. The compounds which serve the function of iron accumulation for these organisms are called siderochromes (1). The siderochromes are divided into two categories according to their function: sideramines which are growth factors and sideromycins which are antibiotics. Both sideramines and sideromycins have a high affinity for ferric iron which ensures efficient chelation of the metal even at low iron concentrations. The unusual properties of these compounds are discussed in the review by *Neilands* (1).

There are also iron transport proteins transferrin, conalbumin, and lactoferrin which occur in birds and mammals and have many of the same properties as the siderochromes described in the preceeding paragraph, in particular a strong affinity for ferric iron and a much weaker affinity for ferrous iron. There are other similarities which will be revealed later in this discussion. The transferrins and their characteristics are discussed in the review by *Feeney* and *Kumatsu* (2).

c) Spectroscopy in Biological Materials — What can be Seen?

Many different spectroscopic techniques have been employed in the study of biological materials. These methods include optical absorption, infrared and Raman spectroscopy, electron spin resonance (ESR), nuclear magnetic resonance (NMR) and more recently Mössbauer effect spectroscopy.

Each of these spectroscopic methods involves a source of radiation, a sample to absorb or scatter the radiation and a detector arranged as in Fig. 1. The counting rate (the output of the detector) is measured as a function of the energy of the source radiation in absorption experiments with $h\nu$ variable; or there is a fixed source frequency ($h\nu$ is constant) and the scattered radiation $h\nu'$ is analyzed (as in the Raman Effect); or the detector output is measured as some external field is varied (as in ESR) while the source radiation is held fixed.

In each technique there are two levels of information to be obtained. The upper level information is the observation of characteristic spectral
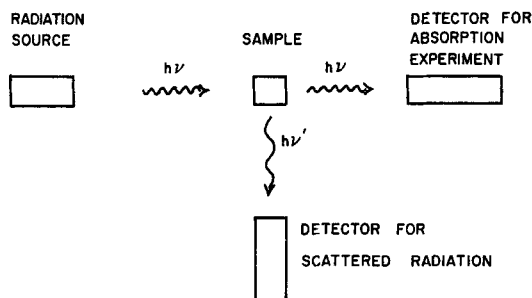
Fig. 1. Schematic diagram for nearly any spectroscopic experiment in which radiation is incident on the sample to be studied. The sample either transmits or scatters the radiation which is detected as a function of energy

features such as the Soret band in the optical spectrum of heme proteins or the $g = 4.3$ resonance in the ESR spectrum of the iron transport compounds. Another example would be the characteristic $g = 1.94$ resonance observed in the iron-sulfer proteins. Each member of a class of materials has some spectral feature in common and it is the signature which identifies the classification. This qualitative information is, of course, extremely valuable in the classification of a species and the strength of this signal can be used to measure the quantity of material present in a sample.

On the other hand, there is a deeper level of information to be gained by the understanding of each spectral profile in detail, which leads to the fundamental knowledge of the electronic states involved and how they are affected by the atomic arrangements in a molecule. This problem is more easily visualized perhaps by the assumption that if one knows the electronic wave functions in a molecule and the interaction of radiation with these electronic states, then it is certainly possible to compute the spectral features that should be observed in an experiment. It is the work of a spectroscopist to do the experiment and follow this procedure in reverse as far as possible to obtain the molecular arrangement or crystal structure which in turn determines the details of the electronic states.

It is interesting that no one of the spectroscopies mentioned above can give complete information about the electronic or molecular structure, but that they provide complementary information to each other. X-ray structures can stand by themselves, of course, but by themselves give no direct information about the electronic energy levels involved in the biochemical processes as in the absorption of light by chlorophyll for example.

In this article we will discuss the electronic states that are responsible for the features observed in ESR and Mössbauer effect spectroscopy of the iron transport materials. These electronic states are parameterized by a set of coupling constants which also characterize a class of materials, but we then are making comparisons between the electronic states of molecules rather than between the spectral features. If one knows the electronic state, then predictions of other phenomena can be made. If one merely knows the spectral features, then at best one can only classify the compound.

II. Mössbauer Spectroscopy

a) Magnetic and Electric Hyperfine Interactions

In recent years there have appeared several reviews in which Mössbauer spectroscopy of various biological iron compounds are discussed. For most of the experimental details, the reader is referred to the papers by *DeBrunner* (3), *Weissbluth* (4), *Bearden* and *Dunham* (5) and *Lang* (6). The review by *Lang* (6) is especially recommended since it deals with the paramagnetic hyperfine structure (PHS) observed in so many of these complexes and treats several different spin configurations. There are several excellent references concerning instrumentation; one of the most recent is by *Kalvius* and *Kankeleit* (7).

The electronic configuration and the local environment can be studied through the magnetic and electric hyperfine interactions which determine the features of the Mössbauer spectrum of the ^{57}Fe nucleus.

The magnetic hyperfine interaction between the atomic nucleus with spin I and its n electrons is

$$\mathscr{H}_\mathrm{m} = 2g_N\beta_N\beta_e \sum_{i=1}^{n} \left\{ \frac{I \cdot l_i}{r_i{}^3} + \frac{3\,(I \cdot \hat{r}_i)\,(s_i \cdot \hat{r}_i) - I \cdot s_i}{r_i{}^3} - \frac{8\pi}{3}\,\delta(\hat{r}_i)\,I \cdot s_i \right\}$$

$$(1)$$

The sum is over the n electrons of the iron ion. The vectors l_i and s_i are quantum mechanical operators which act on the electronic states while I acts on the nuclear wave function.

The first term is the interaction of the nuclear magnetic moment (spin I) with the current loops made by the orbiting electrons with angular momentum l_i. The second term is the dipole-dipole interaction between the nuclear (I) and electronic (s_i) spin magnetic moments. The last term is the Fermi contact term which describes the interaction of the nuclear

moment with the s-electrons which are polarized by the unpaired electrons of the ion with spin s_i. For the high spin ferric ions in the iron transport compounds with electronic state ^6S, only the Fermi contact term is important and $\mathscr{H}_m$ can be represented by $A\mathbf{I} \cdot \mathbf{S}$.

The electric quadrupole interaction for ^{57}Fe is given by

$$\mathscr{H}_Q = P\{I_z^2 - I(I+1)/3 + \eta(I_x^2 - I_y^2)/3\}, \; \eta = \frac{V_{xx} - V_{yy}}{V_{zz}} \qquad (2)$$

where $P = \dfrac{e^2 Q V_{zz}}{4}$; $Q =$ quadrupole moment of ^{57}Fe ($Q = 0.18 \times 10^{-24}$

cm^2) and $V_{zz} = \dfrac{\partial^2 V}{\partial Z^2}$ is the electric field gradient (EFG) in the z direction

which is a measure of the distortion of the electric charge cloud about the ^{57}Fe nucleus. In the absence of a magnetic interaction the EFG splits the nuclear excited state ($I = 3/2$) into two ($m_I = \pm 3/2$ and $m_I = \pm 1/2$) while the nuclear ground state ($I = 1/2$) is unsplit. The resulting Mössbauer spectrum is then a two-line pattern (Fig. 2).
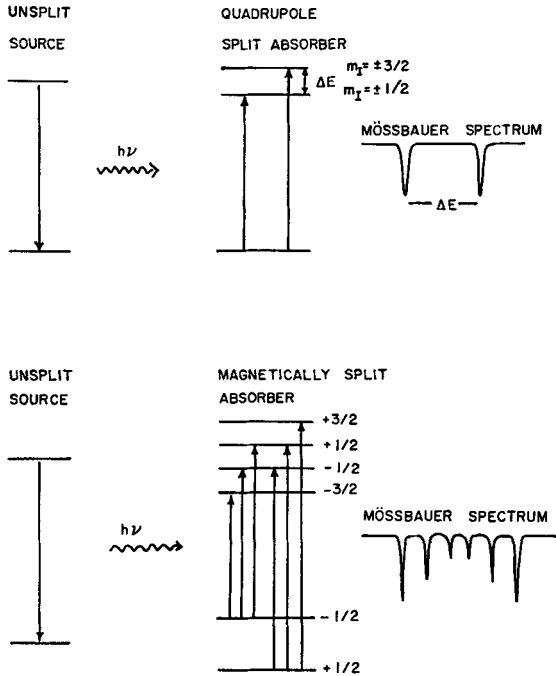
Fig. 2. Resonance absorption between the nuclear ground state and the first excited state in ^{57}Fe. The upper diagram shows the effect of an electric quadrupole splitting while the lower diagram shows the magnetic splitting of the nuclear levels

The magnetic *and* electric hyperfine interactions acting together give much more information than the sum of the two acting independently. It is our goal, therefore, to create experimental conditions such that the magnetic interaction becomes visible in the Mössbauer spectrum; the quadrupole interaction will always be seen if it is present. Even in powder or frozen solution samples, the relative orientation of the EFG and magnetic axes can be determined (*8*). The profile of the Mössbauer spectrum can be related to the electronic state of the iron and its ligand field for many of the different electronic configurations of iron (*9–14*). As an example of the simultaneous action of the quadrupole and magnetic hyperfine interactions, we show in Fig. 3 the spectra of a powder sample
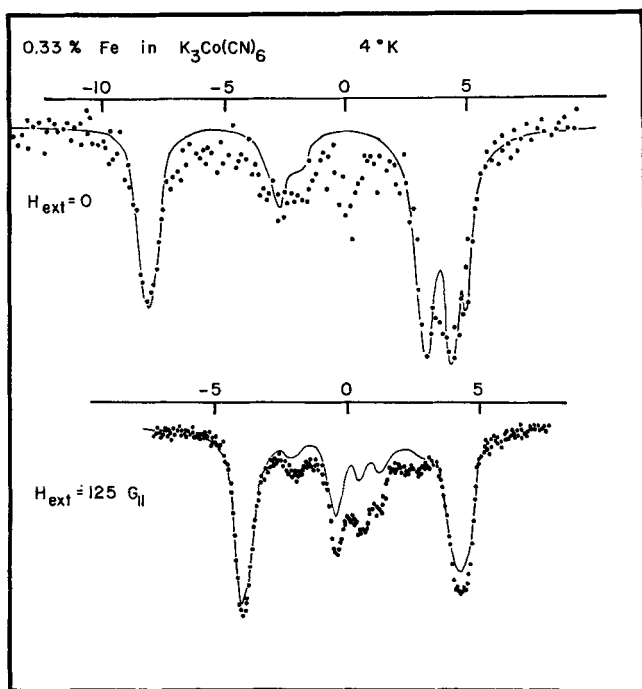
Fig. 3. Experimental data for a powder sample of ^{57}Fe diluted in $K_3Co(CN)_6$ taken at 4.2 K in applied fields of zero and 125 Gauss parallel to the gamma beam. This figure shows the broadening of the absorption lines due to the angular dependence of the hyperfine interactions

of $K_3Fe(CN)_6$ [diluted in $K_3Co(CN)_6$]. This is a low spin ferric complex ($S = 1/2$) with one unpaired electron. The solid curve in the figure is calculated from an electronic model (*15*) which takes into account the

spin-orbit coupling and the small departures from cubic symmetry which are manifest in the EFG, the magnetic hyperfine interaction, and the g-tensor. The analysis for strict cubic symmetry of a low spin ferric complex is given in Ref. (16). The behavior of the Mössbauer spectrum under variable local symmetry has also been examined (15, 16).

One remaining electron-nuclear interaction which is measureable is the isomer shift which is the centroid of the absorption spectrum. This is a measure of the electronic charge density at the ^{57}Fe nucleus, and can be used to group iron compounds according to their oxidation state. The isomer shift varies because of the shielding effects of the valence electrons on the s-electrons at the nucleus.

b) Paramagnetic Hyperfine Structure (PHS)

In paramagnetic iron molecules, the unpaired electrons bound to the iron can give rise to a magnetic interaction with the nucleus which splits the nuclear states. The resulting magnetic structure in a Mössbauer spectrum together with the electric quadrupole interaction gives information about the symmetry of the iron site and also some indication of the strength of the interaction with the local environment. This information can be obtained even from randomly oriented samples such as powders or frozen solutions.

For a non-Kramers paramagnetic ion (an even number of electrons) in a site of non spherical symmetry, there is no electronic magnetic moment in the absence of an external field or a cooperative magnetic interaction (17). This is to say that the expectation values $<s>$ and $<l>$ are zero and therefore the expectation value of Eq. (1) is zero because the nuclear magnetic moment has nothing to which it can couple. This is why there is no PHS observed in the zero field spectra of high spin ferrous ions $(S=2)$ which are certainly paramagnetic. However, the application of an external magnetic field will create a magnetic moment in each electronic state, which in turn will produce a hyperfine field which acts on the nucleus.

For Kramers ions (odd number of electrons) there is a non-zero magnetic moment (the expectation value $<S>$ is not zero) and magnetic hyperfine structure can be observed even in zero magnetic field. We will be concerned here with the spectra in iron transport proteins where the iron is in the high spin ferric (^6S) configuration with five unpaired 3d electrons, one in each of the five 3d orbital states leaving no orbital angular momentum $(L=0)$ and spin $S=5/2$. This is a spherically symmetric electronic state which in first order gives no contribution to the hyperfine field from the orbital and dipole terms so that only the Fermi contact term is unequal to zero. The EFG from this electronic state is

zero as well. If the electronic spin changes direction, then so does the hyperfine field sensed by the ^{57}Fe nuclear moment. When the spin direction changes rapidly compared to the Larmor precession of the ^{57}Fe nucleus, then the field sensed by the nucleus is time averaged to zero. The electronic spin lattice relaxation can be slowed by going to low temperatures to reduce the vibrations of the lattice which can flip the electronic spin direction. The paramagnetic iron centers can be separated by large distances in these macromolecules so that the spin-spin relax-
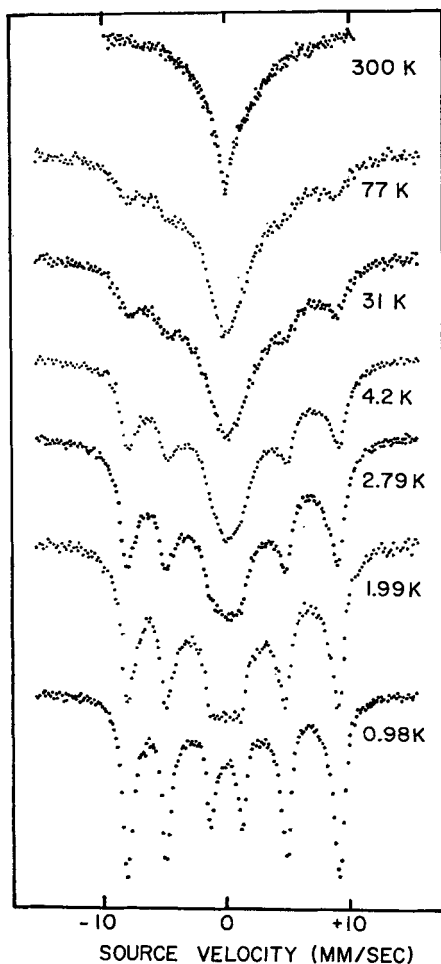
Fig. 4. Experimental data for ^{57}Fe bound to ferrichrome-A taken by *Wickman et al.* (18). These data show temperature effects due to changing spin-lattice relaxation. The spins are slowed enough at the lowest temperature for there to be complete coupling between the electronic and nuclear magnetic moments

ation effects are small. In the limit where the electronic relaxation time τ is very long compared to the Larmor precession time τ_L of the ^{57}Fe nucleus, the nuclear magnetic moment can couple strongly to the electronic moment giving rise to sharp magnetically split Mössbauer patterns. However, as the electronic relaxation time τ is shortened, the Mössbauer resonances become less sharp and a very broad background appears. This is because the magnetic hyperfine field changes its orientation during the precession of the nucleus. At faster relaxation rates $(\tau \ll \tau_L)$ the magnetic hyperfine field is averaged to zero so that only the electric quadrupole interaction is left to split the Mössbauer spectrum. (If there is a non-zero field gradient) One of the first examples of this behavior was observed in ferrichrome A (Fig. 4) an inactive sideramine, and the essentials of the time dependent behavior were put forth by *Wickman et al. (18)*.

If an external field is applied at low temperatures, PHS can still be observed even in the fast relaxation regime if the populations of the electronic spin states are unequal *(19)*. However, we are concerned with the long relaxation time limit since the iron transport compounds are often magnetically dilute and the spins are slowly relaxing at low temperature.

The zero field data may be only partly resolved at low temperature in some cases such as ferrichrome A and mycobactin P, since the size of the molecule may not be large enough to separate the paramagnetic centers and prevent spin-spin relaxation. In such cases it is sometimes possible to dilute these molecules in a diamagnetic solvent such as alcohol, glycerol, or DMSO to achieve the necessary separation. The heme proteins are large enough to achieve the necessary separation naturally. The application of a magnetic field can help to give better resolution in the spectrum *(20, 9)*, if it can overcome the coupling between different paramagnetic spins.

III. Electron Spin Resonance (ESR)

The ESR technique has been employed for many years in the study of biological materials and several books dealing with ESR and its applications are in existance *(21—25)*. A comprehensive treatment of the entire field of ESR by *Abragam* and *Bleaney (26)* has recently appeared. The reader is encouraged to consult these references for the experimental details and the general discussion of spin resonance.

The goal in this section is to discuss the information that can be obtained from ESR experiments, to compare this with the information obtained from Mössbauer experiments and present a more complete picture of the electronic states that exist in the iron transport compounds.

a) Electronic Structure

In a conventional ESR experiment, radiation of fixed frequency v is sent into a paramagnetic sample where it is resonantly absorbed whenever the radiation encounters a pair of energy levels which are separated by energy hv, causing a transition in the absorbing ion from the lower electronic state to the higher electronic state. The conservation of angular momentum and of parity determine the selection rules which govern the transition probability and thus the intensity of the absorption in the spectrum.

In order to examine the electronic energy levels, the resonance can be tuned in by changing the energy level separation to match the microwave quantum (hv) which is easily accomplished in paramagnetic materials by the use of an applied magnetic field which splits those energy levels with magnetic moments (Fig. 5). A typical ESR spectrum will contain one or more resonance peaks as a function of the applied field which can be interpreted in terms of the energy level structure of the paramagnetic ion. This is the information that is obtained and is parameterized in terms of several constants which appear in the spin Hamiltonian to be discussed in detail in a later section. One is dealing with microwaves $(hv \sim 0.3$ to 2.5 cm$^{-1})$ which have very small quantum energies so that in order to observe a resonance, one usually has to start out with a pair of energy levels that are degenerate or at least come close enough under the action of a magnetic field so that the radiation hv can be absorbed (see Fig. 5).
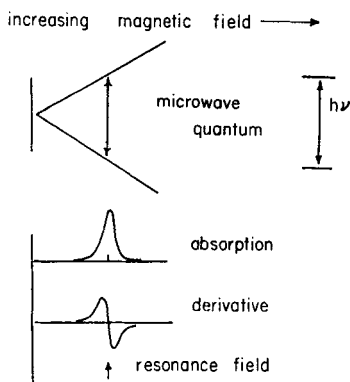
Fig. 5. As the applied magnetic field increases in strength, the electronic energy levels split at a rate given by the "g-value". At resonance, the energy of the microwave quantum matches the energy separation between the states and can be absorbed

For this reason, ESR is much more easily done in Kramers ions which have an odd number of electrons and at least a two fold degeneracy in the absence of an applied magnetic field (Kramers theorem). This restricts one to those paramagnetic iron materials which have half integer spin (1/2, 3/2, 5/2) and eliminates those iron materials with spins of 0, 1, 2 unless special efforts are made which we won't discuss here.

b) Comparison with Mössbauer Effect Experiments

Mössbauer spectroscopy in ^{57}Fe on the other hand, has radiation whose absorption depends only on the presence of a *nucleus* (^{57}Fe) with the right set of energy levels in the absorber. Thus Mössbauer spectroscopy will detect the presence of iron with *any* electronic configuration including diamagnetic iron and can also determine the chemical state of the iron being observed. Mössbauer spectroscopy or nuclear gamma resonance is done by varying the frequency of the source radiation and keeping the external field fixed in contrast to the fixed frequency variable field ESR experiment. Thus one could observe a set of electronic levels at a constant field value (chosen by the experimenter) or even in zero field. This simplifies the analysis as we shall see later.

ESR does have one clear cut advantage which should be mentioned and that is the precision with which measurements can be made. The ESR resonance line is much narrower and more sensitive to small changes in the electronic state. This has been shown in the case of transferrin (*27*) where small differences were observed in the states of the two iron sites which were not detectable with Mössbauer spectroscopy (*28*). Furthermore, ESR can be done on any isotope of iron so that samples need not be enriched with ^{57}Fe as in the case of Mössbauer experiments.

c) Complementary Information by ESR and Mössbauer Spectroscopy

Since one is dealing with the same set of energy levels in each experiment one should look for a model consistant with each experiment. In the case of the iron transport compounds the experimental results are parameterized by the coupling coefficients D, λ, μ, A, P in the spin Hamiltonian to be discussed in the next section. The parameter P in ^{57}Fe can be measured only with Mössbauer spectroscopy since it comes about through the excited nuclear state which is not available in an ESR experiment.

The magnetic hyperfine coupling constant, A, is in principle measurable in both ESR and Mössbauer effect, but will be observed only in the case of ^{57}Fe which has a nuclear magnetic moment. Since ^{57}Fe is only 2% naturally abundant the ESR spectrum with unenriched samples

will not have much of a contribution from the ^{57}Fe ions. It would be possible to use isotopically enriched iron to enhance the magnetic hyperfine contribution to the ESR spectrum. The parameters λ and μ reflect the symmetry of the electronic environment and cause admixtures in the electronic wave functions giving rise to the features in an ESR or Mössbauer spectrum. The actual energy level separation is scaled by D which can be determined by thermal population effects in the spectrum but because of experimental difficulties (such as a changing cavity resonance with temperature in an ESR experiment) D can be found more easily from thermal population effects in the Mössbauer spectra. However, if the microwave quantum is large enough so that transitions between different Kramers doublets are possible, then it should be possible to measure D quite accurately with ESR. The mixing parameters λ and μ can also be determined from Mössbauer experiments but not to such a high accuracy as in ESR.

IV. Spin Hamiltonian with $S = 5/2$

a) Description of the Interactions

The detailed structure of the Mössbauer and ESR spectra for the iron transport compounds can be described in terms of a spin Hamiltonian $\mathscr{H}$ with effective spin $S = 5/2$ for the high spin ferric ion. These parameters can give information about the site symmetry of the iron. Since there is no orbital angular momentum in the ^6S state, the effective spin is the same as the real spin of the iron ion. There is spherical symmetry in the ^6S state to first order, but spin-orbit coupling to excited (nonspherical) orbital states gives rise to asymmetries about the iron site which are reflected in the spin Hamiltonian. The general form of the spin Hamiltonian which we will use here is a quantum mechanical operator $\mathscr{H}$ which acts on the electronic states $|m_s\rangle$ and nuclear states $|m_I\rangle$.

$$\mathscr{H} = D\left[S_z^2 - \frac{35}{12} + \lambda(S_x^2 - S_y^2) + \frac{\mu}{6}\left(S_\xi^4 + S_\eta^4 + S_\zeta^4 - \frac{707}{16}\right)\right] +$$
$$+ A\mathbf{I} \cdot \mathbf{S} + 2\,\beta_e\,\mathbf{H} \cdot \mathbf{S} + P\left[I_z^2 - \frac{5}{4} + \lambda(I_x^2 - I_y^2)\right] - g_N\beta_N\,\mathbf{H} \cdot \mathbf{I} \quad (3)$$

The terms in D, λ and μ give the zero field splitting of the six spin states of the ^6S state. The quadratic interaction described by D and λ usually dominates except when the applied field makes the Zeeman term larger (Fig. 6). In several of the iron transport compounds, the zero

field splitting is comparable to the Zeeman energy in a field of a few kilo Gauss so that there may be considerable mixing of the states and perturbation theory is not applicable. Usually the quartic term has been neglected ($\mu = 0$) but there have recently appeared some cases which are strongly dependent on μ (*29, 30*). (Note: $\lambda = E/D$ and $\mu = a/D$ where E and a are the coupling constants used by other authors.)

This splitting in zero field reflects the symmetry of the local crystalline environment and it arises out of the spin-orbit interaction which
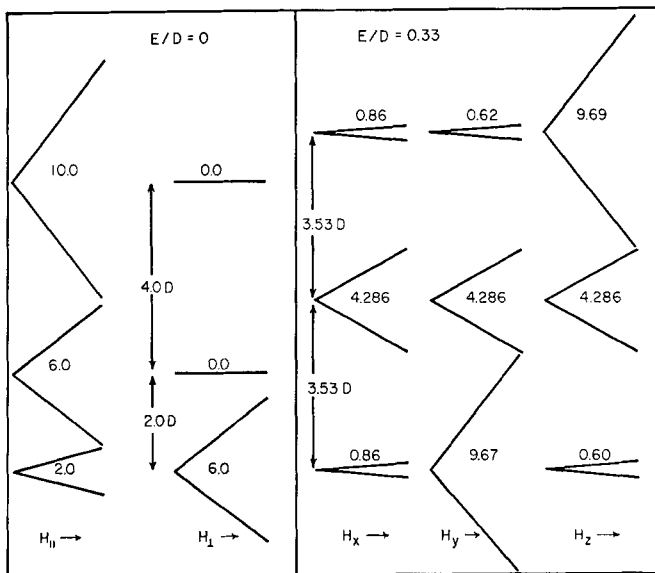
Fig. 6a and b. A diagram showing the behavior of the three Kramers doublets in an applied magnetic field for (a) axial ($E/D = 0$) and (b) rhombic ($E/D = 1/3$) symmetry. The ESR spectra would look quite different for the two cases

couples the ground (^6S) state with higher orbital states which in turn are more sensitive to distortions in the local environment. The origin of the zero field splitting in S-state ions has been studied (*31*) rather extensively but there is still no agreement about the specific origin of D, λ and μ.

The term with μ as a coefficient represents the cubic crystal field energy and arises from coupling with higher excited states (*32*). This contribution can usually be neglected except for those ions with nearly cubic symmetry. If there is rhombic symmetry then the (η, ξ, ζ) axes

coincide with the (x, y, z) axes of the zero field splitting. However, in trigonal symmetry the z-axis is in the (111) direction with respect to to the (η, ξ, ζ) axes.

It might be worthwhile to point out that in the wide variety of crystal fields possible, the *symmetry* at the metal site can be orthorhombic which has fewer symmetry operations than an axially symmetric complex for example. However, the *strength* of the axial distortion might disturb the local environment more severely (as in the heme complexes) in contrast to the *weak* rhombic departures from cubic symmetry in the sideramines discussed later. The electronic wave functions which determine the hyperfine interactions depend on the parameters λ and μ which reflect the degree of asymmetry in the local environment.

The Zeeman interaction $2\,\beta \boldsymbol{H} \cdot \boldsymbol{S}$ is isotropic for the ^6S state and describes how the energy levels behave in a small external field. Small corrections due to admixtures of excited states can destroy the isotropy.

Similarly, the magnetic hyperfine interaction [Eq. (1)] can be written as $A\boldsymbol{I} \cdot \boldsymbol{S}$ if the A tensor is isotropic although anisotropy can arise from non-zero orbital and dipole contributions due to admixtures with higher electronic states. Only small departures from isotropy have been found in A for one of iron transport compounds (28) with the spherically symmetric ^6S state.

The electric field gradient (EFG) is zero in the ^6S state with spherical symmetry, but of course, there are contributions from the charge asymmetries about the iron site and from the anisotropic admixtures mentioned above. Since the EFG has its origin in the same asymmetry as D and λ, the asymmetry parameter η can be constrained by $\eta = 3\lambda$ (33). The last term in Eq. (3) is the Zeeman interaction of the nuclear magnetic moment with the externally applied field and is negligible for fields less than a few kilo Oersted. Mössbauer data in powder samples or frozen solutions can give valuable information because the simultaneous action of EFG and magnetic hyperfine coupling yield a spectral profile that can be interpreted in terms of the electronic states of the iron complex.

b) Tetragonal Symmetry $(\lambda \simeq 0,\ \mu \simeq 0)$

In the heme proteins, there is a large axial crystal field which gives a value of D (≈ 5 to 10 cm^{-1}) large enough to dominate all the other terms in the spin Hamiltonian. These give Mössbauer spectra such as those of *Lang* (34) for cytochrome-c peroxidase fluoride, in which only the ground state is populated at helium temperature. ESR experiments have been done on several heme complexes (35) and the g-values are interpreted in terms of the energy level diagram of Fig. 6a. The strong anisotropy in the g-values is indicative of the strong axial ligand field experienced

at the iron site. The quartic term in the spin Hamiltonian is quite negligible in these cases ($\mu = 0$).

c) Rhombic Symmetry ($\lambda > 0$, $\mu \neq 0$, $z = \, <100>$)

In each of the iron transport proteins there is a rhombic crystal field which is strong enough to make E comparable to D, (Actually, D is rather weak in these cases.) In fact $E = D/3$ or $\lambda = 1/3$ is the condition for which the extreme rhombic asymmetry exists (33, 36). A value for $\lambda > 1/3$ merely implies that the principal axis of the zero field splitting is no longer the z axis.

Of the Kramers doublets in extreme rhombic symmetry ($\lambda = 1/3$) Fig. 6b, the middle doublet has an isotropic g-value ($g = 4.3$) which means that the magnetic moment in those states will follow the field in any direction and so the contribution of that doublet to the Mössbauer spectrum indicates the hyperfine field to be antiparallel to the applied field. The $g = 4.3$ resonance in ESR is found in each of the iron complexes considered here. However, the magnetic moment of the lowest doublet will continue to point in the y direction unless the field is almost directly along the x or z axes and the moment of the highest doublet will likewise stay in the z direction; unless the applied field strength becomes comparable to the zero field splitting energy and causes mixing of the states. The "g" values of these states which describe the rate at which a fictitious spin $1/2$ would split in an applied field are (with $\lambda = 1/3$),

$$
\begin{aligned}
&E_3 \quad g_x = g_y \simeq 0.6,\ g_z \simeq 9.6 && \text{(highly anisotropic)} \\
&E_2 \quad g_x = g_y = g_z = 4.286 && \text{(isotropic)} \\
&E_1 \quad g_x = g_z \simeq 0.6,\ g_y \simeq 9.6 && \text{(highly anisotropic)}
\end{aligned}
$$

A value of $\lambda > 1/3$ implies that the principal distortion is along the y-axis as explained by *Blumberg* (36). The inclusion of the quartic term in the spin Hamiltonian doesn't change his argument since the quartic term has cubic symmetry. We will transform all reported values for λ and D so as to compare like quantities.

Although it has been the usual practice to neglect the quartic term in the spin Hamiltonian it has been found recently that it cannot be neglected, especially in these iron transport complexes in which the magnitude of D is small and more nearly comparable to a. If one includes the quartic term, rather striking effects can be seen in the Mössbauer spectrum and although another parameter should, of course, allow a better fit to the data, this is not to say that the interaction does not exist. In order to carry out a calculation one must decide whether the z axis (of the EFG and of DS_z^2) is in the $<100>$ or $<111>$ direction

relative to the ξ, η, ζ axes of the cubic term. The axes (ξ, η, ζ) are usually taken as the metal-ligand directions, but there is no reason *a priori* not to choose another set as long as it has cubic symmetry.

If we first consider z to be in the $<100>$ direction, we then have a situation with orthorhombic symmetry where x, y, z are the symmetry axes. It has been found that the inclusion of the quartic term with coefficient μ in the spin Hamiltonian allows a range of values for $\lambda = E/D$, and still maintains an isotropic $g = 4.3$. If one *demands* that the g's in one Kramers doublet be isotropic, then it follows that $g = 4.3$ (actually $g = 4.286$) for that doublet and a linear relationship [Eq. (4)] between D, E and $a = \mu D$ follows from this demand (29, 30).

$$\{4a = 3D - 9E\} \quad \text{or} \quad \{4\mu = 3 - 9\lambda\} \tag{4}$$

Thus, we can have an isotropic $g = 4.3$ even for near axial symmetry ($\lambda \to 0$) as long as $\mu = 3/4$. Over the years, $g = 4.3$ has come to be known as the signature for extreme "Rhombic" iron complexes, but now it is clear that this is not necessarily so. Several experimental examples such as enterobactin and mycobactin-P have shown this to be true. However, the pure axial case with $E \equiv 0$ will still give the electronic states as described in Fig. 6a.

If ($\lambda = 1/3$, $\mu = 0$) then the energy levels are separated by a constant amount ($3.53D$) as shown in Fig. 6b. However, if $\lambda \neq 1/3$ and μ is constrained by Eq. (4), the isotropic $g = 4.3$ is maintained (in the middle Kramers doublet) but the energy level separation is varied as λ changes.

d) Trigonal Symmetry ($\lambda = 0$, $\mu \neq 0$, $z \equiv <111>$)

If we have z in the $<111>$ direction (trigonal symmetry) and if we again demand that g be isotropic in one doublet, we find that $g = 3.3$ and $a = (-9)D$. In this case we begin with trigonal symmetry ($\lambda = 0$). This clearly is no help to us since experimentally we find $g = 4.3$ in ESR and the Mössbauer results also indicate rhombic symmetry. Since several of the iron complexes discussed below are thought to have nominal trigonal symmetry (based on other experiments) we have a bit of a dilemma.

V. Calculation of Spectra from the Spin Hamiltonian Model

a) Calculated ESR Spectra for $S = 5/2$

We begin with the spin Hamiltonian in Eq. (3) with the omission of the terms involving the nuclear spin (I) leaving only those interactions which

determine the electronic behavior. Since an ESR experiment is done in an applied magnetic field of at least a few hundred Gauss, the nuclear moment with an effective field strength of about ten Gauss at the site of the electron is negligible compared to the external field.

To calculate an ESR spectrum we first of all assume the applied field to be in some direction (θ, ϕ) with respect to the crystal or molecular axes. The matrix elements of the spin Hamiltonian are loaded into a (6×6) Hermitian matrix (Tables 1 or 2) which is diagonalized numeri-

Table 1. The spin Hamiltonian in orthorhombic symmetry $(z \equiv <001>)$

$\mid 5/2>$	$\mid 3/2>$	$\mid 1/2>$	$\mid -1/2>$	$\mid -3/2>$	$\mid -5/2>$
$\frac{10}{3} + \frac{1}{2}\mu$	0	$\sqrt{10}\,\lambda$	0	$\frac{\sqrt{5}}{2}\mu$	0
	$-\frac{2}{3} - \frac{3}{2}\mu$	0	$3\sqrt{2}\,\lambda$	0	$\frac{\sqrt{5}}{2}\mu$
		$-\frac{8}{3} + \mu$	0	$3\sqrt{2}\,\lambda$	0
			$-\frac{8}{3} + \mu$	0	$\sqrt{10}\,\lambda$
				$-\frac{2}{3} - \frac{3}{2}\mu$	0
					$\frac{10}{3} + \frac{1}{2}\mu$

Table 2. The spin Hamiltonian in trigonal symmetry $(z = <111>)$

$\mid 5/2>$	$\mid 3/2>$	$\mid 1/2>$	$\mid -1/2>$	$\mid -3/2>$	$\mid -5/2>$
$\frac{10}{3} - \frac{1}{3}\mu$	0	$\sqrt{10}\lambda$	$\frac{2\sqrt{5}}{3}\mu$	0	0
	$-\frac{2}{3} + \mu$	0	$3\sqrt{2}\,\lambda$	0	0
		$-\frac{8}{3} - \frac{2}{3}\mu$	0	$3\sqrt{2}\,\lambda$	$-\frac{2\sqrt{5}}{3}\mu$
			$-\frac{8}{3} - \frac{2}{3}\mu$	0	$\sqrt{10}\lambda$
				$-\frac{2}{3} + \mu$	0
					$\frac{10}{3} - \frac{1}{3}\mu$

All matrix elements are in units of D. $(\lambda = E/D$ and $\mu = a/D)$.

cally on a computer to find the energies and wave functions. Then the transition probability for the absorption of radiation between any pair of these levels is computed, a lineshape function with width Γ is folded in and the contribution to the absorption of the radiation $h\nu$ *at that field strength and* at *that field direction* is determined. This calculation is repeated for many different directions over the unit sphere (although rhombic symmetry allows us to do only one octant of the unit sphere since all octants are equivalent) and all contributions are added with equal weights to simulate the spectrum for a randomly oriented absorber. This angular average is not appropriate, of course, if one has single crystal absorbers. At this point the absorption of $h\nu$ at one field value has been calculated. The next step is to increase the applied field strength and repeat everything from the beginning. It is somewhat unfortunate that the ESR is very sensitive to small changes in the direction of the applied field because this makes it necessary to do the powder averages over one octant of the unit sphere on a much finer grid (*i.e.* to do separate computations for small changes in the field direction). In some of the examples studied, a linewidth (full width at half max) of 100 G was used and a grid of 400 field directions distributed uniformly over one octant of the unit sphere was necessary to get rid of computational artifacts. This makes the calculation very costly in terms of computer time. Such a calculation with 25 different field strengths takes 47 min of CPU time on the CMU 1108 computer.

An X-band ($h\nu = 0.3$ cm^{-1}) spectrum computed from 500 G to 4300 G is shown in Fig. 7. Because we are dealing with iron complexes in rhombic environments, there are few shortcuts that one can take to decrease the computation time.

The profile of the calculated ESR spectrum depends strongly on the spin Hamiltonian parameters D, λ, and μ which are adjusted to maximize the agreement with experiment. In the dashed curve of Fig. 7 we see the influence of the parameter $\mu = a/D$ in the $g = 4.3$ region.

It is found that the graininess in the calculated ESR spectra is a problem if the *derivatives* of the absorption spectra are compared. For this reason, it would be more economical (given the cost of computing time) to compare the absorption spectra, even though this is in contrast to the usual experimental arrangement in ESR experiments.

b) Calculated Mössbauer Spectra

We assume that the electronic spin relaxation is very slow so that we don't consider time dependent effects in the spectrum. This can be arranged experimentally by magnetic dilution and low temperatures. The electronic basis states are the six states $|m_s\rangle = |-5/2\rangle$, $|-3/2\rangle$,
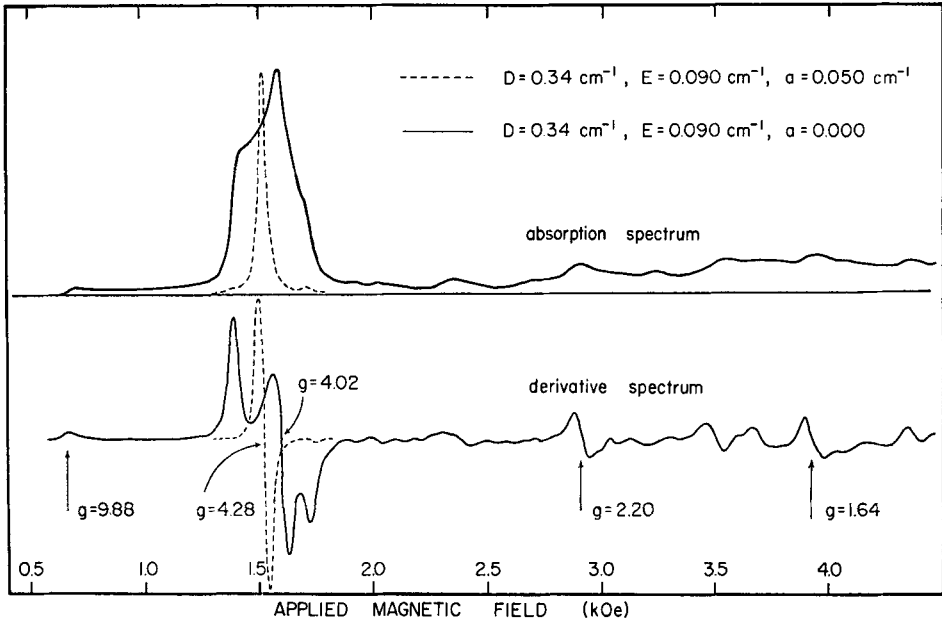
Fig. 7. Calculated ESR spectrum for a randomly oriented absorber at X-band ($hv = 0.3$ cm^{-1}) with $D = 0.34$ cm^{-1}, $\lambda = E/D = 0.265$, $\mu = a/D = 0$ and with a linewidth of 100 Gauss folded in using a Lorentzian line shape. The dashed curve shows the effect of the fourth order term in the $g = 4.3$ region. The intensity of the dashed curve is reduced on the figure by a factor of two

---, $|+5/2>$. These together with the nuclear basis states $|m_I>$ form product states $|m_s>|m_I>$ and the spin Hamiltonian operates on these product states. The spin Hamiltonian matrix which results from Eq. (3) is given in Table 3 for the nuclear ground state. The corresponding 24×24 matrix for the nuclear excited state is similar but not explicitly given here. The various terms mix the basis states and the $(n \times n)$ matrix is diagonalized to find the energies and eigenstates. $[n = (2S + 1)(2I + 1)]$.

This procedure is followed for the nuclear excited state ($I = 3/2$) and the ground state ($I = 1/2$) and then the 288 transition probabilities and line positions are calculated with a Lorentzian line shape of width Γ folded in to give the Mössbauer spectrum. This has been done on the computer assuming the applied magnetic field and the gamma beam in some fixed direction relative to the crystal axes. Then this calculation is repeated for all other directions of the field and gamma beam and the spectra are added with equal weights to simulate the spectrum for a randomly oriented absorber. It generally takes about ten minutes

78
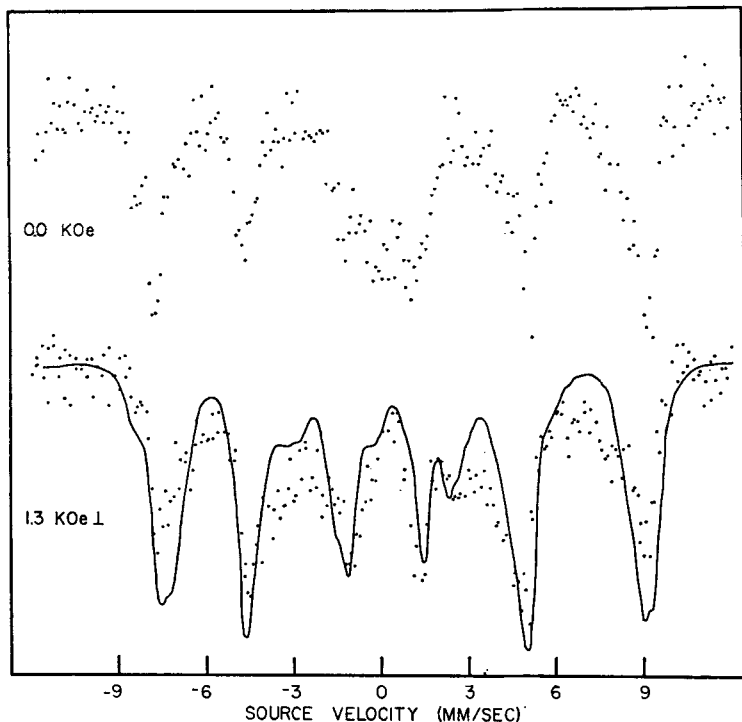
Fig. 8. Mössbauer spectra for ^{57}Fe bound to mycobactin-P in a frozen methanol solution at $T = 1.5$ K. The data in zero field and 1.3 kOe are shown. The solid curve is calculated using $D = 0.22$ cm^{-1}, $\lambda = 0.45$, $\mu = -0.26$, $A_{ex} = 1.51$ mm/sec and $P = -0.20$ mm/sec

for the computer to generate one spectrum with 100 different orientations of the magnetic field over one octant of the unit sphere.

The profile of the resulting spectrum depends on the spin Hamiltonian parameters which are adjusted to maximize the agreement between the calculated spectrum and the experiment.

Mössbauer spectra for mycobactin P, a growth factor (sideramine) for mycobacterium Phlei, which is slightly soluble in ethanol were observed at 4.2 K (Fig. 8), and the spin Hamiltonian parameters D, λ, μ, A and P were found to give a reasonably good simulation of the data (37). Notice the effect of the applied field in stablizing the spin states as evidenced by the decrease in the broad background of the zero field spectrum.

In the slow relaxation situation, there is one Mössbauer spectrum associated with each electronic state and the spectra due to the various electronic states are superimposed on each other with weights given by

Table 3. Explicit matrix elements for the $S = 5/2$ electronic state and the $I = 1/2$ nuclear ground state $<m_s m_I | \mathcal{H} | m_s m_I>$

$\mid 5/2, 1/2>$	$\mid 5/2, -1/2>$	$\mid 3/2, 1/2>$	$\mid 3/2, -1/2>$	$\mid 1/2, 1/2>$	$\mid 1/2, -1/2>$
$5A/4 + 10D/3 + a/2 + 5H_{ez} + H_{nz}$	H_{n-}	$\sqrt{5}\beta H_-$	0	$\sqrt{10}E$	0
	$-5A/4 + 10D/3 + a/2 + 5H_{ez} - H_{nz}$	$\sqrt{5}A/2$	$\sqrt{5}\beta H_-$	0	$\sqrt{10}E$
		$3A/4 - 2D/3 - 3a/2 + 3H_{ez} + H_{nz}$	H_{n-}	$\sqrt{8}\beta H_-$	0
			$-3A/4 - 2D/3 - 3a/2 + 3H_{ez} + H_{nz}$	$\sqrt{2}A$	$\sqrt{8}\beta H_-$

Where:

$$\beta_e H_z = H_{ez}$$

$$\tfrac{1}{2}\beta_n g_n H_z = H_{nz}$$

$$H_- = H_x - iH_y$$

$$g_n \beta_n H_- = H_{n-}$$

$A/4 - 8D/3 + a + H_{ez} + H_{nz}$	H_{n-}
$-A/4 - 8D/3 + a + H_{ez} - H_{nz}$	
$-A/4 - 8D/3 +$	

their Boltzmann factors. Thus one can get significant changes in the Mössbauer spectrum by depopulating some of the electronic states at low temperatures. An example of this is in enterobactin shown in Fig. 9. If this applied field is small enough so that there is no significant mixing of the electronic states by the applied field, then each member of a Kramers doublet will yield the same Mössbauer spectrum although different Kramers doublets give different spectra.

The Mössbauer spectra calculated for each Kramers doublet assuming $\lambda = \frac{D}{E} = 0.46$ and $\mu = -0.27$ is shown in Fig. 9 where there is a small field of 1.3 kOe assumed to be perpendicular to the gamma beam. Good agreement with experiment is obtained. The reader can observe the different contributions from each Kramers doublet in the composite spectrum. Each contribution is weighted by the appropriate Boltzmann

$\lvert -1/2,\ 1/2\rangle$	$\lvert -1/2,-1/2\rangle$	$\lvert -3/2,\ 1/2\rangle$	$\lvert -3/2,-1/2\rangle$	$\lvert -5/2,\ 1/2\rangle$	$\lvert -5/2,\ -1/2\rangle$
0	0	$\sqrt{5}a/2$	0	0	0
0	0	0	$\sqrt{5}a/2$	0	0
$3\sqrt{2}E$	0	0	0	$\sqrt{5}a/2$	0
0	$3\sqrt{2}E$	0	0	0	$\sqrt{5}\,a/2$
$3\beta H_-$	0	$3\sqrt{2}\,E$	0	0	0
$3A/2$	$3\beta H_-$	0	$3\sqrt{2}E$	0	0
$a-H_{ez}+H_{nz}$	H_{n-}	$\sqrt{8}\beta H_-$	0	$\sqrt{10}E$	0
$A/4-8D/3+a-H_{ez}-H_{nz}$	$\sqrt{2}A$	$\sqrt{8}\beta H_-$	0	$\sqrt{10}E$	
	$-3A/4-2D/3-3a/2-3H_{ez}+H_{nz}$	H_{n-}	$\sqrt{5}\beta H_-$	0	
		$3A/4-2D/3-3a/2-3H_{ez}-H_{nz}$	$\sqrt{5}A/2$	$\sqrt{5}\beta H_-$	
			$-5A/4+10D/3+a/2-5H_{ez}+H_{nz}$	H_{n-}	
				$5A/4+10D/3+a/2-5H_{ez}-H_{nz}$	

factor. Similar spectra are obtained by *Bock* and *Lang* (*38*) for defer-oxamine.

In Fig. 10 are presented some computer generated Mössbauer spectra with different degrees of rhombic asymmetry ($\lambda < 1/3$ and $\mu = 0$) so that the effect of the variation of λ can be seen. Both Mössbauer effect and ESR show easily measurable differences between spectra calculated from models with $z = \langle 100\rangle$ and $z = \langle 111\rangle$. The Mössbauer spectra are really quite different for the two models as seen in Fig. 11 and the ESR spectra give an isotropic $g = 3.3$ for the trigonal case (if $\mu = -9$) and isotropic $g = 4.3$ for the rhombic case [if $\mu = 0.75\ (1-3\lambda)$]. Thus we have an experimental method to distinguish between these two possibilities. It is striking that the Mössbauer data in the cases ferrichrome A, enterobactin and benzohydroxamic acid are best fit with z in $\langle 100\rangle$

81
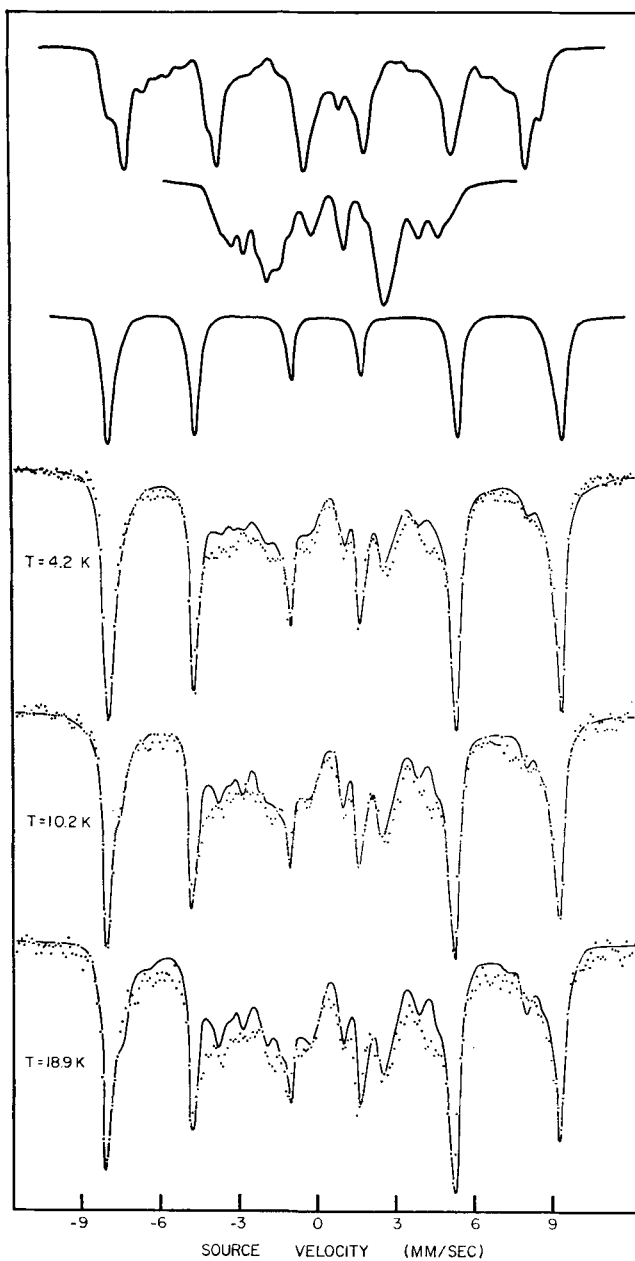
Fig. 9. Mössbauer data for a methanol solution of ^{57}Fe bound to enterobactin in an applied field of 1.3 kOe at 4.2, 10.2, 18.9 K. The solid curves are calculated from the electronic model with rhombic symmetry and the parameters given in Table 4. The contributions from the three Kramers doublets are given at the top in descending order of energy
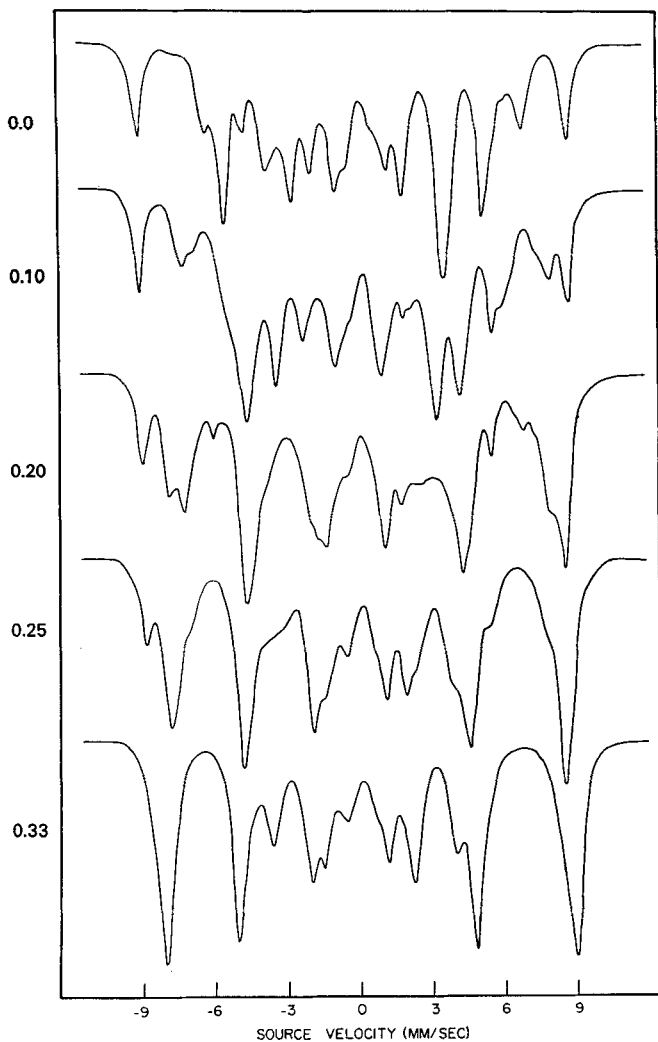
Fig. 10. Calculated Mössbauer spectra using the rhombic model with $D = 0.50$ cm^{-1}, λ is varied, $\mu = 0$, $A = 1.5$ mm/sec, $P = 0.25$ mm/sec, $|H| = 1.3$ kOe and $T = 4.2$ K. The various degrees of distortion from axial symmetry ($\lambda = 0$) to extreme rhombic distortion ($\lambda = 1/3$) are shown

direction and with $\mu \neq 0$. This would imply rhombic symmetry in the spin Hamiltonian and also in the site symmetry. However, other experimental evidence for enterobactin (*39*), ferrichrome A (*40*), and benzohydroxamic acid (*41*) indicates the molecular structure to be *trigonal*!
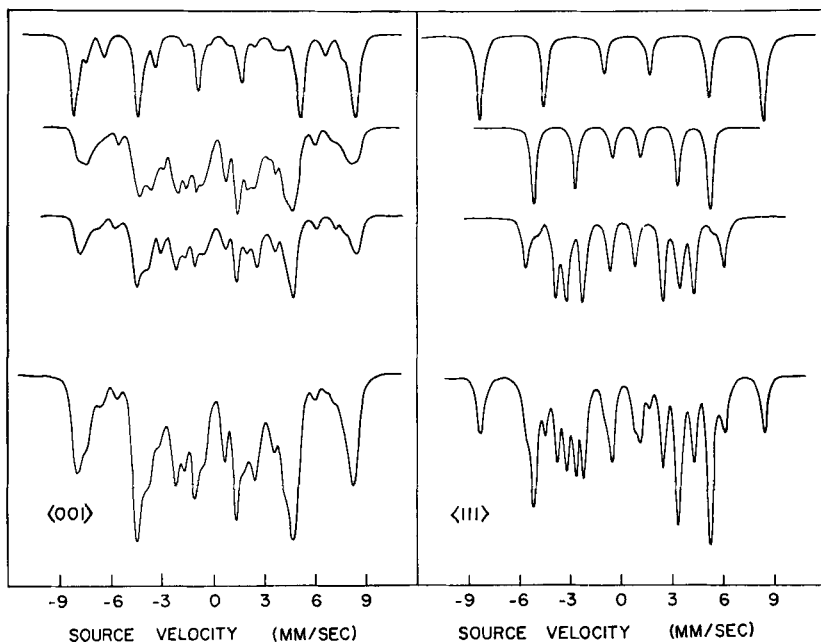
Fig. 11. Calculated Mössbauer spectra with the same spin Hamiltonian parameters $D = 0.50$ cm^{-1}, $\lambda = 0.0$, $\mu = 0.75$, $A = 1.51$ mm/sec, $P = -0.15$ mm/sec in rhombic (left) and trigonal (right) symmetry. The bottom spectrum is a Boltzmann average of the contributions from each of the three Kramers doublets shown above. We assume for this calculation that the sample is at 4.2 K in an applied field of 1.3 kOe perpendicular to the gamma beam. One can observe the marked difference in the spectra for the trigonal and rhombic model calculations

Thus there is a dilemma at this point: How can one get $g = 4.3$ in ESR and Mössbauer spectra indicative of a *rhombic* environment when the complexes are known to be *trigonal* (axial)? It is impossible to get $g = 4.3$ from a spin Hamiltonian with trigonal symmetry; and the Mössbauer data don't reflect trigonal symmetry! It may be that the relationship between the spin Hamiltonian symmetry and the crystal symmetry is not as strong as we have thought. Or perhaps the ESR and Mössbauer data are very sensitive to *small* departures from axial symmetry which are not picked up by the X-ray techniques.

Many of the iron transport compounds have hydroxamic acid ligands which bind the ferric ion and so synthetic iron (III) hydroxamic acid compounds have been prepared.
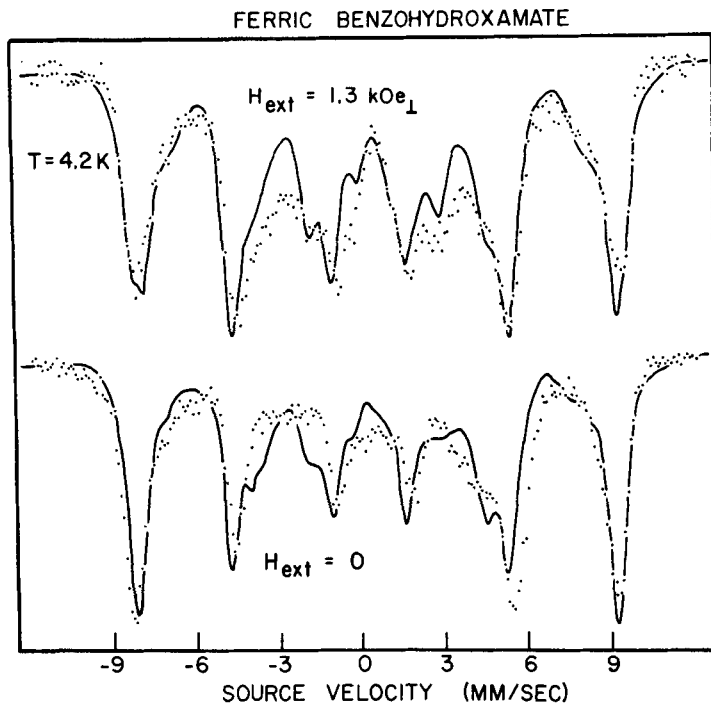
Fig. 12. Mössbauer data for ferric benzohydroxamate showing agreement with the rhombic model. The zero field calculation assumes a randomly oriented field of about 30 Gauss to be acting of the unpaired electrons of the iron due to neighboring nuclear moments

Experiments on these synthetic tri-hydroxamic acids have shown the rhombic symmetry effects in the Mössbauer data (Fig. 12). Other experiments using Mössbauer spectroscopy on low symmetry sites have been published by *Lang et al.* (*33*) in EDTA and by *Zabinski et al.* (*42*) in protocatechuic acid 4, 5-oxygenase, and ESR by *Peisach et al.* (*43*) in rubredoxin.

If the iron is complexed by three identical bidentate ligands, there are two possibilities for the ligand field as shown in Fig. 13. There is the trigonal (facial) arrangement which has a true threefold axis (either left or right handed); and there is also the "rhombic" (meridional) conformation whose ligand field can be represented by a Hamiltonian with rhombic symmetry. If we assume that the electronic state has the same symmetry as the conformation of the iron complex then we can distinguish between the trigonal and the rhombic conformations using either Mössbauer or
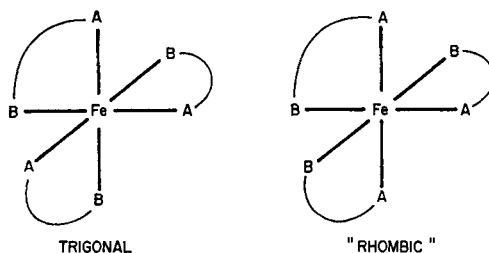
Fig. 13. Diagrams showing how asymmetric bidentate ligands can be arranged in either trigonal (facial) or rhombic (meridional) symmetry about the iron

ESR spectroscopy. The differences in the Mössbauer spectra for the rhombic case with z in the <100> direction and the trigonal case with z in the <111> direction are shown in Fig. 11.

VI. Method for Analyzing Mössbauer Spectra with Paramagnetic Hyperfine Structure

The usual procedure to follow in the analysis of the Mössbauer data for the spin Hamiltonian parameters is to go first to the data taken in a small applied field of several hundred Gauss. This is done in order to break the coupling between neighboring paramagnetic ions which give rise to spin-spin relaxation and also to break the (Back-Goudsmit) coupling between the electronic spin and the ligand nuclear magnetic moments (44). In the absence of an applied field, this ligand nuclear moment effect can have drastic effects on the Mössbauer spectrum. We see this in the case of transferrin (28) (Fig. 14), where the spin Hamiltonian parameters (D, A, P, λ) used to fit the data in an applied field can also be used to calculate the spectrum expected in zero applied field. The result of the calculation is in sharp disagreement with the experiment in zero field even though the spectrum from the same sample in an applied field gives good agreement for the applied field.

a) Neighbor Nucleus Effects in Zero Field

The ligand nuclear moments (I_j) interact with the electronic spin which is covalently shared to some extent between ^{57}Fe and the ligands. The proper term to add to the Hamiltonian [Eq. (3)] is $\sum_j I_j \cdot B_j \cdot S$ where B_j is a coupling tensor for the jth ligand nucleus.
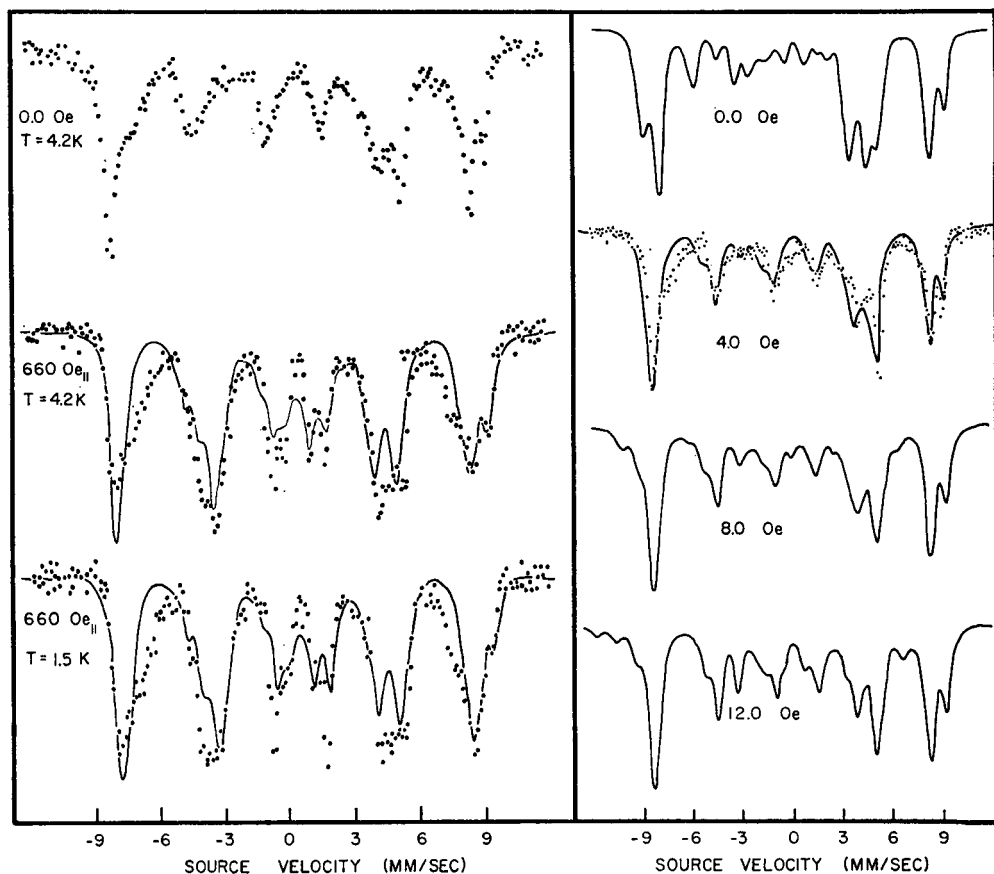
Fig. 14. Mössbauer data for transferrin in variable conditions and the calculation from the electronic model. Each spectrum on the right was calculated with the assumption of a small randomly oriented field acting on the electronic moment. The data on the right were collected in exactly zero applied field

This could be done on a computer and has been fairly successful (45). However, if there are several ligand nuclear moments then the computation rapidly gets out of hand because the dimension of the matrix to be diagonalized goes as $(2I_{Fe} + 1) (2S + 1) \prod_j (2I_j + 1)$ so that it is useful to approximate the sum of the ligand interactions acting on the electron spin S, by a random magnetic field H_R with strength of several Gauss. Then one simply adds the term $g\beta H_R \cdot S$ to Eq. (3) and calculates the spectrum. This is done for varying field strengths H_R and indeed this does improve the agreement with experiment (44) (Fig. 14).

87

VII. Experimental Studies

a) Ferrichrome A

Ferrichrome A is one of the most studied iron transport compounds. It is found in the smut fungus *Ustilago sphaerogena* and has a structure similar to several molecules which are growth factors for several micro-organisms. The molecule consists of a ferric ion bound by three bidentate hydroxamic acid residues which form a left-handed propeller as established by the X-ray crystallographic studies by *Zalkin, Forrester* and *Templeton (40)*. There is a three-fold axis through the iron corresponding to the axis of the propeller. The ferric complex is a red-brown color like most of the natural iron complexes discussed below. The iron is bound very tightly as indicated by the dissociation constant K where $pK = \log K \simeq 32$. Nevertheless iron is found to exchange rapidly with free iron in a solution (1).

Electron spin resonance (ESR) experiments were done on ferrichrome A by *Wickman, Klein* and *Shirley (46)* and a strong resonance was observed at $g = 4.3$. Their results were interpreted in terms of a "rhombic" spin Hamiltonian in which $D > 0$ and $\lambda = E/D = 0.25 \pm 0.04$.

Mössbauer experiments were then done by the same authors (18) who were not only among the first to observe paramagnetic hyperfine structure and spin relaxation effects in Mössbauer spectra but also formulated a theory to describe the effects of time dependent hyperfine fields in the Mössbauer spectrum. The data in Fig. 4 show the effect of increasing the electronic spin relaxation time by lowering the temperature. The spin Hamiltonian parameters are found in the long relaxation time limit to be 220 kOe/unit spin for the hyperfine field ($A \approx 1.50$ mm/sec) and $D \simeq 1$ cm^{-1} estimated from thermal depopulation effects in the Mössbauer spectrum. The zero field data still show a broad parabolic background which is indicative of the existance of relaxation effects even at the lowest temperature and concentration. The application of a small magnetic field can help to sharpen the resonance lines (20) and facilitates the determination of the hyperfine coupling constant A which is found to be 1.47 mm/sec for the nuclear excited state of ^{57}Fe or 216 kOe/unit spin. A refined analysis (62) of Mössbauer data gives $D = 0.53$ cm^{-1}, $\lambda = 0.51$, $\mu = -0.133$, and $P = -0.50$ mm/sec.

Dowsing and *Gibson (47)* have deduced values of $D = 0.5 \pm .03$ cm^{-1} and $\lambda = 0.28 \pm .02$ from their ESR experiments.

Recently *Brackett, Richards* and *Caughey (48)* have done far infrared measurements on ferrichrome A and report that $D = -0.27$ cm^{-1} and $\lambda = 0.25$.

b) Deferoxamine

Deferoxamine (desferrioximine B) is a growth factor (sideramine) for several micro-organisms in which three hydroxamic acid residues bind ferric iron very tightly with pK $\simeq$ 30.5 (49). The iron complexing ability of this substance is used in cases of severe iron poisoning to chelate excess iron and is available for clinical use under the name "desferal". The ferric complex is red-brown and magnetic susceptibility measurements yield $\mu_{\text{eff}} = 5.86$ Bohr magnetons at room temperature. The molecular complex is probably such that the hydroxamic acid ligands form a propeller arrangement about the iron.

A rather complete Mössbauer study of the ^{57}Fe complexed by deferoxamine has been done by *Bock* and *Lang* (38) and their results are in excellent agreement with a model spin Hamiltonian in which the coupling constants have the values $D = 0.5$ cm^{-1}, $\lambda = \eta/3 = 0.46$, $A_{\text{ex}} = 1.474$ mm/sec, $P = -0.30$ mm/sec (or $\Delta E_Q = 0.77$ mm/sec in absence of magnetic interactions). The asymmetry parameter $\lambda = \eta/3 > 1/3$ merely means that the principal distortion axis is in the y-direction instead of the z-direction for the axis system assumed for the spin Hamiltonian. We will use an axis system in which $0 < \lambda < 1$ and $D > 0$ so that we can compare with other molecules. Some of the data and the fitted curves show the typical features associated with these iron transport compounds.

c) Various Hydroxamic Acid Complexes of ^{57}Fe

The natural hydroxamic acid complexes of iron have been the central topic of discussion here, but since the naturally occuring compounds are somewhat complicated by the organic residues, it is probable that some valuable insight into the iron-binding abilities of the natural compounds can be gained through the study of some model hydroxamic acid complexes.

Again, these ferric complexes are very stable (pK $\sim$ 28) as are the natural iron chelating compounds and they bind ferrous iron relatively weakly (50). In an acid medium ($pH \sim 2-6$) the hydroxamic acid forms a deep purple 1:1 complex with ferric iron while in neutral or basic solution a brown-red 3:1 complex is formed in which the hydroxamates act as three bidentate ligands which occupy the six octahedral positions about the iron. The 1:1 purple complex has an absorption maximum at 5000–5200 Å depending on the nature of the hydroxamic acid ligand. The 3:1 red-brown complex (it becomes yellow-orange on dilution) has an absorption maximum usually between 4250–4400 Å with many of the same spectral features as the naturally occurring complexes of ferric iron.

Mössbauer experiments on a few of the concentrated powder hydroxamic acid complexes with Fe^{3+} were reported by *Epstein* and *Straub* (*51*) who observed only a small variation in the spectral features by comparing the different hydroxamic acid complexes. They studied complexes with benzo, acetyl, oley, napthal, nicotinyl, and salicyl hydroxamates. *Epstein* and *Straub* concluded that there is a high degree of ionic binding to the iron (thus a small amount of covalency) based on the isomer shifts which are among the largest observed for ferric complexes so far. This conclusion is in agreement with the observations by *Spartalian* and *Oosterhuis* (*29, 30*) in which paramagnetic hyperfine structure was observed and the magnetic splitting was among the largest observed for any ferric ion so far, which is interpreted as being due to very little delocalization of the magnetic electrons.

Epstein and *Straub* note that there are two geometrical isomers possible for these MA_3B_3 complexes as shown in Fig. 13. It is possible to determine the differences between the spectral profiles of the facial or trigonal conformer and the meridional or rhombic conformer as discussed above.

A crystal structure has been determined for the Fe(III) (benzohydroxamate)$_3$ complex by *Lindner* and *Gottlicher* (*41*) and shows the 3-fold propeller coordination of the ferric ion. This may be the case for the solid but one wonders if this coordination persists in solution or frozen solution since the spin Hamiltonian parameters from Mössbauer experiments seem to indicate rhombic symmetry. These parameters are listed in Table 4. If in fact there is a 3-fold symmetry in the molecular arrangement, then one must question the relationship between the symmetry of the spin Hamiltonian and the symmetry of the local crystal or ligand field (*52*).

d) Mycobactin P

Mycobactins are growth factors for most species of mycobacteria such as *Mycobacterium johnei, M. phlei, M. Tuberculosis* (*53*) and their production by the mycobacterium is stimulated by iron deficiency in the growth medium. They were originally thought to act as scavengers for ferric iron, but recent work by *Ratledge* (*54*) has shown that they are located in the lipid rich regions of the cell wall and participate in the passage of iron through the cell wall by the capture of Fe^{3+} ions at the outer surface and releasing the iron to the cytoplasm inside as Fe^{2+}.

The mycobactins consist of two hydroxamic acid residues which bind the ferric ion as well as a third bidentate ligand with a nitrogen and an oxygen at the iron site. *Snow* (*53*) has deduced a probable molecular

structure in which there is a charge associated with three of the oxygen ligands. The crystal structure of mycobactin-P has been determined recently by *Hough* and *Rogers* (*55*) and has verified the molecular arrangement proposed by Snow in which the charged oxygen ligands are in a meridional configuration as contrasted with the facial arrangement. The details of the crystal structure of mycobactin-P show the ferric ion to be exposed because of the strained octahedral coordination of five oxygens and one nitrogen. The dimensions offer some insight into the high stability of the ferric complex and also for the ease of release according to *Hough* and *Rogers* (*55*).

Mycobactin-P is a molecule of molecular weight 925.9 which readily forms a red-brown complex ion with iron (absorption maximum at 4450 Å) which is quite soluble in chloroform and somewhat less soluble in alcohol. It is insoluble in water. The ferrimycobactin is extremely stable with pK~30. Mössbauer experiments have been done (*37*) on the frozen alcohol solution and the data were fit using the spin Hamiltonian [Eq. (3)]. The best agreement with $\mu = 0$ was obtained with $D = 0.34$ cm^{-1}, $\lambda = E/D = 0.27$, $\Delta E = -0.76$ mm/sec, and $A = 221$ kOe unit spin.

However, subsequent ESR experiments (*29*) have shown a rather narrow resonance at $g = 4.3$ which is incompatible with $\lambda = 0.27$ and $\mu = 0$ (Fig. 15). A value of $\lambda = 0.33$ would be better suited for the narrow (isotropic) $g = 4.3$ resonance, but is in disagreement with the Mössbauer experiment. These contradictory experimental results were reconciled by the inclusion of the quartic term ($\mu \neq 0$) in the spin Hamiltonian. A new set of parameters was found to give agreement with both ESR and Mössbauer experiments. (They are listed in Table 4). The low symmetry of the spin Hamiltonian is consistant with the low symmetry molecular environment determined from the X-rays.
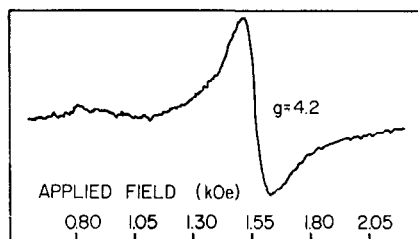
Fig. 15. ESR data at X-band for mycobactin-P showing the large unsplit resonance at $g = 4.2$

e) Enterobactin

Enterobactin (MW 669) is derived from certain enteric bacteria such as *Escherichia coli* and is classified as a siderochrome by *Neilands (1)* in which the iron is bound by three bidentate catechol groups instead of the hydroxamic acid ligands described above. There are three "charged" oxygens which bind the iron either in a facial or meridional configuration.

hydroxamic acid   catechol
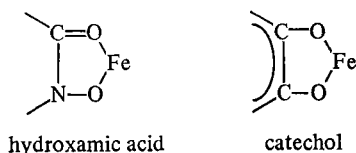
Fig. 16. Catechol and hydroxamate ligand binding to ferric iron

Enterobactin is described *(1)* as the prototype of the catechol siderochromes and is produced by enteric bacteria when placed in an iron-deficient medium. Enterobactin has a high affinity for iron pK >25 and is soluble in ethanol (or water). ESR experiments indicate *(56)* the characteristic $g = 4.3$ resonance found in the other high spin ferric compounds mentioned in this chapter which have been described by a "rhombic field" spin Hamiltonian and would indicate a meridional configuration. Proton and Carbon 13 NMR studies have been done by *Llinas, Wilson* and *Neilands (39)* which indicate the ferric ion to be in a propeller type of configuration leaving the iron on a 3-fold axis of the molecule. This would of course indicate the facial configuration in contrast to the "rhombic field" discription used to interpret the $g = 4.3$ ESR-signals.

Mössbauer effect experiments have been done on ^{57}Fe-enterobactin and show unusually well resolved paramagnetic hyperfine structure and the spectral features have been reproduced extremely well with a spin Hamiltonian with rhombic symmetry *(57)*. An attempt to fit the Mössbauer data with a trigonal spin Hamiltonian corresponding to the 3-fold propeller arrangement fails completely. Some of the spectra and the computer fits are shown in Fig. 9 and the parameters are listed in Table 4. In this figure, the temperature dependence is due to the population of the excited electronic states which then make a larger contribution to the composite spectrum at higher temperatures.

f) Transferrins

The transferrins are iron chelating agents found in the various fluids of vertebrates including humans (2). They are powerful iron chelators with binding constants for ferric iron of $pK \sim 30-31$. They have molecular weights up to about 80,000 and two iron binding sites per molecule. Other transition metals can occupy the two iron sites although iron will displace them.

The transferrins include serum transferrin found in blood serum, ovo transferrin or conalbumin found in egg whites and lacto transferrin found in the milk of mammals. Serum transferrin has the primary role of transporting iron throughout the system from the iron storage areas to the bone marrow for incorporation into hemoglobin in the immature red blood cells. It also appears to have the function of sweeping free iron ions out of the serum to prevent iron poisoning.

The functions of ovotransferrin and lacto transferrin are hypothesized to be the inhibition of bacterial growth in the egg white or milk respectively, perhaps by limiting the available iron necessary for bacterial growth.

A question of recent interest is whether the two iron sites in each molecule are equivalent (58), Mössbauer effect studies (28) and ESR studies (59) of human serum transferrin could detect no difference in the spectra of the two iron sites, but recently a very careful study by *Aasa* (27) has shown small differences in the ESR spectrum due to a small change in the ESR parameter λ. The Mössbauer data were shown to be in good agreement with a calculation by *Spartalian* and *Oosterhuis* (28) and more recently by *Tsang, Boyle* and *Morgan* (60). The spin Hamiltonian parameters for each experimental study are presented in Table 4.

The ESR experiment by *Aasa* (27) yields two sets of spin Hamiltonian parameters — one for each iron site. A Mössbauer spectrum calculated from each set of Aasa's parameters has been found to be no different from the calculation assuming identical sites. This indicates that the ESR experiment is much more sensitive to small effects than the Mössbauer technique.

The zero field data show the effects of neighboring nuclear magnetic moments (Fig. 14) which are represented by a random magnetic field of about 4 Oersted acting on the electronic moment of the iron. Aasa's experiments (27) on the transferrin of Hagfish show it to be quite different from that of human serum transferrin and distinctly shows the differences in the two iron sites. Conalbumin or ovotransferrin is similar to serum transferrin in that they both form pink complexes with ferric iron with absorption maximum at 465 mm and both bind iron tightly in two different sites. A recent Mössbauer study by *Aisen, Lang* and

Table 4. Spin hamiltonian parameters for some ^6S iron complexes

	Material	$D(\text{cm}^{-1})$	λ	μ	$A(\text{kOe}/\text{spin})^{[a]}$	$P(\text{mm/sec})$	Ref.
1)	Ferrichrome-A	0.53	0.51	−0.133	216	−0.50	(62)
		0.50	0.28	—	—	—	(47)
		∼1.0	0.25	—	220	−0.37	(18, 46)
		−0.27	0.25	—	—	—	(48)
2)	Deferoxamine	0.5	0.46	—	217	−0.30	(38)
3)	Enterobactin	0.48	0.46	−0.27	222	−0.15	(57)
4)	Mycobactin-P	0.34	0.27	—	221	−0.38	(37)
		0.22	0.45	−0.26	221	−0.20	(29)
5)	Human serum transferrin	1.7	0.31	—	—	—	(47)
		0.27	0.31	—	—	—	(59)
		0.15	0.31	—	{221 / 215 / 223}	+0.37	(28)
		0.12	{0.25 / 0.32 / 0.26}	—	215	0.09	(60)
		0.30		—	—	—	(27)
6)	Hagfish transferrin	0.30	0.315	—	—	—	(60)
7)	Conalbumin	1.0	0.31	—	—	—	(27)
		0.3	{0.31 / 0.22}	—	—	—	(47)
							(27)
8)	Ferric benzohydroxamate	0.50	0.31	−0.35	225	−0.30	(30)
9)	Rubredoxin	1.51	0.28	—	—	—	(43)

	Compound						Ref.
10)	Coprogen	0.47	0.32	—	—	—	(47)
11)	Ferricrocin	0.46	0.31	—	—	—	(47)
12)	Ferrichrysin	0.42	0.267	—	—	—	(47)
13)	Ferrirubin	0.44	0.30	—	—	—	(47)
14)	GaEDTA:Fe	0.8	0.267	—	220	0.15	(33)
	FeEDTA glycerol	0.7	0.327	—	219	0.26	(33)
15)	Protocatechualdehyde-PCA-4,5-oxygenase	0.7	0.33	—	220	0.33	(42)
Heme complexes							
16)	Met myoglobin	10.0	~ 0	—	198	0.65	(44,63,64)
17)	Myoglobin flouride	6.3	~ 0	—	210	0.40	(64)
18)	Hemoglobin flouride	7.0	~ 0	—	212	0.30	(65)
19)	Cytochrome-c peroxidase	15.0	~ 0	—	196	0.60	(34)
20)	Cytochrome-c peroxidase flouride	7.3	~ 0	—	206	0.425	(34)
21)	Hemin	7.0	~ 0	—	192	0.40	(63)
Inorganic Fe^{3+}							
22)	$LiAl_5O_8:Fe^{3+}$	— 0.104	0	~ 0.1	206	0.33	(9)
23)	$Al_2O_3:Fe^{3+}$	0.172	0	0.133	219	0.25	(10)
24)	$Alum:Fe^{3+}$	0.024	0	0.535	228	0.055	(66)

a) The magnetic hyperfine coupling constant A is given in units of kilo Oersted per *unit* spin. Thus the nucleus which senses a total hyperfine field of 550 kOe due to five unpaired electrons would have A listed as 220 (kOe/unit spin).

Woodworth (*61*) has shown that differences in the two iron sites are detectable in this molecule but the data are not fit as yet. Other ESR studies of conalbumin (*45*) show the $g = 4.3$ resonance. No ESR or Mössbauer studies of lacto transferrin have been reported yet.

Each of the other iron binding agents discussed above have either catechol or hydroxamic acid residues. No hydroxamic acid residues are found in transferrin although there are most certainly some nitrogens as well as oxygens gripping the iron which also binds a bicarbonate ligand.

g) Discussion

Each of the natural iron binding compounds above has a very strong affinity for ferric iron, but relatively weak attraction for ferrous iron. Since these molecules most certainly give up the iron at some point in the biological cycle, the importance of binding is of crucial interest here.

The mechanism by which these compounds give up the ferric ion is not yet understood nor is it understood whether or how the iron gains entrance through a cell wall or in what chemical state the iron is as it passes through the cell wall. One interesting application would be to study the mechanism by which iron enters the immature red blood cell for incorporation into hemoglobin. If the electronic states of the initial (transferrin) and final products (hemoglobin) are known then it may be possible to observe other chemical states or to deduce the mechanisms by which the iron enters the cell.

There are many other iron complexes of a similar nature yet to be investigated including many model complexes such as cupferron and ferric acetyl acetonate as well as the hydroxamates and the catechols.

We see in Table 4 the similarities of the spin Hamiltonian components among the classes of the iron proteins and transport compounds and the differences between the classes. Each of the natural iron binding compounds (1–15 in Table 4) has λ with values ranging from 0.25 to 0.51 and in those cases where a non-zero μ was considered in the analysis we find μ in the range from —0.13 to —0.35. Although each of these iron complexes has a strong, nearly isotropic ESR resonance at $g = 4.3$ it would appear to be too much of a coincidence for each complex to have the same ligand field symmetry as given by λ. The consideration of the fourth order terms in the spin Hamiltonian allows a wider variety of ligand fields and still allows the isotropic $g = 4.3$ signal.

It is also noteworthy that the spin Hamiltonian (and therefore the electronic wave functions) have rhombic symmetry although in several cases there have been other experiments which indicate trigonal symmetry in the local environment for the iron atom.

The heme complexes show axial symmetry in the spin Hamiltonian as expected and D is an order of magnitude larger than in the iron transport compounds. The hyperfine fields are considerably larger in the iron transport compounds compared to nearly all other high spin ferric complexes. This indicates a high degree of localization on the iron of the magnetic valence electrons. The quadrupole splittings are of the same magnitude as other high spin ferric complexes but have the extreme rhombic symmetry in the electric field gradient.

The study of the natural iron-binding compounds has brought forth several new and interesting aspects concerning the electronic states of the ferric ion and has stimulated some new thinking with regard to the ligand fields acting on the metal ion.

It is also interesting to speculate about the feed back system in which the low iron stress causes an organism to produce much larger than normal quantities of a siderochrome. This question and the question of how a siderochrome binds to or passes through a cellular membrane are undoubtedly related to the molecular conformation which can be studied via the electronic states using Mössbauer and ESR Spectroscopy.

VIII. References

1. *Neilands, J. B.:* Struct. Bonding *1*, 59 (1966); *11*, 145 (1972).
2. *Feeney, R. E., Komatsu, K.:* Struct. Bonding *1*, 149 (1966).
3. *DeBrunner, P.:* In: Spectroscopic approaches to biomolecular conformation, ed. by *Urry, D. W.* American Medical Association Press 1969.
4. *Weissbluth, M.:* Struct. Bonding *2*, 1 (1967).
5. *Bearden, A. J., Dunham, W. R.:* Struct. Bonding *8*, 1 (1970).
6. *Lang, G.:* Quart. Rev. Biophys. *3*, 1 (1970).
7. *Kalvius, G. M., Kankeleit, E.:* In: Mössbauer spectroscopy and its applications, p. 9, IAEA, Vienna, 1972.
8. *Oosterhuis, W. T.:* Phys. Rev. *B 3*, 546 (1971).
9. *Viccaro, P. J., de S. Barros, F., Oosterhuis, W. T.:* Phys. Rev. *B 5*, 4257 (1972).
10. *Wickman, H. H., Wertheim, G. K.:* Phys. Rev. *148*, 211 (1968).
11. *Oosterhuis, W. T., Lang, G.:* J. Chem. Phys. *50*, 1381 (1969).
12. *Paez, E. A., Weaver, D. L., Oosterhuis, W. T.:* J. Chem. Phys. *57*, 3709 (1972).
13. *Oosterhuis, W. T., Weaver, D. L., Paez, E. A.:* J. Chem. Phys. *60*, 1018 (1974).
14. *Oosterhuis, W. T., de S. Barros, F.:* J. Chem. Phys. *57*, 4304 (1972).

15. *Oosterhuis, W. T., Lang, G.:* Phys. Rev. *178*, 439 (1969).
16. *Lang, G., Oosterhuis, W. T.:* J. Chem. Phys. *51*, 3608 (1969). — *Oosterhuis, W. T.:* In: Mössbauer effect methodology, Vol. 7, p. 97, ed. by *Gruvermon. I. J.* New York: Plenum 1971.
17. *Van Vleck, J. H.:* In: Electric and magnetic susceptibilities, p. 273. Oxford Press 1932.
18. *Wickman, H. H., Klein, M. P., Shirley, D.:* Phys. Rev. *152*, 345 (1966).
19. *Johnson, C. E.:* Phys. Letters *21*, 491 (1966).
20. *Afanasev, A. M., Kagan, Yu. M.:* Sov. Phys. JETP Letters *8*, 382 (1968).
21. *Poole, C. P., Farach, H. A.:* Theory of magnetic resonance. New York: Wiley 1972.
22. Magnetic resonance in biological systems, ed. by *Ehrenberg, A., Malström, B. G.* and *Vänngård, T.* Oxford: Pergamon Press 1967.
23. *Slichter, C. P.:* Principles of magnetic resonance. Harper and Row 1963.
24. *Pake, G. E.:* Paramagnetic resonance. Benjamin Pub. 1962.
25. *Carrington, A. S., McLachlan, A. D.:* Introduction to magnetic resonance. Harper and Row 1967.
26. *Abragam, A., Bleaney, B.:* Electron paramagnetic resonance of transition metal ions. London: Oxford University Press 1970.
27. *Aasa, R.:* Biochem. Biophys. Res. Commun. *49*, 806 (1972).
28. *Spartalian, K., Oosterhuis, W. T.:* J. Chem. Phys. *59*, 617 (1973).
29. *VanderVen, N. S., Spartalian, K., Oosterhuis, W. T., Ashkin, J.:* Bull. Am. Phys. Soc. *19*, 373 (1974); ibid. *19*, 373 (1974).
30. *Spartalian, K.:* Ph. D. Thesis, Carnegie-Mellon University (1973) (unpublished).
31. *Sharma, R. R., Das, T. P., Orbach, R.:* Phys. Rev. *149*, 257 (1966) and references therein.
32. *Watanabe, H.:* Progr. Theoret. Phys. (Kyoto) *18*, 405 (1957).
33. *Lang, G., Aasa, R., Garbett, K., Williams, R. J. P.:* J. Chem. Phys. *55*, 4539 (1971).
34. *Lang, G., Asakura, T., Yonetani, T.:* J. Phys. C (Solid State Phys.) *2*, 2246 (1969).
35. *Kotani, M., Morimoto, H.:* In: Magnetic resonance in biological systems, p. 135, ed. by *Ehrenberg, A., Malmström, B. G., Vänngård, T.* Oxford: Pergamon Press 1967.
36. *Blumberg, W.:* In: Magnetic resonance in biological systems, p. 119, ed. by *Ehrenberg, A., Malmström, B. G.,* and *Vänngård, T.* Oxford: Pergamon Press 1967.
37. *Spartalian, K., Oosterhuis, W., Window, B.:* Mössbauer effect methodology, Vol. 8, p. 137, edited by *I. J. Gruverman.* New York: Plenum Press 1973.
38. *Bock, J. L., Lang, G.:* Biochem. Biophys. Acta *264*, 245 (1972).
39. *Llinas, M., Wilson, P. M., Neilands, J. B.:* Biochemistry *12*, 3836 (1973).
40. *Zalkin, A., Forrester, J. D., Templeton, D. H.:* J. Am. Chem. Soc. *88*, 1810 (1966).
41. *Lindner, H. J., Gottlicher, S.:* Acta Cryst. B *25*, 832 (1969).
42. *Zabinski, R., Munck, E., Champion, P., Wood, J. M.:* Biochemistry *11*, 3212 (1972).
43. *Peisach, J., Blumberg, W. E., Lode, E. T., Coon, M. J.:* J. Biol. Chem. *19*, 5877 (1971).
44. *Oosterhuis, W. T., Viccaro, P. J.:* Biochim. Biophys. Acta *264*, 11 (1972).
45. *Lang, G.:* Phys. Letters *26A*, 223 (1968).
46. *Wickman, H. H., Klein, M. P., Shirley, D. A.:* J. Chem. Phys. *42*, 2113 (1965).
47. *Dowsing, R. D., Gibson, J. F.:* J. Chem. Phys. *50*, 294 (1969).
48. *Brackett, G. C., Richards, P. L., Caughey, W. S.:* J. Chem. Phys. *54*, 4383 (1971).

49. *Anderegg, G., L'Eplattenier, F., Schwarzenbach, G.:* Helv. Chim. Acta *46*, 1409 (1963).
50. *Neilands, J. B.:* Science *156*, 3781 (1967).
51. *Epstein, L. M., Straub, D. K.:* Inorg. Chem. *8*, 453 (1969).
52. *Griffiths, J. S.:* Mol. Phys. *8*, 217 (1964); ibid. *8*, 213 (1964).
53. *Snow, G. A.:* Bacteriol. Rev. *1970*, 99.
54. *Ratledge, C., Marshall, B. J.:* Biochim. Biophys. Acta *279*, 58 (1972).
55. *Hough, E., Rogers, D.:* Biochim. Biophys. Res. Commun. *57*, 73 (1974).
56. *O'Brien, I. G., Cox, G. B., Gibson, F.:* Biochim. Biophys. Acta *237*, 537 (1971).
57. *Oosterhuis, W. T., Spartalian, K.:* Bull. Am. Phys. Soc. *19*, 101 (1974).
58. *Aisen, P., Aasa, R., Redfield, A. G.:* J. Biol. Chem. *244*, 4628 (1969).
59. *Aasa, R.:* J. Chem. Phys. *52*, 3919 (1969).
60. *Tsang, C. P., Boyle, A. J. F., Morgan, E. H.:* Biochim. Biophys. Acta *328*, 84 (1973).
61. *Aisen, P., Lang, G., Woodworth, R.:* J. Biol. Chem. *248*, 649 (1973).
62. *Lang, G., Spartalian, K.:* (private communication).
63. *Lang, G., Asakura, T., Yonetani, T.:* Phys. Rev. Letters *24*, 981 (1970).
64. *Lang, G., Asakura, T., Yonetani, T.:* Biochim. Biophys. Acta *214*, 381 (1970).
65. *Lang, G., Marshall, W.:* J. Mol. Biol. *18*, 385 (1966).
66. *Campbell, L. E., De Benedetti, S.:* Phys. Rev. *167*, 556 (1968).

Mössbauer Spectroscopy on Heme Proteins*

Alfred Trautwein

Fachbereich Angewandte Physik, Universität des Saarlandes, 66 Saarbrücken, Germany

Table of Contents

I. Introduction

The general versatility of the Mössbauer technique in biology was described in detail by *Debrunner* (1) and *Lang* (2). Of the elements which are important in biology only a limited number is applicable as Mössbauer isotopes. These are K^{40}, Fe^{57}, Zn^{67}, I^{127}, and I^{129}. The spectroscopic difficulties with K^{40} and specifically with Zn^{67}, however, restrict the Mössbauer technique to the investigation of biological compounds containing only either iron or iodine. Despite this limitation, the first applications of Mössbauer spectroscopy to be used in biophysics by *Gonser et al.* (3) (1963, 1965) *Karger* (4) (1963), and *Lang et al.* (5) (1966) released an avalanche of work dealing with "Mössbauer Spectroscopy of Biological Materials". All relevant publications have been collected in an index under this title by *May* (6).

The purpose of the present work is to describe the applicability of the Mössbauer effect to heme compounds, particularly with regard to more recent work in this field. Two earlier contributions to this series (Structure and Bonding) partly dealt with the same subject: *M. Weissbluth* (7) in Vol. 2 (1967) with "The Physics of Hemoglobin", and *A. J. Bearden* and *W. R. Dunham* (8) in Vol. 8 (1970) with "Iron Electronic Configurations in Proteins: Studies by Mössbauer Spectroscopy". After a short description of the effect and the experimental set-up (Section II), the study of iron heme compounds is considered (Sections III–VIII). Sections IV–VII represent an attempt to investigate the heme geometry of deoxy- (Mb, Hb), oxy- (MbO$_2$, HbO$_2$), and carbomonoxy-(MbCO, HbCO) myoglobin or hemoglobin by comparing experimental and theoretical Mössbauer data. From the work of *Parak et al.*, which is described in Section VIII, we may learn about the difficulties and expectations concerning γ-ray scattering experiments with myoglobin single crystals.

For completeness the reader should refer to two review articles, by *Lang* (9) and *Münck* (10), which are in preparation. Both articles deal mainly with the interpretation of magnetically hyperfine split Mössbauer spectra of ferric heme proteins and other biological molecules.

Also in the present volume of "Structure and Bonding", *W. T. Oosterhuis* contributes to an understanding with his article on "The Electronic State of Iron in Some Natural Iron Transport Compounds; Determination of Mössbauer and ESR Spectroscopy".

II. Mössbauer Effect

1. Recoilless Emission and Absorption

Since *Mössbauer's* first publication (11) on "recoilless emission or absorption of γ-rays" several extensive articles and books (12–24) have

been published on the Mössbauer effect. The application of the effect has been discussed (*25–31*) at several international conferences. A very illustrative description of the method was given by *Frauenfelder* (*32*) during the symposium "Mössbauer Spectroscopy in Biological Systems" at Urbana, Illinois (USA), in March 1969, which is essentially given here:

"Consider a cannon fixed rigidly to the earth, and a target at a distance E_0. If we trace a large number of shots and measure their distances E, we find that not all have flown the same distance; there exists a straggling as sketched in Fig. 1a. We characterize the distribution by the full
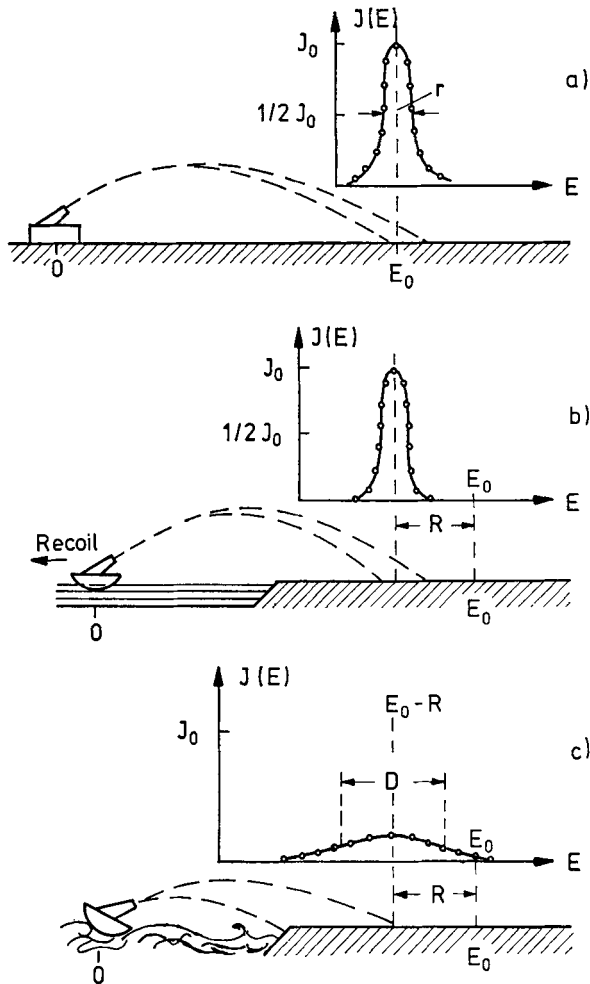
Fig. 1. Model for explaining the Mössbauer effect. [Taken from Ref. (*32*)]

width at half-height and we call this quantity, Γ, the "natural line width". $J(E)$ is the number of projectiles observed at the distance E. Next, we mount our cannon on a small boat and try to hit the same target again. We expect the same natural line width and indeed it appears. However, the small boat recoils in order to conserve momentum and the shots fall short (Fig. 1 b). The distance they fall short, R, can be calculated from energy and momentum conservation. Actually, the situation is usually not nearly as clean. Unless the lake is quiet, the distance distribution will be much wider than shown above. In a storm, the boat will pitch and roll, and the distribution will experience an additional broadening, which we call the "Doppler broadening" (Fig. 1c). Shots fired from a cannon mounted on a small boat in a rough sea experience both a recoil (R) and a Doppler broadening (D). Is there a way to avoid the recoil R and the Doppler broadening D? Rudolf Mössbauer found the answer in a somewhat different context: If we wait till the lake is frozen, Doppler broadening and recoil will disappear!"

With the simple picture described so far, part of the Mössbauer effect can be understood in a straightforward way:

A nucleus in an excited state corresponds to the cannon and the nuclear γ-decay to its firing. Excited nuclei of atoms can emit during their decay from their excited state to their ground state. The γ-radiation has a specific energy, E_γ, and a certain energy spread (line width), Γ, which is determined by the mean lifetime τ of the excited nuclear state through the Heisenberg relation $\Gamma \cdot \tau \approx \hbar$. For the most commonly used Mössbauer isotope, Fe^{57}, E_γ and Γ are 14.4 keV and $4.6 \cdot 10^{-9}$ eV, respectively. During the emission process a recoil energy $E_R = E_\gamma^2/2\, Mc^2$ ($M =$ mass of the emitting nucleus, $c =$ velocity of light, $E_R = 2 \cdot 10^{-3}$ eV for Fe^{57}) is transferred to the nucleus, thus decreasing the energy of the emitted γ-quantum by the same amount E_R because of energy conservation. During the absorption process the γ-quantum "knocks" at the absorbing nucleus and again loses the same amount of energy. The resulting total energy loss of the γ-quantum during the emission–absorption process is therefore $2\, E_R$, and since $2\, E_R = 4 \cdot 10^{-3}$ eV is considerably larger than $\Gamma = 4.6 \cdot 10^{-9}$ eV, resonance absorption is impossible, provided that source and absorber have a velocity of $v \approx 0$ with respect to each other.

The basis for an observation of the nuclear γ-resonance emission and absorption (Mössbauer effect) is the fact that for nuclei of atoms bound tightly in a solid, the recoil energy can be taken up by the crystal as a whole under favorable conditions ("cannon frozen in the lake" analogy). For this purpose the atomic force constants of the emitting or absorbing atom bound in the solid must be strong enough (*i.e.* a high Debye temperature θ_D is required); and, furthermore, the temperature of the

solid must be low enough to prevent excitation of lattice vibrations. Then a fraction f of γ-quanta does not experience recoil energy losses. The quantity f is called the Debye-Waller factor (*33*) or the recoilless free fraction (see Table 1, first column).

Because of the narrow energy line width of the Fe^{57} γ-radiation small relative displacements between source and absorber nuclear levels can be measured by the Mössbauer effect. The position of the nuclear energy levels is, influenced by electrostatic and magnetic interactions between the atomic electron shell and the Mössbauer nucleus. Three different types of interaction are of interest and will be described briefly.

2. Isomer Shift

The Coulomb interaction between the nuclear charge distribution and electronic charges, which penetrate into the nucleus, is proportional to the amount of electron density, $\varrho(o)$, within the nuclear volume. This electrostatic interaction alters the energy separation between nuclear ground state and excited state. Since $\varrho(o)$ is influenced by the chemical surrounding of the atom under study, one expects different nuclear level shifts for the same Mössbauer atom in different compounds. For example, for a metallic source of radioactive Co^{57} in Rhodium and an absorber of ferrous high-spin Fe^{57} in deoxygenated myoglobin, the different transition energies E_S and E_A (Table 1) give rise to a net isomer shift of $\delta = E_A - E_S$, of the order $+0.8$ mm/sec.

3. Electric Quadrupole Splitting

The interaction of the nuclear quadrupole moment Q with the local electric field gradient (EFG) at the nuclear site causes a splitting of the nuclear energy levels. Table 1c illustrates the situation for an Fe^{57} absorber atom embedded in a crystal with lower than cubic point symmetry for the iron lattice site. Since the nuclear ground state of Fe^{57} has zero quadrupole moment it remains unsplit. The excited state of Fe^{57}, characterized by $Q > 0$, however, splits into two sublevels.

4. Magnetic Hyperfine Splitting

If a nucleus possesses magnetic dipole moments in its ground-excited states it can interact in both states with magnetic fields. The effective magnetic fields at the nuclear site, H_{eff}, may be produced either by applied external fields, H_0, or by intrinsic fields, H_{int}, due to contributions of the electron shell. Under the action of H_{eff} the ground state of the Fe^{57} nucleus splits into two, and the excited state into four sublevels (Zeeman splitting). According to selection rules for magnetic dipole

radiation six transitions are usually possible then from the ground state to the excited state in an Fe^{57} absorber nucleus, as indicated in Table 1d. (A more general situation, where we may expect eight transitions, is described in IV. 2.1 and Fig. 11).

5. Apparatus

A Mössbauer experiment is performed in practice (Fig. 2a) by mounting the radioactive source S on a velocity drive L. By applying well-known velocities v to the source one can modulate the energy of the emitted
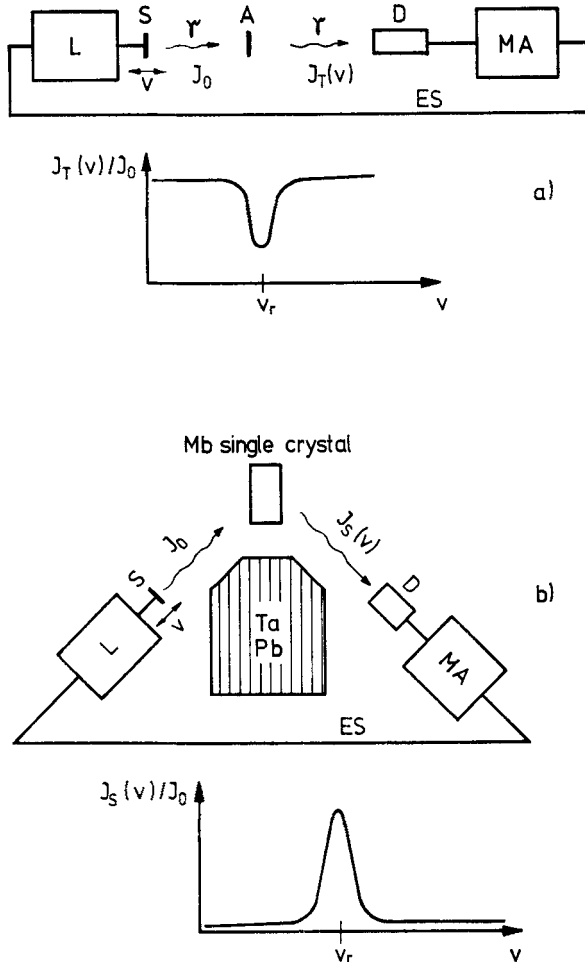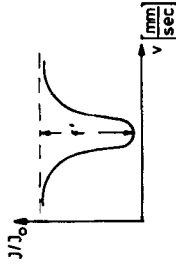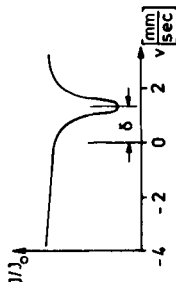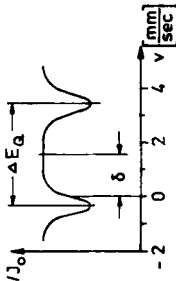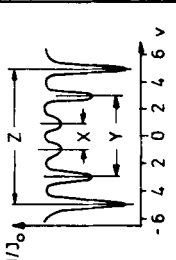
Fig. 2. Apparatus (a) Mössbauer transmission experiment, (b) Mössbauer scattering experiment

Table 1. Mössbauer parameters (a)

Mossbauer parameter	recoilless free fraction f [b]	isomer shift [c]	quadrupole splitting [d]	magn. hyperfine splitting [e]
nuclear property	transition energy E_γ	nuclear charge distribution	nuclear quadrupole moment	magn. dipole moment
atomic property	Debye temperature θ_D	change in electron charge density $\rho(0)$	electric field gradient components V_{ZZ} and η	magn. hyperfine field $\vec{H}_{eff} = \vec{H}_{int} + \vec{H}_0$
interaction energies	$f = \exp\left[-\dfrac{E_\gamma}{2Mc^2\theta_D}\left(\dfrac{3}{2} + \dfrac{\pi^2 T^2}{\theta_D^2}\right)\right]$ with $T \ll \theta_D$	$\delta = E_A - E_S = \alpha \cdot \Delta\rho(0)$	$\Delta E_Q = \frac{1}{2}e\,QV_{ZZ}\left(1 + \dfrac{\eta^2}{3}\right)^{1/2}$	$E_M = -g_N \cdot \mu_N \cdot \vec{H}_{eff} \cdot \vec{J}$
energy diagram of nuclear levels		excit. state E_A, E_S, ground state; source, absorber	$J_z = \pm 3/2$, $J_z = \pm 1/2$; $V_{ZZ} > 0$, $V_{ZZ} < 0$; source, absorber	$J_z = +3/2, +1/2, -1/2, -3/2; -1/2, +1/2$; source, absorber
typical Mössbauer absorption spectra [f] of iron compounds	the measured quantity f' is the product of f-factors from source and absorber $f = f_S \cdot f_A$	J/J_0; source: Co57 in Rh, absorber: KFeF3, $\delta = +1.2$ mm/sec	J/J_0; ΔE_Q, δ; source: Co57 in SS 310, absorber: FeSO4·7H2O; 78 K, $\delta = +1.4$ mm/sec, $\Delta E_Q = 3.4$ mm/sec; $\eta = 0$	J/J_0; Z, X, Y; source: Co57 in SS 310, absorber: Fe in α-Fe; 300 K, $\delta = -0.09$ mm/sec; $H_{eff}(0) = 330$ kOe; $\eta = 0$, X=1.677, Y=6.167, Z=10.657 mm/sec

(a) Numerical values are taken from *Stevens, J. G.,* and *Stevens, V. E.:* Mössbauer Effect Data Index, 1969–72. London: Adam Hilger.

(b) M = mass of emitting or absorbing nucleus; c = velocity of light.

(c) For Fe^{57} α takes the value $\alpha = -0.225 \pm 0.025$ a_0^3 mm/sec^{-1} [Ref. (83, 84)].

(d) For Fe^{57} the nuclear quadrupole moment Q takes the value $+0.21b$ [Ref. (76, 77, 79, 90)]. Tha asymmetry parameter η is defined by

$$\eta = \frac{|V_{xx} - V_{yy}|}{|V_{zz}|}, \text{ with } |V_{zz}| \geqslant |V_{yy}| \geqslant |V_{xx}|.$$

e = elementary charge (positive!). I_z = magnetic component of nuclear spin I.

(e) For Fe^{57} g_N (ground state) takes the value $g_N = 0.1805$, g_N (excited state) the value $g_N = -0.103$, and μ_N the nuclear magneton, the value $\mu_N = 3.15 \ 10^{-12}$ eV/Oe.

The ratio I/I_0 represents the relative intensity being transmitted through the absorber (see II.5 and Fig. 2a).

(f) All absorption lines at resonance velocities v_r have Lorentzian line shape

$$J(v) = \frac{J_0 \Gamma}{2\pi} \frac{1}{(v - v_r)^2 + (\Gamma/2)^2},$$

provided that source and absorber are thin, *i.e.* the effective thickness of both is $T = fma\sigma_0 t < 1$. The total line width Γ is the sum of source and absorber contributions, given by $\Gamma = \Gamma_S + \Gamma_A$. f is the Debye-Waller factor either of source or absorber, m is the number of atoms/cc, a the fractional abundance of Fe^{57}, σ_0 the resonance absorption cross-section, and t the source or absorber thickness.

radiation through the Doppler effect. The velocities are defined as positive if the source approaches the absorber. In a Mössbauer transmission experiment (Fig. 2a) the γ-beam with intensity J_0 passes through an absorber. The transmitted intensity $J_T(v)$ is counted as a function of the source velocity v by a detector D and is stored in the memory of a multichannel analyser MA. The velocity of S and the channel number of MA are adjusted to each other by electronic synchronization ES. Single γ-line sources are usually used to simplify the absorption spectra. Resonance absorption of γ-rays occurs for specific velocities v_r, namely under the resonance condition $E_S \left(1 + \frac{v_r}{c}\right) = E_A$. The decrease of the transmitted γ-intensity $J_T(v)$ by approaching resonance velocities v_r is described by $J_T(v) = J_0 - J_0 \frac{\Gamma}{2\pi} \left[(v - v_r)^2 + \left(\frac{\Gamma}{2}\right)^2\right]^{-1}$ and shown in Fig. 2a.

Mössbauer scattering experiments (Fig. 2b) are characterized by scattered γ-intensities $J_S(v) = J_0 \frac{\Gamma}{2\pi} \left[(v - v_r)^2 + \left(\frac{\Gamma}{2}\right)^2\right]^{-1}$. In this case the resonantly absorbed γ-quanta are reemitted isotropically. These reemitted ("scattered") γs are then counted by the detector D which is shielded from direct irradiation of the source S by tantal (Ta) or lead (Pb) screening. In Section VIII, however, where a short review is given on the Mössbauer scattering technique for the solution of the phase problem for protein-structure determination, we shall be concerned with γ-waves rather than with γ-quanta, since interference phenomena of radiation are adequately described in the wave picture.

More detailed descriptions of Mössbauer equipment may be found in the literature (*18, 34, 35*).

III. Experimental Considerations

From Section II we know that the key point of the Mössbauer effect is the recoilless emission and absorption of γ-rays. This has the important consequence that the Mössbauer nuclei must be bound in a solid system, or equivalently, that the myoglobin or hemoglobin samples cannot be studied in aqueous solution. They have to be frozen, crystallized, lyophilized or, at least, they have to be embedded in a material with high viscosity. Because of these unphysiological conditions under which biological compounds are investigated one may doubt the reliability of experimental Mössbauer results with respect to the real physiological state of a molecule. This same problem arises in other experiments: susceptibility, ESR, X-ray diffraction, X-ray, and neutron small-angle scattering. There, however, one can argue: (a) that the protein structure

of hemoglobin in aqueous solution as inferred by X-ray and neutron small-angle scattering (36—38) is in agreement with the atomic coordinates determined by X-ray diffraction analysis from hemoglobin single crystals (39, 40), and (b) that the electronic structure of the heme iron is not detectably changed by going from liquid to solid state as exemplified by susceptibility measurements (41). Thus, we may assume that the molecular or electronic structure under certain circumstances undergoes only undetectably small changes upon freezing or crystallizing the sample. As further confirmation for the validity of this assumption we found the quadrupole splittings of an Mb single crystal at 77 °K and of a frozen Mb solution at 77 °K (from which the single crystal was originally grown at around 300 °K) to be equal within the error limit (42). In order to conserve the "native" state of the sample it is very important, however, to freeze the Mb or Hb solution as fast as possible. Slow freezing will allow the growth of relatively large crystals of ice, changing the concentration and pH-value of the solution. Fast freezing probably prevents these changes which have been found to affect the Mössbauer spectra significantly (43—45).

After cooling the sample to the temperature of liquid N_2 we sometimes found it very important not to raise the temperature of the sample above about 200 °K for a long time. After keeping an *in vitro* Fe^{57} enriched Mb sample for about 20 h at 220 °K we found a significant amount of heme iron irreversibly transformed to a different electronic structure, indicated by different Mössbauer spectra (Fig. 3). Similar changes have been observed by *G. Lang* with Hb (46). This strange behavior of a frozen myoglobin or hemoglobin sample at relatively low temperatures may correspond to the anomalies which have been observed
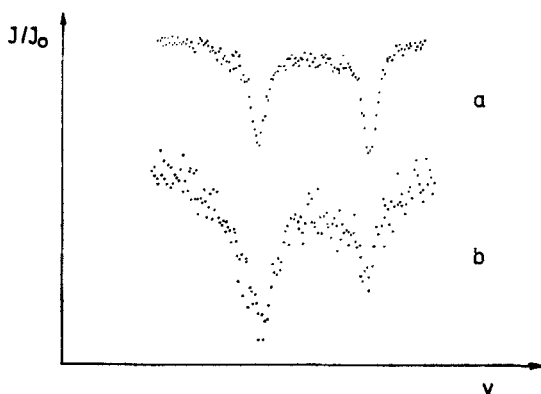
Fig. 3. Mössbauer spectra of frozen Mb solution: (a) at 77 °K, (b) at 220 °K after keeping the sample for about 20 h at this temperature

with high-spin ferrous and ferric ions in ice (47): at 183 °K the Möss-
bauer lines vanish, that means the f-factor which is a measure for the
recoilless absorption of γ-rays becomes zero, indicating rapid molecular
motion in the sample; increase in the temperature causes the ice to
recrystallize and the Mössbauer absorption lines reappear. Similar
effects have been found in frozen solutions of iron compounds at about
190 °K (45) (Fig. 4). Further systematic studies are necessary to elucidate
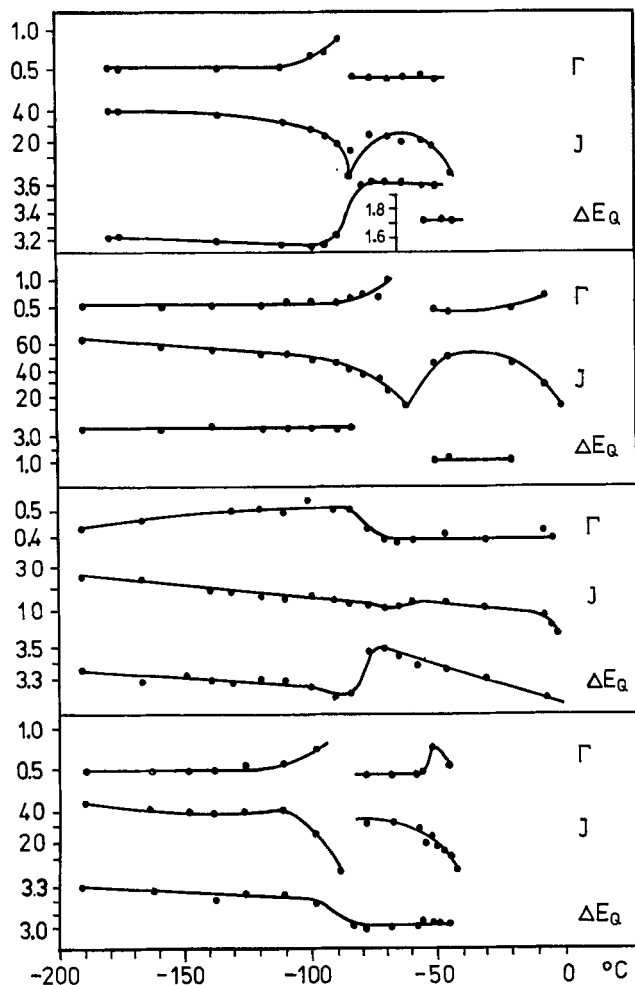
Fig. 4. Temperature dependence of Mössbauer parametrs ofe frozen solution of
(a) Fe Cl$_2$, (b) Fe (NH$_4$)$_2$ (SO$_4$)$_2$, (c) FeSO$_4$, and (d) Fe (ClO$_4$)$_2$ Γ: line width.
J: intensity of the absorption lines. ΔE_Q: quadrupole splitting. [Taken from Ref.
(54)]

whether the phase transition of ice or the melting of glass phases can affect the bio-molecule and generate denatured protein chains which can then be detected by Mössbauer spectroscopy through the change of electronic state of the heme iron. Due to this problem it might be wise to limit the study of temperature-dependent Mössbauer parameters of biological samples to a temperature of $T \lesssim 200\ °\mathrm{K}$.

Upon lyophilization the conformation of a protein can change too. From Mössbauer investigations of Hb (human) (*41, 48*) and Mb (horse heart) (*48*) in frozen solution and in dehydrated from it is known that the high-spin ferrous state in Hb is converted to an equal mixture of ferrous high-spin and low-spin iron in anhydrous Hb, whereas Mb and anhydrous Mb both contain ferrous high-spin iron only (Fig. 5).
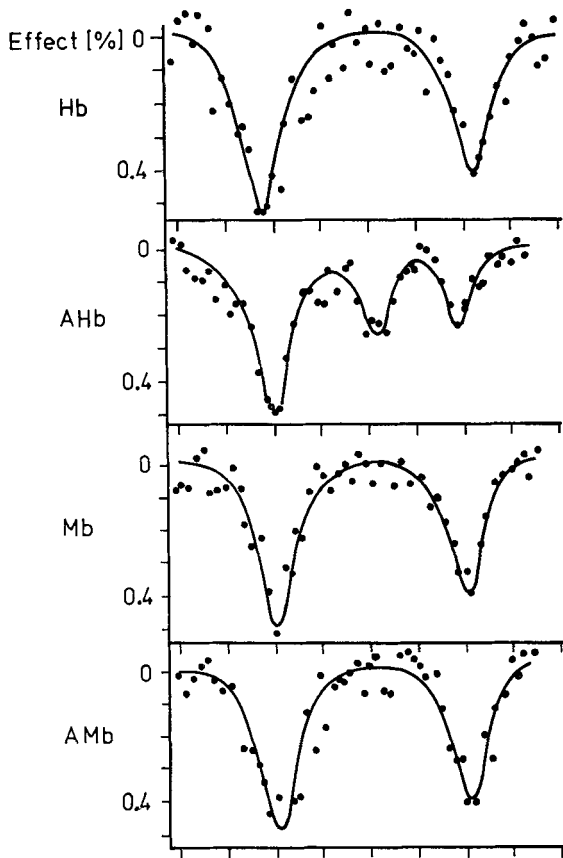
Fig. 5. Quadrupole splittings of Hb (human) at 80 °K, of AHb (human) at 80 °K, of Mb (horse) at 83 °K, and of AMb (horse) at 83 °K. [Taken from Ref. (*48*)]

Further experimental problems upon Mössbauer inspection of heme proteins can arise because of the relatively low abundance of Fe^{57} within natural iron (2.2%). We therefore give an estimate of the amount of biological material which is necessary to produce a feasible effect in a reasonable amount of time. The resonance cross-section σ_0 for Fe^{57} is $2 \cdot 10^{-18}$ cm². We divide this value by a factor of 8 (a factor of 2 comes from the finite line-width of the spectrum which is at least double the natural line-width; a second factor of 2 because we assume the spectrum to consist of two absorption lines; and another factor of 2 because we assume the product of recoilless emission (f_S)- and recoilless absorption (f_A)-probability to be 0.5). Due to this factor of 8 and the limited abundance of only 2.2% of Fe^{57} we derive an effective resonance cross-section of $\sigma_{eff} \approx 0.5 \cdot 10^{-20}$ cm². In order to measure an absorption effect of 2.5% we therefore need about 10^{17} Fe^{57} atoms per cm², which is equivalent to $5 \cdot 10^{18}$ iron atoms per cm² (now including all isotopes or iron). Using a solution with a 10% concentration of hemoglobin (0.1 g Hb/cm³) from which a sample, 0.5 cm thick, was prepared (containing H_2O and Hb) the total amount of 0.05 g Hb/cm² in the absorber, corresponded to about $5 \cdot 10^{17}$ Hb molecules per cm² or $2 \cdot 10^{18}$ iron atoms per cm². Comparing this value with the foregoing values we find that a hemoglobin absorber with an effective thickness of 0.5 g/cm², with a concentration of 0.1 g Hb/cm³, and with a natural abundance of 2.2% Fe^{57} produces an effect of roughly 1%. Since we are limited by the absolute thickness of an absorber due to strong mass absorption of the 14.4 keV Fe^{57} Mössbauer line (about 60% of the 14.4 keV γ-beam passing through 0.5 g/cm² of hemoglobin or myoglobin solution is absorbed), and because it is desirable sometimes to work with less concentrated material and within a reasonable time limit for the measurement, it is necessary to enrich the sample with Fe^{57}. With *in vitro* enrichment artificial abundances up to 90% of Fe^{57} may be obtained, (49) whereas with *in vivo* enrichment artificial abundances may be up to about 30% (44).

Assuming that our absorber contains enough Fe^{57} to produce an effect of 2.5% we can estimate the time of measurement if we know the counting rate N' per sec of the 14.4 keV γ-radiation (which depends on the activity of the source and on the geometry of the experimental set-up), and if we limit the accuracy of the measured effect to 5%. Under this condition we need N counts in each of the 400 channels of the multichannel analyzer and from Fig. 6 we see that the total error of the measured effect is given by $2 \sqrt{N}/0.025 \, N = 0.05$, leading to $N = 2.5 \cdot 10^6$ counts per channel. With a source activity of 100 mCi, a source detector distance of about 12 cm, a detector window of 2.54 cm diameter, and an absorber with effective thickness of about 0.5 g/cm²
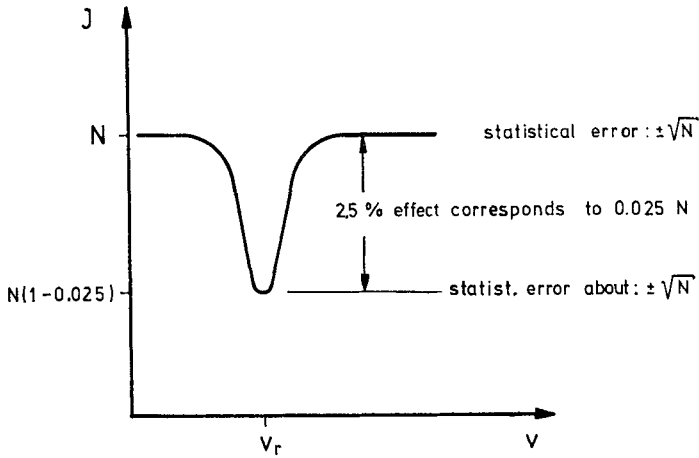
Fig. 6. Typical single line absorption spectrum

of Hb solution a counting rate $N' \approx 5 \cdot 10^5$ of 14.4 keV γ-particles per sec was measured. In order to collect 10^9 counts per 400 channels we therefore needed approximately 35 min. In cases where we are concerned with magnetic hyperfine split spectra, the time required for measurement easily increases by a factor of 20 because the two absorption lines for which this estimate was carried out may spread out to a variety of absorption lines with much smaller intensity.

IV. Experimental Results of Frozen Solutions and Their Computer Analysis

1. Experimental Results

From the application of the recoilless γ-absorption technique to MbCO, HbCO, MbO_2, HbO_2, Mb, and Hb Mössbauer results have been derived which are presented in this section. Fig. 7 shows Mössbauer spectra of a frozen solution of MbCO (pH 7.0) at 4.2 °K (50), a typical candidate for ferrous low-spin state. Curve (a) coresponds to a measurement with zero applied magnetic field. Assuming a Lorentzian line shape (see Table 1), a least-squares fit to this spectrum leads to the following values for the Mössbauer parameters: Γ (line width) $= 0.328 \pm 0.011$ mm/sec, δ (isomer shift, relative to iron metal) $= 0.266 \pm 0.010$ mm/sec, and ΔE_Q (quadrupole splitting) $= 0.363 \pm 0.006$ mm/sec. Curve (b) shows a spectrum taken with a magnetic field of $H_0 = 47$ kOe applied perpendicularly to the γ-beam. Both spectra have been found
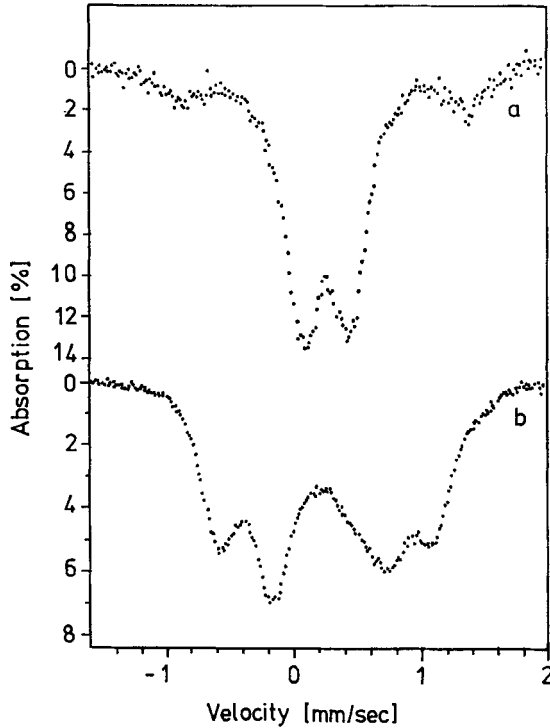
Fig. 7. Experimental Mössbauer spectra of frozen solution of MbCO. (a) $T = 4.2\,°K$ $H_0 = 0$. (b) $T = 4.2\,°K$, $H_0 = 47$ kOe, $\vec{H}_0 \perp \vec{\gamma}$. The additional resonances at -0.9 mm/sec and $+1.33$ mm/sec are due to oxygenated myoglobin (MbCO$_2$) which remained in the sample through the preparation of MbCO. The broad shoulders in (b) are probably due to the impurity effect of MbO$_2$. [Taken from Ref. (50)]

to be nearly temperature independent within the wide range of $4.2\,°K \leq T \leq 200\,°K$.

Since MbO$_2$ is a relatively unstable compound, which easily shows autoxidation to metmyoglobin, most of the investigations concerning oxygenated heme proteins have been made using HbO$_2$ of different species. Fig. 8 shows Mössbauer spectra of oxyhemoglobin in red cells at 4.2 °K with: (a) $H_0 = 0$, and with (b) $H_0 = 30$ kOe applied perpendicularly to the γ-beam (5). From analysis of curve (a) the following parameters are derived: $\Gamma = 0.44$ mm/sec, δ (relative to iron metal) $= 0.2$ mm/sec, and $\Delta E_Q = 2.2$ mm/sec. ΔE_Q of HbO$_2$ is found to be temperature dependent, falling to about 1.9 mm/sec at 195 °K.

Spectra of deoxygenated hemoglobin Hb, a typical candidate for a ferrous high-spin ground state, are presented (5, 51) in Fig. 9. Curve (a) corresponds to $H_0 = 0$ and 4.2 °K, (b) to $H_0 = 60$ kOe, $\vec{H}_0 \perp \vec{\gamma}$, and
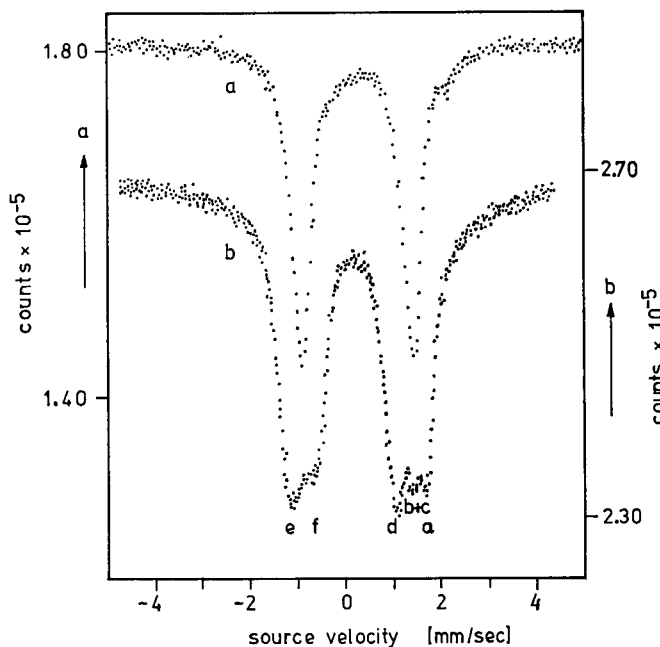
Fig. 8. Experimental Mössbauer spectra of HbO_2 in red cells. (a) $T = 4.2$ °K, $H_0 = 0$, (b) $T = 4.2$ °K, $H_0 = 30$ kOe, $\vec{H}_0 \perp \vec{\gamma}$. [Taken from Ref. (5)]. Absorption lines in (b) approximately correspond to transitions a–f for $V_{ZZ} < 0$ in Fig. 10

$T = 4.2$ °K, (c) to $H_0 = 60$ kOe, $\vec{H}_0 \perp \vec{\gamma}$, and $T = 16$ °K, and (d) to $H_0 = 60$ kOe, $\vec{H}_0 \perp \vec{\gamma}$, and $T = 35$ °K. From the analysis of curve (a) the following parameters are derived: $\Gamma = 0.46$ mm/sec, δ (relative to iron metal) $= 0.9$ mm/sec, and $\Delta E_Q = 2.4$ mm/sec. To demonstrate the strong temperature dependence of electronic properties of Mb or Hb of different species, Fig. 9e shows experimental $\Delta E_Q(T)$ data of Hb (rat, pH 10) (52) and Mb (sperm whale) (42, 53).

2. Analysis of Magnetic Hyperfine Spectra

2.1 Diamagnetic Heme Proteins

Starting with the simplest case, when no electric quadrupole interaction is present and when either an externally controllable magnetic field, H_0, is applied or, as in the case of metallic iron, when there is an internal magnetic field, H_{int}, we shall be concerned with Zeemann splittings of the nuclear levels as indicated in Table 1. The energy level positions E_M are then dependent upon the effective magnetic field $\vec{H}_{eff} = \vec{H}_0 + \vec{H}_{int}$,

117
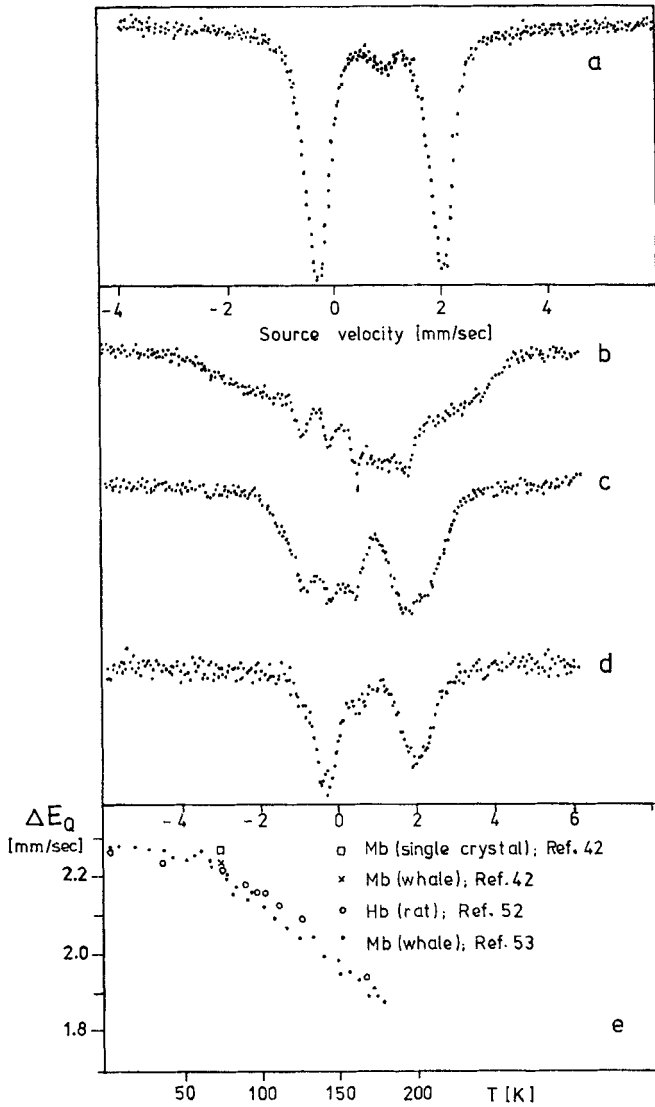
Fig. 9. Experimental Mössbauer spectra of Mb and Hb. (a) Hb at 4.2 °K, $H_0 = 0$, (b) Hb at 4.2 °K, $H_0 = 60$ kOe, $\vec{H}_0 \perp \vec{\gamma}$, (c) Hb at 16 °K, $H_0 = 60$ kOe, $\vec{H}_0 \perp \vec{\gamma}$, (d) Hb at 35 °K, $H_0 = 60$ kOe, $\vec{H}_0 \perp \vec{\gamma}$. [Taken from Refs. (5, 51)]. (e) Temperature dependent quadrupole splittings for Mb and Hb

(as detected at the nuclear site of Fe^{57}) through the relation $E_M = -g_N \mu_N \vec{H}_{eff} \vec{I}$. Here g_N is the nuclear g factor, which is different in the ground state and the excited state: $g_N = 0.1805$ and $g_N = -0.103$ for

Fe^{57}. The quantity $\mu_N = e\hbar/2\ Mc = 3.15 \cdot 10^{-12}$ eV/Oe is the nuclear magneton, and $I_z = \pm 1/2$ and $I_z = \pm 3/2,\ \pm 1/2$ stand for the magnetic components of the nuclear spin I in the ground and excited state of Fe^{57}, respectively. In diamagnetic compounds we do not expect electronic contributions to the effective magnetic field at the Fe^{57} nucleus, $i.e.$ $\vec{H}_{eff}$ is equal to $\vec{H}_0$. In the two diamagnetic compounds discussed here, namely MbCO and HbO_2, electric quadrupole interaction must be considered in addition to nuclear Zeemann splitting. From Fig. 8b for HbO_2 it is obvious that the applied field H_0 causes only a small magnetic hyperfine splitting of the nuclear levels, $\Delta E_M\ (\pm 3/2)$ and $\Delta E_M\ (\pm 1/2)$, compared to the quadrupole splitting ΔE_Q of Fig. 8a. Under the approximations $\Delta E_Q \gg \Delta E_M\ (\pm 3/2)$, with $\Delta E_M\ (\pm 3/2) = -g_N\ \mu_N\ H_0\ (-3/2 - 3/2) = 3\ g_N\ \mu_N\ H_0$, $H_0 = 30$ kOe, and η (asymmetry parameter, see Table 1) ≈ 0, the nuclear levels $|I = 1/2,\ I_z = \pm 1/2>$ for the groundstate, and $|3/2,\ \pm 1/2>$ and $|3/2,\ \pm 3/2>$ for the excited state will be split into $|1/2,\ +1/2>$ and $|1/2,\ -1/2>$ by 0.566 mm/sec, into $|3/2,\ +3/2>$ and $|3/2,\ -3/2>$ by 0.969 mm/sec, and into $|3/2,\ +1/2>$ and $|3/2,\ -1/2>$ by 0.323 mm/sec, respectively. Acocrding to the sign convention for V_{zz} from Table 1c we then get a different energy sequence of the eigenfunctions $|3/2,\ I_z>$ for $V_{zz} > 0$ than for $V_{zz} < 0$. Further, taking into account that we are concerned in the Fe^{57} Mössbauer transitions with magnetic dipole transitions, for which we have to consider the selection rules $\Delta I_z = 0,\ \pm 1$, transition or absorption lines are obtained as indicated in Fig. 10. Comparing this result with the experimental magnetic hyperfine pattern for HbO_2 in Fig. 8b we derive that the EFG component V_{zz} of Fe^{57} in HbO_2 is negative. This information is important for the further interpretation of the results. The reason that the experimental spectrum of Fig. 8b shows unequal intensities for the transitions e and f, or for d and a, compared to the ideal case of Fig. 10, is due to the fact that η in HbO_2 is slightly larger than zero, and hence the real nuclear levels will be linear combinations of basis functions $|I,\ I_z>$,

For the analysis of the magnetic hyperfine spectrum of HbCO (Fig. 7b) the approximation $\Delta E_Q \gg \Delta E_M\ (\pm 3/2)$ is no longer valid. In this more general case the Fe^{57} nuclear eigenstates were derived with the aid of the hamiltonian.

$$\hat{H} = \frac{eQ\,V_{zz}}{4\,I\,(2I-1)}\,[3\,\hat{I}_z^2 - I(I+1) + \eta(\hat{I}_x^2 - \hat{I}_y^2)] - g_N\,\mu_N\,\vec{H}_0\hat{I} \qquad (1)$$

All parameters of Eq. (1) have been defined in Table 1 as well as the nuclear magnetic moment operators $\hat{I}_x$ and $\hat{I}_y$ which may be substituted by $\hat{I}_x = 1/2\ (\hat{I}_+ + \hat{I}_-)$ and $\hat{I}_y = 1/2\ (\hat{I}_+ - \hat{I}_-)$, respectively.

119
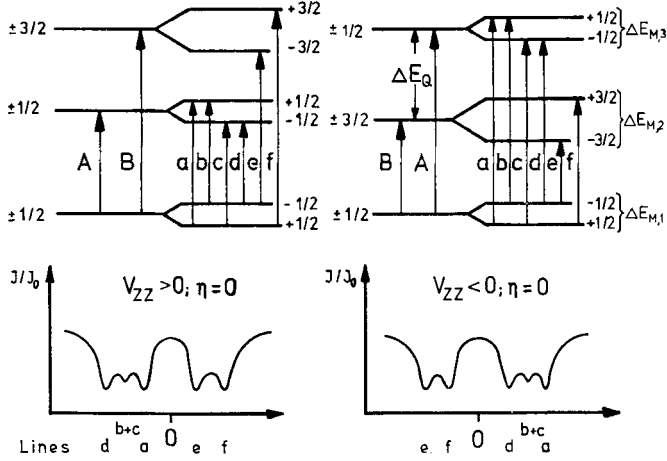
Fig. 10. Determination of sign V_{ZZ} under conditions $\eta = 0$ and $\Delta E_Q \gg \Delta E_M$

Together with the definition that the quantization axis z is parallel to the direction of $\vec{H}_0$ Eq. (1) becomes

$$\hat{H} = \frac{eQ\,V_{zz}}{4\,I(2I-1)}\left[3\,\hat{I}_z^2 - I(I+1) + \frac{\eta}{2}\left(\hat{I}_+^2 + \hat{I}_-^2\right)\right] - g_N\,\mu_N\,H_0\,I_z. \quad (2)$$

Only for the special case that $\vec{V}_{ZZ} \parallel \vec{H}_0$ and $\eta = 0$, the resulting matrix $<I, I_z'|\hat{H}|\,I, I_z>$ is diagonal and the states $|I, I_z>$ are eigenfunctions of $\hat{H}$. Assuming the EFG to be axial in its main axis system, x', y', z' $\left(\eta' = \frac{|V_{x'x'} - V_{y'y'}|}{|V_{z'z'}|} = 0\right)$, but having nonparallel $\vec{V}_{ZZ}$ and $\vec{H}_0$, the transformation $\vec{z}' \to \vec{z} = \vec{H}_0/|\vec{H}_0|$ will cause a non-zero asymmetry parameter $\eta = \frac{|V_{xx} - V_{yy}|}{|V_{zz}|} \neq 0$ in the new axis system x, y, z. In this "low symmetry"-case the operators $\hat{I}_+^2$ and $\hat{I}_-^2$ produce off-diagonal matrix elements $<I, I_z \pm 2|\hat{H}|\,I, I_z>$, and the eigenfunctions to $\hat{H}$ contain admixtures with $\Delta I_z = \pm 2$. Thus, new eigenfunctions $|I, \alpha>$ can be expanded in terms of the basis functions $|I, I_z>$: $|I, \alpha> = \sum_{I_z} C_{\alpha, I_z}\,|I, I_z>$.

In order to find the nuclear eigenstates E_a^n and the expansion coefficients, C_{α, I_z} the two matrixes $<I_g, I_z'|\hat{H}|\,I_g, I_z>$ for the ground state and $<I_e, I_z'|\hat{H}|\,I_e, I_z>$ for the excited state of the Fe^{57} nucleus have to be diagonalized. To calculate transition (absorption) probabilities

$$V_{\alpha'\alpha} = |<I_e, \alpha'|\hat{V}|I_g, \alpha>|^2 = |\sum_{I_z', I_z} C_{\alpha', I_z'}C_{\alpha, I_z} <I_e, I_z'| \\ |\hat{V}|I_g, I_z>|^2 \quad (3)$$

during the absorption of an unpolarized single γ-line with energy $E\gamma$ and γ-propagation direction $\vec{k}$ we have to bear in mind that $|<|\hat{V}|>|^2$ depends on the angle θ between $\vec{H}_0$ and $\vec{k}$. For Fe^{57}, as already mentioned, the radiation is of a pure magnetic dipole type with allowed transitions specified by $I'_z - I_z = 0' \pm 1$. The θ-dependence of $|<|\hat{V}|>|^2$ is then given by

$$\left|<\frac{3}{2}, +\frac{3}{2} \mid \hat{V} \mid \frac{1}{2}, +\frac{1}{2}>\right|^2 = \left|<\frac{3}{2}, -\frac{3}{2} \mid \hat{V} \mid \frac{1}{2}, -\frac{1}{2}>\right|^2 \sim$$
$$(1 + \cos^2\theta)/8$$

$$\left|<\frac{3}{2}, +\frac{1}{2} \mid \hat{V} \mid \frac{1}{2}, +\frac{1}{2}>\right|^2 = \left|<\frac{3}{2}, -\frac{1}{2} \mid \hat{V} \mid \frac{1}{2}, -\frac{1}{2}>\right|^2 \sim \sin^2\theta/6$$

$$\left|<\frac{3}{2}, -\frac{1}{2} \mid \hat{V} \mid \frac{1}{2}, +\frac{1}{2}>\right|^2 = \left|<\frac{3}{2}, +\frac{1}{2} \mid \hat{V} \mid \frac{1}{2}, -\frac{1}{2}>\right|^2 \sim (1 +$$
$$\cos^2\theta)/24 . \tag{4}$$

So far we have considered only a line absorption spectrum with in general eight lines (Fig. 11) having energies E_a^n, and E_a^n, ($\alpha = 1,2$ and
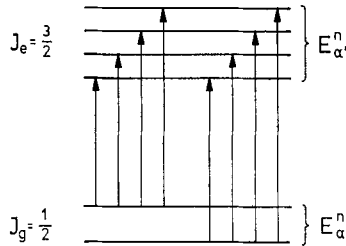
Fig. 11. Generally possible nuclear transitions $E_a^n \rightarrow E_a^n$, for $\alpha = 1,2$ and $\alpha' = 1,2,3,4$ in the case of Fe^{57}

$\alpha' = 1,2,3,4$), and intensities $V_{\alpha'\alpha}$ as given by Eqs. (3) and (4). In order to get a Mössbauer spectrum $J(E)$ a Lorentzian line shape characteristic of the energy widths of emitting (Γ_{em}) and absorbing (Γ_{abs}) nuclei has to be folded into the line absorption spectrum:

$$J(E) = \frac{3\Gamma}{16\pi^2} \sum_{\alpha',a} \frac{|\sum_{I'_z, I_z} C_{a', I_z} C_{a, I_z} <I_e, I'_z \mid \hat{V} \mid I_g, I_z>|^2}{(E_\gamma - E_{a'a})^2 + (\Gamma/2)^2}, \tag{5}$$

with $\Gamma = \Gamma_{em} + \Gamma_{abs}$, and $E_{\alpha'\alpha} = E_{\alpha'} - E_\alpha$.

121

A corresponding relationship for $J(v)$ results from replacing the energy unit "eV" by the Doppler velocity units "mm/sec": 1 mm/sec $\longleftrightarrow$ $4.8 \cdot 10^{-8}$ eV. Eq. (5) describes an absorption spectrum of a single crystalline absorber, since only a single orientation of the EFG tensor V_{pq} relative to $\vec{H}_0$ has been regarded so far. For the simulation of spectra as derived from frozen solutions or polycrystalline samples, all orientations of V_{pq} relative to $\vec{H}_0$ must be taken into account by an appropriate average over possible single-crystal spectra of Eq. (5).

The spectrum shown in Fig. 7b was analyzed by calculating a Mössbauer spectrum for polycrystalline MbCO along the lines decribed above. Fig. 12 shows calculated spectra obtained by using the input parameters
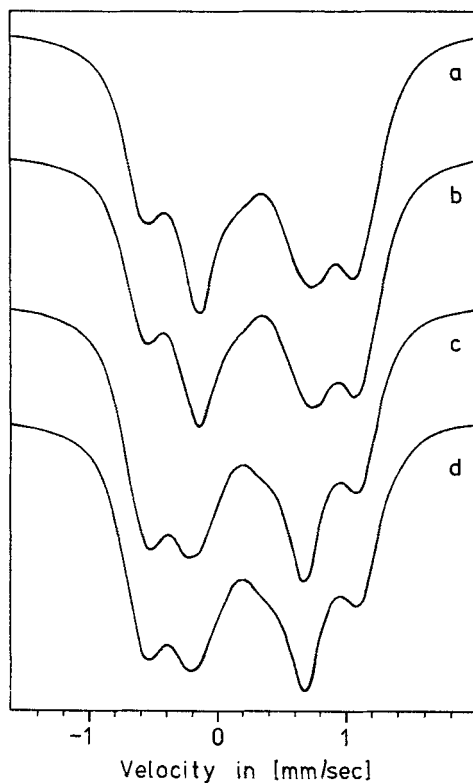
Fig. 12. Theoretical Mössbauer spectra for frozen solution of MbCO, calculated along the lines described in IV.2.1. (a) $V_{ZZ} > 0$, $\eta = 0$. (b) $V_{ZZ} > 0$, $\eta = 0.4$. (c) $V_{ZZ} < 0$, $\eta = 0$. (d) $V_{ZZ} < 0$, $\eta = 0.4$. All spectra have in common: $\Gamma = 0.328$ mm/sec, $\delta = 0.266$ mm/sec, $\Delta E_Q = 0.363$ mm/sec, $H_0 = 47$ kOe, and $\vec{H}_0 \perp \vec{\gamma}$. [Taken from Ref. (50)]

$\Gamma = 0.328$ mm/sec, $\delta = 0.266$ mm/sec, $V_{zz} = \dfrac{2 \, \Delta E_Q}{eQ\left(1+\dfrac{\eta^2}{3}\right)^{1/2}}$, with $\Delta E_Q =$

0.363 mm/sec, $H_0 = 37$ kOe, and $\vec{H}_0 \perp \bar{\gamma}$. Curves (a) and (b) are for $V_{zz} > 0$ and correspond to $\eta = 0$ and $\eta = 0.4$, respectively; curves (c) and (d) are for the same η-values but with $V_{zz} < 0$. A comparison of the experimental spectrum of Fig. 7 b with the calculated spectra leads to the conclusion that V_{zz} at the Fe^{57} nucleus in HbCO is positive. Again this information will be important for the further interpretation of the results as shown in Section VII.

2.2. Paramagnetic Heme Proteins

In computing Mössbauer spectra of paramagnetic compounds (54) it should be taken into account that due to spin-lattice or spin-spin relaxation the paramagnetic centers may fluctuate between their eigenstates. In the cases of (i) fast, and (ii) slow relaxation the calculation of a Mössbauer spectrum remains relatively simple [*Kündig* (54)]. In the first case (i) the spectrum is determined by the thermal average of the hyperfine fields, in the second case (ii) the spectrum results from a superposition of spectra, which correspond to the hyperfine fields of the electronic states, weighted according to thermal population. The intermediate case becomes much more complicated [*Blume* (54)]. As an example of magnetic hyperfine interaction in paramagnetic heme compounds we describe case (i) and refer to the literature for other cases.

The magnetic hyperfine interaction in paramagnetic compounds consists of nuclear and electronic components. The strength of this interaction in the case of Fe^{57} corresponds to a nuclear field of order 10 Oe acting on the electrons, or to an effective electron field of a few 100 kOe, acting on the nucleus. Thus, in general, the magnetic hyperfine interaction hamiltonian $\hat{H}_{hf}$ operates on basis states which have both electronic and nuclear components. Because the contribution of the hyperfine interaction to the electronic energy in ferrous iron is usually small compared to typical electronic zero field splittings, the electronic and nuclear parts of the problem can be solved separately. Only in the case of ferric complexes, which have half integral spin, does the Kramers degeneracy prevent the separation of the two problems. A magnetic field of $H_0 \gg 10$ Oe ($H_0 = 10$ kOe corresponds to some cm^{-1}), externally applied to the spin degenerated system, however, will lift the Kramers degeneracy and again makes the problem separable. Under this condition, in $\hat{H}_{hf}$ the spin operators $\hat{S}_x$, etc. are replaced by spin expectation values $<S_x>$, etc.; then we are only concerned with a nuclear spin hamiltonian.

123

The Fe^{57} nucleus now experiences a net expectation value of the electronic spin which is a thermal average taken over all spin states being populated by temperature:

$$<S_i>_{\text{av}} = \sum_N <S_i>_N \exp\left(-\frac{\Delta E_N}{kT}\right) \Big/ \sum_N \exp\left(-\frac{\Delta E_N}{kT}\right). \quad (6)$$

In Eq. (6) the index i designates the components x, y, z of the electron spin, and N is the sum of all the populated states; ΔE_N is the energy of the Nth electronic spin state relative to the lowest one. The nuclear Hamiltonian, containing the magnetic hyperfine interaction between nucleus and paramagnetic valence shell, the nuclear Zeemann term $(-g_N \mu_N \vec{H}_0 \vec{I})$, and the quadrupole interaction H_Q, is given by

$$\hat{H} = <\vec{S}>_{\text{av}} \tilde{A} \vec{I} - g_N \mu_N \vec{H}_0 \vec{I} + \hat{H}_Q$$
$$= -g_N \mu_N \left[\vec{H}_0 - \frac{<\vec{S}>_{\text{av}} \tilde{A}}{g_N \mu_N}\right] \vec{I} + \hat{H}_Q, \quad (7)$$

with $\tilde{A}$ representing the so-called magnetic hyperfine tensor. The quantity $-\dfrac{<\vec{S}>_{\text{av}} \tilde{A}}{g_N \mu_N}$ is commonly called the internal magnetic field $\vec{H}_{\text{int}}$ at the nucleus, produced by the electronic system. At this point we should bear in mind that this quantity entering (7) usually applies well for ferric low-spin ($S = 1/2$) and ferrous high-spin ($S = 2$) compounds, since their paramagnetic centers are characterized by fast spin-lattice relaxation (case i). In some specific ferrous high-spin compounds (*Zimmermann (54)*) and in most of the ferric high-spin ($S = 5/2$) compounds, however, we are concerned with slow spin-lattice relaxation (case (ii)). One ferric high-spin compound for which Eq. (7) applies in order to calculate its magnetic hyperfine split Mössbauer spectrum is hemin, because of fast spin–spin relaxation. Thus, the nucleus experiences an effective magnetic field $\vec{H}_{\text{eff}}$, which is the vector sum $\vec{H}_{\text{eff}} = \vec{H}_0 + \vec{H}_{\text{int}}$. Observe that H_{int} in general is quite a complicated quantity and depends on the $\tilde{A}$-tensor, through $<\vec{S}>_{\text{av}}$ on the temperature because of the thermal averaging procedure, on the construction of the energetically low lying molecular orbitals and their mutual spin-orbit coupling, which itself may be dependent on $\vec{H}_0$. To specify a theoretical Mössbauer spectrum according to Eq. (5) completely, the parameters $<S_x>_{\text{av}}$, $<S_y>_{\text{av}}$, $<S_z>_{\text{av}}$, A_x, A_y, A_z, V_{ZZ}, η, $\vec{H}_0$, δ, Γ, the nine Euler angles defining the orientation of the $\tilde{A}$-tensor, of the EFG tensor V_{pp}, and of the vector $<\vec{S}>_{\text{av}}$ with respect to $\vec{H}_0$ are needed. The task is then to measure Mössbauer spectra at various temperatures in applied magnetic fields

of different strengths and directions and to find a consistent set of parameters describing all spectra. Fortunately some of these parameters are known from theoretical estimates or from other measurements. The expectation values $<S_i>_{\text{av}}$ may be approximated in terms of zero-field splitting D and rhombicity E, which sometimes are available from far-infrared and susceptibility measurements, and in terms of the g-tensor, which for compounds containing ferric iron often is known from ESR-measurements. Endor measurements can provide the absolute values for the components of the $\tilde{A}$-tensor of ferric iron and its orientation relative to the g-tensor. High temperature Mössbauer data give the line width Γ, the isomer shift δ, and the quadrupole splitting ΔE_Q, and if single crystals are available, V_{ZZ} and η, and the orientation of V_{pp} with regard to a fixed framework can be derived. Computer programs available to handle the complicated problem of simulating Mössbauer spectra of paramagnetic heme proteins have been written separately by G. *Lang* (55) and E. *Münck* (56).

Generally the spin lattice relaxation between spin states of high-spin ferrous iron is known to be fast. If the relaxation time is small compared with the precession time τ of the Fe^{57} nucleus ($\tau = \dfrac{\hbar}{\Delta E}$, where ΔE is a typical energy splitting of about 10^{-7} eV of the nuclear levels), the nucleus then sees a net expectation value of the electronic spin, $<\vec{S}>_{\text{av}}$, which is zero. This is the case for deoxymyoglobin, deoxyhemoglobin, reduced cytochromes, and reduced peroxidases etc., which show with zero applied field ($\vec{H}_0 = 0$) only a quadrupole doublet (see Fig. 9a). With applied field ($\vec{H}_0 \neq 0$) the spins align more or less along $\vec{H}_0$, thus producing a non-zero $\dfrac{<\vec{S}>_{\text{av}} \tilde{A}}{g_N \mu_N}$ — contribution to the effective magnetic field $\vec{H}_{\text{eff}}$ at the Fe^{57} nucleus.

Fig. 9b shows the experimental Mössbauer spectrum of Hb at 4.2 K with $H_0 = 30$ kOe and $\vec{H} \perp \vec{\gamma}$. So far, it has not been possible to compute a theoretical Mössbauer spectrum, which fits the experimental pattern of Fig. 9b, mainly due to the fact that most of the parameters required for such a fit have not been available.

Magnetic measurements ($\vec{H}_0 \neq 0$) of high-spin ferrous systems at elevated temperatures sometimes have the advantage that the thermal average $<\vec{S}>_{\text{av}}$ is zero. Figures 9c and d show spectra of Hb (57) measured at 16 °K and 35 °K, respectively, with $H_0 = 60$ kOe perpendicular to the transmitting γ-rays. The spectra are similar to that found for diamagnetic HbO_2 (Fig. 8b), indicating that $<\vec{S}>_{\text{av}}$ is approximately zero. Only the pronounced isomer shift of $\delta \approx +0.9$ mm/sec (relative to iron metal) indicates that we are concerned with a high-spin ferrous compound, for which an isomer shift (relative to metallic iron) of the order of

$+1$ mm/sec is characteristic. From the line-triplet on the low-energy side (Fig. 9c) it appears that the sign of V_{zz} for Hb is positive (cf. Fig. 10). This conclusion agrees with the findings from single crystal measurements with Mb (42), which are described in the following section (V).

From inspection of the spectrum of reduced cytochrome P450 (Fig. 13), measured by *Münck et al.* (57) at 200 °K with $H_0 = 45$ kOe parallel to the transmitting γ-rays, it was concluded by a similar argument (line triplet on the high-energy side) that V_{zz} is negative (57). A most recent computational analysis of 4.2 °K- and 220 °K-spectra of reduced cytochrome P450 by *Münck* (private communication, May 1974), however indicates that the "triplet" argumentation concerning sign V_{zz} is very deceptive, at least for this compound; the overall theoretically derived intensities now seem to favor $V_{zz} > 0$.
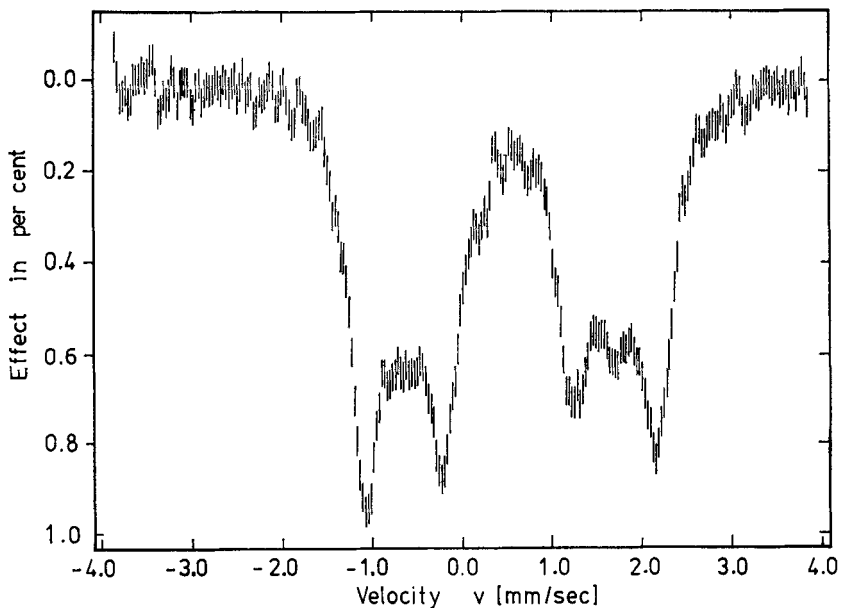
Fig. 13. Experimental Mössbauer spectra of frozen solution of reduced cytochrome P 450 at 200 °K, $H_0 = 45$ kOe, $\vec{H}_0 \| \vec{\gamma}$. [Taken from Ref. (57)]

In order to complete the discussion of magnetic hyperfine interactions in paramagnetic heme proteins as detected by Mössbauer spectroscopy, reference should be made to the work of *Champion et al.* (58). There the influence of the halides F, Cl, and I on ferric chloroperoxidase was studied. The results presented in this work indicate that halide anions,

which are substrates for chloroperoxidase halogenation reactions, can form complexes with the enzyme and cause significant changes in the heme environment and the spin state of the iron. Fig. 14a–c show signif-
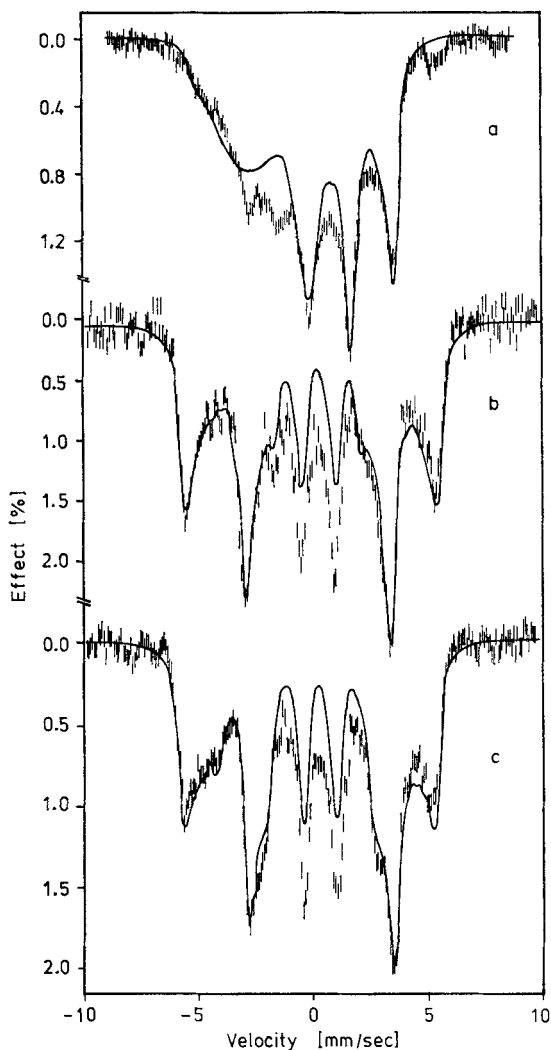
Fig. 14. Experimental and theoretical Mössbauer spectra of ferric chloroperoxidase and its halide complexes. (a) Native chloroperoxidase, pH 3, $T = 4.2$ °K, $H_0 = 1.3$ kOe, $\vec{H}_0 \perp \vec{\gamma}$. An identical spectrum was found for the chlorine-complex measured under the same conditions. (b) Iodine complex, pH 3, $T = 1.5$ °K, $H_0 = 1,3$ kOe, $\vec{H}_0 \perp \vec{\gamma}$. (c) Fluoride complex, pH 3, $T = 4.2$ °K, $H_0 = 1.3$ kOe, $\vec{H}_0 \perp \vec{\gamma}$. [Taken from Ref. (58)]

127

icant changes in the Mössbauer spectra of chloroperoxidase upon complex formation with different halides; this feature is remarkable especially under the aspect that the halides are probably not directly coordinated to the iron. The change in the magnetic hyperfine patterns in Fig. 14a–c, which have been simulated by *Champion et al.* (*58*) along the lines described above (solid lines in Fig. 14a–c), might suggest the "presence of transferred hyperfine interactions between the halides and the iron" (*58*).

V. Experimental Results of Myoglobin Single Crystals and Their Analysis

1. Experimental Methods and Results

Myoglobin (instead of hemoglobin) was chosen for single crystal Mössbauer measurements (*42*) because myoglobin contains only two hemes within one unit cell, one being transformed into the other by a subsequent rotational (180° around the crystallographic b axis) and translational transformation. This condition together with the geometric arrangement shown in Fig. 15, with the γ-ray direction always perpendicular to the b-axis, has the advantage that identical Mössbauer spectra are measured for the two heme groups (*59*).

Single crystals were grown from a solution of sperm whale myoglobin. The iron of the myoglobin was enriched to 80% with Fe^{57}. A met myoglobin (met Mb) crystal with a diameter of about 0.5 mm was fixed in a Debye capillary with the aid of two smaller Debye capillaries. The reduction of a met Mb crystal was accomplished by washing the crystal in the capillary with a solution of 4 M $(NH_4)_2SO_4 + Na_2S_2O_4$ in water. The capillary was then closed by wax and mounted on a goniometer head. The orientation of the deoxy-myoglobin (Mb) single crystal was determined on a precession camera (*50*), with the sample kept at 77 °K by washing the capillary with a fine spout of liquid nitrogen. After the orientation was determined the whole goniometer head was placed in liquid nitrogen until it was used for measurements. During the transfer of the goniometer head to the cryostat the capillary was carefully washed again with liquid nitrogen. The crystal remained at 77 °K throughout the Mössbauer experiments. After that the goniometer head was back — again the sample was maintained at 77 °K — to the precession camera to recheck the orientation of the crystal.

During the freezing procedure the crystal water expands, therefore the crystal is somewhat damaged. Since X-ray pictures on the precession camera were also obtained after freezing, the crystal remained satis-
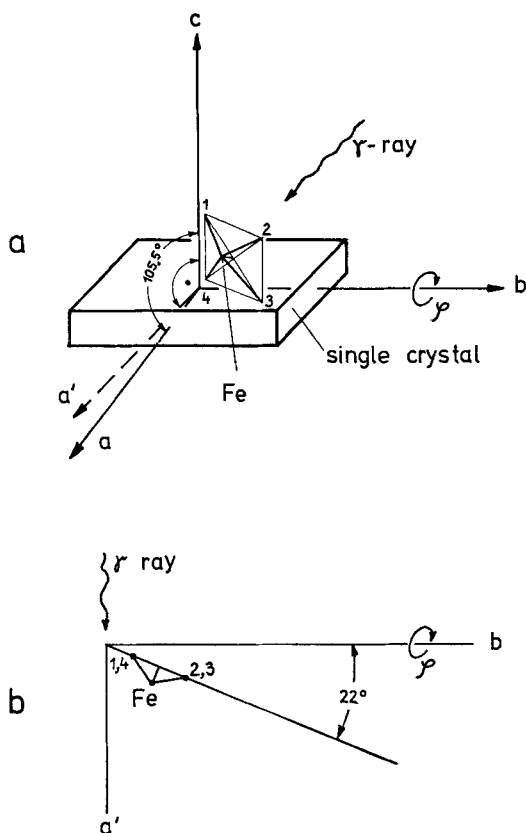
Fig. 15. (a) Schematic of the orientation relations in the Mb single crystal experiments. (b) Projection of the heme on the a'b plane. Heme nitrogens are denoted by nos. 1 to 4. φ is the angle of rotation around the crystallographic b axis

factory for the purpose of the experiment; the misorientation of the whole single crystal remained smaller than $5°$.

The single crystal orientation in the experimental arrangement is shown in Fig. 15. The crystallographic axes are represented by a, b, and c. To simplify the description of the experiment a' is introduced, so that the axes a', b, and c are mutually orthogonal. The propagation direction of the γ-ray, $\vec{\gamma}$, remained perpendicular to b throughout all experiments. The crystal was rotated about the b axis by the angle φ. The angle $\varphi = 45°$ corresponds to the situation $\vec{\gamma} \parallel a'$, and $\varphi = 135°$ to $\vec{\gamma} \parallel c$. The heme plane is also shown in Fig. 15. When projected on the $a'b$ plane, it makes an angle of $22°$ to b (Fig. 15b).

A typical spectrum of an Mb single crystal is shown in Fig. 16. The small contamination at velocities -0.913 mm/sec and $+1.357$ mm/sec is due to MbO_2. Table 2 summarizes line widths Γ, quadrupole splittings ΔE_Q, and isomer shifts δ (relative to metallic iron) for Mb and MbO_2 as derived from the single crystal spectra, for Mb in frozen solution and
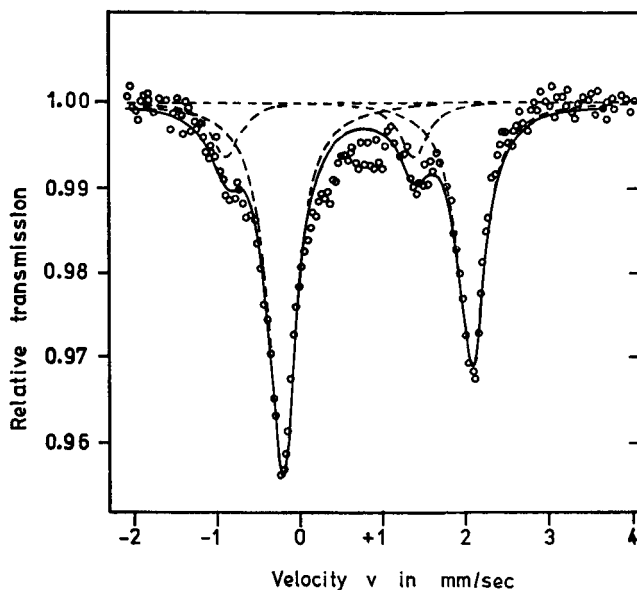
Fig. 16. Experimental Mössbauer spectrum of a Mb single crystal with orientation $b \perp \vec{\gamma}$ and $\varphi = 156°$ ($\varphi = 45°$ corresponds to $a' \parallel \vec{\gamma}$ and $\varphi = 135°$ to $c \parallel \vec{\gamma}$). Side peaks originate from MbO_2. [Taken from Ref. (42)]

Table 2. Experimental[a] Mössbauer line widths Γ, quadrupole splittings ΔE_Q and isomer shifts δ for oxygenated and deoxygenated myoglobin

Material	Γ (mm sec^{-1})	ΔE_Q (mm sec^{-1})	δ[b] (mm sec^{-1})
mbO_2[c]	0.402 ± 0.017	2.269 ± 0.017	$+0.222 \pm 0.017$
Deoxy mb[c]	0.402 ± 0.017	2.286 ± 0.017	$+0.900 \pm 0.017$
mbO_2[d]	0.36 ± 0.03	2.27 ± 0.03	$+0.22 \pm 0.03$
Deoxy mb[e]	0.37 ± 0.03	2.24 ± 0.03	$+0.86 \pm 0.03$

[a] All experiments at 77 °K.
[b] Isomer shift relative to α-Fe at 300 °K.
[c] Single crystal A, see text and Fig. 16.
[d] Polycrystalline powder.
[e] Frozen solution.

for MbO_2 in polycrystalline powder. Table 3 contains the intensity ratios R (see Eq. 8) for the eight different orientations of Mb single crystal A and for two different orientations of Mb single crystal B. In Fig. 17 the values from Table 3 are plotted in a R-φ framework (closed circles).

Table 3. Experimental ratios of quadrupole split Mössbauer lines of deoxy mb single crystals under various orientations

A		B	
$\varphi^{a)}$	$R^{b)}$	$\varphi^{a,c)}$	$R^{b)}$
45	0.823 ± 0.140	50 ± 7	1.065 ± 0.192
66	1.017 ± 0.163		
88.5	1.121 ± 0.179		
111	1.100 ± 0.176		
135	0.875 ± 0.140	135 ± 7	0.783 ± 0.140
156	0.705 ± 0.119		
178.5	0.658 ± 0.118		
200.5	0.700 ± 0.126		

a) Angles given in degrees.
b) R is the ratio of intensity at position $+2.043$ mm/sec. and of intensity at position -0.243 mm/sec: $R = I(+2.043)/I(-0.243)$.
Deoxy mb single crystal (A) was calibrated on precession camera (see text). The $R(\varphi)$ — values are plotted in Fig. 17.
c) Deoxy mb single crystal (B) was calibrated by visual adjustment only; therefore we give an error for φ.
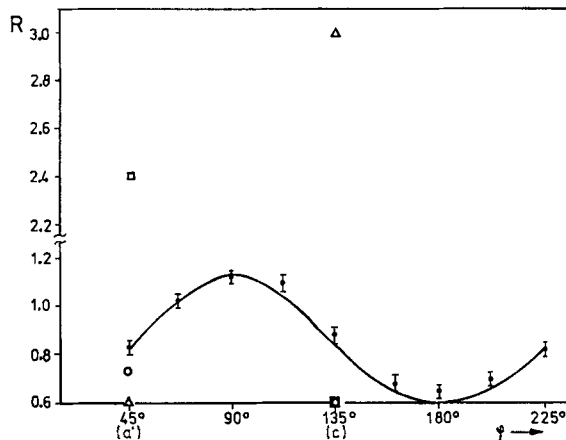
Fig. 17. Relative line intensity R (see Table III and text) versus angle φ. [Taken from Ref. (42)]

131

2. Analysis of Myoglobin Single Crystal Mössbauer Spectra

The relative line intensity R of a quadrupole split spectrum is determined by the angle θ between $\vec{\gamma}$ and the principal axis of the electric field gradient $z = V_{ZZ}$. From Eqs. (3) and (4) and assuming the assymmetry parameter η to be zero, the intensity ratio R of the two absorption lines of the quadrupole split Mb single crystal spectrum is derived to be:

$$R = \frac{I_{3/2}}{I_{1/2}} = \frac{1 + \cos^2 \theta}{\frac{2}{3} + \sin^2 \theta} . \tag{8}$$

Because η has little influence (67) on R, it is assumed to be zero for a first estimate. The angle between z and the b axis is designated by α. The three angles under consideration φ, θ, and α are related to each other as shown in Eq. (9):

$$\cos \theta = \sin \alpha \cdot \sin \varphi . \tag{9}$$

From the R-values in Table 3 and Fig. 17 it is obvious that V_{ZZ} is positive. By rotating the z-axis around b there will be $\theta = 90°$ for one specific φ and therefore R will be either 0.6 or 1.667, depending on whether V_{ZZ} is positive or negative. As the R-values in Fig. 17 never exceed a value of about 1.2 it is concluded that V_{ZZ} is positive.

If it is assumed that z is perpendicular to the heme plane, then, under the condition $\vec{\gamma} \| a'$ ($\varphi = 45°$), R is calculated to be about 2.3 (indicated by a square in Fig. 17). However, if it is assumed that z is in the heme plane parallel to $a'b$, then R is about 0.73 (as indicated by a circle in Fig. 17). In both cases $R = 0.6$ should be found for $\vec{\gamma} \| c$ ($\varphi = 135°$, also indicated by square and circle in Fig. 17), because the z's become perpendicular to $\vec{\gamma}$. Assuming z is in the heme plane but perpendicular to $a'b$, R is calculated to be $R = 0.6$ for $\vec{\gamma} \| a'$ and $R = 3$ for $\vec{\gamma} \| c$ (indicated by triangles in Fig. 17). The experiment (closed circles in Fig. 17) obviously shows quite a different behavior.

The minimum and the maximum in R occur at $\varphi = 180°$ and $\varphi = 90°$, respectively. At these positions $\vec{\gamma}$ forms an angle of 45° to both the a' and c axes. The minimum $R \approx 0.6$ at $\varphi = 180°$ indicates [Eq. (8)] that $\theta = 90°$ or $\vec{\gamma} \perp z$. At $\varphi = 90°$, R is about 1.13 and the smallest angle, $\theta = 50°$, between $\vec{\gamma}$ and z is obtained. Under this condition, $\vec{\gamma}$, z, and b are all in one plane and therefore $\theta + \alpha = 90°$. It follows that the angle between z and b is $\alpha = 40°$ ($\pm 8°$), which is considerably larger than the angle of 22° indicated in Fig. 15. Calculation of R using Eqs. (8) and (9) and taking $\alpha = 40°$, yields the solid line drawn in Fig. 17, which is in

good agreement with the experimental points. In Ref. *(42)* the angle $\alpha = 40° \pm 8°$ was derived assuming η to be zero. A most recent computational analysis of the experimental data of Table 3 by Y. *Maeda et al.* *(62)* by taking use of Eq. (5) with $\hat{H}_0$ setting zero, however, indicates that $\alpha = 40° \pm 8°$ is consistent also with an η-parameter in the range $0 \le \eta \le 0.3$.

Now it is possible to locate z in the single crystal. z forms an angle of $40° \pm 8°$ with the b axis, and when projected on the $a'c$ plane forms an angle of about 45° to both axes. Then, in regard to the heme plane two alternatives of the z or V_{ZZ} orientation are consistent with the measurements: V_{ZZ} forms an angle of about 45° with the heme plane or it is oriented rather close to the heme plane and is directed toward one of the nitrogen atoms of the heme ring. The latter seems more likely considering the structure around the Fe nucleus. In Section VII we shall discuss a further confirmation of this assumption as derived from molecular orbital calculations.

VI. Interpretation of Experimental Quadrupole Splittings in Crystal Field Approximation

The interpretation of experimental quadrupole splittings, ΔE_Q, of Hb was first based on electric field gradient contributions from Fe $3d$ single-electron orbitals weighted by an appropriate Boltzmann factor *(3, 63)*. However, it turned out that a single electron in a Fe $3d_{xy}$ orbital would produce a ΔE_Q value which is nearly twice the experimental value measured for Hb at 4.2 °K. Therefore, it was investigated which of the various electron terms within the $3d^6$ configuration may lie close enough in energy to the high-spin ground state in Hb, in order to mix negative EFG contributions into the positive ground state EFG via spin-orbit coupling between ground and excited electron states *(52)*. *Otsuka (64)* and *Eicher et al.* *(52)* have shown independently that in a ligand field of tetragonal symmetry (taking the heme normal as symmetry axis) the energy levels $^5B_2$, ^5E, ^3E, and $^1A_1$ may fulfill this requirement. This situation is illustrated by the results in Fig. 18, which have been computed by taking into account the proper tetragonal point symmetry (C_{4v}) of the heme iron and the Coulomb repulsion of Fe $3d$ electrons. From Fig. 18 it is obvious how the many-electron term energies depend on the single electron energies ε_i ($i = 1, 2, 3$), which are defined by $\varepsilon_1 = E (d_{xz}, d_{yz}) - E (d_{xy})$, $\varepsilon_2 = E (d_{3z^2-r^2}) - E (d_{xy})$, and $\varepsilon_3 = E (d_{x^2-y^2}) - E (d_{xy})$. For energies $\varepsilon_3 \gtrsim 20\,000$ cm^{-1} the spin triplet ^3E is found to be ground state, which is the case for Fe in iron phthalocyanine *(65)*; for

133
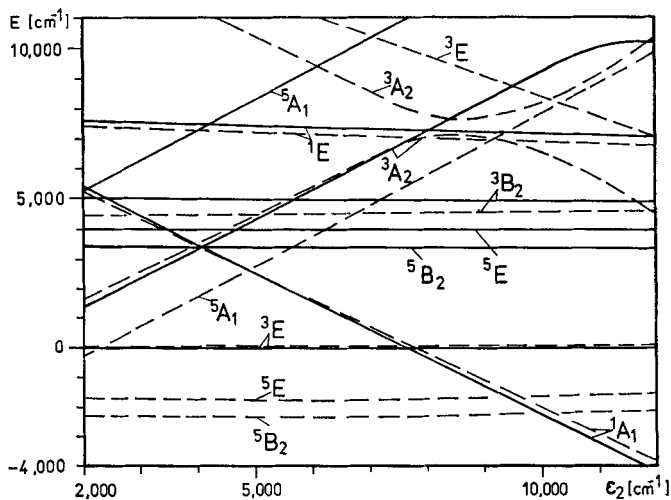
Fig. 18. Crystal field results for energy positions of low lying many-electron states, relative to the lowest ^3E term within the $3d^6$ configuration, plotted as a function of single-electron energy ε_2. The solid and dashed lines represent two different calculations using $\varepsilon_1 = 600$ cm^{-1}, $\varepsilon_3 = 22\,000$ cm^{-1}, and $\varepsilon_1 = 600$ cm^{-1}, $\varepsilon_3 = 16\,000$ cm^{-1}, respectively. [Taken from Ref. (52)]

strong ligand fields characterized by $\varepsilon_2 \gg 10\,000$ cm^{-1}, $\varepsilon_3 \gtrsim 15\,000$ cm^{-1} we expect the spin singlet as ground state, which is the case for the diamagnetic compounds MbCO and HbCO. In the weak field approximation (small ε_i) obviously a spin quintet will be ground state. Using the estimate (66—69) for ε_i (Fig. 19) from various experiments with heme
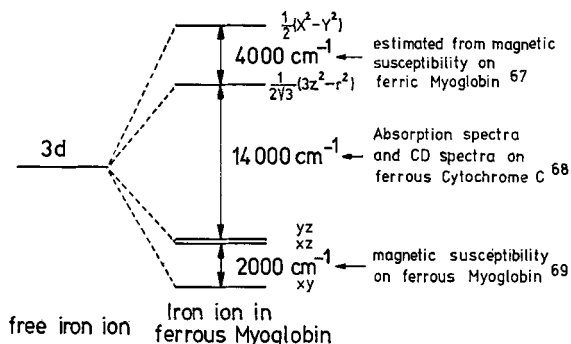
Fig. 19. Differences of single-electron $3d$ energies in reduced heme proteins. The arrows indicate the procedures of the estimates of these energies. [Taken from Ref. (66)]

compounds it seems reasonable to take into account spin-orbit inter-action between the terms $^5B_2$, ^5E, ^3E, and $^1A_1$ in order to calculate $\Delta E_Q(T)$ for Mb or Hb. The solution of the corresponding secular problem for the low lying levels $^5B_2$, ^5E, ^3E, and $^1A_1$, is expressed by the energies ε_i; and the 22 spin eigenvectors $|e_\alpha>$ are certain linear combinations of the base vectors each contributing to ΔE_Q by typical high-spin, intermediate-spin, and low-spin values. In order to evaluate the tempera-ture dependence of ΔE_Q it is necessary to average the EFG components V_{ZZ}^a and η^a of the individual substates $|e_\alpha>$ according to Boltzmann statistics. A detailed description of the evaluation of $\Delta E_Q(T)$ will be given in the following section.

The basic results from *Eicher's* and *Trautwein's* calculations (52) of $\Delta E_Q(T)$ for Mb and Hb follow from inspection of Figs. 20 and 21. Comparing experimental and theoretical $\Delta E_Q(T)$ data the following energy sequence of many electron terms relative to the ground state $^5B_2$, is derived: $E(^5B_2) = 0$, $E(^3E) \approx 250$ cm^{-1}, $E(^1A_1) \approx 2000$ cm^{-1}, and $E(^5E) \approx 2500$ cm^{-1}. The energies may be altered due to rhombic perturbations, which split the doublets ^3E and ^5E by about 120 cm^{-1} and 200 cm^{-1}, respectively: $E(^5B_2) = 0$, $E(^3E) \approx 250 \pm 60$ cm^{-1}, $E(^1A_1) \approx 2000$ cm^{-1}, and $E(^5E) \approx 2000 \pm 100$ cm^{-1}. This term scheme for Mb or Hb with the relatively low lying spin triplet ^3E, however, must be questioned, because: (i) the recent single crystal Mössbauer investigation of Mb (42) indicates that V_{ZZ} is more likely to be parallel to the heme plane than perpendicular, in contrast to the former assumption (52), (ii) temperature-dependent susceptibilities $\chi(T)$ derived with this energy term scheme for Hb are inconsistent with experiment (70), and (iii) taking account of direct ligand influence on the heme iron only through an isotropic covalency factor (an assump-tion which is typical for crystal field approaches) seems to be a too rigorous assumption.

Crystal field calculations by *Huynh et al.* (70) on the basis of *Eicher's et al.* (52) approach, but taking $V_{ZZ} > 0$ and V_{ZZ} as being parallel to the heme plane, led to a new energy term scheme for Hb which is consistent with both the temperature dependence of the quadrupole splitting in the range of $77°K \leq T \leq 200°K$ and the magnetic susceptibility, $\chi(T)$. The energies corresponding to *Huynh's et al.* $\Delta E_Q(T)$ and $\chi(T)$ fit curves are:

$E(^5E) = 300 \pm 346$ cm^{-1}, $E(^5B_2) = 0$ cm^{-1}, $E(^1A_1) = 287$ cm^{-1},
$E(^3E) = 1026 \pm 207$ cm^{-1}, and $\lambda = 76$ cm^{-1} (λ: spin-orbit coupling constant).

To study the reliability of this result further it remains to discuss the direct ligand influence on the heme iron. This task leads us to the
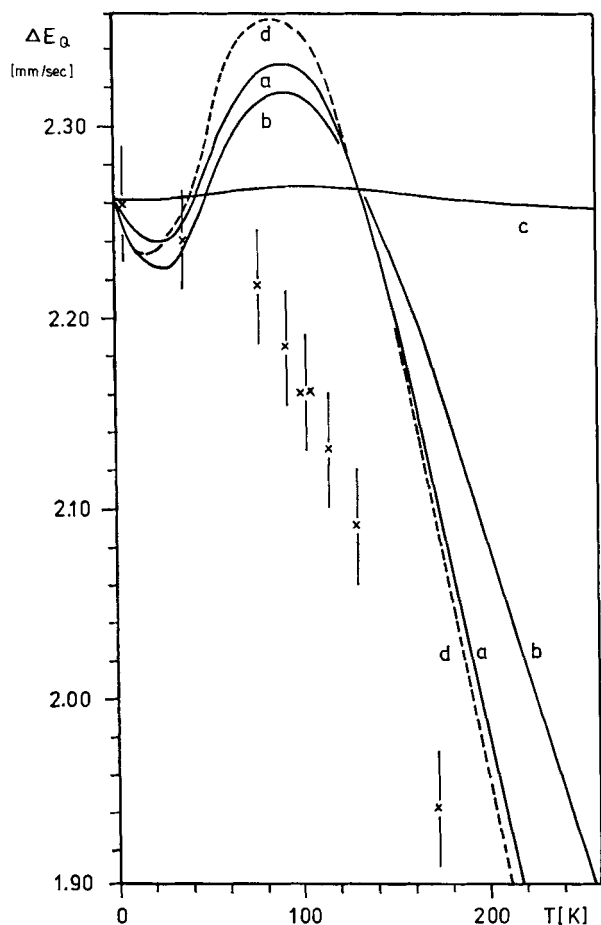
Fig. 20. Temperature dependent experimental quadrupole splittings of Hb (rat). The theoretical $\Delta E_Q(T)$ curves result from crystal field calculations (see Section VI) taking (a) $\varepsilon_1 = 228$ cm^{-1} and λ (spin-orbit coupling constant) $= 82$ cm^{-1}; (b) $\varepsilon_1 = 268 \pm 139$ cm^{-1}, $\lambda = 82$ cm^{-1}; (c) $\varepsilon_1 = 1000 \pm 980$ cm^{-1}, $\lambda = 82$ cm^{-1}; (d) $\varepsilon_1 = 234$ cm^{-1}, $\lambda = 77$ cm^{-1}. [Taken from Ref. (52)]

estimate of Mössbauer parameters and susceptibility data on the basis of molecular orbital (MO) calculations, which include the three-dimensional structure of heme compounds beyond the heme iron and its immediate neighbors and which moreover, include all relevant valence electrons.
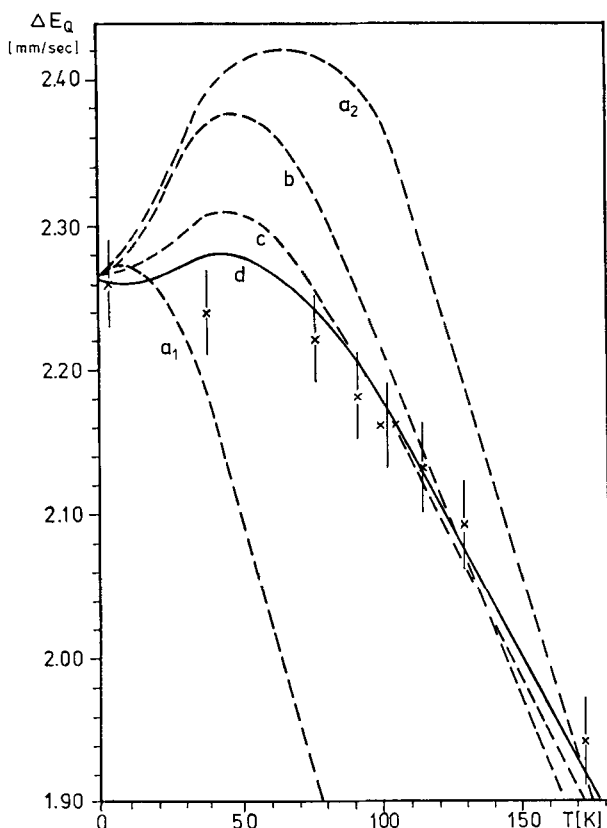
Fig. 21. Crystal field results for the temperature dependent quadrupole splitting in Hb, involving spin-orbit interaction between energetically low lying levels $^5B_2$, ^3E, $^1A_1$, and ^5E. Their energies relative to the groundstate $^5B_2$ are (for E (^3E), E ($^1A_1$), and E (^5E) in cm^{-1}):

(a$_1$)	269	2085	695		(c)	256	1883	1737
(a$_2$)	338	1390	695		(d)	247	1883	2432
(b)	283	1730	1042					

VII. Interpretation of Experimental Mössbauer and Susceptibility Data by Molecular Orbital Theory

1. General Considerations

Since heme complexes involve to varying extends covalent binding between iron and ligands and charge rearrangements within the ligand structure, a theoretical description of the electronic behavior of such

complexes should not be limited to the valence electrons of iron only. Rigorous all-valence electron treatments of systems as large as hemin, however, are prohibitive in cost, even at the self-consistent field (SCF) level of approximation. It is even extremely costly to pursue semi-empirical antisymmetrized molecular orbital theory or approximations based on neglect of differential overlap, such as the CNDO/2 method (77). The key simplification appearing to permit calculation at reasonable cost is to avoid the construction of an explicit antisymmetrized many-electron wave function. Methods in this category include those of the Hückel type (72, 73) and the multiple scattering χ_α method of *Johnson et al.* (74).

2. Hückel and Configuration Interaction Calculations

The following theoretical studies are based on an iterative extended Hückel method described in detail previously (72). The Hückel one-electron Hamiltonian H was assumed to have diagonal elements $H_{aa} = -\alpha_a - q_a \Delta \alpha_a$, where α_a is the "α" parameter (ionization potential) for atomic orbital a (of real form) in a neutral atom, q_a is the net charge of the atom at which orbital a is centered, and $\Delta\alpha_a$ is an additional parameter controlling the variation of H_{aa} with net atomic charge. The off-diagonal elements H_{ab} were determined from H_{aa} and H_{bb} by the Cusachs approximation (75) $H_{ab} = S_{ab} (1 - \frac{1}{2} |S_{ab}|) (H_{aa} + H_{bb})$. Here S_{ab} is the overlap integral of atomic orbitals a and b, calculated assuming Slater-type orbitals (STO's). In evaluating H_{ab}, all aperations are performed in a coordinate system passing through the orbital centers so as to retain full invariance with respect to rotation of the molecule in the coordinate system.

Iterations were carried out until the occupied-orbital solutions of the matrix equation $(H - E_i S) c_i = 0$ were consistent with the net atomic charges used in calculating H. Here E_i is the orbital energy of the molecular orbital whose atomic-orbital coefficients are represented by the vector c_i. The overlap matrix S is built from the S_{ab} as already defined. The iterative process must be sophisticated enough to over-come the strong nonlinearity of the theory; a combination of damping and second-order extrapolations has been used and thereby convergence to ± 0.01 electronic charge units in atomic charge in five to ten iterations was achieved. The net atomic charges are obtained by apportioning exactly-computed overlap charges among the atoms involved.

The calculations include all valence orbitals, *i.e.* $1s$ for H, $2s$ and $2p$ for C, N, and O; and $3d$, $4s$, and $4p$ for Fe. All orbital parameters have been taken from literature and were adjusted to a consistent parameter set in a variety of MO studies (72, 76—80).

The Hückel model is inadequate for distinguishing spin eigenstates and for the calculation of energy differences between them, but Mb and Hb exist in "high-spin" states necessitating the use of singly-occupied molecular orbitals (MO's). For such problems the Hückel calculations are supplemented by proceeding to a limited configuration interaction (CI), simplifying the computations by using the Hückel SCF MO's to construct configurations. As even a limited CI study is expensive for large systems, and since the present needs are to characterize the MO structure and to compare different spin states, attention is confined to calculation of energies relative to that of a "reference configuration". If the reference configuration has energy E_0, energies relative thereto can be obtained as eigenvalues of $H - E_0 S$, where H and S now refer to many electron space-spin states of appropriate symmetries. As E_0 can be written in terms of the integrals occuring in the elements of H, the elements of $H - E_0 S$ will depend only upon the orbitals affected by passage from the reference configuration to the configurations actually used in H and S. A more detailed description of this CI procedure was given earlier by *Trautwein* and *Harris* (76), and was applied to study Mössbauer parameters of several iron-containing compounds.

3. Heme Models for Molecular Orbital Calculations

The model which represents the heme group in MbCO, HbCO, MbO$_2$, HbO$_2$, Mb, and Hb for the MO calculations is shown in Fig. 22a. This planar representation of the heme (73) is based on Koenig's (81) X-ray structure analysis of hemin. Fig. 22b indicates the steric arrangement in a plane perpendicular to the heme. The proximal histidine group was represented by a water molecule. To study the ligand influence upon the electronic structure of iron in MbCO, HbCO various assumptions were made as to the Fe—C bond length, the Fe—C—O bond angle β, the position of the Fe atom relative to the heme, and the occupancy of one of the two axial ligand binding sites of iron (see Table 7). Corresponding changes will be studied for MbO$_2$, HbO$_2$. It is specific to the three sterostructural models used for Mb, Hb (Fig. 23) that the ferrous iron is pentacoordinated and out of the heme plane. This assumption seems to be reasonable from the interpretation of X-ray data of *Muirhead et al.* on deoxyhemoglobin (82). The MO calculations for Mb, Hb have been carried out with the axes convention as defined in Fig. 23; this is only as a reminder that the EFG component is probably oriented more parallel to the heme than perpendicular to it. For MbCO, HbCO the common convention used is that the z-axis is parallel to the heme normal.

139
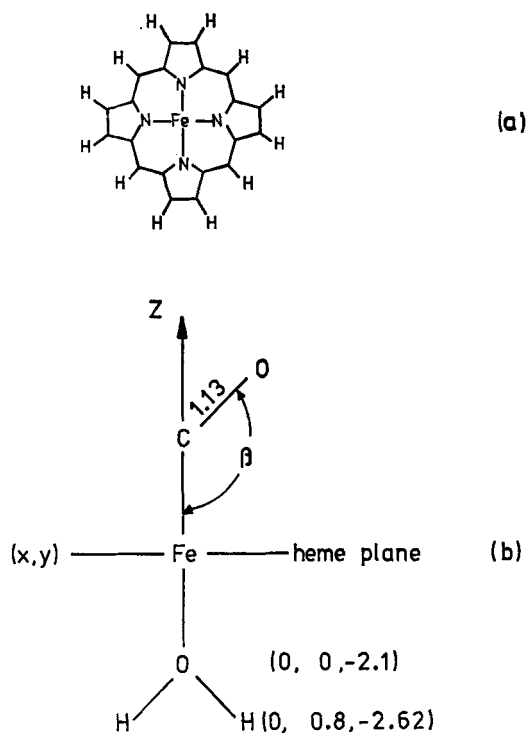
Fig. 22. Molecular structure of the heme group (a) and of MbCO or HbCO (b) for MO calculations. The proximal histidine group was replaced by a water molecule

4. Isomer Shift

The isomer shift in Mössbauer spectroscopy, δ, depends upon the electron density at the nucleus under study, $\varrho(0)$. Values of δ are proportional to changes in $\varrho(0)$ from a reference compound: $\delta = \alpha \cdot \varrho(0)$, where α is known as the calibration constant, having a value of $\alpha = -0.249 \pm 0.025\ a_0^3$ mm/sec (83, 84) for Fe^{57}. An estimate of δ or $\varrho(0)$ from approximate MO calculations is based on ideas developed by Flygare and Havemeister (85). Since only Fe $3d$, $4s$, $4p$, and ligand $2s$, $2p$ atomic orbitals (AO's) are included in the iterative extended Hückel (IEH) and CI-calculations, the Fe $1s$, $2s$, $3s$ contributions to $\varrho(0)$ have to be estimated by taking into account: (i) the lack of orthogonality of Fe $1s$, $2s$, $3s$ AO's to IEH MO's or CI MO's ϕ_i, and (ii) the shielding effects on $|\Psi_{ns}(0)|^2$ due to the specific electronic configuration $3d^q 4s^r$ of the compound under study. The electron density at the Fe nucleus may then

140
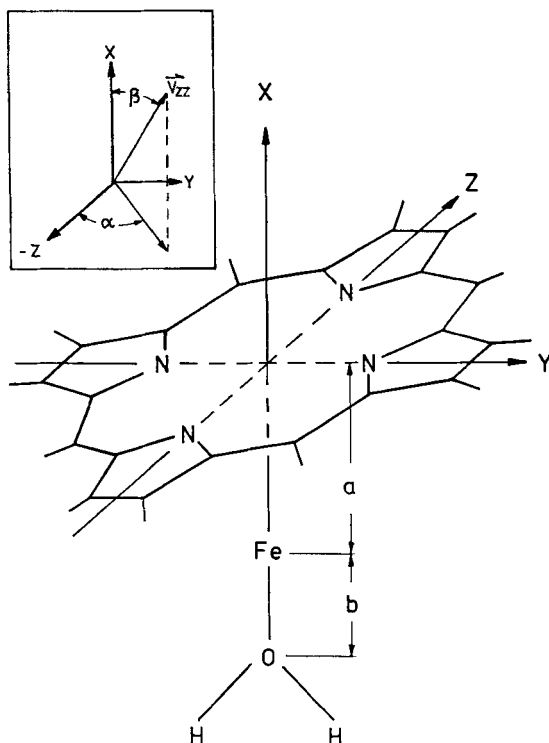
Fig. 23. Stereostructural models for Mb or Hb: (1) $a = 0.4$ Å, b $= 2.09$ Å; (2) $a = 0.4$ Å, b $= 2.34$ Å; (3) $a = 0.8$ Å, $b = 2.34$ Å. The insert defines the orientation of $\vec{V}_{ZZ}$ with respect to the heme coordinate system

be written (*83*):

$$\varrho(0) = r|\Psi_{4s}(0)|^2 + 2 \cdot \sum_{n=1}^{3} |\phi_{ns}(0)|^2 , \text{ with} \tag{10}$$

$$\phi_{3s}(0) = N_{3s}(\Psi_{3s}(0) - \sum_{i \, \neq \, 3_S} <\phi_i|\Psi_{3s}> \phi_i(0)) ,$$

$$\phi_{2s}(0) = N_{2s}(\Psi_{2s}(0) - \sum_{i \, \neq \, 2_S} <\phi_i'|\Psi_{2s}> \phi_i'(0)) , \text{ and} \tag{11}$$

$$\phi_{1s}(0) = N_{1s}(\Psi_{1s}(0) - \sum_{i \, \neq \, 1_S} <\phi_i''|\Psi_{1s}> \phi_i''(0)) .$$

In Eqs. (10) and (11) Ψ_{ns} refers to Fe AO's and ϕ_i to IEH MO's or CI MO's, depending on the level of approximation. For the diamagnetic (low-spin ferrous) compounds MbCO and HbCO the use of closed-shell

141

IEH MO's will be a reasonable approximation, whereas one must take open-shell CI MO's for the description of paramagnetic (high-spin ferrous) compounds like Mb and Hb. The wave functions ϕ_i' and ϕ_i'' in Eq. (11) are given by $\phi_i' = \phi_{3s} + \phi_i$ and $\phi_i'' = \phi_{2s} + \phi_{3s} + \phi_i$. Thus in $\varrho(0)$ all cross-terms $\Psi_{ns}(0)\Psi_{ms}(0)$ which have been attributed to be significant $(83, 86, 87)$ are included. The Fe $4s$ population factor r, the normalization factor N_{ns}, and the MO's ϕ_i are determined through IEH MO calculations for MbCO and HbCO and through CI MO calculations for Mb and Hb. The evaluation of overlap integrals $<\phi_i|\Psi_{ns}>$ is based on Hartree-Fock atomic orbitals (88). The values $\Psi_{ns}(0)$ in Eqs. (10) and (11) were taken from fully relativistic Dirac-Fock calculations, carried out by *Freeman et al.* (89). The actual values of $\Psi_{ns}(0)$ used either for MbCO, HbCO or Mb, Hb were determined for the appropriate electronic configuration $3d^q 4s^r$ of iron by interpolation between the values given in Table 4. The direct ligand contributions $\Psi_{lig}(0)$ at the iron nucleus entering Eq. (11) have been estimated by using STO's and were found to be negligible.

Table 4. Electron densities (in a_0^{-3}) for iron as derived from fully relativistic mixed configuration Dirac-Fock calculations. (Taken from Ref. 84)

Configuration	$3d^7 4s^1$	$3d^7$	$3d^6 4s^1$	$3d^6$	$3d^5 4s^1$	$3d^5$
$|\Psi_{1s}(0)|^2$	6799.018	6799.054	6798.881	6798.917	6798.653	6798.688
$|\Psi_{2s}(0)|^2$	644.299	644.259	644.231	644.169	644.225	644.153
$|\Psi_{3s}(0)|^2$	87.753	87.477	88.727	88.480	90.380	90.206
$|\Psi_{4s}(0)|^2$	3.092		5.575		8.213	

Comparing electron densities $\varrho(0)$ of similar systems, *i.e.* $\varrho(0)$ of MbCO, HbCO with $\varrho(0)$ of Mb, Hb, it may be believed that systematic uncertainties in $\varrho(0)$ for example due to the approximate character of the IEH and CI calculations are cancelled in evaluating $\Delta\varrho(0)$.

The calculated change in $\varrho(0)$ under complex-formation of Mb, Hb with CO is then compared with the difference in experimental isomer shifts, $\Delta\delta = \delta_{Mb, Hb} - \delta_{MbCO, HbCO}$. By applying the Eq. $\Delta\delta = \alpha \cdot \varrho(0)$ it is possible to compare the ratio $\dfrac{\Delta\delta}{\Delta\varrho}$ with the known value of α. In Table 5 the electron densities $\varrho_{ns}(0)$ calculated as described above for MbCO, HbCO (model 9, see Fig. 22b and Table 7) and for Mb, Hb (model 1, see Fig. 23) together with the calculated orbital occupancies $3d^q 4s^r$ and the experimental values of δ are summarized. Taking $\Delta\varrho$

Table 5. Experimental isomer shifts δ, calculated electronic configurations $3d^q 4s^r$ for iron, and caculated electron densities $\varrho_{ns}(0)^c)$ at the Fe nucleus for MbCO, HbCO and Mb, Hb

Compound	exp. $\delta^a)$ (mm/sec)	Configuration$^b)$	$\varrho_{1s}(0)$	$\varrho_{2s}(0)$	$\varrho_{3s}(0)$	$\varrho_{4s}(0)$
MbCO, HbCO	0.27 ± 0.03	$3d^{6.36} 4s^{0.18}$	13600.9	1280.9	184.6	0.82
Mb, Hb	0.93 ± 0.03	$3d^{6.25} 4s^{0.22}$	13599.8	1283.2	180.46	1.16

a) Values of δ versus metallic iron are mean values taken from MbCO, HbCO and Mb, Hb of various species.

b) Configurations $3d^q 4s^r$ as derived from IEH MO calculations for MbCO, HbCO and from CI MO calculations for Mb, Hb.

c) Values of $\varrho_{ns}(0)$ as derived from Eq. (10) and (11) of the text.

and $\varDelta\delta$ from Table 5 the isomer shift calibration constant is derived as $\alpha = -0.253 \pm 0.023 \; a_0^3$ mm/sec, which is in reasonable agreement with the value $\alpha = -0.249 \pm 0.025 \; a_0^3$ mm/sec from other investigations (*83, 84*).

From examination of the heme geometries of Figs. 22, 23 and the results listed in Table 5 it is obvious that the drastic decrease of δ, *i.e.* the drastic increase of $\varrho(0)$ during the reaction of CO with Mb or Hb, is mainly due to the increased overlap distortion contributions $- \sum <\phi_i|\Psi_{3s}> \phi_i(0) > 0$ and $N_{3s} > 1$ to $\phi_{3s}(0)$, since in $<\phi_i|\Psi_{3s}>$ the contributions $<\Psi_{CO}|\Psi_{3s}>$ for MbCO, HbCO are considerably larger than the corresponding contributions $<\Psi_{H_2O}|\Psi_{3s}>$ for Mb, Hb. In other words: due to the stronger interaction between ligands and iron in MbCO, HbCO compared to Mb, Hb the Fe $3s$ contribution $\phi_{3s}^2(0)$ to $\varrho(0)$ is considerably higher in MbCO, HbCO than in Mb, Hb.

5. Quadrupole Splitting and Electric Field Gradient Tensor

From the calculated electronic MO structures for the various models of Fig. 23 one obtains quadrupole splittings

$$\varDelta E_Q = \frac{1}{2} e Q V_{ZZ} \left(1 + \frac{\eta^2}{3}\right)^{1/2}. \tag{12}$$

The nuclear quadrupole moment Q is taken to be $+0.21$ b (*76, 77, 79, 90*). The main component of the EFG tensor, V_{ZZ}, is defined by $|V_{ZZ}| \geq |V_{yy}| \geq |V_{xx}|$ and results together with the asymmetry parameter

$$\eta = \frac{|V_{xx} - V_{yy}|}{|V_{ZZ}|} \tag{12a}$$

143

from diagonalizing the EFG tensor V_{pq}, which contains valence and lattice contributions

$$V_{pq} = V_{pq}^{\mathrm{val}} + V_{pq}^{\mathrm{lat}} \; ; \; p,q = x,\, y,\, z \, . \tag{13}$$

The tensor V_{pq}^{val} has been calculated with the equivalence

$$V_{pq}^{\mathrm{val}} = <\|\mathrm{EFG}\|> e\,(1-R) <r^{-3}> L_{pq} \, . \tag{13a}$$

The reduced matrix element $<\|\mathrm{EFG}\|>$ takes the value 2/7 for d electrons, 6/5 for p electrons, and 0 for s electrons. The quantity e represents the (positive!) elementary charge, and $<r^{-3}>$ is the radial factor resulting from taking the expectation value of $(3z^2 - r^2)/r^5$. The $<r^{-3}>_{3d}$ are taken from estimates (91) based on *Clementi's* (88) atomic Hartree-Fock wave functions: 4.49 a.u. for Fe configuration $3d^7$, 5.09 a.u. for $3d^6$, and 5.73 a.u. for $3d^5$. The actual value of $<r^{-3}>_{3d}$ is determined for each model from its calculated Fe $3d$ orbital occupancy by interpolation between the foregoing values. The *Sternheimer* shielding correction (92) is taken as $(1-R)_{3d} = 0.68$. Since we find for the three models of Mb, Hb the configuration $3d^{6.25}$ from MO calculations we derive for ΔE_Q^0 (Mb, Hb) $= (1/2)\, e^2 Q\,(1-R)_{3d} <r^{-3}>_{3d}\, 4/7$ the value 4.1 mm/sec. For Fe $4p$ electrons the quantity $(1-R)_{4p} <r^{-3}>_{4p}$ is taken to be 1/3 of the corresponding quantity for the $3d$ electrons (77, 93). Finally the tensor L_{pq} results from an appropriate summation over expectation values $<\Psi_{h'}|\hat{l}_{pq}|\Psi_h>$, namely

$$L_{pq} = \sum_{h'h} <\Psi_{h'}|\hat{l}_{pq}|\Psi_h> \, , \tag{13b}$$

where $\Psi_{h'}$ and Ψ_h are single-electron atomic orbitals (AO) of iron, and the single-electron operators l_{pq} acting an Ψ_h are:

$$\hat{l}_{pq} = \frac{1}{2}(\hat{l}_p\hat{l}_q + \hat{l}_q\hat{l}_p) = \frac{1}{2}\hat{l}(\hat{l}+1)\,\delta_{pq} \, . \tag{14}$$

For iron $3d$, $4s$, and $4p$ AO's all possible matrix elements are summarized in Table 6.

6. Spin-Orbit Coupling and Temperature-Dependent Electric Field Gradient Tensor

In high spin ferrous compounds we are concerned with electronic states $|\Gamma,\gamma,S,\gamma_s>$ characterized by irreducible representations Γ and by total spin $S = 2$. All irreducible representations Γ of the regarded symmetry

Table 6. Matrix elements $\langle\Psi_h|\hat{l}_{pq}|\Psi_h\rangle$ with Fe AO's having the sequence $|3d, yz\rangle$, $|3d, xz\rangle$, $|3d, xy\rangle$, $|3d, z^2\rangle$, $|3d, x^2-y^2\rangle$, $|4s\rangle$, $|4p, x\rangle$, $|4p, y\rangle$, $|4p, z\rangle$. l_{zz} is obtained from $l_{zz} = -l_{xx} - l_{yy}$

$$l_{xx} = \begin{bmatrix}
2 & 0 & 0 & & & & & & \\
0 & -1 & 0 & & & & & & \\
0 & 0 & -1 & & & & & & \\
& & & 1 & \sqrt{3} & & & & \\
& & & \sqrt{3} & -1 & & & & \\
& & & & & 0 & & & \\
& & & & & & -2/3 & 0 & 0 \\
& & & & & & 0 & 1/3 & 0 \\
& & & & & & 0 & 0 & 1/3
\end{bmatrix}$$

$$l_{yy} = \begin{bmatrix}
-1 & 0 & 0 & & & & & & \\
0 & 2 & 0 & & & & & & \\
0 & 0 & -1 & & & & & & \\
& & & 1 & -\sqrt{3} & & & & \\
& & & -\sqrt{3} & -1 & & & & \\
& & & & & 0 & & & \\
& & & & & & 1/3 & 0 & 0 \\
& & & & & & 0 & -2/3 & 0 \\
& & & & & & 0 & 0 & 1/3
\end{bmatrix}$$

$$l_{xz} = \frac{1}{2}\begin{bmatrix}
0 & 0 & -3 & & & & & & \\
0 & 0 & 0 & & & & & & \\
-3 & 0 & 0 & & & & & & \\
& & & 0 & -\sqrt{3} & & & & \\
& & & \sqrt{3} & 0 & & & & \\
& -\sqrt{3} & & & & 0 & & & \\
& & & & & & 0 & 0 & -1 \\
& & & & & & 0 & 0 & 0 \\
& & & & & & -1 & 0 & 0
\end{bmatrix}$$

$$l_{yz} = \frac{1}{2}\begin{bmatrix}
0 & 0 & 0 & & & & & & \\
0 & 0 & -3 & & & & & & \\
0 & -3 & 0 & & & & & & \\
& & & -\sqrt{3} & & & & & \\
& & & 3 & & & & & \\
& & & & & 0 & & & \\
& & & & & & 0 & 0 & 0 \\
& & & & & & 0 & 0 & -1 \\
& & & & & & 0 & -1 & 0
\end{bmatrix}$$

$$l_{xy} = \frac{1}{2}\begin{bmatrix}
0 & -3 & 0 & & & & & & \\
-3 & 0 & 0 & & & & & & \\
0 & 0 & 0 & & & & & & \\
& & & 0 & 0 & & & & \\
& & & 2\sqrt{3} & 0 & & & & \\
& & & 0 & 2\sqrt{3} & 0 & & & \\
& & & & & & 0 & -1 & 0 \\
& & & & & & -1 & 0 & 0 \\
& & & & & & 0 & 0 & 0
\end{bmatrix}$$

145

group C_{2V} are one-dimensional, and thus γ can be neglected. For convenience the spin states $|S=2, \gamma_s>$ are linear combinations of the spin states $|S=2, m_s>$, which transform according to irreducible representations of C_{2V}. This can be achieved similar to the construction of d-orbitals $|yz>$, $|xz>$ ... from $|L=2, m_L>$.

The five-fold spin degeneracy of each state is lifted by spin-orbit interaction:

$$\hat{H}_{\text{s.o.}} = -\lambda \hat{L} \cdot \hat{S}, \tag{15}$$

where the coupling constant λ is commonly related to the free ion value, $\lambda_0 = 103$ cm^{-1}, by a reduction factor $\alpha^2 : \lambda = \alpha^2 \lambda_0$ (94). The eigenvectors $|e_\alpha>$ of this problem, having energies E_α are certain linear combinations of the base vectors $|\Gamma, S, \gamma_s>$:

$$|e_\alpha> = \sum_{\Gamma, \gamma_s} C^a_{\Gamma, \gamma_s} |\Gamma, S, \gamma_s> . \tag{16}$$

The coefficients C^a_{Γ, γ_s} and the corresponding energies E_α result from diagonalizing the spin-orbit interaction matrix $<\Gamma', S, \gamma_s' |\hat{H}_{\text{s.o.}}|\Gamma, S, \gamma_s>$. Since we are interested in quadrupole splittings, ΔE_Q, we calculate for each state $|e_\alpha>$ its relevant EFG tensor:

$$V^a_{pq} = <e_\alpha|\hat{V}_{pq}|e_\alpha>, \tag{17}$$

where V_{pq} is defined through Eqs. (13) and (14). In order to evaluate the temperature dependence of the EFG one must average the components V^a_{pq} of the individual substates $|e_\alpha>$ according to Boltzmann statistics:

$$<V_{pq}>_T = \sum_a V^a_{pq} \exp\left(-\frac{E_\alpha}{kT}\right) \Big/ \sum_a \exp\left(-\frac{E_\alpha}{kT}\right). \tag{18}$$

Diagonalization of $<V_{pq}>_T$ leads to $V_{ZZ}(T)$, to $\eta(T)$, to the orientation of $V_{ZZ}(T)$ and finally through Eq. (12) to $\Delta E_Q(T)$.

The spin-orbit interaction matrix $<\Gamma', S, \gamma_s' |\hat{H}_{\text{s.o.}}|\Gamma, S, \gamma_s>$ and the EFG tensor elements $<\Gamma', S, \gamma_s'|\hat{V}_{pq}|\Gamma, S, \gamma_s>$ may be simplified by

$$<\Gamma', S, \gamma_s'|\lambda\hat{L} \cdot \hat{S}|\Gamma, S, \gamma_s> = \lambda <\Gamma'|\hat{L}|\Gamma><S, \gamma_s'|\hat{S}|S, \gamma_s>$$

$$<\Gamma', S, \gamma_s'|\hat{V}_{pq}|\Gamma, S, \gamma_s> = <\Gamma'|\hat{V}_{pq}|\Gamma> \delta_{\gamma_s' \gamma_s}.$$

The evaluation of matrix elements $<\Gamma'|\hat{Q}|\Gamma>$, with $\hat{Q} = \hat{V}_{pq}$ or $\hat{L}_p$ are discussed in the following section.

7. Spin-Orbit Matrix and Electric Field Gradient Tensor Derived from Many-Electron Molecular Orbital Wave Functions

From the Hückel one-electron wave functions $\phi_k = \sum_h a_{kh} \Psi_h$, with ϕ_k representing MO's and Ψ_h AO's, configurations (CFG) are built up by constructing appropriate Slater determinants $|\mathrm{CFG}> = \{\phi_{\overline{k1}}, \phi_{\overline{k2}}, ..., \phi_{\overline{km}}\}$. Here $\phi_{\overline{ki}}$ is a molecular spin orbital (MSO). If the CFG's describing high-spin ferrous states are different from each other by only a single MSO, which may be denoted by $\overline{k}$, we write $|\mathrm{CFG}, \overline{k}> = \{\phi_{\overline{k1}}, \phi_{\overline{k2}}, ..., \phi_{\overline{km-1}}, \phi_{\overline{k}}\}$.

Taking into account Coulomb interaction (configuration interaction CI) one gets new terms $|\mathrm{CI}, l>$ which are in general linear combinations of $|\mathrm{CFG}, \overline{k}>$:

$$|\mathrm{CI}, l> = \sum_{\overline{k}} m_{l\overline{k}} |\mathrm{CFG}, \overline{k}> . \tag{20}$$

With the wave functions defined in Eq. (20) we now calculate matrix elements of the operator $\hat{Q}$, which stands here for the EFG tensor operator $\hat{V}_{pq}$ or the orbital angular momentum. We get

$$<\mathrm{CI}, l'|\hat{Q}|\mathrm{CI}, l> = \sum_{\overline{k}', \overline{k}} m_{l'\overline{k}'} \, m_{l\overline{k}} <\mathrm{CFG}, \overline{k}'|\hat{Q}|\mathrm{CFG}, \overline{k}> . \tag{21}$$

The matrix elements $<\mathrm{CFG}, \overline{k}'|\hat{Q}|\mathrm{CFG}, \overline{k}>$ in Eq. (21) are represented by (95)

$$<\mathrm{CFG}, \overline{k}|\hat{Q}|\mathrm{CFG}, \overline{k}> = <\phi_{\overline{k}}|\hat{Q}|\phi_{\overline{k}}> + \sum_{i=1}^{m-1} <\phi_{ki}|\hat{Q}|\phi_{ki}> \tag{22a}$$

for $\overline{k}' = \overline{k}$, and

$$<\mathrm{CFG}, \overline{k}'|\hat{Q}|\mathrm{CFG}, \overline{k}> = <\phi_{\overline{k}'}|\hat{Q}|\phi_{\overline{k}}> \tag{22b}$$

for $\overline{k}' \neq \overline{k}$.

Using the convention $k = \overline{k}$, k_i the quantities $<\phi_{k'}|\hat{Q}|\phi_k>$ are given in terms of AO's by

$$<\phi_{k'}|\hat{Q}|\phi_k> = \sum_{h', h} a_{k'h'} \, a_{kh} <\Psi_{h'}|\hat{Q}|\Psi_h> . \tag{23}$$

Thus Eq. (21) becomes:

$$<\mathrm{CI}, l'|\hat{Q}|\mathrm{CI}, l> = \sum_{h', h} C_{(l'l)(h'h)} <\Psi_{h'}|\hat{Q}|\Psi_h> , \tag{24}$$

where the coefficients $C_{(l'l)(h'h)}$ are defined by

$$C_{(l'l)(h'h)} = \delta_{l'l} \, C_{h'h} + \overline{C}_{(l'l)(h'h)} ,$$

$$C_{h'h} \qquad = \sum_k a_{kh'} \, a_{kh} \, ,$$

$$\overline{C}_{(l'l)(h'h)} = \sum_{k'} m_{l'k'} \, m_{k'h'} \sum_k m_{lk} m_{kh} \, .$$

Now, concerning $<\Psi_{h'}|\hat{Q}|\Psi_h>$ of Eq. (24) we distinguish three different matrix elements $<\Psi_{h'}|\hat{Q}|\Psi_h>$, $<\Psi_{h'}|\hat{Q}|\Psi_{h''}>$, and $<\Psi_{h''}|\hat{Q}|\Psi_{h'''}>$ where the indices h, h' stand for Fe AO's and h'', h''' for ligand AO's, respectively. With this convention Eq. (24) can be rewritten into:

$$
\begin{aligned}
<\mathrm{CI},l'|\hat{Q}|\mathrm{CI},l> = &\sum_{h',h} C_{(l'l)(h'h)} <\Psi_{h'}|\hat{Q}|\Psi_h> \\
&+ \sum_{h',h''} (C_{(l'l)(h'h'')} \pm C_{(l'l)(h''h')}) <\Psi_{h'}|\hat{Q}|\Psi_{h''}> \quad (25) \\
&+ \sum_{h'',h'''} C_{(l'l)(h''h''')} <\Psi_{h''}|\hat{Q}|\Psi_{h'''}> \, .
\end{aligned}
$$

The "$+$" sign in Eq. (25) corresponds to the case where $\hat{Q}$ represents a real operator (EFG), the "$-$" sign to the case where $\hat{Q}$ represents a complex operator (orbital momentum). The matrix elements $<\Psi_{h'}|\hat{Q}|\Psi_{h''}>$, representing cross-terms between iron AO's and ligand AO's, can be transformed by introducing a completeness relation of orthogonal terms $|\Psi_{\bar{h}}>$, which contain the iron AO's $|\Psi_{h'}>$:

$$<\Psi_{h'}|\hat{Q}|\Psi_{h''}> = \sum_{\bar{h}} <\Psi_{h'}|\hat{Q}|\Psi_{\bar{h}}><\Psi_{\bar{h}}|\Psi_{h''}> \, . \qquad (26)$$

Since $\hat{Q}$ does not lead out of the subspace of $|\Psi_{h'}>$, the summation can be restricted to iron orbitals, and we get:

$$<\Psi_{h'}|\hat{Q}|\Psi_{h''}> = \sum_h <\Psi_{h'}|\hat{Q}|\Psi_h> S_{hh''} \, , \qquad (27)$$

where $S_{hh''}$ stands for the overlap integrals between iron AO's Ψ_h and ligand AO's $\Psi_{h''}$.

From Eqs. (25) and (27) matrix elements for the spin-orbit interaction and for the EFG tensor can be calculated. For the evaluation of matrix elements $<\hat{H}_{s.o.}>$ from Eq. (25) we use the "$-$" sign and neglect the pure ligand contributions $<\Psi_{h''}|\hat{Q}|\Psi_{h'''}>$. In the case of the EFG, V_{pq} is derived using the "$+$" sign in Eq. (25). Two parts can be distinguished: (i) the so-called valence contribution

$$
\begin{aligned}
V_{pq}^{\mathrm{val}} = \sum_{h',h} [C_{(l'l)(h'h)} + \sum_{h''} (C_{(l'l)(h'h'')} + C_{(l'l)(h''h')}) S_{hh''}] \\
<\Psi_{h'}|\hat{V}_{pq}|\Psi_h>
\end{aligned}
\qquad (28)
$$

with $<\Psi_{h'}|\hat{V}_{pq}|\Psi_h>$ being obtained from Eqs. (13a), (13b), and (14), and (ii) the so-called lattice contribution

$$V_{pq}^{\text{lat}} = \sum_{h'', h'''} C_{(l'\,l)(h''\,h''')} <\Psi_{h''}|\hat{V}_{pq}|\Psi_{h'''}> . \qquad (29)$$

Assuming the ligand charges q_a to be localized at lattice points (R_{xa}, R_{ya}, R_{za}) we can approximatel V_{pq}^{lat} of Eq. (29) to

$$V_{pq}^{\text{lat}} = (1 - \gamma_\infty) \sum_a q_a (3\,R_{pa}\,R_{qa} - \delta_{pq}\,R_a^2)/R_a^5, \; (p,q = x, y, z), \qquad (30)$$

where q_a and (R_{xa}, R_{ya}, R_{za}) are the charge and the cartesion coordinates of the ath ligand, and $(1 - \gamma_\infty)$ represents the Sternheimer antishielding (92) of iron-core electrons due to ligand charges.

Information is obtained from the MO calculations concerning the coefficients $C_{(l'\,l)\,(h'\,h)}$, $C_{(l'\,l)\,(h''\,h')}$, and $C_{(l'\,l)\,(h'\,h'')}$, the overlap $S_{hh''}$, and the atomic charges q_a. Thus the problem of calculating $\Delta E_Q(T)$, $\eta(T)$ and the orientation of the EFG component V_{ZZ} is easily solved using the formalism described in the foregoing sections.

8. Discussion of Molecular Orbital Quadrupole Splittings for MbCO, HbCO

From IEH MO calculations for MbCO, HbCO total energies E, quadrupole splittings ΔE_Q and atomic charges q_a of iron and its nearest neighbors have been derived for ten different molecular structures (96). The results in Table 7 show that the original molecular geometry of *Zerner et al.* (73) (no. 1 in Table 7) results in a ΔE_Q far from the experimental value ($\Delta E_{Q, \text{exp}} \approx 0.35$ mm/sec). Adding a water molecule to the system lowers E but increases ΔE_Q (no. 2). Rotating the water around the z-axis in steps of $20°$ has no significant effect on E or ΔE_Q. Moving the iron into the plane of the four nitrogens reduces both E and ΔE_Q (no. 3). By taking away the water molecule and reducing the Fe—C distance to 1.64 Å (no. 4) E increases but ΔE_Q decreases. The total energy is decreased by changing the heme geometry from planar (Z) to nonplanar (K) (no. 5), and ΔE_Q was lowered further. Therefore it was used for the remaining calculations f molecular geometry K, without water, and iron in the plane of the four nitrogens; all three conditions have the effect of reducing ΔE_Q in the direction of the experimental value. Further reduction of ΔE_Q and E was obtained by reducing the Fe–C distance to 1.54 Å.

We then rotated the CO molecule from $\beta = 180°$ to $135°$ in steps of $15°$ (nos. 6–9). The total energy increased slightly. However, our estimate

149

Table 7. Mössbauer and MO parameters as derived from IEH MO calculations for several molecular geometries of MbCO, HbCO

Structure no.	1	2	3	4	5	6	7	8	9	10
Geometry of heme[a]	Z_0	Z_0	Z_i	Z_i	K_i	K_i	K_i	K_i	K_i	K_i
H_2O[b]	no	yes	yes	no	no	no	no	no	no	no
Fe–C distance, Å[c]	1.84	1.84	1.84	1.64	1.64	1.54	1.54	1.54	1.54	1.40
β[c]	180°	180°	180°	180°	180°	180°	165°	150°	135°	135°
Total energy E, eV[d]	−2137.0	−2271.6	−2274.8	−2137.9	−2141.4	−2141.09	−2141.07	−2141.04	−2140.5	−2139.5
E_Q calc, mm/sec[e]	1.85	2.25	1.75	1.15	0.87	0.73	0.66	0.60	0.52	0.60
Atomic Charges Fe	0.25	0.26	0.27	0.29	0.27	0.30	0.28	0.28	0.30	0.30
N_1–N_4	−0.11	−0.12	−0.12	−0.10	−0.10	−0.10	−0.10	−0.10	−0.09	−0.10
C of CO	−0.04	−0.04	0	−0.06	−0.01	−0.03	−0.02	−0.02	−0.03	−0.05

a) Z denotes the planar heme geometry described in Ref. (73). K stands for the nonplanar heme geometry as derived by X-ray analysis of α-chlorohemin, Ref. (81). The indices i and o indicate, respectively, that the iron is in the heme plane or that it is out of plane by 0.5 Å in the direction of the CO.

b) "yes" and "no" indicates whether or not there is a water molecule bound to iron as shown in Fig. 22b.

c) Fe–C distance and bond angle β are defined in Fig. 22b.

d) Total energy as derived from IEH calculations.

e) Calculated EFG is positive for all structures; V_{zz} is approximately aligned along the z-axis (heme normal) of Fig. 22b.

of ΔE_Q indicates that a bending angle $\beta \approx 135°$ is more favorable than a linear geometry. A further decrease of the Fe–C distance seems undesirable, because both E and ΔE_Q increase again (no. 10). For all geometries, the net charge calculated for the iron atom is in agreement with previous calculations for other low-spin compounds (73, 76). Calculated spin multiplicities (96) and the ΔE_Q data of Table 7 for the ground electronic state both favor a bent geometry (no. 9) for Fe–C–O in MbCO, HbCO, in opposition to the fact that the linear geometry has a slightly lower calculated total energy. The indicators for the bent geometry are probably more reliable than the total energy, as simple approximate closed shell MO studies are known to be far better at describing gross charge distributions than they are at predicting electron repulsion energies. Incidentally, it should be noted that the present results suggest that it might be unwise to attach too much significance to the energy minimum found recently by Halton (97), and which we also reproduced (98), (at a closed shell level of approximation) for bent Fe–O–O in oxyhemoglobin.

Overall, the results for the bent geometry are remarkably close to those found for the linear geometry by *Zerner et al.* (73, 91). This near coincidence is due to the fact that their study used different atomic parameters than ours. Zerner's parameters were chosen to fit transition energies of the porphyrin system itself, while ours (72, 76–80, 96) were based on a total of approximately 60 molecules of diverse structure, non-heme compounds, and not all containing iron. We therefore argue, that our parameter set may be the more reliable for discussing changes in predicted spectral properties with changes in geometry. A bent structure is also consistent with X-ray studies on the carbon monoxide complex of erythrocruorine (99) which indicate an Fe–C–O angle of $145° \pm 15°$. However, note that our calculations do not take into account any side chains which might stabilize the CO in a bent geometry.

The final conclusion from a MO interpretation of Mössbauer results then is that in MbCO, HbCO the bonding between the heme iron and the proximal histidine is very weak, the iron is situated in or nearly in the heme plane, in agreement with recent findings (99), the Fe–C distance is somewhat smaller than the typical iron-carbonyl distance of 1.84 Å; and a Fe–C–O bond angle of $< 180°$ is more likely than a linear geometry.

9. Remarks Concerning MbO_2, HbO_2

An estimate of ΔE_Q for MbO_2, HbO_2 by *Weissbluth et al.* (91) on the basis of MO results of *Zerner et al.* (73) for a heme model with O_2 binding parallel to the porphyrin ring (Griffith model), led to $\Delta E_Q = 2.1$ mm/sec

with $V_{ZZ} < 0$. This is in agreement with experimental findings (see Fig. 8b and 10); V_{ZZ}, here, is oriented parallel to the heme plane.

Preliminary MO results for MbO_2, HbO_2 on an approximate closed shell level have been presented recently (98). These results indicate that there are energetically close-lying, unoccupied MO terms above the highest doubly occupied MO's. Recent Heitler-London calculations on the bonding of oxygen to hemoglobin by *Otsuka et al.* (100) indicate, that paramagnetic electronic configurations indeed play an important role for the explanation of the diamagnetism of MbO_2 or HbO_2. For these reasons the use of configuration interaction (CI) seems necessary to derive a satisfactory picture of structure and bonding of $Fe-O_2$ in MbO_2, HbO_2. Such CI calculations for several stereostructural arrangements of O_2 with respect to the heme are in progress.

10. Discussion of Molecular Orbital Quadrupole Splittings and Susceptibilities for Mb, Hb

For the following discussion spin-orbit interaction has been restricted to states which are defined by Fig. 24 and which have been found to be lowest in energy by CI calculations. According to C_{2v} symmetry of the three models (Fig. 23) presently under study these states may be characterized by irreducible representations $^5A_2$, $^5B_1$, and $^5B_2$. To study the effect of an energetically low-lying, low-spin term on $\Delta E_Q(T)$ and $\eta(T)$ we added the state $^1A_1$ (Fig. 24) to our investigation. Since the

$$\phi_{66} = 0.4584 \,|\, 3z^2-r^2 > - \ 0.7977 \,|\, x^2-y^2 > + \text{lig.}$$

$$\phi_{65} = 0.7247 \,|\, 3z^2-r^2 > - \ 0.4178 \,|\, x^2-y^2 > + \text{lig.}$$

$$\phi_{64} = 0.9944 \,|\, yz > + \text{ligand contributions}$$

$$\phi_{63} = 0.9223 \,|\, xy > + \quad '' \qquad ''$$

$$\phi_{62} = 0.9174 \,|\, xz > + \quad '' \qquad ''$$

doubly occupied MO states ϕ_i $\quad i = 1 - 61$
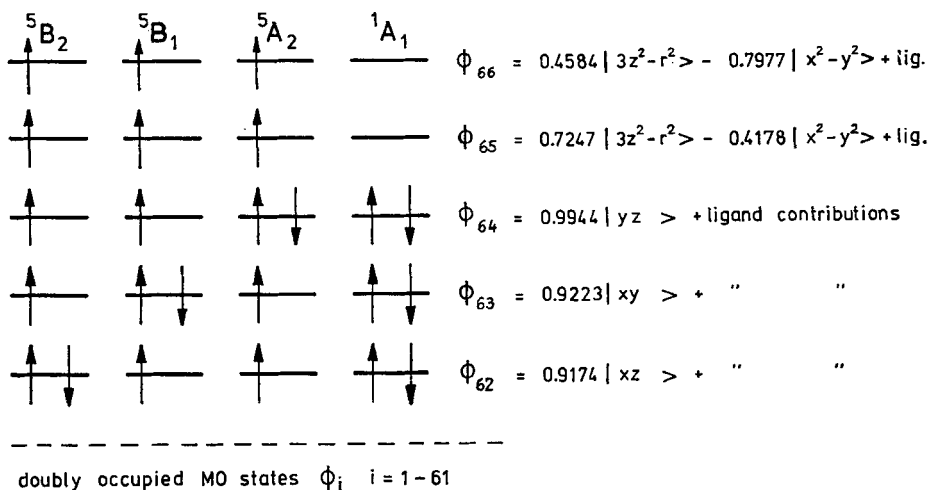
Fig. 24. Many-electron states which are used to calculate $\Delta E_Q(T)$, $\eta(T)$, and $\chi(T)$. The coefficients of $\phi_{i+n}(n = 1, ..., 5)$ represent the situation for model (1) of Fig. 23

four states have different irreducible representations the coefficient matrix $m_{l\bar{k}}$ of Eq. (20) will remain diagonal, independent of the energy separations of the four states. Thus, one gets the simple relation $|CI, l> = |CFG, \bar{k}>$ instead of Eq. (20). This allows variation of the mutual energy separations between $^5A_2$, $^5B_1$, $^5B_2$ and $^1A_1$ without changing the states $|CI, l>$.

For each of the three models in Fig. 23 calculations along the lines described above have been carried out (101) to obtain $\Delta E_Q(T)$, $\eta(T)$, sign V_{ZZ}, and the orientation of $\vec{V}_{ZZ}$ relative to the heme coordinate system. Some from the variety of resulting $\Delta E_Q(T)$ curves for various energies $E (^5A_2)$, $E (^5B_1)$, $E (^5B_2)$ and $E (^1A_1)$ are shown in Figs. 25–27 for spin-orbit coupling constant $\lambda = 90$ cm^{-1}, and in Figs. 28 and 29 for $\lambda = 75$ cm^{-1}. The "+" or "−" sign at each curve indicate the calculated sign of the EFG component V_{ZZ}. The energies, asymmetry parameters, and orientations of $\vec{V}_{ZZ}$ corresponding to each $\Delta E_Q(T)$ curve of Fig. 28a and 29a are tabulated in Table 8. Experimental $\Delta E_Q(T)$ data for frozen Mb solution (53) are indicated by closed circles, for a Mb single crystal (42) by "x" and error bars, and for frozen Hb (rat) solution (52) by open circles and error bars; the sign of V_{ZZ} was experimentally determined to be positive from Mb single crystal Mössbauer measurements (42) and from magnetic hyperfine split Mössbauer spectra of Hb (51) (Figs. 9c and d).

Comparing theoretical $\Delta E_Q(T)$ curves with experimental $\Delta E_Q(T)$ data from Mb and Hb reasonable coincidence of computational and experimental results is found only for curve b in Fig. 28a. From inspection of Table 8 it is obvious that this $\Delta E_Q(T)$ curve corresponds to an EFG component $\vec{V}_{ZZ}$ being oriented along the heme axis y. This result agrees well with the recent findings from Mössbauer investigations of Mb single crystals at 77 °K (42). There an angle of $\alpha = 40° \pm 8°$ was found between $\vec{V}_{ZZ}$ and the crystallographic b axis of the Mb single crystal, indicating that $\vec{V}_{ZZ}$ possibly is oriented along one of the two heme axes y or z.

The asymmetry parameters $\eta(T)$ (from Table 8) which are related with the $\Delta E_Q(T)$ and fit curve b of Fig. 28a also agree with the Mb single crystal Mössbauer results. In Ref. (42) the angle $\alpha = 40° \pm 8°$ was derived assuming η to be zero. A most recent computational analysis of our former Mb single crystal Mössbauer data by Maeda et al. (62), however, indicates that $\alpha = 40° \pm 8°$ is consistent also with an η-parameter in the range of $0 \leq \eta \leq 0.3$.

The energy separation $E (^1A_1) - E (^2B_2)$ which was varied in some cases (Figs. 25–27) between 50 and 10,000 cm^{-1} is sensitive only to the slope of the theoretical $\Delta E_Q(T)$ curves for temperatures $T > 50$ °K, and, further, $\Delta E_Q(T)$ curves up to $T = 200$ °K are identical for $E (^1A_1) - E (^2B_2) = 300$ cm^{-1} and $E (^1A_1) - E (^5B_2) = 10,000$ cm^{-1}.

Table 8. Energies of spin quintet states (in cm^{-1}), temperature dependent quadrupole splittings (in mm/sec), and asymmetry parameters. The angles α and β (in degrees) defining the orientation of $\vec{V}_{ZZ}$ with respect to the heme coordinate system of Fig. 23 are for all curves 28a and 29a and for temperatures $4.2 \leq T \leq 200\,°$K given by $\alpha = 90°$, $\beta = 90°$

Figure	Curve	Energies of			Calculated parameters for temperatures T (in °K)					
		$^5B_2$	$^5B_1$	$^5A_2$	4.2	50	75	100	150	200
	a	0	150	150	ΔE_Q 2.157	2.118	2.139	2.101	1.934	1.748
					η 0.461	0.436	0.420	0.419	0.447	0.494
28a	b	0	150	175	ΔE_Q 2.228	2.211	2.235	2.196	2.019	1.820
					η 0.355	0.341	0.327	0.325	0.341	0.377
	c	0	150	200	ΔE_Q 2.299	2.303	2.330	2.290	2.103	1.891
					η 0.249	0.246	0.236	0.230	0.235	0.261
29a	a	0	120	160	ΔE_Q 2.242	2.181	2.204	2.175	2.025	1.850
					η 0.369	0.326	0.309	0.307	0.320	0.336
	b	0	120	180	ΔE_Q 2.313	2.269	2.294	2.265	2.112	1.931
					η 0.421	0.371	0.352	0.352	0.372	0.394

Though we find $\Delta E_Q(T)$ curves corresponding to $E(^1A_1) - E(^5B_2) \approx 100$ cm^{-1}, which fit the experimental $\Delta E_Q(T)$ data, we present arguments why an energy separation of $E(^1A_1) - E(^5B_2) \gtrsim 300$ cm^{-1} seems to be more realistic. In addition to the static molecular structure of Fig. 23 one has to consider lattice vibrations which have the effect that the potential V of the iron contains higher terms than the static ligand field potential $V^{(0)}$ (102):

$$V = V^{(0)} + V^{(1)} \varepsilon + V^{(2)} \varepsilon^2 + \cdots . \tag{31}$$

The quantity ε in Eq. (31) represents an isotropic average of the strain tensor, and $V^{(1)}$, $V^{(2)}$, ... describe orbital-lattice interactions. The transition probability of a direct process between states $|a>$ and $|b>$ is given by

$$
\begin{aligned}
W_{ab}^{\text{dir}} &= \tfrac{2\pi}{\hbar} |<a, N-1 | V^{(1)} \varepsilon | b, N>|^2 \varrho(E) \\
&= \tfrac{2\pi}{\hbar} |<a | V^{(1)} | b>|^2 |<N-1 | \varepsilon | N>|^2 \varrho(E) ,
\end{aligned} \tag{32}
$$

where $N = $ occupation number of phonons, and $\varrho(E) = $ phonondensity of final states. W_{ab} is zero if $|a>$ stands for a spin quintet and $|b>$ for a spin singlet, because $V^{(1)}$ is spin independent and spin-orbit coupling mixes high-spin and low-spin states via intermediate spin-triplets only. Thus
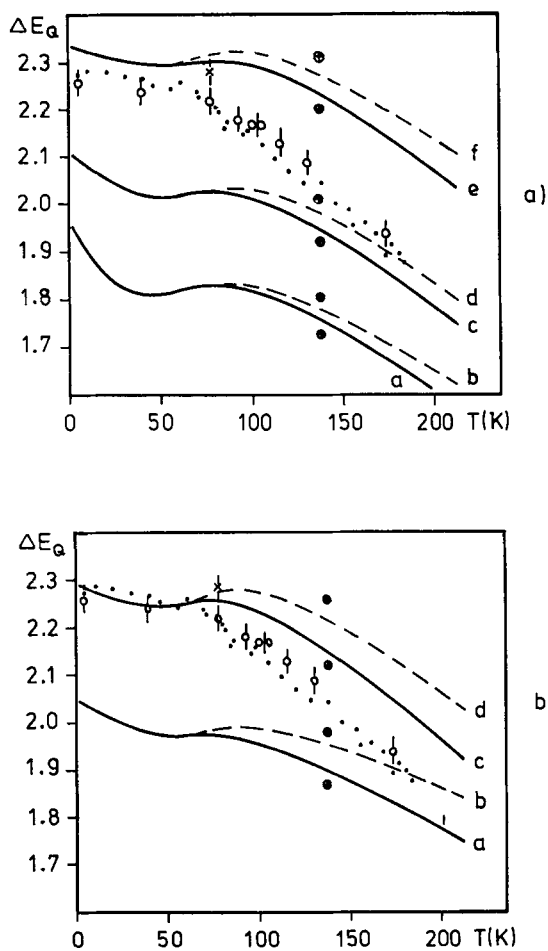
Fig. 25. Temperature dependent quadrupole splittings for model (3). $\lambda = 90$ cm^{-1}. Experimental $\Delta E_Q(T)$ data for frozen Mb solution [Ref. (53)] are indicated by closed circles, for a Mb single crystal [Ref. (42)] by "x" and error bars, and for frozen Hb (rat) solution [Ref. (52)] by open circles and error bars. Energies $^5B_2$, $^5B_1$, $^5A_2$, and $^1A_1$ in cm^{-1} corresponding to $\Delta E_Q(T)$ curves are:

(25a)					(25b)				
a	0	150	100	50	a	0	50	300	50
b	0	150	100	10000	b	0	50	300	10000
c	0	200	100	50	c	0	100	300	50
d	0	200	100	10000	d	0	100	300	10000
e	0	300	100	50					
f	0	300	100	10000					
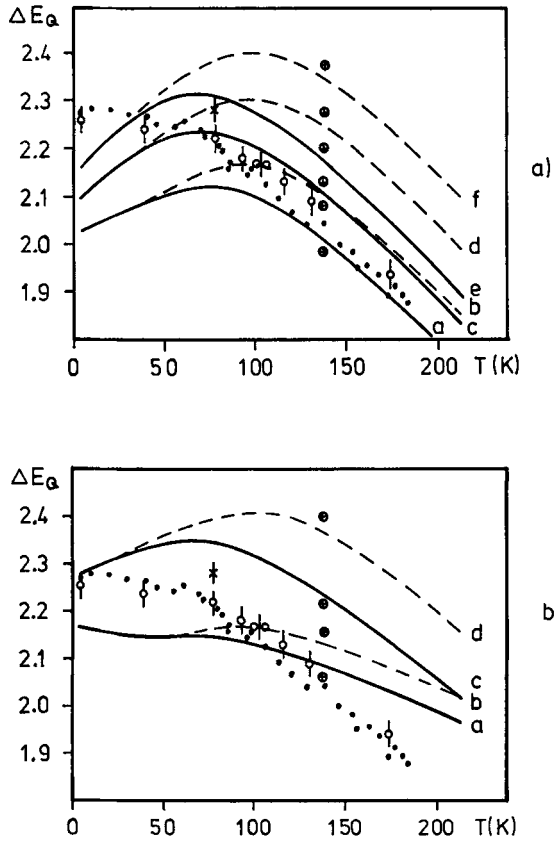
Fig. 26. Temperature dependent quadrupole splittings for model (2). $\lambda = 90$ cm^{-1}. Experimental $\Delta E_Q(T)$ data are defined in Fig. 25. Energies for $^5B_2$, $^5B_1$, $^5A_2$ and $^1A_1$ in cm^{-1} corresponding to ΔE_Q curves are:

(26a)	a	0	300	400	50	(26b)	a	0	400	200	50
	b	0	300	400	10000		b	0	400	200	10000
	c	0	300	600	50		c	0	400	400	50
	d	0	300	600	10000		d	0	400	400	10000
	e	0	300	1000	50						
	f	0	300	1000	10000						

$<a|V^{(1)}|b> = 0$. In the real case the transition probability W_{ab} might be slightly different from zero since the state $|a> (|b>)$ might be a linear combination of a spin quintet (spin singlet) state and a small contribution of its counterpart due to spin–spin interactions.
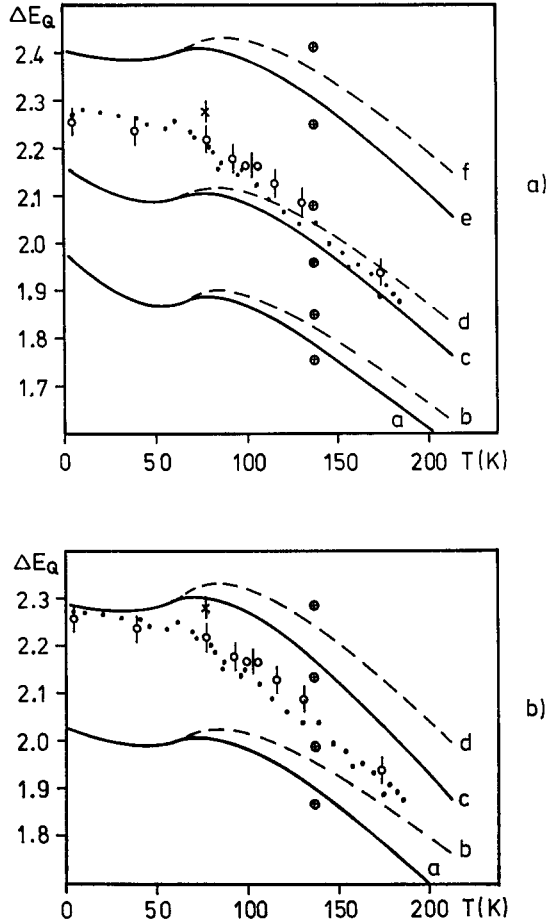
Fig. 27. Temperature dependent quadrupole splittings for model (1). $\lambda = 90$ cm^{-1}. Experimental $\Delta E_Q(T)$ data are defined in Fig. 25. Energies for $^5B_2$, $^5B_1$, $^5A_2$, and $^1A_1$ in cm^{-1} corresponding to ΔE_Q curves are:

(27a)	a	0	150	150	50	(27b)	a	0	100	300	50
	b	0	150	150	10000		b	0	100	300	10000
	c	0	200	150	50		c	0	150	300	50
	d	0	200	150	10000		d	0	150	300	10000
	e	0	300	150	50						
	f	0	300	150	10000						

W_{ab} being very small, however, means that the spin-lattice relaxation between $|a>$ and $|b>$ is very slow. With the spin-lattice relaxation time becoming larger than the precession time of the Fe^{57} nucleus

two separate Mössbauer spectra would appear, one corresponding to the spin quintet $|a>$ and the other to the spin singlet $|b>$, and the thermal average for evaluating $\Delta E_Q(T)$ should be only over the high-spin states. There are several examples of such high-spin low-spin transitions in the literature (103) for compounds containing ferrous iron. In believing in slow spin-lattice relaxation between high- and low-spin states in deoxygenated myoglobin and hemoglobin one might try to explain Mössbauer spectra of deoxygenated hemoglobins, containing small-intensity lines (see Fig. 9a) by thermal mixtures of high- and low-spin quadrupole splittings. The ΔE_Q value associated with the $^1A_1$ state of about 1.3 mm/sec would be just in agreement with the "impurity" line positions of Fig. 9a. However, the intensity ratio, R, of low-spin to high-spin lines should be temperature dependent, in contrast to the experimental results for example of deoxygenated hemoglobin single chains (104), which sometimes under certain preparational conditions also show these "impurity" lines. Assuming the $^1A_1$ state to lie in energy above the spin quintet ground state by 50 cm^{-1} (300 cm^{-1}) the intensity ratio R would be unmeasurably small at $T = 4.2$ °K; at an elevated temperature of $T = 300$ °K the ratio R is estimated from energies E_α to be about 8% (2%). For these reasons we believe the energy separation $E(^1A_1) - E(^5B_2)$ to be at least 300 cm^{-1}, thus the spin singlet $^1A_1$ does not influence our $\Delta E_Q(T)$ curves at all.

To assess the reliability of the MO results further the energy terms E_α corresponding to curve b in Fig. 28a are taken to compute temperature-dependent magnetic susceptibilities $\chi(T)$. The χ-tensor χ_{pq} with $p, q = x, y, z$ is defined by

$$\chi_{pq} = \left. \frac{\partial M_p}{\partial H_q} \right|_{H_q \approx 0}. \tag{33}$$

M_p represents the magnetization per mole. According to Eq. (33) we may write

$$M_p = \sum_q \chi_{pq} H_q; \tag{33a}$$

and the tensor elements χ_{pq} we derive from

$$\chi_{pq} = \mu_B^2 A \sum_{\alpha', \alpha} <e_\alpha | \hat{L}_p + 2\hat{S}_p | e_{\alpha'}> <e_{\alpha'} | \hat{L}_q + 2\hat{S}_q | e_\alpha>$$
$$\cdot \left[\frac{\exp(-E_{\alpha'}/kT) - \exp(-E_\alpha/kT)}{E_{\alpha'} - E_\alpha} \right]. \tag{34}$$
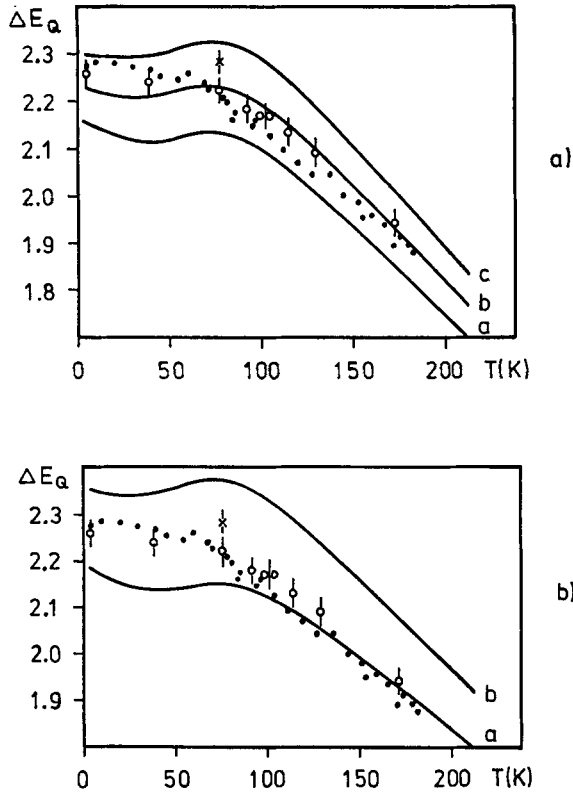
Fig. 28. Temperature dependent quadrupole splittings for model (1). $\lambda = 75$ cm^{-1}. Experimental $\Delta E_Q(T)$ data are defined in Fig. 25. Energies for $^5B_2$, $^5B_1$, $^5A_2$ and $^1A_1$ in cm^{-1} corresponding to ΔE_Q curves are:

(28a)						(28b)				
	a	0	150	150	10000		a	0	200	100	10000
	b	0	150	175	10000		b	0	200	150	10000
	c	0	150	200	10000						

The spin states $|e_\alpha>$ have already been defined by Eq. (16), and the E_α are their corresponding energies. Symbol A stands for the Avogadro number. For cases of degeneracy we simply take

$$\lim_{E_{a'} \to E_a} \frac{\exp(-E_{a'}/kT) - \exp(-E_a/kT)}{E_{a'} - E_a} = \frac{\exp(-E_a/kT)}{kT}.$$

The final powder susceptibility $\chi(T)$ results from $\chi(T) = (1/3) \sum_p \chi_{pp}$, where $p = x, y, z$. The solid $\chi(T)$ curve in Fig. 30 corresponds to the $\Delta E_Q(T)$ fit curve b in Fig. 28a. Closed circles in Fig. 30 are experimental
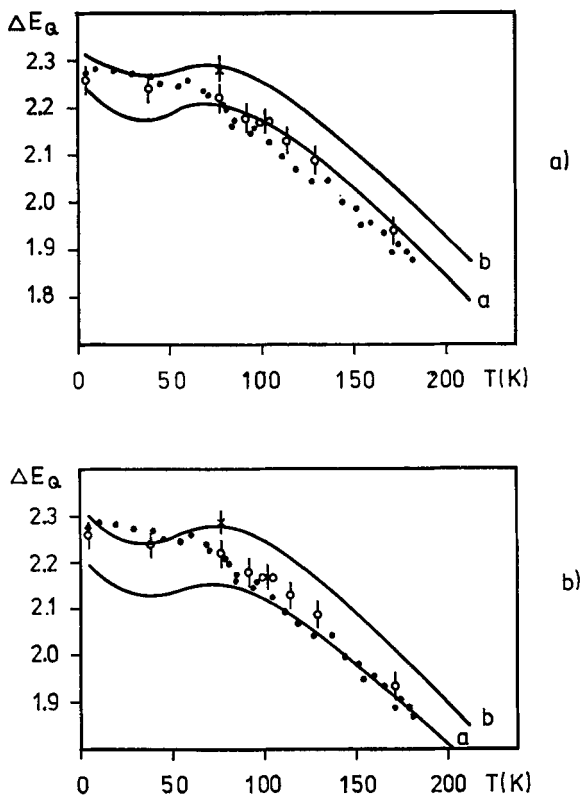
Fig. 29. Temperature dependent quadrupole splittings for model (3). $\lambda = 75$ cm^{-1}. Experimental $\Delta E_Q(T)$ data are defined in Fig. 25. Energies for $^5B_2$, $^5B_1$, $^5A_1$ and $^1A_1$ in cm^{-1} corresponding to ΔE_Q curves are:

(29a)	a	0	120	160	10000	(29b)	a	0	180	100	10000
	b	0	120	180	10000		b	0	180	120	10000

points taken from the susceptibility investigation of Mb and Hb by *Nakano et al.* (69). The $\chi(T)$ curves corresponding to $\Delta E_Q(T)$ curves a and b in Fig. 29a are nearly identical to the solid line of Fig. 30; the broken line, however, represents the situation that spin triplet states lie close to the spin quintet ground state with energy separations $E(^3E\,\eta) - E(^5B_2) = 200$ cm^{-1} and $E(^3E\,\xi) - E(^5B_2) = 300$ cm^{-1}. Thus, by comparing solid line, broken line, and experimental points in Fig. 30, we conclude that the energy sequence $^5B_2$, $^5B_1$, $^5A_1$ gives a more realistic picture for deoxygenated heme compounds than the formerly derived ligand field result (52) with an energy sequence of $^5A_2$, ^3E (105).
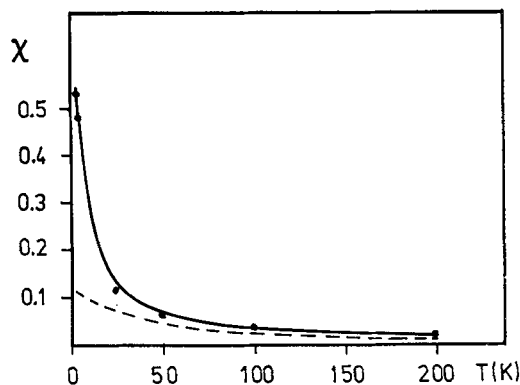
Fig. 30. Temperatures dependent suceptibilities. Solid line corresponds to energies as specified for $\Delta E_Q(T)$ curve b of Fig. 28a. Broken line corresponds to energetically low-lying spin triplet states (see text). Experimental points are taken from Ref. (69). χ is given in emu per mole

Summarizing the results, the present MO interpretation of experimental Mössbauer and susceptibility data of deoxygenated heme proteins is approximate, in the sense that in the three models under study (Fig. 23) we neglected the protein part of the molecule, several peripheral side chains and the probable non-planarity of the heme group, that we represented the histidine group by a water molecule, and further, that we assumed all interatomic distances to remain constant within the whole temperature range of $4.2\,^\circ K \leq T \leq 200\,^\circ K$; moreover, the MO procedure itself is approximate as described in Refs. (72) and (76). These simplifications, however, are believed to be secondary in the present attempt to derive a gross description of the structural situation of the heme iron in deoxygenated heme compounds. From the work described it is therefore concluded that the MO interpretation of experimental Mössbauer and susceptibility data consistently agrees with the assumption that the heme iron in Mb and Hb is pentacoordinated and significantly out of "plane" (by $0.4-0.8$ Å, Fig. 23). The interpretation of recent X-ray data of Mb (106) and of Hb (82) partly support these findings, namely that the heme iron in Mb, Hb is penta-coordinated.

VIII. Experimental Solution of the Phase Problem for Protein Structure Determination by Mössbauer Scattering

The principle of phase determination by utilizing the interference between electronic and nuclear resonance scattering and its application to proteins has been described in detail by *Parak et al.* (107). Here, we

briefly review the expectations and difficulties concerning the application of this new method to heme proteins.

For the determination of the electron density map of a molecule the amplitudes and phases of the waves scattered by a single crystal are required for a number of Bragg reflections. Common X-ray techniques yield the product $(A_H e^{i\varphi_H}) \cdot (A_H e^{-i\varphi_H}) = A_H^2$, where A_H is the amplitude and φ_H the phase of the sum of all waves scattered by the electrons of the molecule into the Bragg reflection H. Thus, the scattering amplitude A_H is obtained, but the phase information is lost. The solution of this phase problem for protein structure determination is based on Perutz' and Kendrew's isomorphous replacement method (108–111). In this procedure Bragg reflections have to be measured at least three times, first on a crystal of native molecules, and then on two crystals, in which reference scatterers (for example Hg atoms) have been substituted at well-defined positions. From the difference of the measured intensities one can calculate the relative phases without ambiguity.

A supplementary method for the isomorphous replacement method is to provide an additional scatterer in the crystal. Applying the Mössbauer scattering technique (see II.5 and Fig. 2b) to single crystals of hemeproteins has the advantages that the Fe^{57} scatterer is originally built into the protein, and that the nuclear scattering amplitude theoretically amounts to 6.215 times the scattering amplitude for the 80 electrons of one mercury atom. Therefore, Fe^{57} obviously is well suited as a reference scatterer in iron-containing proteins. Further, the wave-length of the Fe^{57} 14.4 keV γ-radiation of $\lambda = 0.86$ Å is comparable to atomic spacings in the crystal, and the radiation scattered by the Fe^{57} nucleus can interfere with the radiation scattered by the electron shell of an atom (112, 113). Additionally, it is important to note, that for a unique phase determination, the Fe^{57} nucleus is sufficient as a single reference scatterer compared to the twofold heavy atom substitution in the isomorphous replacement method. This can be understood in the following way. The phase of resonantly scattered γ-radiation is shifted by $\frac{\pi}{2}$ with respect to the incident γ-radiation from the source S in Fig. 2b. Moving the source with a Doppler velocity $v \gg v_r$ relative to the heme protein single crystal destroys the nuclear resonance scattering which occurs at resonance velocity v_r by Doppler effect. The nuclear scattering amplitude is then equal to zero, and the phase shift between incoming and the non-resonantly scattered wave also becomes zero. Decreasing the Doppler velocity v and approaching v_r increases both the phase shift and the nuclear scattering amplitude. By arbitrary choice of two different Doppler velocities close to v_r, two different nuclear scattering amplitudes with known absolute value and phase can be selected as an alternative for the two

heavy atom scattering amplitudes of the isomorphous replacement method (107, 114). The construction of the phase angle φ_H with the use of the two known nuclear scattering amplitudes. n_{Fe} and $\tilde{n}_{Fe}$ and the primarily known scattering amplitude $F_0(H)$, not including nuclear resonance scattering, then is analogous to the procedure for the X-ray structure analysis (Fig. 31).

Fig. 31. Principle of the phase determination [Taken from Ref. (114)]. $n_{Fe}(\tilde{n}_{Fe})$ is the nuclear resonance scattering amplitude, $F_0(H)$ is the scattering amplitude of the unit cell, not including nuclear resonance scattering, $F_{0A}(H)$ $(\tilde{F}_{0A}(H))$ represents the scattering amplitude of the unit cell, including the nuclear resonance scattering. n_{Fe} and $F_{0A}(H)$ correspond to Doppler velocity v_r, and $\tilde{n}_{Fe}$, $\tilde{F}_{0A}(H)$ to $\tilde{v}$ ($\tilde{v}$ is very clos to v_r). $\varphi_0(H) = \tilde{\varphi}_0(H)$ is the correct phase, which should be determined.

For these reasons the Mössbauer scattering technique in principle is a suitable alternative to the isomorphous replacement method. Several experimental difficulties, however, as for example the preparation of strong Co^{57} sources (up to 500 mCi/mm^2), the enrichment of heme-protein single crystals with Fe^{57} (49), and the experimentation at low temperatures (77 °K) (115), have prevented the nuclear resonance

scattering method for protein structure determination from becoming successful so far; in particular the struggle continues for the determination of the first phase value φ_H.

IX. References

1. *Debrunner, P.:* In: Spectroscopic approaches to biomolecular conformation (ed. *D. W. Urry*), p. 209—262. Chicago: American Medical Ass. Press 1969.
2. *Lang, G.:* Quart. Rev. Biophys. *3*, 1 (1970).
3. *Gonser, U., Grant, R. W., Kregdze, J.:* Appl. Phys. Letters *3*, 189 (1963); Science *143*, 680 (1964). — *Gonser, U., Grant, R. W.:* Biophys. J. *5*, 823 (1965).
4. *Karger, W.:* Ber. Bunsenges. Physik. Chem. *68*, 793 (1963).
5. *Lang, G., Marshall, W.:* Proc. Phys. Soc. (London) *87*, 3 (1966).
6. *May, L.:* Index of Publications in Mössbauer Spectroscopy of Biological Materials, *1961—1973*. The Catholic University of America, Washington, D.C., 20017.
7. *Weissbluth, M.:* Struct. Bonding *2*, 2—125 (1967).
8. *Bearden, A. J., Dunham, W. R.:* Struct. Bonding *8*, 1—52 (1970).
9. *Lang, G.:* (in preparation).
10. *Münck, E.:* (in preparation).
11. *Mössbauer, R. L.:* Z. Physik *151*, 125 (1958); Naturwissenschaften *45*, 538 (1958).
12. *Frauenfelder, H.:* The Mössbauer effect. New York: Benjamin Inc. 1962.
13. *Boyle, A. F. J., Hall, H. E.:* Rept. Progr. Phys. *25*, 441 (1962).
14. *Abragam, A.:* L'effet Mössbauer. New York: Gordon and Breach 1964.
15. *Wertheim, G. K.:* Mössbauer effect. Principles and applications. New York: Academic Press 1964.
16. *Goldanskii, V. I.:* The Mössbauer effect and its applications in chemistry. New York: Consultants Bureau 1964.
17. *Wegener, H.:* Der Mössbauer Effekt und seine Anwendungen in Physik und Chemie. Mannheim: Bibliographisches Institut AG 1965.
18. *Gruverman, I. J.* (ed.): Mössbauer effect methodology, Vol. 1—5, New York: Plenum Press 1965, 1966, 1967.
19. *Krivoglaz, M. A.:* The Mössbauer effect and its application in solid state physics. Inst. Nauchn. Inform. Akad. Nauk SSSR, Moscow 1965 (in Russian).
20. Applications of the Mössbauer effect in chemistry and solid state physics. Intern. At. Energy Agency, Techn. Repts. Ser. No. 50, Vienna 1966.

21. *Freeman, A. J., Frankel, R. B.* (eds): Hyperfine interactions. New York–London: Academic Press 1967.
22. *Matthias, E., Shirley, D. A.* (eds.): Hyperfine structure and nuclear reaction. Amsterdam: North-Holland 1968.
23. *Goldanskii, V. I., Herber, R. H.* (eds.): Chemical applications of Mössbauer spectroscopy. New York: Academic Press 1968.
24. *Greenwood, N. N., Gibb, T. C.:* Mössbauer spectroscopy. London: Chapman and Hall 1971.
25. *Frauenfelder, H., Lustig, H.* (eds.): First Conf. on the Mössbauer Effect. Univ. of Illinois, Urbana, Ill., 1960, U.S. Air Force Rept. TN-60-698.
26. *Compton, D. M. T., Schoen, A. H.* (eds.): Proc. Second Intern. Conf. on the Mössbauer Effect, Saclay, France 1961. New York: Wiley 1962.
27. *Bearden, A. J.* (ed.): Proc. Third. Intern. Conf. on the Mössbauer Effect. Cornell Univ., Ithaca, N.Y. 1963, published in Rev. Mod. Phys. *36*, 333 (1964).
28. *Goldring, G., Kalish, R.* (ed.): Hyperfine interactions in excited nuclei, Vol. 1—4. Gordon and Breach 1971.
29. *Cohen, S. G., Pasternak, M.* (ed.): Perspectives in Mössbauer spectroscopy. Plenum Press 1973.
30. *Dezsi, I.* (ed.): Proceeding of the Conference on the Application of the Mössbauer Effect. Tihany, Hungary, Akameiai Kiado, Budapest, 1971.
31. Proceedings of the "5th International Conference on Mössbauer Spectroscopy", (to be published), Bratislava (CSSR), Sept. 3—7, 1973.
32. *Frauenfelder, H.:* Proceedings of Mössbauer spectroscopy in biological systems (ed. by *P. Debrunner, J. C. M. Tsibris, E. Münck*). University of Illinois, Urbana, Ill., 17th—18th March, 1969.
33. *Visscher, W. M.:* Ann. Phys. 9, 194 (1960).
34. *Chow, H. K., Weise, R. F., Flinn, P.:* Report NSEC-4023-1 AEC, 1969, Nuclear ScienceDivision, Intern. Chem. and Nuclear Corp., Irvine, Calif. 92664.
35. *Cohen, R. L., McMullin, P. S., Wertheim, G. K.:* Rev. Sci., Instr. *34*, 671 (1963).
36. *Conrad, H., Mayer, A., Thomas, H. P., Vogel, H.:* J. Mol. Biol. *41*, 225 (1969).
37. *Schneider, R., Mayer, A., Schmatz, W., Kaiser, B., Scherm, R.:* J. Mol. Biol. *41*, 231 (1969).
38. *Schneider, R., Schmatz, W., Mayer, A., Eicher, H., Schelten, J., Franzel, R.:* (private communication).
39. *Perutz, M. F., Muirhead, H., Cox, J. M., Goaman, L. C. G., Mathews, F. S., Mc Gandy, E. L., Webb, C. E.:* Nature *219*, 29 (1968).
40. *Perutz, M. F., Muirhead, H., Cox, J. M., Goaman, L. C. G.:* Nature *219*, 131 (1968).
41. *Grant, R. W., Cape, J. A., Gonser, U., Topol, L. E., Saltman, P.:* Biophys. J. 7, 651 (1967).
42. *Trautwein, A., Maeda, Y., Gonser, U., Parak, F., Formanek, H.:* Proceedings of the 5th International Conference in Mössbauer Spectroscopy, Bratislava (CSSR), Sept. 1973. — *Gonser, U., Maeda, Y., Trautwein, A., Parak, F., Formanek, H.:* Z. Naturforsch. *296*, 241 (1974).
43. *Cooke, R., Debrunner, P.:* J. Chem. Phys. *48*, 4532 (1958).
44. *Trautwein, A., Eicher, H., Mayer, A., Alfsen, A., Waks, M., Rosa, J., Beuzard, Y.:* J. Chem. Phys. *53*, 963 (1970).
45. *Dézsi, I.:* Proceedings of the International Conference on the Application of the Mössbauer Effect, Israel, August 1972.
46. *Lang, G.:* (private communication, 1974).
47. *Nozik, A. J., Kaplan, M.:* Chem. Phys. Letters *1*, 391 (1967).
48. *Trautwein, A., Eicher, H., Mayer, A.:* J. Chem. Phys. *52*, 2473 (1970).

49. *Parak, F., Formanek, H.:* Acta Cryst. *A 27,* 573 (1971).
50. *Trautwein, A., Maeda, Y., Harris, F. E., Formanek, H.:* Theoret. Chim. Acta (in press).
51. *Lang, G., Yonetani, T.:* (unpublished results).
52. *Eicher, H., Trautwein, A.:* J. Chem. Phys. *50,* 2540 (1969); J. Chem. Phys. *52,* 932 (1970).
53. *Eicher, H., Parak, F., Bade, D., Tejada, X., Kalvius, G. M.:* Presented at the International Conference on the Application of the Mössbauer Effect, Bendor (France), Sept. 1974.
54. *Wickman, H. H., Wertheim, G. K.:* In: Chemical applications of Mössbauer spectroscopy. New York: Academic Press 1968. — *Kündig, W.:* Nucl. Instr. Methods *48,* 219 (1967). — *Blume, M.:* Phys. Rev. *174,* 351 (1968). — *Blume, M., Tjou, I. A.:* Phys. Rev. *165,* 446 (1968). — *Zimmermann, R., Spiering, H., Ritter, G.:* Chem. Phys. *4,* 133 (1974).
55. *Lang, G.:* J. Phys. (Paris) Colloq. *32* C1—822 (1971).
56. *Münck, E., Groves, J. L., Tumollillo, T. A., Debrunner, P. G.:* Comput. Phys. Commun. *5,* 225 (1973).
57. *Münck, E., Champion, P. M.:* Heme proteins and model compounds: Mössbauer absorption and emission spectroscopy (preprint).
58. *Champion, P. M., Münck, E., Debrunner, P. G., Hollenberg, D. F., Hager, L. P.:* Biochemistry *12,* 426 (1973).
59. *Zory, P.:* Phys. Rev. *140,* A 1401 (1965).
60. *Buerger, M. J.:* In: The precession method. New York: Wiley 1964.
61. *Gonser, U., Grant, R. W.:* Phys. Stat. Solidi *21,* 331 (1967).
62. *Maeda, Y., Gonser, U., Trautwein, A.:* (in preparation).
63. *Kappler, H. M., Trautwein, A., Mayer, A., Vogel H.:* Nucl. Instr. Methods *53,* 157 (1967).
64. *Otsuka, J.:* J. Physical. Soc. Japan *24,* 885 (1968).
65. *Dale, B. W., Williams, R. J. P., Edwards, P. R., Johnson, C. E.:* J. Chem. Phys. *49,* 3445 (1968).
66. *Otsuka, J., Seno, Y.:* In: Symposium papers of the IVth International Biophysical Congress. Japan, 1973.
67. *Tasaki, A., Otsuka, J., Kotani, M.:* Biochim. Biophys. Acta *140,* 284 (1967).
68. *Eaton, W. A., Charney, E.:* J. Chem. Phys. *51,* 4502 (1969).
69. *Nakano, N., Otsuka, J., Tasaki, A.:* Biochim. Biophys. Acta *236,* 222 (1971).
70. *Huynh, B. H., Papaefthymion, G. C., Yen, C. S., Groves, J. L., Wu, C. S.:* preprint (1974).
71. *Pople, J. A., Beveridge, D. L.:* Approximate molecular orbital theory. New York: McGraw Hill 1970).
72. *Rein, R., Fukuda, N., Win, H., Clarke, G. A., Harris, F. E.:* J. Chem. Phys. *45,* 4743 (1966). — *Rein, R., Clarke, G. A., Harris, F. E.:* Quantum aspects of heterocyclic compounds in chemistry and biochemistry. II. Jerusalem, Israel Academy of Sciences and Humanities, 1970).
73. *Zerner, M., Gouterman, M., Kobayashi, H.:* Theoret. Chim. Acta *6,* 363 (1966).
74. *Johnson, K. H., Smith, F. C.:* Chem. Phys. Letters *7,* 541 (1970).
75. *Cusachs, L. C.:* J. Chem. Phys. *43,* 157 (1965). — *Cusachs, L. C., Reynolds, J. W.:* J. Chem. Phys. *43,* 160 (1965).
76. *Trautwein, A., Harris, F. E.:* Theoret. Chim. Acta *30,* 45 (1973).
77. *Trautwein, A., Harris, F. E.:* Phys. Rev. *B 7,* 4755 (1973).
78. *Trautwein, A., Regnard, J. R., Harris, F. E., Maeda, Y.:* Phys. Rev. *B 7,* 947 (1973).

79. *Trautwein, A., Kreber, E., Gonser, U., Harris, F. E.:* J. Phys. Chem. Solids (in press).
80. *Trautwein, A., Harris, F. E., Dézsi, I.:* Theoret. Chim. Acta (in press).
81. *Koenig, D. F.:* Acta Cryst. *18*, 663 (1965).
82. *Muirhead, H., Greer, J.:* Nature *228*, 516 (1970).
83. *Regnard, J. R., Pelzl, J.:* Phys. Stat. Solidi *56*, 281 (1973)
84. *Trautwein, A., Harris, F. E., Freeman, A., Desclaux, J. P.:* Phys. Rev. B (in press).
85. *Flygare, W. H., Hafemeister, D. W.:* J. Chem. Phys. *43*, 789 (1965).
86. *Šimánek, E., Šroubek, Z.:* Phys. Rev. *163*, 275 (1967).
87. *Šimánek, E., Wong, A. Y. C.:* Phys. Rev. *166*, 348 (1968).
88. *Clementi, E.:* IBM J. Res. Develop. Suppl. *9*, 2 (1965).
89. *Freeman, A., Desclaux, J. P.:* (private communication).
90. *Sharma, R. R.:* Phys. Rev. Letters *26*, 563 (1971).
91. *Weissbluth, M., Maling, J. E.:* J. Chem. Phys. *47*, 4166 (1967).
92. *Sternheimer, R. M.:* Phys. Rev. *130*, 1423 (1963).
93. *de Vries, J. L. K. F., Kreyzers, C. P., de Boer, F.:* Inorg. Chem. *11*, 1343 (1972).
94. *Ingalls, R.:* Phys. Rev. *133*, A 787 (1964).
95. *Griffith, J. S.:* The theory of transition metal ions. Cambridge: University Press 1964.
96. *Trautwein, A., Maeda, Y., Harris, F. E., Formanek, H.:* Theoret. Chim. Acta (in press).
97. *Halton, M. P.:* Theoret. Chim. Acta *23*, 208 (1971).
98. *Trautwein, A.:* In: Perspectives in Mössbauer effect spectroscopy (eds. S. C. Cohen and M. Pasternak), p. 101. New York: Plenum Press 1973.
99. *Huber, R., Epp, O., Formanek, H.:* J. Mol. Biol. *52*, 349 (1970).
100. *Otsuka, J., Matsuoka, O., Fuchikami, N., Seno, Y.:* J. Phys. Soc. Japan *35*, 854 (1973). — *Seno, Y., Otsuka, J., Matsuoka, O., Fuchikami, N.:* J. Phys. Soc. Japan *33*, 1645 (1972).
101. *Trautwein, A., Zimmermann, R., Harris, F. E.:* Theoret. Chim. Acta (in press).
102. *Orbach, R.:* Proc. Roy. Soc. (London) *A 264*, 458 (1961).
103. *König, E., Ritter, G.:* In: Mössbauer effect methodology, Vol. 9, *Gruverman*, ed.), 1974. — *König, E., Ritter, G., Zimmermann, R.:* J. Chem. Phys. (in press).
104. *Alpert, Y., Maeda, Y., Trautwein, A.:* (unpublished results).
105. In the investigation of Ref. (52), the symmetry was assumed to be C_{4v}. The $^5B_2$ term there corresponds to the irreducible representation $^5A_2$ of the symmetry group C_{2v} with our axes convention of Fig. 23.
106. *Nobbs, C. L., Watson, H. C., Kendrew, J. C.:* Nature *209*, 339 (1966).
107. *Parak, F., Mössbauer, R. L., Hoppe, W.:* Ber. Bunsenges. Physik. Chem. *74*, 1207 (1970).
108. *Green, D. W., Ingram, V. M., Perutz, M. F.:* Proc. Roy. Soc. (London) *A 225*, 287 (1954).
109. *Bragg, W. L., Perutz, M. F.:* Proc. Roy. Soc. (London) *A 225*, 315 (1954).
110. *Bodo, G., Dintris, H. M., Kendrew, J. C., Wyckoff, H. W.:* Proc. Roy. Soc. (London) *A 253*, 70 (1959).
111. *Perutz, M. F.:* In: Scientific American, Nov. 1964, p. 2.
112. *Black, P. J., Longworth, G., O'Connor, D. A.:* Proc. Phys. Soc. *83*, 925 (1964).
113. *Bernstein, S., Campell, E. C.:* Phys. Rev. *132*, 1625 (1963).
114. *Parak, F., Mössbauer, R. L., Biebl, U., Formanek, H., Hoppe, W.:* Z. Physik *244*, 456 (1971).
115. *Thomanek, U. F., Parak, F., Mössbauer, R. L., Formanek, H., Schwager, P., Hoppe, W.:* Acta Cryst. *A 29*, 263 (1973).

Structure and Bonding: Index Volume 1–20

STRUCTURE AND BONDING

Contents: J.-M.Lehn: Design of Organic Complexing Agents. Strategies towards Properties. - M.R.Truter: Structures of Organic Complexes with Alkali Metal Ions. - W.Simon, W.E.Morf, P.C.Meier: Specificity for Alkali and Alkaline Earth Cations of Synthetic and Natural Organic Complexing Agents in Membranes. - R.M.Izatt, D.J.Eatough, J.J.Christensen: Thermodynamics of Cation-Macrocyclic Compound Interaction.

Contents: U.Weser: Structural Aspects and Biochemical Function of Erythrocuprein. - R.R.Crichton: Ferritin. - M.Llinás: Metal-Polypeptide Interactions: The Conformational State of Iron Proteins. - F.L.Siegel: Calcium-Binding Proteins.

Contents: J.-H.Fuhrhop: The Oxidation States and Reversible Redox Reactions of Metalloporphyrins. - G.Blauer: Optical Activity of Conjugated Proteins. - T.J.R.Weakley: Some Aspects of the Heteropolymolybdates and Heteropolytungstates. - A.Novak: Hydrogen Bonding in Solids. Correlation of Spectroscopic and Crystallographic Data.

Contents: R.D.Shannon, H.Vincent: Relationships between Covalency, Interatomic Distances, and Magnetic Properties in Halides and Chalcogenides. - A.Kjekshus, T.Rakke: Considerations on the Valence Concept. - A.Kjekshus, T.Rakke: Geometrical Considerations on the Marcasite Type Structure. - G.C.Allen, K.D.Warren: The Electronic Spectra of the Hexafluoro Complexes of the Second and Third Transition Series.

Prices are subject to change without notice

**Springer-Verlag
Berlin
Heidelberg
New York**